Dynamic modeling and vibration analysis of mistuned bladed disks

Gísli Óttarsson

DYNAMIC MODELING AND VIBRATION ANALYSIS OF MISTUNED BLADED DISKS

by

Gísli Sigurbjörn Óttarsson

A dissertation submitted in the partial fulfillment
of the requirements for the degree of
Doctor of Philosophy
(Mechanical Engineering)
in The University of Michigan
1994

Doctoral Committee:

Associate Professor	**Christophe Pierre,**	Chairman
Professor	**William J. Anderson**	
Assistant Professor	**Gregory M. Hulbert**	
Associate Professor	**Ralph Peek**	
Associate Professor	**Noel C. Perkins**	

Never put off till tomorrow, what you can do the day after tomorrow

Til pabba

Acknowledgments

Initial thanks go to my advisor, Prof. Christophe Pierre, for his patient guidance, generosity and integrity.

My eternal love and gratitude to my wife and children for the wonderful years at 1502 McIntyre Drive and for supporting me through the rough moments. I would also like to thank my dear parents for *everything*.

Many thanks to my fellow students, in the Dynamics lab, for all the fruitful discussions. I won't name you but you know who you are.

A special thank you to Matt Castanier for his contributions to our joint efforts.

TABLE OF CONTENTS

CHAPTER

LIST OF FIGURES

Figure

CHAPTER I

INTRODUCTION

One of the most important problems that plague turbomachinery rotors is the existence of rogue blades — lone blades that exhibit unexpected fatigue failure. It has been recognized that rotor mistuning might be the cause of rogue blades through a phenomenon called normal mode localization, whereby vibration energy is confined to a few blades of the assembly [1–14]. The goals of this dissertation are **(1)** to achieve a thorough understanding of the fundamental mechanisms governing mistuning effects, **(2)** the development of mathematical models of turbomachinery rotors suitable for mistuning analysis, and **(3)** the development of techniques for designers interested in the mistuning sensitivity of a particular rotor design.

1.1. The Localization Phenomenon

1.1.1. Periodic Structures

A structure is said to be periodic, or tuned, if it consists of a chain of identical, identically connected substructures. Some examples of periodic structures are truss beams [15, 16] and multi-span beams [17]. In the special case where the first substructure is connected to the last one, the structure is said to have cyclic symmetry. Some models of turbomachinery rotors and large radial-rib antennas are excellent examples of periodic structures with cyclic symmetry.

Brillouin [18] published his pioneering research on electrical periodic structures in 1946. Subsequently many methods have been proposed for the analysis of periodic structures. Of these, combined transfer matrix and wave propagation methods [16, 19, 20, 21] have become the most prevalent tool and are used extensively throughout this dissertation.

Periodic structures may be classified by the number of coordinate through which the substructures interact, normally referred to as *coupling coordinates*. Brillouin [18] demonstrated that a periodic structure possesses as many pairs of characteristic waves

as there are coupling coordinates. Characteristic waves were shown to exhibit three types of frequency dependent behavior: unattenuated propagation waves in frequency *passbands,* attenuated standing waves in frequency *stopbands* and, in the case of multiple coupling coordinates, attenuated propagating waves in frequency *complexbands.*

Another property of periodic structures is that the free vibration natural frequencies belong to the passbands, with corresponding extended or periodic mode shapes. The number of natural frequencies in each passband is equal to the number of substructures in the periodic assembly and the number of passbands is equal to the number of degrees of freedom in each substructure. Continuous systems, for example, a string with uniformly attached masses or a multi-span beam, feature an infinite number of passbands. The width of a passband is governed by the strength of substructure coupling, the passband narrowing down to a single frequency for zero coupling. The frequency to which the passband converges corresponds to a natural frequency of an uncoupled substructure. Therefore, high modal density (the number of natural frequencies per unit frequency) is synonymous with weak substructure coupling and a large number of substructures.

1.1.2. Mistuned, Nearly Periodic Structures

In real life perfectly periodic structures are a rarity. The inevitable material defects, manufacturing tolerances and in-service degradation break the perfect periodicity, giving the structure some degree of structural disorder, or mistuning. Mistuning can alter qualitatively the dynamical behavior described in Section 1.1.1. The present section gives a brief description of the phenomena caused by mistuning.

In his ground breaking work in solid state physics, Anderson [22] showed that electron eigenstates in disordered lattices may become localized, resulting in a reduction in the conductivity of wires. For his discovery of the mode localization phenomenon, Anderson was awarded the Nobel prize. Anderson's findings were first applied to engineering structures by Hodges [23], who showed that the presence of disorder in a nearly periodic structure may invalidate the results of a tuned analysis. Localization, like damping, manifests itself as a spatial decay of the vibration amplitude along the structure, but through vastly different mechanisms. In the case of damping, energy is dissipated as vibrations are transmitted through the system, whereas in the case of localization, the energy is merely confined to a small geometric region within the structure. Localization occurs because waves propagating away from the energy source are reflected at the boundaries between the slightly dissimilar subsystems making up the nearly periodic structure. The resulting confinement of energy may lead to much higher amplitudes locally than would be predicted if perfect periodicity were assumed,

with possibly disastrous effects, as seen in turbomachinery research [2, 3, 5, 24].

In mistuned structures passbands do not occur, since waves of all frequencies are attenuated. The natural frequencies of free vibrations that were located in the passbands of the tuned periodic structure remain clustered in a frequency range that widens as the mistuning strength increases.

The localization phenomenon has recently received wide attention in the literature. It has been shown to occur in various types of engineering structures, such as truss beams [19, 25], multi-span beams [25–29], generic chains of coupled oscillators [23, 30, 31], a loaded string [32, 33], some large space structures [34, 35] and last, but not least, blade assemblies [13, 14]. A review paper by Ibrahim [36] summarizes these localization studies.

1.2. History of the Analysis of Rotor Mistuning

Designers are widely aware of inherent differences among rotor blades due to material and manufacturing tolerances and in-service degradation, commonly referred to as blade mistuning. In the past it has been widely accepted that mistuning causes a reduction in the risk of flutter instability [37, 38, 39], therefore, rotor mistuning has been viewed mostly as a positive feature. Through the ability to strategically place blades on a disk, designers have devised schemes for balancing and improving stability against flutter. The negative effect of mistuning, namely the potential for increased response amplitudes of some blades due to mode localization, has not played a large role in design, partially because it is very difficult to analyze and partially because of robust designs with sufficiently large damping, *e.g.,* in the blade-disk attachment and through dry friction dampers between blades.

With the advent of blisks, single piece bladed disks, the focus on blade mistuning as an unwanted phenomenon has increased. In a blisk the blades are permanently attached to the disk and it is no longer possible to discard or strategically place blades that fall outside acceptable manufacturing tolerances. Furthermore, blisks have much lower internal damping than blade-disk assemblies and are therefore more prone to adverse mistuning effects.

A large number of studies have been conducted in order to gain insight into the effects of mistuning on the dynamics of turbomachinery rotors [40–44]. These studies have been based on a variety of mathematical models with widely different parameters and have often led to conflicting results. Nevertheless, much has been achieved in understanding mistuning effects on the free response of bladed disks [6, 13, 14, 37, 45]. One of the few undisputed results is that mode localization increases monotonically with decreased interblade coupling, a finding that has yet to be expanded to

the forced response case. Recent studies [46, 47] have evidenced that in the forced response case additional mechanisms come into play and that a study of the mistuned modes of free vibration is insufficient in predicting the sensitivity of forced response blade amplitudes to mistuning. In their work, Wei and Pierre [46, 47] have attempted a systematic exploration of the effect of various parameters in simple models of blade assemblies. These investigations have yielded improved understanding of the forced response of mistuned rotors, but have not resulted in a satisfactory understanding of the governing physical phenomena. One of the objectives of this thesis is the physical interpretation of some of the phenomena observed but inadequately explained in references [46] and [47].

1.3. Mistuned Forced Response as a Statistical Problem

Much of the work in the literature fails to address the importance of a full understanding of the complete statistics of the forced response of mistuned rotors. In many cases [2, 7] mistuning has been assumed to be deterministic, which is a significant limitation. Even if the mistuning pattern of the blade assembly could be know when the rotor is first put into service, this analysis would not account for additional mistuning that may be caused during the life of the rotor. Some research effort has gone into optimization of deterministic mistuning patterns, but this work has also failed to answer any questions about statistics of forced response. Indeed, one could go as far as saying that deterministically ordering blades with different properties, *i.e.,* by alternating blades with two different types of stiffness, does nothing more than change the period of the assembly from one blade to two blades and should perhaps be referred to as *detuning* instead of mistuning.

Recognizing the random nature of blade mistuning but focusing only on the mean and standard deviation of the response statistics also misses the mark. Without the knowledge of the full statistics there can be no estimation of confidence intervals of response amplitudes and thus of stress and fatigue life.

Some authors have fully acknowledged the need for a complete stochastic analysis of the effects of blade mistuning [9, 48, 49]. However, while focusing on the statistics of the response of individual blades in the assembly, the more important topic of the statistics of the *largest amplitude, i.e.,* the amplitude of the blade in the assembly that exhibits the largest resonant response at any frequency, has not been addressed. The approximation of the statistics of forced response is a formidable task, indeed. Some authors [48, 49] have had limited success in deriving analytical approximations of the response statistics of individual blades but these are not easily expanded to yield the statistics of the largest amplitude. Chapter VI addresses this issue and gives a basic

introduction into the field of the *Statistics of Extreme Values.* Analytical evaluations of the statistics of largest forced response are extremely complicated and are beyond the scope of this thesis. Approximation of the extreme statistics may however be obtained using Monte Carlo simulations but only at a considerable cost.

1.4. Practical Aspects of Mistuned Rotor Modeling

Current analysis of rotordynamics is generally performed on a finite element model, based on the assumption that the rotor is tuned. This results in tremendous computational savings and is generally the only realistic option. From the dynamics of a single blade disk sector (one period in the bladed disk assembly), the dynamics of the entire assembly may then be deduced. When blade mistuning is accounted for, cyclic symmetry is lost and the entire assembly must be modeled, with an obvious increase in cost. Furthermore, the analysis of the statistics of the forced response of a mistuned rotor calls for multiple realizations of mistuned assemblies, yielding computational costs that are so large that the problem is rendered unsolvable by today's technology.

Many simple mathematical models have been developed and extensively used for the analysis of mistuned turbomachinery rotors. The most common of those. are coupled-oscillator models of varying sophistication. While these models may provide a great deal of insight into basic physical phenomena, they present a complicated identification problem when they are required to represent actual engineering rotors.

The development of accurate yet efficient modeling techniques for blade assemblies is a high priority and is one of the principal contributions of this thesis. Even if analytical methods are to be developed for the study of mistuning sensitivity, these methods are likely to be based on simple models of bladed disks and a simple accurate model will be required for verification of any new approach.

1.5. Directions of Mistuned Forced Response Analysis

Current research efforts in forced response are mostly divided into three main areas. Some researchers focus their efforts on obtaining approximations of the statistics of the forced response, for example, via perturbation methods [10, 48, 49]. Others concentrate on the development of very reduced order modeling of turbine rotors that achieve a compromise between reasonable computational efficiency and accurate modeling of mistuning effects [10, 38]. Finally there is the study of the underlying physical mechanisms with the goal of understanding which factors influence high sensitivity to mistuning [14, 50]. All of these areas of research are represented in this thesis in one way or another, and all of them are deemed equally important.

1.6. Dissertation Outline

When arranging the material accumulated during the course of the research for this thesis, an attempt was made to avoid the concatenation of previously written articles. However, a chronological ordering is very much preserved. Hopefully this will not be confusing to the reader.

The outline of the dissertation is as follows. In Chapter II we give a thorough account of all the information that has been accumulated on the topic of cyclic symmetry. Chapter III is dedicated to the study of modeling techniques, and in particular to the development of a new methodology based on a novel component mode approach. Chapter IV examines some special concepts in turbomachinery, such as engine order excitation and aerodynamic coupling. Chapter V contains an investigation of mistuning effects in a general mono-coupled coupled-oscillator model of a cyclic structure. In the chapter we derive a general approximation of the localization factor, the quantitative measure of the average exponential decay of propagating waves due to mistuning in the assembly. In addition to this, we suggest a universal measure of mistuning sensitivity in a mono-coupled model of a blade assembly. Finally, Chapter V includes a study of the effects of additional coupling coordinates on the localization phenomenon. A solid understanding of the mechanisms governing the statistics of forced response is obligatory if any conclusions are to be reached. This is the subject of Chapter VI. In Chapter VI we study in great detail the statistics of the forced response of a very simple model of a bladed disk. Some valuable conclusions are obtained that give a new understanding of localization as a forced response phenomenon. Chapter VII presents a large amount of work that was performed in order to validate and demonstrate the modeling techniques introduced in Chapter III. An investigation of some prototype rotors leads to a dramatically improved insight into the forced response phenomena. Chapter VIII gives a brief demonstration of the novel component-mode modeling approach developed in Chapter III.

CHAPTER II

CYCLIC SYMMETRY

Tuned turbomachinery rotors belong to a class of periodic structures called cyclic structures. A structure is said of have cyclic symmetry when its structural properties and geometry are rotationally periodic. Typically the period is one *sector* of the bladed disk, consisting of one blade and the corresponding portion of the disk. In this chapter we examine the mathematical properties shared by all cyclic structures.

2.1. Circulant Matrices

The analysis of structures with cyclic symmetry cannot be accomplished without a thorough understanding of the properties of circulant and block circulant matrices. A matrix is said to be circulant if every line in the matrix is obtained by shifting the previous line one column to the right and wrapping the line so that the last element of the previous line becomes the first element of the current line. Hence, an $N \times N$ circulant matrix

$$\mathbf{C} = \mathbf{circ}[c_1, c_2, \ldots, c_N] = \begin{bmatrix} c_1 & c_2 & c_3 & \cdots & c_{N-1} & c_N \\ c_N & c_1 & c_2 & \cdots & c_{N-2} & c_{N-1} \\ c_{N-1} & c_N & c_1 & \cdots & c_{N-3} & c_{N-2} \\ \vdots & \vdots & \vdots & \ddots & \vdots & \vdots \\ c_3 & c_4 & c_5 & \cdots & c_1 & c_2 \\ c_2 & c_3 & c_4 & \cdots & c_N & c_1 \end{bmatrix} \tag{2.1}$$

only has N distinct elements. If $\mathbf{C}$ is symmetric *and* circulant, the number of distinct elements is reduced even further and two separate cases emerge, depending on whether N is odd or even.

$$\mathbf{C} = \begin{cases} \mathbf{circ}[c_1, c_2, \ldots, c_{\frac{N}{2}}, c_{\frac{N+2}{2}}, c_{\frac{N}{2}}, \ldots, c_3, c_2] & \text{if } N \text{ is even} \\ \\ \mathbf{circ}[c_1, c_2, \ldots, c_{\frac{N}{2}}, c_{\frac{N+1}{2}}, c_{\frac{N+1}{2}}, c_{\frac{N}{2}}, \ldots, c_3, c_2] & \text{if } N \text{ is odd} \end{cases} \tag{2.2}$$

Note that in the case where N is even there are two unique elements in each line of the matrix, whereas in the N odd case there is only one unique value. The two cases

must always be treated separately, which complicates somewhat the dynamic analysis of rotors.

The concept of a circulant matrix can be generalized to block circulant matrices, defined as

$$\mathbf{C} = \mathbf{Bcirc}[\mathbf{C}_1, \mathbf{C}_2, \ldots, \mathbf{C}_N] = \begin{bmatrix} \mathbf{C}_1 & \mathbf{C}_2 & \mathbf{C}_3 & \cdots & \mathbf{C}_{N-1} & \mathbf{C}_N \\ \mathbf{C}_N & \mathbf{C}_1 & \mathbf{C}_2 & \cdots & \mathbf{C}_{N-2} & \mathbf{C}_{N-1} \\ \mathbf{C}_{N-1} & \mathbf{C}_N & \mathbf{C}_1 & \cdots & \mathbf{C}_{N-3} & \mathbf{C}_{N-2} \\ \vdots & \vdots & \vdots & \ddots & \vdots & \vdots \\ \mathbf{C}_3 & \mathbf{C}_4 & \mathbf{C}_5 & \cdots & \mathbf{C}_1 & \mathbf{C}_2 \\ \mathbf{C}_2 & \mathbf{C}_3 & \mathbf{C}_4 & \cdots & \mathbf{C}_N & \mathbf{C}_1 \end{bmatrix}, \tag{2.3}$$

where each line of blocks is generated by shifting the previous line of block to the right by one block. The block circulant, block symmetric case follows; it is analogous to the symmetric circulant case.

In reference [51] Davis provides a rigorous mathematical treatment of circulant matrices. An important tool in the discussion of circulant matrices is the permutation matrix , $\mathbf{\Pi}$.

$$\mathbf{\Pi} = \mathbf{circ}[0, 1, 0, \ldots, 0] = \begin{bmatrix} 0 & 1 & 0 & \cdots & 0 & 0 \\ 0 & 0 & 1 & \cdots & 0 & 0 \\ 0 & 0 & 0 & \cdots & 0 & 0 \\ \vdots & \vdots & \vdots & \ddots & \vdots & \vdots \\ 0 & 0 & 0 & \cdots & 0 & 1 \\ 1 & 0 & 0 & \cdots & 0 & 0 \end{bmatrix}. \tag{2.4}$$

It can be shown that a matrix $\mathbf{C}$ is circulant if and only if the matrices $\mathbf{C}$ and $\mathbf{\Pi}$ commute, that is

$$\mathbf{C\Pi} = \mathbf{\Pi C}.$$

The powers of the permutation matrix are:

$$\begin{aligned} \mathbf{\Pi}^2 &= \mathbf{circ}[0, 0, 1, 0, \ldots, 0] \\ \mathbf{\Pi}^3 &= \mathbf{circ}[0, 0, 0, 1, 0, \ldots, 0] \\ &\vdots \\ \mathbf{\Pi}^N = \mathbf{\Pi}^0 &= \mathbf{circ}[1, 0, \ldots, 0] = \mathbf{I} \end{aligned} \tag{2.5}$$

where N is the order of the matrix. This yields a form for writing a general circulant matrix

$$\mathbf{C} = \mathbf{circ}[c_1, c_2, \ldots, c_N] = \sum_{k=1}^{N} c_k \mathbf{\Pi}^{k-1} = p_{\mathbf{C}}(\mathbf{\Pi}) \tag{2.6}$$

where $p_{\mathbf{C}}$ is a polynomial of degree $N-1$. In the case of a block circulant matrix Eq. (2.6) must be written as

$$\mathbf{C} = \mathbf{circ}[\mathbf{C}_1, \mathbf{C}_2, \ldots, \mathbf{C}_N] = \sum_{k=1}^{N} \mathbf{\Pi}^{k-1} \otimes \mathbf{C}_k \tag{2.7}$$

where $\otimes$ denotes the Kronecker product, which is discussed in Appendix A.

In general, a model of a rotor will be represented with block-circulant matrices with block size equal to the number of degrees of freedom of each sector. Circulant matrices only occur when a rotor is modeled with single degree of freedom sectors (or multiple degree of freedom sectors that have been condensed down to a single representative degree of freedom).

2.2. The Cyclic Eigenvalue Problem.

For the discussion of the eigenvalues of circulant matrices we introduce the Fourier matrix, **E**, as

$$\mathbf{E} = \frac{1}{\sqrt{N}} \begin{bmatrix} 1 & 1 & 1 & \cdots & 1 \\ 1 & w & w^2 & \cdots & w^{N-1} \\ 1 & w^2 & w^4 & \cdots & w^{2(N-1)} \\ \vdots & \vdots & \vdots & \ddots & \vdots \\ 1 & w^{N-1} & w^{2(N-1)} & \cdots & w^{(N-1)(N-1)} \end{bmatrix} \tag{2.8}$$

where

$$w = e^{\frac{2j\pi}{N}} \qquad (j = \sqrt{-1}). \tag{2.9}$$

The Fourier matrix is *unitary*, *i.e.* $\mathbf{E}\mathbf{E}^* = \mathbf{I}$ where * denotes the complex conjugate transpose of a matrix. This may be shown by observing that each element (i,k) in $\mathbf{E}\mathbf{E}^*$ represents a geometric series

$$\begin{aligned} \left(\mathbf{E}\mathbf{E}^*\right)_{i,k} &= \frac{1}{N} \sum_{r=1}^{N} e^{\frac{2j\pi(i-1)(r-1)}{N}} e^{\frac{2j\pi(1-k)(r-1)}{N}} \\ &= \frac{1}{N} \sum_{r=1}^{N} \left[e^{\frac{2j\pi(i-k)}{N}} \right]^{(r-1)} = \frac{1}{N} \sum_{r=1}^{N} q^{(r-1)} \end{aligned} . \tag{2.10}$$

where we have defined $q = e^{2j\pi(i-k)/N}$. By observing that $q^N = 1$, and that $q = 1$, for $i = k$, we find

$$\left(\mathbf{E}\mathbf{E}^*\right)_{i,k} = \begin{cases} \dfrac{1}{N} \displaystyle\sum_{r=1}^{N} 1^{(r-1)} = 1 & \text{if } i = k \\ \dfrac{1}{qN} \dfrac{1-q^N}{1-q} = 0 & \text{if } i \neq k. \end{cases} \tag{2.11}$$

2.2.1. General Circulant Matrices

The fundamental theorem is that *the Fourier matrix diagonalizes any circulant matrix, through the transformation* $\mathbf{E}^*\mathbf{C}\mathbf{E}$. This proven below. The significance of this property is that all circulant matrices share the same eigenvectors — the columns of the Fourier matrix.

In order to prove this, we first show that $\mathbf{E}$ diagonalizes the permutation matrix, $\mathbf{\Pi}$, (see Eq. (2.4)) by proving the relationship

$$\mathbf{\Pi} = \mathbf{E}\mathbf{\Omega}\mathbf{E}^* \qquad \text{where} \qquad \mathbf{\Omega} = \mathbf{diag}[1, w, w^2, \ldots, w^{N-1}] \tag{2.12}$$

which holds because

$$\begin{aligned}(\mathbf{E}\mathbf{\Omega}\mathbf{E}^*)_{i,k} &= \frac{1}{N}\sum_{r=1}^{N} w^{(i-1)(r-1)} w^{(r-1)} w^{(1-k)(r-1)} \\ &= \frac{1}{N}\sum_{r=1}^{N} e^{\frac{2j\pi}{N}(i-k+1)(r-1)} = \begin{cases} 1 & \text{if } i = k-1 \text{ or} \\ & \quad i = N+k-1 \\ 0 & \text{otherwise} \end{cases}\end{aligned} \tag{2.13}$$

(see proof in Eqs. (2.10) and (2.11)) which is the precisely the form of the permutation matrix $\mathbf{\Pi}$ in Eq. (2.4). By applying Eq. (2.6) we find

$$\mathbf{C} = p_{\mathbf{C}}(\mathbf{\Pi}) = p_{\mathbf{C}}(\mathbf{E}\mathbf{\Omega}\mathbf{E}^*) = \mathbf{E}\, p_{\mathbf{C}}(\mathbf{\Omega})\, \mathbf{E}^* = \mathbf{E}\,\mathbf{diag}\left[p_{\mathbf{C}}(1), p_{\mathbf{C}}(w), \ldots, p_{\mathbf{C}}(w^{N-1})\right]\mathbf{E}^* \tag{2.14}$$

or

$$\mathbf{E}^*\mathbf{C}\mathbf{E} = \mathrm{diag}[\lambda_1, \lambda_2, \ldots, \lambda_N] \tag{2.15}$$

where

$$\lambda_i = p_{\mathbf{C}}(w^{i-1}) = \sum_{k=1}^{N} c_k e^{\frac{2j\pi(i-1)(k-1)}{N}} \qquad (i = 1, \ldots, N) \tag{2.16}$$

are the eigenvalues of $\mathbf{C}$, with the corresponding eigenvectors

$$\begin{aligned}\mathbf{e}_i &= \frac{1}{\sqrt{N}}\left[1, w^{i-1}, w^{2(i-1)}, \ldots, w^{(N-1)(i-1)}\right]^T \\ &= \frac{1}{\sqrt{N}}\left[1, e^{j\sigma_i}, e^{2j\sigma_i}, \ldots, e^{(N-1)j\sigma_i}\right]^T\end{aligned} \qquad (i = 1, \ldots, N) \tag{2.17}$$

where

$$\sigma_i = \frac{2(i-1)\pi}{N} \qquad (i = 1 \ldots N) \tag{2.18}$$

is the phase angle between adjacent sectors of the cyclic structure, usually referred to as the interblade-phase angle.

In the turbomachinery literature [37, 3, 38, 2, 44, 24, 5] these modes are frequently referred to as constant-interblade-phase-angle modes (See Section 2.5) since

they feature a vibration shape in which all blades are vibrating with the same amplitude and a uniform interblade-phase angle. These are traveling wave modes that appear in counter-rotating pairs ($\sigma_{N+2-i} = -\sigma_i$), represented by a complex conjugate pair of columns for the Fourier matrix. Counter-rotating constant-interblade-phase-angle modes are illustrated in Fig. 2.1.

2.2.2. Symmetric Circulant Matrices

If the matrix **C** is both symmetric and circulant, the number of distinct elements in the matrix is only $\frac{N+2}{2}$ when N is even and $\frac{N+1}{2}$ when N is odd. The expression for the eigenvalues thus takes on a simplified form, but different expressions are required depending on whether N is odd or even. If N is odd,

$$\lambda_i = c_1 + c_2\left(w^{(i-1)} + w^{(N-1)(i-1)}\right) + \ldots + c_{\frac{N+1}{2}}\left(w^{(\frac{N-1}{2})(i-1)} + w^{(\frac{N+1}{2})(i-1)}\right). \quad (2.19)$$

If N is even,

$$\lambda_i = c_1 + c_2\left(w^{(i-1)} + w^{(N-1)(i-1)}\right) + \ldots + c_{\frac{N}{2}}\left(w^{(\frac{N}{2}-1)(i-1)} + w^{(\frac{N}{2}+1)(i-1)}\right) + c_{\frac{N+2}{2}} w^{(\frac{N}{2})(i-1)}. \quad (2.20)$$

Noting that $w^{k(i-1)} + w^{(N-k)(i-1)} = 2\cos\left(\frac{2\pi k}{N}(i-1)\right)$ the eigenvalues may be written as:

$$\lambda_i = \begin{cases} c_1 + 2\sum_{k=2}^{\frac{N+1}{2}} c_k \cos\left(\frac{2\pi(k-1)}{N}(i-1)\right) + (-1)^{i-1} c_{\frac{N+2}{2}} & \text{for even } N \\ c_1 + 2\sum_{k=2}^{\frac{N}{2}} c_k \cos\left(\frac{2\pi(k-1)}{N}(i-1)\right) & \text{for odd } N \end{cases} \qquad i = 1, \ldots, N \quad (2.21)$$

Due to the fact that $\cos x = \cos(2\pi - x)$ it can be seen that the eigenvalues of symmetric circulant matrices appear in pairs, $\lambda_i = \lambda_{N+2-i}$, except λ_1 which is a single eigenvalue. For N even, $\lambda_{\frac{N+2}{2}}$ is also a single eigenvalue.

Even though they feature double eigenvalues, symmetric, circulant matrices do possess a full set of eigenvectors. For a pair of double eigenvalues, one choice of independent eigenvectors is the corresponding pair of complex conjugate eigenvectors from the Fourier matrix. The eigenspace corresponding to a double natural frequency may be spanned by any linear combination of the complex conjugate eigenvector pair from the Fourier matrix. One common choice is the real and the imaginary parts of the complex eigenvectors.

2.2.3. Block Circulant Matrices

Recall that the circulant matrix

$$\mathbf{C} = \mathbf{circ}[c_1, c_2, \ldots, c_N] = \sum_{k=1}^{N} c_k \mathbf{\Pi}^{k-1} \tag{2.22}$$

is diagonalized using the Fourier transformation $\mathbf{E}^*\mathbf{C}\mathbf{E}$. Similarly, a block circulant matrix

$$\mathbf{C} = \mathbf{Bcirc}[\mathbf{C}_1, \mathbf{C}_2, \ldots, \mathbf{C}_N] = \sum_{k=1}^{N} \mathbf{\Pi}^{k-1} \otimes \mathbf{C}_k \tag{2.23}$$

is block-diagonalized using the transformation $(\mathbf{E}^* \otimes \mathbf{I})\,\mathbf{C}\,(\mathbf{E} \otimes \mathbf{I})$ where, again, $\otimes$ denotes the Kronecker product and $\mathbf{I}$ is an identity matrix of dimension equal to that of the individual blocks $\mathbf{C}_k$. We find

$$\begin{aligned}
(\mathbf{E}^* \otimes \mathbf{I})\,\mathbf{C}\,(\mathbf{E} \otimes \mathbf{I}) &= (\mathbf{E}^* \otimes \mathbf{I}) \left[\sum_{k=1}^{N} \mathbf{\Pi}^{k-1} \otimes \mathbf{C}_k \right] (\mathbf{E} \otimes \mathbf{I}) \\
&= \sum_{k=1}^{N} (\mathbf{E}^* \otimes \mathbf{I}) \left[\mathbf{\Pi}^{k-1} \otimes \mathbf{C}_k \right] (\mathbf{E} \otimes \mathbf{I}) \\
&= \sum_{k=1}^{N} \left(\mathbf{E}^* \mathbf{\Pi}^{k-1} \mathbf{E} \right) \otimes \mathbf{C}_k \\
&= \sum_{k=1}^{N} \mathbf{\Omega}^{k-1} \otimes \mathbf{C}_k \\
&= \mathbf{Bdiag}[\mathbf{\Lambda}_1, \mathbf{\Lambda}_2, \ldots, \mathbf{\Lambda}_N],
\end{aligned} \tag{2.24}$$

where $\mathbf{\Omega}$ was defined in Eq. (2.12). This is a result similar to the one obtained earlier for the diagonalization of the regular circulant matrix. The blocks are,

$$\mathbf{\Lambda}_i = \sum_{k=1}^{N} \mathbf{C}_k e^{\frac{2j\pi(i-1)(k-1)}{N}} \qquad (i = 1, \ldots, N) \tag{2.25}$$

and the problem of calculating the eigenvalues and eigenvectors of the block circulant matrix $\mathbf{C}$ has been broken into N simpler eigenvalue problems for the individual $\mathbf{\Lambda}_i$ matrices,

$$\mathbf{\Lambda}_i \tilde{\mathbf{u}}_i = 0 \qquad (i = 1, \ldots, N), \tag{2.26}$$

where each $\mathbf{\Lambda}_i$ corresponds to a spatial harmonic $\mathbf{e}_i$ (see Eq. (2.17)).

An eigenvector for $\mathbf{C}$ is calculated from an eigenvector of a block using the Kronecker product. If $\tilde{\mathbf{u}}_i$ is an eigenvector of the $\mathbf{\Lambda}_i$ block, then the corresponding eigenvector of $\mathbf{C}$ is

$$\mathbf{u}_i = \mathbf{e}_i \otimes \tilde{\mathbf{u}}_i \tag{2.27}$$

2.2.4. Block Circulant, Block Symmetric Matrices.

As in the circulant case, symmetry renders the block-circulant eigenvalue problem degenerate and most eigenvalues become double. The exceptions are the eigenvalues corresponding to the zero harmonic and, if N is even, the $N/2$ harmonic.

The eigenvectors that correspond to a double eigenvalue can be taken as the pair of complex conjugate (counter-rotating) constant-interblade-phase-angle modes. Alternatively, the real eigenvectors that correspond to the real and imaginary parts of the complex pair may be used.

The eigenvectors of $\mathbf{C}$ are calculated from the eigenvectors of a block. If $\tilde{\mathbf{u}}_{ik}$ and $\overline{\tilde{\mathbf{u}}}_{ik}$ are eigenvectors corresponding to a double eigenvalue of the $\mathbf{\Lambda}_i$ block, where $\overline{\tilde{\mathbf{u}}}_{ik}$ denotes the complex conjugate of $\tilde{\mathbf{u}}_{ik}$, then the corresponding eigenvectors of $\mathbf{C}$ are

$$\mathbf{u}_i = \mathbf{e}_i \otimes \tilde{\mathbf{u}}_i \tag{2.28}$$

and

$$\overline{\mathbf{u}}_i = \overline{\mathbf{e}}_i \otimes \overline{\tilde{\mathbf{u}}}_i. \tag{2.29}$$

Expanding yields

$$\overline{\mathbf{u}}_i \,,\, \mathbf{u}_i = \left[\mathbf{e}_i^{\Re} \otimes \tilde{\mathbf{u}}_i^{\Re} - \mathbf{e}_i^{\Im} \otimes \tilde{\mathbf{u}}_i^{\Im}\right] \pm j\left[\mathbf{e}_i^{\Im} \otimes \tilde{\mathbf{u}}_i^{\Re} + \mathbf{e}_i^{\Re} \otimes \tilde{\mathbf{u}}_i^{\Im}\right] \tag{2.30}$$

where the superscripts $^{\Re}$ and $^{\Im}$ denote the real and imaginary parts, respectively. Selecting the real and imaginary parts of $\overline{\mathbf{u}}_i$ and $\mathbf{u}_i$ results in the alternative pair of eigenvectors in the real domain, as:

$$\begin{aligned} \mathbf{v}_{1,i} =& \mathbf{e}_i^{\Re} \otimes \tilde{\mathbf{u}}_i^{\Re} - \mathbf{e}_i^{\Im} \otimes \tilde{\mathbf{u}}_i^{\Im} \\ \mathbf{v}_{2,i} =& \mathbf{e}_i^{\Im} \otimes \tilde{\mathbf{u}}_i^{\Re} + \mathbf{e}_i^{\Re} \otimes \tilde{\mathbf{u}}_i^{\Im} \end{aligned} \tag{2.31}$$

2.3. Coordinate Systems and Coordinate Transformations

Let us introduce some terminology for the various coordinate systems that enter into the analysis of systems with cyclic symmetry. As an aid in the discussion, we present the eigenvalue problem for a generic cyclic structural system

$$\left(\begin{bmatrix} \mathbf{K}_1 & \mathbf{K}_2 & \mathbf{K}_3 & \cdots & \mathbf{K}_3 & \mathbf{K}_2 \\ \mathbf{K}_2 & \mathbf{K}_1 & \mathbf{K}_2 & \cdots & \mathbf{K}_4 & \mathbf{K}_3 \\ \mathbf{K}_3 & \mathbf{K}_2 & \mathbf{K}_1 & \cdots & \mathbf{K}_5 & \mathbf{K}_4 \\ \vdots & \vdots & \vdots & \ddots & \vdots & \vdots \\ \mathbf{K}_3 & \mathbf{K}_4 & \mathbf{K}_5 & \cdots & \mathbf{K}_1 & \mathbf{K}_2 \\ \mathbf{K}_2 & \mathbf{K}_3 & \mathbf{K}_4 & \cdots & \mathbf{K}_2 & \mathbf{K}_1 \end{bmatrix} - \omega^2 \begin{bmatrix} \mathbf{M}_1 & \mathbf{M}_2 & \mathbf{M}_3 & \cdots & \mathbf{M}_3 & \mathbf{M}_2 \\ \mathbf{M}_2 & \mathbf{M}_1 & \mathbf{M}_2 & \cdots & \mathbf{M}_4 & \mathbf{M}_3 \\ \mathbf{M}_3 & \mathbf{M}_2 & \mathbf{M}_1 & \cdots & \mathbf{M}_5 & \mathbf{M}_4 \\ \vdots & \vdots & \vdots & \ddots & \vdots & \vdots \\ \mathbf{M}_3 & \mathbf{M}_4 & \mathbf{M}_5 & \cdots & \mathbf{M}_1 & \mathbf{M}_2 \\ \mathbf{M}_2 & \mathbf{M}_3 & \mathbf{M}_4 & \cdots & \mathbf{M}_2 & \mathbf{M}_1 \end{bmatrix}\right) \begin{bmatrix} \mathbf{q}_1 \\ \mathbf{q}_2 \\ \mathbf{q}_3 \\ \vdots \\ \mathbf{q}_{N-1} \\ \mathbf{q}_N \end{bmatrix} = \mathbf{0} \tag{2.32}$$

where N is the number of sectors in the cyclic structure, and the blocks $\mathbf{K}_i$ and $\mathbf{M}_i$ $(i = 1, \ldots, \text{INT}[(N+2)/2])$ are square matrices of dimension P, where *P is the number of degrees of freedom in the model of each disk-blade sector.* (We have adopted the short-hand notation INT$[(N+2)/2]$ to denote the integer division of $(N+2)/2$ which equals $(N+2)/2$ if N is even and $(N+1)/2$ if N is odd.) The structure is modeled in a physical coordinate system (possibly using the Finite Element Method) where $\mathbf{q}_i$ denotes the degrees of freedom in sector i. As outlined above, Eq. (2.32) may be brought into a block diagonal form using the coordinate transformation

$$\mathbf{q} = (\mathbf{E} \otimes \mathbf{I})\, \mathbf{u}. \tag{2.33}$$

where $\otimes$ denotes the Kronecker product which is discussed in Appendix A. Thus

$$\left(\begin{bmatrix} \widetilde{\mathbf{K}}_1 & \mathbf{0} & \mathbf{0} & \cdots & \mathbf{0} & \mathbf{0} \\ \mathbf{0} & \widetilde{\mathbf{K}}_2 & \mathbf{0} & \cdots & \mathbf{0} & \mathbf{0} \\ \mathbf{0} & \mathbf{0} & \widetilde{\mathbf{K}}_3 & \cdots & \mathbf{0} & \mathbf{0} \\ \vdots & \vdots & \vdots & \ddots & \vdots & \vdots \\ \mathbf{0} & \mathbf{0} & \mathbf{0} & \cdots & \widetilde{\mathbf{K}}_{N-1} & \mathbf{0} \\ \mathbf{0} & \mathbf{0} & \mathbf{0} & \cdots & \mathbf{0} & \widetilde{\mathbf{K}}_N \end{bmatrix} - \omega^2 \begin{bmatrix} \widetilde{\mathbf{M}}_1 & \mathbf{0} & \mathbf{0} & \cdots & \mathbf{0} & \mathbf{0} \\ \mathbf{0} & \widetilde{\mathbf{M}}_2 & \mathbf{0} & \cdots & \mathbf{0} & \mathbf{0} \\ \mathbf{0} & \mathbf{0} & \widetilde{\mathbf{M}}_3 & \cdots & \mathbf{0} & \mathbf{0} \\ \vdots & \vdots & \vdots & \ddots & \vdots & \vdots \\ \mathbf{0} & \mathbf{0} & \mathbf{0} & \cdots & \widetilde{\mathbf{M}}_{N-1} & \mathbf{0} \\ \mathbf{0} & \mathbf{0} & \mathbf{0} & \cdots & \mathbf{0} & \widetilde{\mathbf{M}}_N \end{bmatrix}\right) \begin{bmatrix} \tilde{\mathbf{u}}_1 \\ \tilde{\mathbf{u}}_2 \\ \tilde{\mathbf{u}}_3 \\ \vdots \\ \tilde{\mathbf{u}}_{N-1} \\ \tilde{\mathbf{u}}_N \end{bmatrix} = \mathbf{0} \tag{2.34}$$

For the lack of a better terminology we shall refer to the $\mathbf{u}$ coordinate system as *harmonic coordinates,* since the elements of each subvector of $\mathbf{u}$, $\tilde{\mathbf{u}}_i$, describe the motion of a single bay in the assembly when the system is vibrating in the ith spatial harmonic. The motion of the remaining bays is implied by the known interblade-phase angle, σ_i, in Eq. (2.18).

To fully solve the eigenvalue problem, we must solve the N individual block eigenvalue problems, each of size P:

$$\left(\widetilde{\mathbf{K}}_i - \omega_i^2 \widetilde{\mathbf{M}}_i\right) \tilde{\mathbf{u}}_i = 0 \qquad (i = 1, \ldots, N) \tag{2.35}$$

and find P natural frequencies $\omega_{i,1}, \ldots, \omega_{i,P}$ with the corresponding sector eigenvectors $\tilde{\mathbf{u}}_{i,1}, \ldots, \tilde{\mathbf{u}}_{i,P}$. Assembly eigenvectors are generated from the sector eigenvectors using the Kronecker product

$$\mathbf{u}_{i,k} = \mathbf{e}_i \otimes \tilde{\mathbf{u}}_{i,k} \qquad \begin{matrix} (k = 1, \ldots, P) \\ (i = 1, \ldots, N) \end{matrix}$$

The eigenvectors $\tilde{\mathbf{u}}_{i,k}$ define a transformation to a modal amplitude coordinate system, $a_{i,k}$

$$\tilde{\mathbf{u}}_i = \tilde{\mathbf{U}}_i \mathbf{a}_i \qquad (i = 1, \ldots, N)$$

where the square matrix $\tilde{\mathbf{U}}_i$ contains the ith-harmonic sector eigenvectors, $\tilde{\mathbf{u}}_{i,k}$, as its columns.

A transformation between modal amplitude coordinates and harmonic amplitudes for all harmonics could also be defined as

$$\mathbf{u} = \begin{bmatrix} \tilde{\mathbf{U}}_1 \mathbf{a}_1 \\ \tilde{\mathbf{U}}_2 \mathbf{a}_2 \\ \vdots \\ \tilde{\mathbf{U}}_N \mathbf{a}_N \end{bmatrix} = \begin{bmatrix} \tilde{\mathbf{U}}_1 & \mathbf{0} & \cdots & \mathbf{0} \\ \mathbf{0} & \tilde{\mathbf{U}}_2 & \cdots & \mathbf{0} \\ \vdots & \vdots & \ddots & \vdots \\ \mathbf{0} & \mathbf{0} & \cdots & \tilde{\mathbf{U}}_N \end{bmatrix} \begin{bmatrix} \mathbf{a}_1 \\ \mathbf{a}_2 \\ \vdots \\ \mathbf{a}_N \end{bmatrix} = \tilde{\mathbf{U}} \mathbf{a}$$

Hence, the transformation between modal amplitudes coordinates and physical coordinates may be simply written as

$$\mathbf{q} = (\mathbf{E} \otimes \mathbf{I})\, \tilde{\mathbf{U}}\, \mathbf{a}. \tag{2.36}$$

2.4. A Cyclic System of Equations of Motion

Consider the forced response of a structure with cyclic symmetry. The equations of motion take the form

$$\mathbf{M}\ddot{\mathbf{q}} + \mathbf{D}\dot{\mathbf{q}} + \mathbf{A}\mathbf{q} + \mathbf{K}\mathbf{q} = \mathbf{f} \tag{2.37}$$

where $\mathbf{M}$, $\mathbf{D}$, $\mathbf{A}$ and $\mathbf{K}$ are, respectively, the mass, damping, aerodynamic and stiffness matrices of the structure. Since the structure has cyclic symmetry, the matrices are block-circulant with block size equal to the number of degrees of freedom in each sector.

Since all circulant matrices possess the same set of global eigenvectors, it is customary to apply the coordinate transformation (2.33) to transform the right hand side of Eq. (2.37) into generalized forces corresponding to the harmonic coordinates $\mathbf{u}_i$, $(i = 1, \ldots, N)$. Hence the transformed forcing vector represents the excitation of the various constant-interblade-phase-angle modes. (The physical justification for this is presented in Section 4.1.) Since these modes correspond to the columns of the Fourier

matrix, this amounts to a spatial Fourier decomposition of the forcing vector. Assuming harmonic excitation, Eq. (2.37) may be written as

$$\mathbf{C}\,\mathbf{q} = \sum_{i=1}^{N} (\mathbf{e}_i \otimes \mathbf{f}_i) \tag{2.38}$$

where $\mathbf{f}_i$ is the component of the forcing in the $\mathbf{u}_i$ direction, $\mathbf{e}_i$ is defined in Eq. (2.17) and $\mathbf{C} = (-\omega^2\mathbf{M} + j\omega\mathbf{D} + \mathbf{A} + \mathbf{K})$ is a circulant matrix. A transformation to harmonic coordinates (Eq.(2.33)) yields

$$(\mathbf{E}^* \otimes \mathbf{I})\mathbf{C}(\mathbf{E} \otimes \mathbf{I})\mathbf{u} = \sum_{i=1}^{N} (\mathbf{E}^* \otimes \mathbf{I})\ (\mathbf{e}_i \otimes \mathbf{f}_i) \tag{2.39}$$

or, since

$$\mathbf{e}_k^* \mathbf{e}_i = \begin{cases} 0 & \text{if } i \neq k \\ 1 & \text{if } i = k \end{cases}$$

Equation (2.39) becomes

$$\begin{bmatrix} \mathbf{\Lambda}_1 & \mathbf{0} & \mathbf{0} & \cdots & \mathbf{0} & \mathbf{0} \\ \mathbf{0} & \mathbf{\Lambda}_2 & \mathbf{0} & \cdots & \mathbf{0} & \mathbf{0} \\ \mathbf{0} & \mathbf{0} & \mathbf{\Lambda}_3 & \cdots & \mathbf{0} & \mathbf{0} \\ \vdots & \vdots & \vdots & \ddots & \vdots & \vdots \\ \mathbf{0} & \mathbf{0} & \mathbf{0} & \cdots & \mathbf{\Lambda}_{N-1} & \mathbf{0} \\ \mathbf{0} & \mathbf{0} & \mathbf{0} & \cdots & \mathbf{0} & \mathbf{\Lambda}_N \end{bmatrix} \begin{bmatrix} \mathbf{u}_1 \\ \mathbf{u}_2 \\ \mathbf{u}_3 \\ \vdots \\ \mathbf{u}_{N-1} \\ \mathbf{u}_N \end{bmatrix} = \sum_{i=1}^{N} \left(\hat{\mathbf{1}}_i \otimes \mathbf{f}_i\right) \tag{2.40}$$

where $\hat{\mathbf{1}}_i$ is the ith canonical unit vector, a vector with all zero elements except 1 in the ith element. The significance of Eq. (2.40) is that the forcing harmonic $(\mathbf{e}_i \otimes \mathbf{f}_i)$ only excites the $(\mathbf{e}_i \otimes \tilde{\mathbf{u}}_{i,k})$ modes and the forced response problem in Eq. (2.37) is reduced to solving a series of smaller problems, each of size P:

$$\mathbf{\Lambda}_i\,\mathbf{u}_i = \mathbf{f}_i \qquad (i = 1, \ldots, N)$$

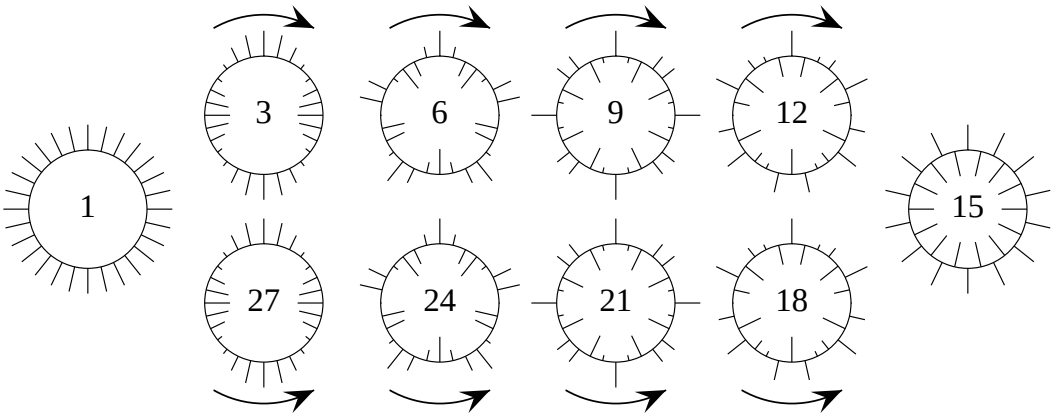

Figure 2.1 Selected constant-interblade-phase-angle modes of a model of a 28-blade bladed disk. The lengths of the radial lines represent the blade displacement amplitudes at an instant of time. Modes 1 and 15 are standing wave modes and correspond to unique eigenvalues. The counter-rotating mode pairs (3,27), (6,24), (9,21), and (12,18) are complex conjugate modes corresponding to a double natural frequency.

2.5. Interblade-Phase-Angle Modes and Energy Methods.

Figure 2.1 illustrates the constant-interblade-phase-angle modes of a cyclic system. These modes can be identified by their number of *nodal diameters*, which are diameters connecting pairs of nodes with zero deflection, positioned on opposite sides of the structure. Table 2.1 shows the relationship between the mode number and the number of nodal diameters in the mode. The number of nodal diameters of a mode is directly related to the interblade-phase angle, σ, through Eq. (2.18). Using this relationship, the number of nodal diameters and the interblade-phase angle may be used interchangeably.

Let us study in more detail the interblade-phase-angle modes in a system with a single-degree-of-freedom per sector, such as the one shown in Fig. 2.2. Assuming harmonic motion, when the assembly is vibrating in the σ_k interblade-phase-angle mode with modal amplitude a_k, the displacement of blade i is,

$$u_i(t) = a_k e^{j\sigma_k i} e^{j\omega t} = a_k e^{j(\sigma_k i + \omega t)} \qquad (i = 1, \ldots, N) \tag{2.41}$$

Taking only the real part we find the familiar expression for the *physical* displacement,

$$u_i(t) = a_k \cos(\sigma_k i + \omega t) \qquad (i = 1, \ldots, N) \tag{2.42}$$

which represents a sinusoidal displacement wave traveling in the positive i direction (ascending blade number) at a constant speed $c = \omega/\sigma_k$. The wave's shape is not

	mode number i	number of nodal diameters
N odd	$1 \le i \le \frac{N+1}{2}$	$i-1$
	$\frac{N+3}{2} \le i \le N$	$N-(1+i)$
N even	$1 \le i \le \frac{N+2}{2}$	$i-1$
	$\frac{N+4}{2} \le i \le N$	$N-(1+i)$

Table 2.1 The relationship between the mode number and the number of nodal diameters in the mode shape.

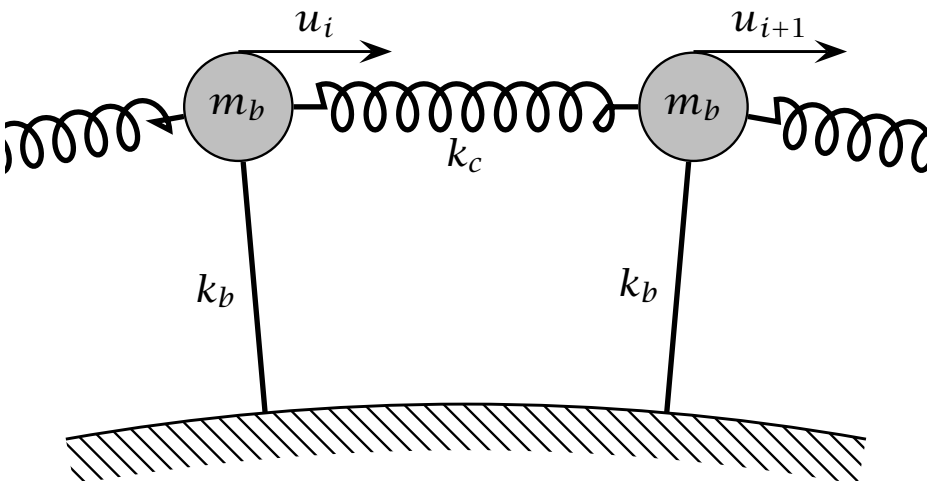

Figure 2.2 A simple model of a tuned bladed disk featuring one-DOF, mono-coupled bays to model each blade/disk sector.

distorted as it propagates. The kth mode's complex conjugate counterpart is

$$\bar{u}_i = a_{N-k+2} e^{ji\sigma_{N-k+2}} e^{j\omega t} = a_{N-k+2} e^{-j\sigma_k i} e^{j\omega t} = a_{N-k+2} e^{j(-\sigma_k i + \omega t)} \qquad (i = 1, \ldots, N) \tag{2.43}$$

since $\sigma_{N-k+2} = -\sigma_k$. The real part of the displacement is

$$u_i(t) = a_{N-k+2} \cos(-\sigma_k i + \omega t) \qquad (i = 1, \ldots, N) \tag{2.44}$$

which is a wave propagating in the opposite direction at the same speed.

Let us examine the kinetic and potential energies of the simple structure depicted in Fig. 2.2 as it vibrates in individual interblade-phase-angle modes. Note that energy

analysis is impossible using a complex representation of motion (Eqs. (2.41) and (2.43)) since the potential and kinetic energies require the squaring of the displacement and velocity respectively. This would prevent us from separating the real and imaginary parts of the motion. The generalized physical velocity of blade i in the σ_k mode is

$$\dot{u}_i(t) = -a_k \omega \sin(\sigma_k i + \omega t) \tag{2.45}$$

From which we find the kinetic energy to be

$$\begin{aligned} T_{k,i} =& \frac{a_k^2}{2} m\omega^2 \sin^2(\sigma_k i + \omega t) = \frac{a_k^2}{4} m\omega^2 \left(1 - \cos(2\sigma_k i + 2\omega t)\right) \\ =& \frac{a_k^2}{4} m\omega^2 \left(1 - \cos(2\sigma_k i)\cos(2\omega t) + \sin(2\sigma_k i)\sin(2\omega t)\right). \end{aligned} \tag{2.46}$$

Summing over the blades, we find the total kinetic energy in the assembly for mode k

$$T_k = a_k^2 \left\{ \frac{N}{4} m\omega^2 + \frac{m\omega^2}{4} \left[\sin(2\omega t) \sum_{i=1}^{N} \sin(2\sigma_k i) - \cos(2\omega t) \sum_{i=1}^{N} \cos(2\sigma_k i) \right] \right\} \tag{2.47}$$

There are two cases. If the mode does not propagate, *i.e.,* if $\sigma_k = n\pi$, $(n = 0, 1, \ldots)$ then

$$T_k = \frac{a_k^2 N}{2} m\omega^2 \sin^2(\omega t) \qquad (\sigma_k = n\pi) \tag{2.48}$$

otherwise the kinetic energy of the system is constant over time,

$$T_k = \frac{a_k^2 N}{4} m\omega^2 \qquad (\sigma_k \neq n\pi) \tag{2.49}$$

Thus, there is a fundamental difference in the kinetic energy in standing wave motion and traveling wave motion: in standing waves, kinetic energy oscillates sinusoidally in time; in traveling waves, the total kinetic energy of the assembly remains fixed in time and is simply being passed from one blade to another.

The strain energy in the ith bay (the ith blade and the spring connecting it with blade $i+1$) in the σ_k interblade-phase-angle mode is

$$\begin{aligned} V_{k,i} =& \frac{1}{2} \left\{ k_d u_i^2 + k_c (u_i - u_{i+1})^2 \right\} \\ =& \frac{a_k^2}{2} \left\{ k_d \cos^2(\sigma_k i + \omega t) + k_c \left(\cos(\sigma_k i + \omega t) - \cos(\sigma_k (i+1) + \omega t)\right)^2 \right\} \\ =& \frac{a_k^2}{2} \left\{ k_d \cos^2(\sigma_k i + \omega t) + 4k_c \left(\sin\left(\frac{\sigma_k}{2}\right) \sin\left(\sigma_k i + \frac{\sigma_k}{2} + \omega t\right) \right)^2 \right\} \\ =& \frac{a_k^2}{4} \left\{ k_d (1 + \cos(2\sigma_k i + 2\omega t)) + 2k_c (1 - \cos(\sigma_k)) (1 - \cos(2\sigma_k i + \sigma_k + 2\omega t)) \right\} \end{aligned} \tag{2.50}$$

The total strain energy in the assembly in the kth mode is therefore

$$\begin{aligned} V_k =& \frac{a_k^2}{4} \sum_{i=1}^{N} \{k_d(1+\cos(2\sigma_k i + 2\omega t)) + k_c\,(1-\cos(\sigma_k))\,(1-\cos(2\sigma_k i + \sigma_k + 2\omega t)\} \\ =& \frac{a_k^2}{4}\Bigg\{ k_d \left(N + \cos(2\omega t) \sum_{i=1}^{N} \cos(2\sigma_k i) - \sin(2\omega t) \sum_{i=1}^{N} \sin(2\sigma_k i) \right) \\ & + 2k_c\,(1-\cos\sigma_k) \Bigg(N - \cos(\sigma_k + 2\omega t) \sum_{i=1}^{N} \cos(2\sigma_k i) \\ & \qquad + \sin(\sigma_k + 2\omega t) \sum_{i=1}^{N} \sin(2\sigma_k i) \Bigg) \Bigg\} \end{aligned} \tag{2.51}$$

but $\sum_{i=1}^{N} \sin(2\sigma_k i) = 0$ for all σ_k and $\sum_{i=1}^{N} \cos(2\sigma_k i) = 0$ for $\sigma_k \neq n\pi$, so

$$V_k = \frac{a_k^2 N}{4}\Big\{ k_d + 2k_c\,(1-\cos\sigma_k) \Big\} \qquad (\sigma_k \neq n\pi) \tag{2.52}$$

which is independent of time, and

$$V_k = \frac{a_k^2 N}{4}\Big\{ k_d\,(1+\cos(2\omega t)) + 2k_c\,(1-\cos\sigma_k)\,(1-\cos(\sigma_k + 2\omega t)) \Big\} \qquad (\sigma_k = n\pi). \tag{2.53}$$

Separating the cases $\sigma_k = 0$ and $\sigma_k = \pi$ yields

$$V_k = \frac{a_k^2 N}{2} k_d \cos^2 \omega t \qquad (\sigma_k = 0) \tag{2.54}$$

which is independent of k_c and

$$V_k = \frac{a_k^2 N}{2}\,(k_d + 4k_c) \cos^2 \omega t \qquad (\sigma_k = \pi) \tag{2.55}$$

For all admissible δa_k we have

$$\delta T - \delta V = 0 \tag{2.56}$$

and we find that the frequency equation of the system in the k the mode is

$$-m\omega_k^2 + k_d + 2k_c\,(1-\cos\sigma_k) = 0 \qquad (k = 1, \ldots, N) \tag{2.57}$$

regardless of whether the corresponding wave mode is traveling or not.

From the above it should be clear that energy methods are not an ideal tool for the analysis of the dynamics of blade assemblies when the motion is described in terms of traveling wave modes. However, by switching to standing wave modes where applicable (see Section 2.2.4), the analysis is greatly simplified. Furthermore, in many simple models where all the degrees of freedom of a single site will vibrate with a zero or π radian phase difference, the equations of motion in harmonic coordinates may be easily be set up by inspection (see Section 3.1.2).

CHAPTER III

MODELS OF TURBOMACHINERY ROTORS

In Chapter II we examined how the structural analysis of structures with perfect cyclic symmetry, such as tuned blade assemblies, may be reduced to the analysis of a single sector of the structure. When blade mistuning prevents the utilization of cyclic symmetry arguments a model of the full assembly is required. In the case of finite element analysis, a much coarser mesh must be considered or the increase in problem size may be so drastic that the problem becomes difficult on engineering workstations. Furthermore, a full analysis of the statistics of response of a randomly mistuned system calls for multiple realizations of mistuned assemblies requiring an even more severe order reduction, lest the problem become unsolvable. A full blown Monte Carlo simulation of a mistuned structure may require thousands of realizations, a monumental task unless the number of degrees of freedom per realization is kept within reason. In many cases this may limit the number of degrees of freedom per sector to less than ten.

Classical Models

Many reduced-order models of bladed disks have been developed for the study of localization and other basic phenomena. There are two main categories of reduced order models. The first category consists of models in which the bladed disk is modeled on a sector by sector basis using coupled lumped mass oscillators. There are no limits to the level of sophistication of these kinds of models. Each blade-disk sector may be modeled with several degrees of freedom and sector to sector coupling may quite elaborate, *e.g.* by allowing coupling to sectors other than the nearest neighboring sectors. Such models capture the basic bladed disk dynamics, and exhibit localization due to mistuning (see Section 1.1). The localization effects may then be analyzed by using Monte Carlo techniques to determine the structure's sensitivity to localization for a given mistuning strength, by investigating the effect of various parameters on the localization, or by other types of analysis. However, in terms of representing actual systems, these models are rather crude. Furthermore, if one wishes to use such

a model to predict the localization in a particular engineering structure, parameter identification can be extremely difficult.

Improved Modeling Approach

The other category is exemplified by a model introduced by Kaza and Kielb [38], in which the disk was modeled as a circular plate with constant thickness, and the blades were modeled by elastic beams. The blades were attached to the disk by maintaining continuity of displacement and slope at the disk-blade junction. The dynamics were described by the standing wave modes of the disk and the traveling wave modes of the blades. This type of model attempts to examine the disk and blade as separate physical entities. This kind of approach has definite advantages over the coupled oscillator models when it comes time to identify parameters in the model of an actual rotor.

There is a clear need for an improved, systematic reduced-order modeling technique for bladed disks. Ideally, this technique would make use of a modal analysis for a single sector finite element model, so that the reduced order model would represent well the actual structure. Furthermore, it should employ a component mode approach, with the disk and blades as the components, so that individual blade properties may be mistuned. Finally, the technique should be able to produce a model with a highly reduced number of degrees of freedom, so that Monte Carlo simulations may be performed at a reasonable cost. Section 3.2 features such an approach.

3.1. Coupled Oscillator Models

Coupled oscillators models result from viewing turbomachinery rotors as a closed periodic chain of oscillators. Each oscillator is the model of one or more blade-disk sectors in the rotor, possessing any number of degrees of freedom, P. We shall refer to an oscillator modeling one or more blade-disk sectors as a bay. Bay to bay coupling occurs through some number of coupling coordinates, M. A bay may be coupled to any number of its neighboring bays. The coupling coordinates are a subset of the degrees of freedom in the bay. Herein lies the advantage of the coupled oscillator model. As the number of coupling coordinates is normally a small number, bay to bay interaction is easily visualized. Furthermore, as we shall presently see, the structure may be modeled solely in terms of the coupling coordinates with a resulting, often dramatic, reduction in the number of degrees of freedom and ensuring very sparse, low bandwidth system matrices. Also, since the number of different energy carrying waves possible in the structure is equal to the number of coupling coordinates (see Chapter V) a coupled oscillator model lends itself readily to a wave analysis which is essential for the fundamental understanding of mode localization.

The coupled oscillator models are not without serious drawbacks. First, the convenient, simple model of interblade coupling is often a drastic oversimplification of the complex coupling that may occur in turbomachinery rotors. Since coupling may be the single most important factor influencing the mistuning sensitivity of a rotor this may be a substantial limitation. Secondly, although the coupled oscillator models may be of great academic interest, due to their transparency, they lose some of their luster in real life applications due to difficulty in parameter identification. Currently, no techniques exist for the automatic calibration of model parameters in the coupled oscillator model leaving the analyst no good way of generating an efficient model of his rotor.

Since the low number of coupling coordinates was toted as a major advantage of coupled oscillator models, only models with one– (mono-coupled) or two coupling coordinates (bi-coupled) will be presented here. We will see that even with this extremely low number of coupling coordinates some very complex behavior may be modeled.

Due to the frequent use of the term *degree of freedom* it will be abbreviated as DOF in most of what follows.

3.1.1. Transfer Matrix Formulation

In the cases where coupled oscillator models are deemed satisfactory it is usually because a bay may be considered to be coupled to very few of its neighboring elements through a low number of coupling elements. These types of models lend themselves to a transfer matrix representation. For example, an assembly which features only coupling between adjacent blades can be modeled efficiently with transfer matrices of dimension twice the number of coupling coordinates [21]. The number of DOFs through which a blade is coupled to its neighbors may be much smaller than the actual number of DOFs accounted for in the blade-disk sector. With the transfer matrix approach, the cyclic nature of the system is taken into account by realizing that the state vector describing the behavior of each blade in an N-blade system is, at any given time, periodic with a period N/n blades long, $n = (0, 1, 2, \ldots, N)$.

Blade assemblies may therefore be modeled as periodic structures with the additional constraint that the dynamics at the two boundaries are identical. The transfer matrix modeling of any periodic or cyclic structure undergoing harmonic motion requires the definition of a *state vector*. For the discussion we introduce the terms *bay* and *interface*. A bay is normally defined as exactly one spatial period in the periodic structure, such that only bays that are nearest neighbors are coupled. An interface is a “point” on the structure which separates two bays. To a state vector for a interface corresponds a transfer matrix that relates the states at two consecutive interfaces.

The dimension of the state vector must be twice the number of coupling coordinates at each interface, M [21]. A state vector is most commonly defined as the coupling coordinate amplitudes at an interface and the amplitudes of the associated forces. Displacements and forces at two consecutive interfaces are thus related as

$$\begin{bmatrix} \mathbf{q} \\ \mathbf{F} \end{bmatrix}_i = \hat{\mathbf{T}}_i \begin{bmatrix} \mathbf{q} \\ \mathbf{F} \end{bmatrix}_{i-1} \qquad i = 1, \ldots, N. \tag{3.1}$$

where $\mathbf{q}$ and $\mathbf{F}$ each have dimension M, where M is the number of coupling coordinates and $\hat{\mathbf{T}}_i$ is the transfer matrix for the ith bay, which depends on the frequency of harmonic motion. If the structure is perfectly periodic then all the transfer matrices are identical, corresponding to a blade assembly that is perfectly tuned.

Alternatively we could define *a state vector for a bay* as the coupling coordinate amplitudes at both ends of the bay. Then

$$\mathbf{u}_i = \mathbf{T}_i \mathbf{u}_{i-1} \qquad i = 1, \ldots, N \tag{3.2}$$

where $\mathbf{u}_i = [\mathbf{q}_{i+1}^T, \mathbf{q}_i^T]^T$ has dimension $2M$, *i.e.*, *twice* the number of coupling coordinates. Note that because of cyclicity $\mathbf{q}_{N+1} = \mathbf{q}_1$ and $\mathbf{q}_N = \mathbf{q}_0$. The work is based on the latter approach of bay state vectors. It is noteworthy that the actual number of DOFs of each bay, P, may be larger (possibly much larger) than the number of coordinates, M, through which it is coupled to the other bays in the assembly. It is M that determines the dimension of the transfer matrix.

Equation (3.2) does not account for motion-independent external forces acting on the system and hence only the free dynamics are considered. Furthermore, this approach will only be used in conjunction with real-valued problems, thus ignoring damping and aerodynamic effects.

As an example of the simplicity and usefulness of the transfer matrix formulation we demonstrate how it may he used to find the modes of a cyclic structure. We search for the modes of a tuned assembly whose dynamics are described by Eq. (3.2). Using the cyclic nature of the N-bay system we obtain

$$\begin{bmatrix} \mathbf{q}_o \\ \mathbf{q}_1 \end{bmatrix} = \begin{bmatrix} \mathbf{q}_N \\ \mathbf{q}_{N+1} \end{bmatrix} = \mathbf{T}_o^N \begin{bmatrix} \mathbf{q}_o \\ \mathbf{q}_1 \end{bmatrix}$$

where $\mathbf{T}_o$ is the transfer matrix for a tuned bay. Hence nontrivial solutions are obtained if and only if

$$\det\left(\mathbf{T_o}^N - \mathbf{I}\right) = 0. \tag{3.3}$$

which after some algebra yields the frequency equations

$$\lambda_i(\omega) = \sqrt[N]{1} = e^{j\sigma_n} \qquad i = 1, \ldots, 2M \tag{3.4}$$

where

$$\sigma_n = \frac{2\pi(n-1)}{N}, \qquad n = 1, \ldots, N. \tag{3.5}$$

Here, λ_i are the eigenvalues of $\mathbf{T}_o$ with corresponding eigenvectors

$$\begin{bmatrix} \mathbf{q}_k \\ \mathbf{q}_{k+1} \end{bmatrix}_i = \begin{bmatrix} 1 \\ e^{\sigma_n} \end{bmatrix} \otimes \tilde{\mathbf{u}}_{ni} \tag{3.6}$$

For each value of n the set of equations (3.4) ($i = 1, \ldots, 2M$) yields P frequency solutions, where P is the number of DOFs of each blade disk sector. The value, n represents the number of nodal diameters and σ represents the constant interblade phase angle throughout the assembly. As before $\tilde{\mathbf{u}}_{ni}$ represents the shape of a single bay as the assembly is vibrating in the ith σ_n-interblade-phase-angle mode

This is precisely the result discussed in Chapter II.

3.1.2. Mono Coupled Models

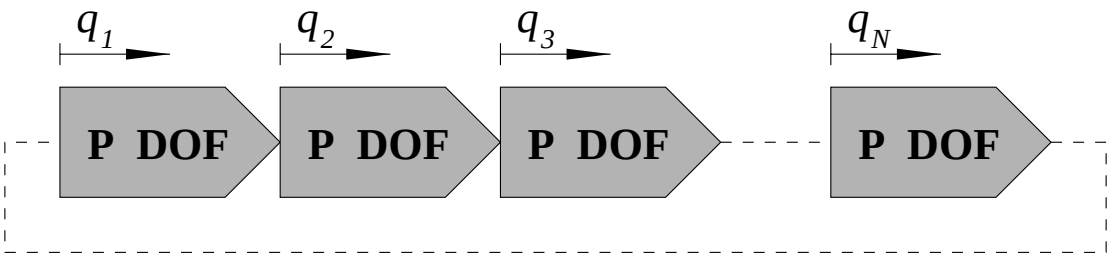

Figure 3.1 A general N-bay nearly cyclic assembly with P DOFs per bay, *one* of which couples adjacent bays.

Figure 3.1 depicts a generic mono-coupled coupled oscillator model as a chain of P-DOF subsystems, coupled through one coupling coordinate. The last subsystem connects with the first one, hence the cyclic symmetry. Since the adjacent bays are only coupled through one coordinate, the difference in the various mono-coupled models arises solely from the modeling of the blade-disk sector.

In the case of a tuned mono-coupled assembly Eq. 3.2 takes the simplified form

$$\begin{bmatrix} q_{i+1} \\ q_i \end{bmatrix} = \mathbf{T}_o \begin{bmatrix} q_i \\ q_{i-1} \end{bmatrix} \qquad i = 1, \ldots, N \tag{3.7}$$

which relates the states of two adjacent bays (recall that because of cyclicity $q_{N+1} = q_1$ and $q_N = q_0$). The formulation of Eq. (3.7) requires two equations relating the coupling coordinates q_{i+1}, q_i and q_{i-1}. One is the equation of motion taken at interface i:

$$-q_{i+1} + \beta_o(\omega) q_i - q_{i-1} = 0, \qquad \beta_o(\omega) \in \mathbb{R}, \tag{3.8}$$

where β_o is a function defined by the equation of motion of the bay, ω is the frequency of harmonic motion and $\mathbb{R}$ is the real domain. Note that Eq. (3.8) is symmetric in q_{i+1} and q_{i-1}, which requires the structure to be symmetric with respect to clockwise and counterclockwise numbering. This is the case only in the absence of aerodynamic and Coriolis forces. The symmetry discussed here is different from Mead's [20] definition of symmetry of individual bays, and Eq. (3.8) holds for either the symmetric or unsymmetric bays as defined by Mead. Equation (3.8) does not account for dissipation since $\beta_o(\omega)$ is assumed to be real valued. The second equation in Eq. (3.2) is simply the identity $q_i = q_i$. Hence each bay of a perfectly cyclic (tuned) mono-coupled structure is described by the same transfer matrix representation

$$\begin{bmatrix} q_{i+1} \\ q_i \end{bmatrix} = \begin{bmatrix} \beta_o(\omega) & -1 \\ 1 & 0 \end{bmatrix} \begin{bmatrix} q_i \\ q_{i-1} \end{bmatrix} = \mathbf{T_o} \begin{bmatrix} q_i \\ q_{i-1} \end{bmatrix}, \qquad \beta_o(\omega) \in \mathbb{R}. \tag{3.9}$$

where Eq. (3.9) accounts for neither damping nor aerodynamic effects. In general each substructure possesses P DOFs (see Fig. 3.1) and the generalized coordinates of the ith substructure are related to the coupling coordinate q_i through $P-1$ equations of motion local to the bay. However, note that the coupling DOF has no special significance, and in fact we may choose any of the P DOFs as our *reference* coordinate q_i. The choice must of course be the same for all bays.

When mistuning is introduced into the above cyclic system its periodicity is broken in one of two ways. First, the mistuning may be caused by a parameter which only appears in relation to the i^{th} interface, *e.g.*, the mistuning of parameters of individual blades. When this is the case the symmetry of Eq. (3.8) is unaffected and Eq. (3.9) is replaced by

$$\begin{bmatrix} q_{i+1} \\ q_i \end{bmatrix} = \begin{bmatrix} \beta(\delta_i) & -1 \\ 1 & 0 \end{bmatrix} \begin{bmatrix} q_i \\ q_{i-1} \end{bmatrix} = \mathbf{T_i} \begin{bmatrix} q_i \\ q_{i-1} \end{bmatrix}, \quad i = 1, \ldots, N, \tag{3.10}$$

where δ_i is the small deviation (order ϵ or smaller) of the parameter from its average value, defining the mistuning for the i^{th} bay. This is a random variable of mean zero. In the notation, the frequency dependence of β has been dropped, for clarity.

Alternatively, the mistuning may be caused by a parameter which appears at both interfaces, i and $(i+1)$, *e.g.*, the stiffness of a spring connecting two interfaces. Then Eq. (3.8) is no longer symmetric and Eq. (3.9) becomes

$$\begin{bmatrix} q_{i+1} \\ q_i \end{bmatrix} = \begin{bmatrix} \beta(\delta_i, \delta_{i-1}) & -\alpha(\delta_i, \delta_{i-1}) \\ 1 & 0 \end{bmatrix} \begin{bmatrix} q_i \\ q_{i-1} \end{bmatrix} = \mathbf{T_{i;i-1}} \begin{bmatrix} q_i \\ q_{i-1} \end{bmatrix}, \quad i = 1, \ldots, N, \tag{3.11}$$

where δ_i and δ_{i-1} are random variables which correspond to the mistuned parameter *on each side* of interface i. Again, the frequency dependence of α and β is implied. Note the use of a semicolon in the index.

One-DOF-sector model

Figure 3.2 depicts what is possibly the simplest possible model of a bladed disk. Indeed, since the model only possesses one coupled DOF in each blade-disk sector, a separate study of blade and disk motion is not possible. In the model, the DOF is conventionally considered as modeling the blade motion, although it more closely models disk type motion. Since much work on this model exists in the literature, and because its single parameter representation of coupling provides a convenient way of examining coupling effects, which have been shown to govern sensitivity to mistuning [31], it is ideal for the study of forced response. The understanding of the fundamental mechanisms of mistuning effects obtained through the use of this model should be fully applicable to more complicated models.

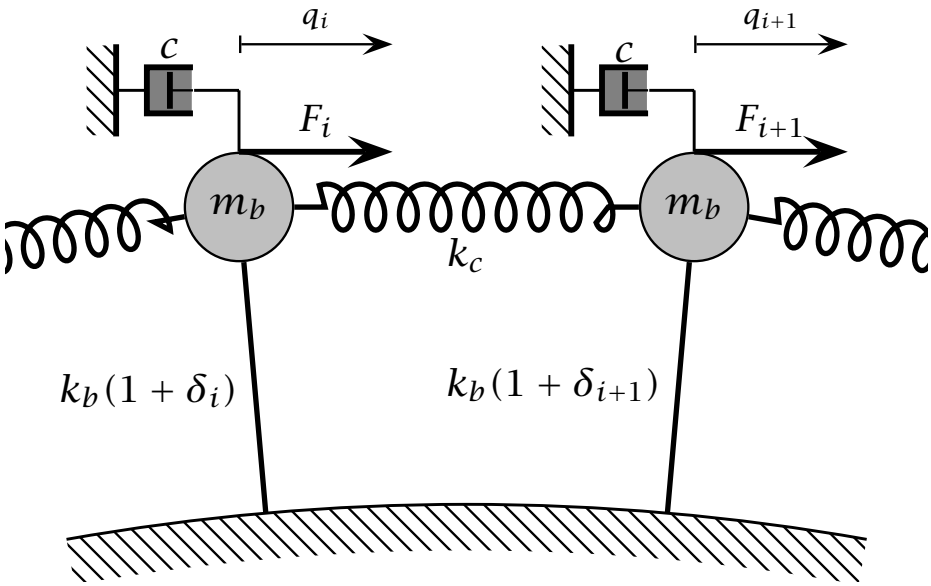

Figure 3.2 A simple model of a bladed disk featuring one-DOF, mono-coupled bays to model each blade/disk sector.

The equations of motion of the system in Fig. 3.2 are

$$m_b\ddot{q}_i + c\dot{q}_i - k_c q_{i-1} + (1+\delta_i)k_b q_i + 2k_c q_i - k_c q_{i+1} = F_i \qquad (i = 1,\ldots,N). \quad (3.12)$$

where $F_i = f\,e^{2j\pi C(i-1)/N}$ is the component of engine order C excitation (see Section 4.1) acting on blade i and δ_i is the mistuning parameter for blade i. Due to the cyclicity of the assembly we have $q_{N+1} = q_1$ and $q_o = q_N$. Normalizing with k_b and m and assuming harmonic motion leads to the form

$$-Rq_{i-1} + (1+\delta_i + 2R - \bar{\omega}^2 + 2j\zeta\bar{\omega})q_i - Rq_{i+1} = \bar{F}_i \qquad (i = 1,\ldots,N) \qquad (3.13)$$

where

$$R = \frac{k_c}{k_b}, \qquad \bar{\omega}^2 = \frac{m_b \omega^2}{k_b}, \quad \zeta = \frac{c}{c_{cr}} = \frac{c}{2\sqrt{k_b m_b}} \quad \text{and} \quad \bar{F}_i = \frac{f}{k_b} e^{2\pi C(i-1)/N} \tag{3.14}$$

To find the modes of free vibration of the tuned system, we examine the tuned, unforced, undamped case. The equations of harmonic motion are:

$$-Rq_{i-1} + (1 + 2R - \bar{\omega}^2)q_i - Rq_{i+1} = 0 \qquad (i = 1, \ldots, N) \tag{3.15}$$

A transformation to harmonic coordinates u_i (See Section 2.3) is as simple as assuming motion such that $q_i = u_k$, where u_k is the amplitude of blade i when the assembly is vibrating in the kth interblade phase angle mode. Then the motion of the adjacent blades is $q_{i-1} = u_k e^{-j\sigma_k}$ and $q_{i+1} = u_k e^{j\sigma_k}$, where $\sigma_k = 2\pi(k-1)/N$ is the phase shift, and Eq. (3.15) may be written as

$$\left[1 + 2R(1 - \cos\sigma_k) - \bar{\omega}_k^2\right] u_k = 0 \tag{3.16}$$

where $\bar{\omega}_k$ is a natural frequency corresponding to the σ_k interblade phase angle mode. Note that in the case of a single DOF per bay, harmonic coordinates and modal amplitude coordinates are the same. The natural frequencies of the tuned system are

$$\bar{\omega}_k^2 = 1 + 2R(1 - \cos\sigma_k) \qquad (k = 1, \ldots, N). \tag{3.17}$$

Since $\cos\sigma_k = \cos\sigma_{N+2-k}$, natural modes appear mostly in pairs corresponding to counterrotating (complex conjugate) interblade phase angle pairs. The natural frequencies of a cyclic structure may be conveniently plotted as a function of the harmonic at which they occur. Such a plot is depicted in Fig. 3.3. In the plot natural frequencies may be seen to rise sharply as the number of nodal diameters increase. This is typical of disk behavior since stiffness increases as tangential waviness of the mode increases.

In the unforced, undamped case the equations of motion may be written in a transfer matrix form

$$\begin{bmatrix} q_{i+1} \\ q_i \end{bmatrix} = \begin{bmatrix} (1 + \delta_i + 2R - \bar{\omega}^2)/R & -1 \\ 1 & 0 \end{bmatrix} \begin{bmatrix} q_i \\ q_{i-1} \end{bmatrix}, \quad i = 1, \ldots, N, \tag{3.18}$$

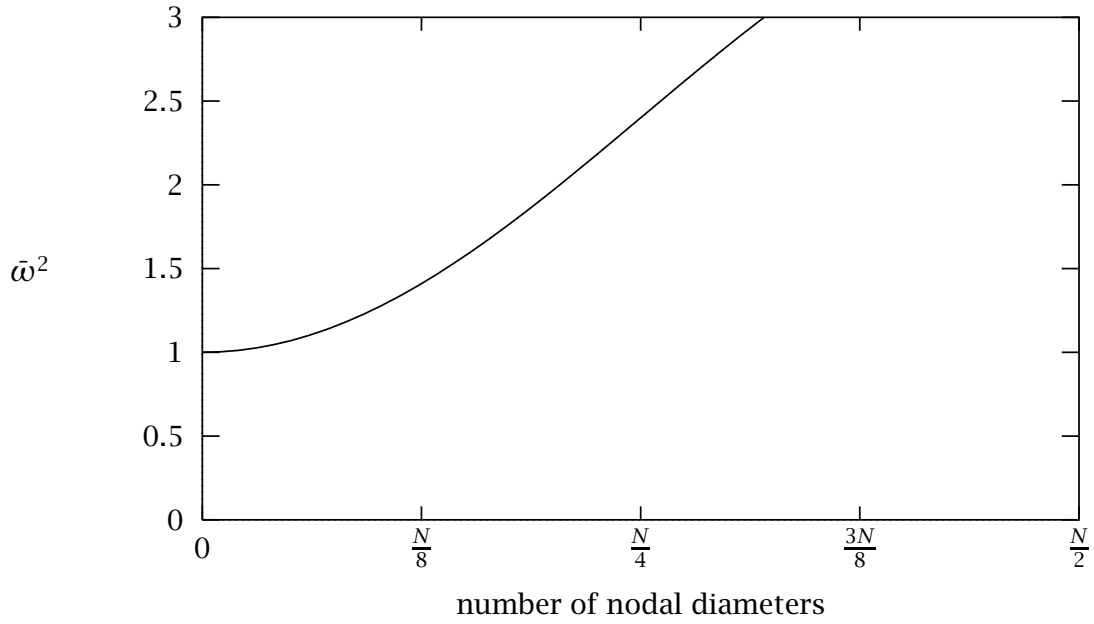

Figure 3.3 The natural frequencies of a one DOF model are plotted as a function of the number of nodal diameters. Disk type dynamics are evidenced. $R = 0.7$

Two-DOF-sector model

The next mono-coupled model of a bladed disk has two DOFs per bay. This model is shown in Fig. 3.4. Dye and Henry [3] were among the first to propose this blade assembly model and it has been used subsequently both for blade assemblies [37] and for large space reflectors [34]. This model will play a large role throughout this work. In Fig. 3.4, q_i^b represents the single-mode motion of the blade and q_i^d accounts for the motion of the disk at the blade root. Corresponding to q_i^b are the blade (modal) mass m_b and nominal (modal) stiffness k_b. The mass m_d simulates the effective mass of the blade root and the corresponding section of the disk. The stiffness k_d represents the nominal stiffness of the rotor disk, whereas k_c provides disk coupling between neighboring blades. It is assumed that all bays have identical masses m_b and m_d and that the blade–, disk– and coupling stiffness may differ from one bay to the next. This reduces complexity and provides adequate means of mistuning the natural frequencies of the individual bays. We write the mistuned stiffnesses as

$$k_d^i = k_d(1+\delta_i^d), \qquad k_b^i = k_b(1+\delta_i^b) \quad \text{and} \quad k_c^i = k_c(1+\delta_i^c), \tag{3.19}$$

where δ_i^d, δ_i^c and δ_i^b are random variables with zero mean and standard deviation s_d, s_c and s_b, respectively. The average values of the stiffnesses are k_b, k_d, and k_c,

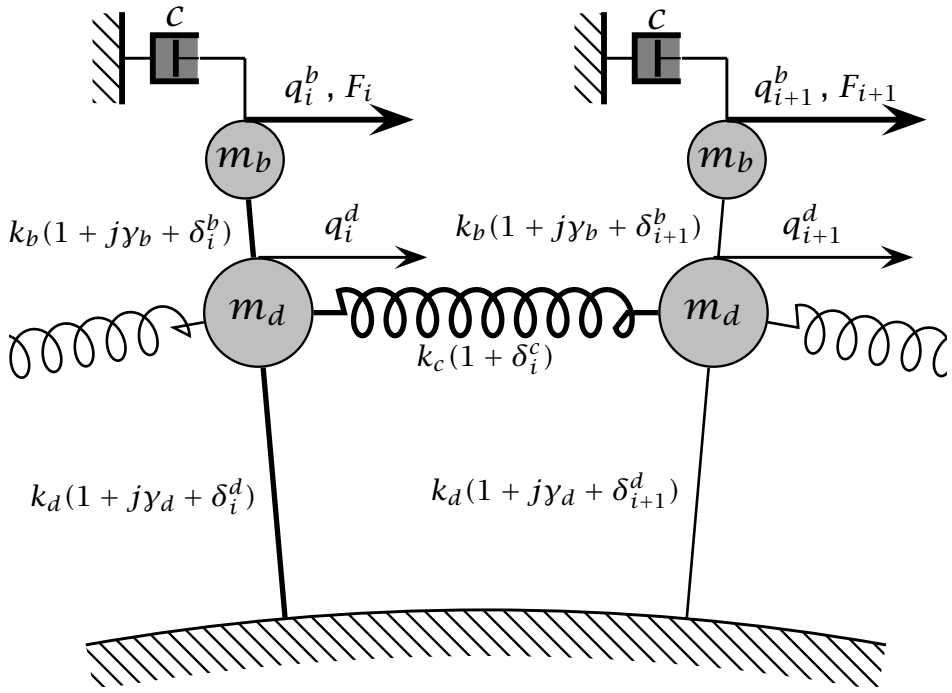

Figure 3.4 A simple model of a bladed disk featuring one disk-DOF and one blade-DOF, mono-coupled bays to model each blade/disk sector.

respectively, and correspond to the stiffnesses in a tuned assembly. This is the only model where we have included all these sources of mistuning since it will be used to study the effects of the different types of mistuning. We also aim to study how different combinations of stiffness and mass values affect the sensitivity of the system to mistuning and how the sensitivity differs when the blade stiffness, the disk stiffness, or the coupling spring stiffness are mistuned.

For the analysis of the forced response of the two-DOF per bay model to an engine order excitation, damping is included in the form of structural, or hysteretic damping for the blades (γ_b) and the disk (γ_d), and of viscous damping for the blades (c). The aim of including viscous damping is to simulate aerodynamic damping, although aerodynamic interblade coupling is clearly not captured by the model. Forcing is assumed to be applied at that blade DOF only.

We now proceed to formulate the equations of motion of a single bay in Fig. 3.4. Bay i is defined as the i^{th} blade-disk element, including the spring connecting it to blade $(i + 1)$. The i^{th} interface is the point where bay i and bay $(i - 1)$ meet. All parameters of bay i except the spring stiffness appear solely in relation with the i^{th} interface, whereas k_c^i connects interfaces i and $i + 1$. For that reason, a dynamic force

equilibrium at interface i will include both k_c^i and k_c^{i-1}. This yields the equations of motion

$$m_b\ddot{q}_i^b + cq_i^b + k_b(1+\delta_i^b+\gamma_b)(q_i^b - q_i^d) = F_i, \tag{3.20}$$

$$\begin{aligned} k_c(1+\delta_{i-1}^c)(q_i^d - q_{i-1}^d) + k_c(1+\delta_i^c)(q_i^d - q_{i+1}^d) + k_d(1+\delta_i^d+\gamma_d)q_i^d \\ + k_b(1+\delta_i^b+\gamma_b)(q_i^d - q_i^b) + m_d\ddot{q}_i^d = 0 \end{aligned} \tag{3.21}$$

Note that Eq. (3.20) is local to the ith blade. Introducing the following dimensionless parameters

$$\bar{k}_d = \frac{k_d}{k_b} \qquad \bar{k}_c = \frac{k_c}{k_b} \qquad \bar{m} = \frac{m_d}{m_b}. \tag{3.22}$$

and assuming harmonic motion, $\ddot{q}_i^b = -\omega^2 q_i^b$, Eq. (3.20) may be rearranged as

$$q_b^i = \frac{(1+\delta_i+j\gamma_b)q_d^i + \bar{F}_i}{(1+\delta_i+j\gamma_b) + 2j\zeta\bar{\omega} - \bar{\omega}^2} \tag{3.23}$$

where

$$\bar{\omega}^2 = \frac{m_b\omega^2}{k_b} \qquad \bar{F}_i = \frac{F_i}{k_b} \qquad \zeta = \frac{c}{c_{cr}} = \frac{c}{2\sqrt{k_b m_b}} \tag{3.24}$$

Equation (3.21) may be similarly nondimensionalized as

$$\begin{aligned} \bar{k}_c(1+\delta_{i-1}^c)(q_i^d - q_{i-1}^d) + \bar{k}_c(1+\delta_i^c)(q_i^d - q_{i+1}^d) + \bar{k}_d(1+\delta_i^d+\gamma_d)q_i^d \\ + (1+\delta_i^b+\gamma_b)(q_i^d - q_i^b) - \bar{\omega}^2\bar{m}q_i^d = 0 \end{aligned}, \tag{3.25}$$

Note that Eq. (3.23) can be used to eliminate the blade coordinates from Eq. (3.25).

In the absence of forcing and damping the equation of motion take a simplified form,

$$q_b^i = \left(\frac{1+\delta_i}{1+\delta_i-\bar{\omega}^2}\right) q_d^i \tag{3.26}$$

and

$$q_{i+1}^d = \frac{1}{1+\delta_i^c}\left[2+\delta_i^c+\delta_{i-1}^c+\frac{\bar{k}_d}{\bar{k}_c}(1+\delta_i^d) - \frac{\bar{\omega}^2(1+\delta_i^b)}{\bar{k}_c(1+\delta_i^b-\bar{\omega}^2)} - \frac{\bar{m}\bar{\omega}^2}{\bar{k}_c}\right]q_i^d - \frac{1+\delta_{i-1}^c}{1+\delta_i^c}q_{i-1}^d. \tag{3.27}$$

where Eq. (3.27) is solely in terms of disk coordinates. Defining

$$\beta_{i;i-1} = \frac{1}{1+\delta_i^c}\left[2+\delta_i^c+\delta_{i-1}^c+\frac{\bar{k}_d}{\bar{k}_c}(1+\delta_i^d) - \frac{\bar{\omega}^2(1+\delta_i^b)}{\bar{k}_c(1+\delta_i^b-\bar{\omega}^2)} - \frac{\bar{m}\bar{\omega}^2}{\bar{k}_c}\right] \tag{3.28}$$

and

$$\alpha_{i;i-1} = \frac{1+\delta_{i-1}^c}{1+\delta_i^c} \tag{3.29}$$

we can write

$$\begin{bmatrix} q_{i+1}^d \\ q_i^d \end{bmatrix} = \begin{bmatrix} \beta_{i;i-1} & -\alpha_{i;i-1} \\ 1 & 0 \end{bmatrix}\begin{bmatrix} q_i^d \\ q_{i-1}^d \end{bmatrix}, \quad i = 1,\ldots,N, \tag{3.30}$$

a transfer matrix form of the free equations of motion of the system in Fig. 3.4 where the state vector consists of the disk generalized coordinates.

For a tuned assembly we have $\delta_i^c = \delta_i^d = \delta_i^b = 0$ and β_o is given by

$$\beta_o = 2 + \frac{\bar{k}_d}{\bar{k}_c} - \frac{\bar{\omega}^2}{\bar{k}_c(1-\bar{\omega}^2)} - \frac{\bar{m}\bar{\omega}^2}{\bar{k}_c}. \tag{3.31}$$

with $\alpha_o = 1$. See Chapter V for a discussion of transfer matrix approaches to wave and mode analysis.

To find the natural frequencies of free motion of the tuned assembly, we break the problem into individual spatial harmonics by a transformation to harmonic coordinates,

$$\mathbf{u}_k = [u_b, u_d]_k^T, \qquad (k = 1 \ldots N), \tag{3.32}$$

such that $\mathbf{q}_i = \mathbf{u}_k$. Here, $\mathbf{u}_k$ is the amplitude vector of bay i as the assembly vibrates in the kth interblade-phase-angle mode. Then the motion of the adjacent blades is $\mathbf{q}_{i-1} = \mathbf{u}_k e^{-j\sigma_k}$ and $\mathbf{q}_{i+1} = \mathbf{u}_k e^{j\sigma_k}$ where $\sigma_k = 2\pi(k-1)/N$ and the equations of motion become

$$m_b \ddot{u}_b^{(k)} + k_b\left(u_b^{(k)} - u_d^{(k)}\right) = 0 \tag{3.33}$$

$$m_d \ddot{u}_d^{(k)} + k_d u_d^{(k)} + 2k_c(1-\cos\sigma_k)u_d^{(k)} - k_b\left(u_b^{(k)} - u_d^{(k)}\right) = 0 \tag{3.34}$$

Assuming harmonic motion of frequency, ω, Eqs. (3.33) and (3.34) may be written in matrix form as:

$$\begin{bmatrix} 1 & -1 \\ -1 & \bar{k}_d + 2(1-\cos\sigma_k)\bar{k}_c + 1 \end{bmatrix} \mathbf{u}_k - \bar{\omega}^2 \begin{bmatrix} 1 & 0 \\ 0 & \bar{m} \end{bmatrix} \ddot{\mathbf{u}}_k = \mathbf{0} \tag{3.35}$$

with the same nondimensionalization scheme as before (see Eqs. (3.22) and (3.24)). Equation (3.35) leads to the characteristic frequency equation

$$\bar{m}\bar{\omega}^4 - \bar{\omega}^2\left(\bar{k}_d + 2(1-\cos\sigma_k)\bar{k}_c + 1 + \bar{m}\right) + \left(\bar{k}_d + 2(1-\cos\sigma_k)\bar{k}_c\right) = 0 \tag{3.36}$$

which has *two* frequency solutions for each admissible interblade phase angle σ_k, $k = 1, \ldots, N$:

$$\bar{\omega}_k^2 = \frac{2\bar{k}_c(1-\cos\sigma_k) + \bar{k}_d + \bar{m} + 1}{2\bar{m}} \left[1 \pm \sqrt{1 - \frac{4\bar{m}\left[\bar{k}_d + 2\bar{k}_c(1-\cos\sigma_k)\right]}{\left[2\bar{k}_c(1-\cos\sigma_k) + \bar{k}_d + \bar{m} + 1\right]^2}}\right] \tag{3.37}$$

with σ_k given in Eq. (2.18). The natural frequencies for an example system are depicted in Fig. 3.5. The corresponding local deflection shapes $\mathbf{u}_k$ may be found using the first equation in Eq. (3.35). It yields

$$\mathbf{u}_k = \begin{bmatrix} 1 \\ 1 - \bar{\omega}_k^2 \end{bmatrix} \tag{3.38}$$

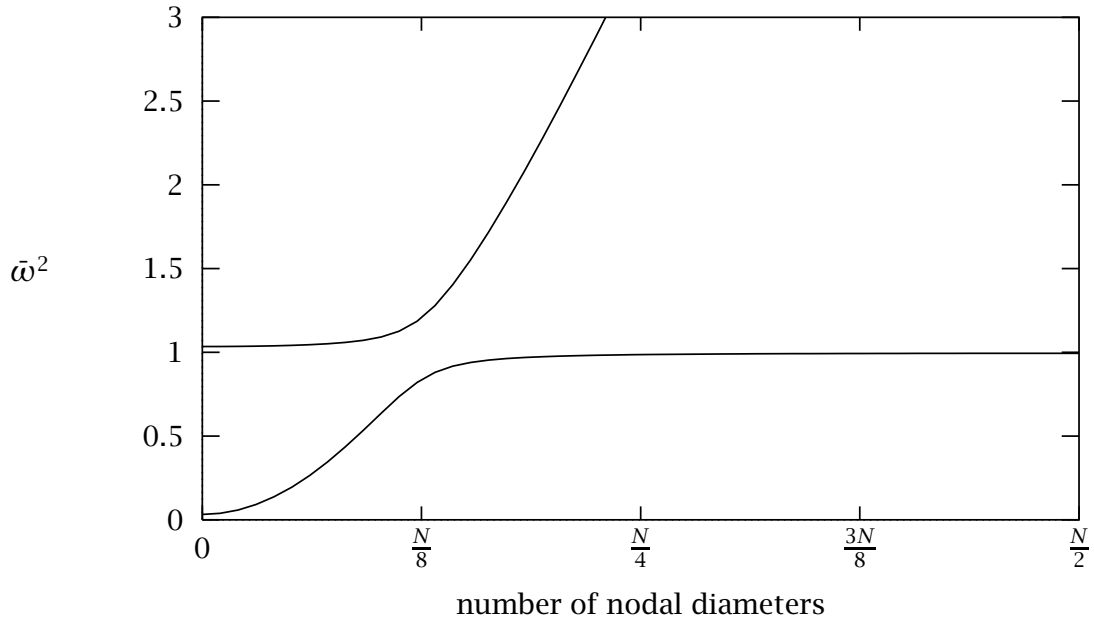

Figure 3.5 The natural frequencies of a two DOF model are plotted as a function of the number of nodal diameters. Distinct blade dynamics (horizontal curve segments) and disk type dynamics are evidenced. $\bar{k}_d = 1.$, $\bar{m} = 30$, $\bar{k}_c = 50$

The free vibration modes of the tuned assembly can be classified as blade- or disk-dominated modes based on the relative magnitudes of the disk and blade motions. We can quantify this by defining a kinetic energy ratio as the ratio of blade kinetic energy to the total kinetic energy in the constant interblade phase angle mode considered:

$$\bar{T}_k = \frac{m_b \left(\dot{u}_b^{(k)}\right)^2}{m_b \left(\dot{u}_b^{(k)}\right)^2 + m_d \left(\dot{u}_d^{(k)}\right)^2} = \frac{1}{1 + \bar{m}(1 - \bar{\omega}_k^2)^2} \tag{3.39}$$

Thus a value of $\bar{T}_k$ close to zero indicates that in that mode the assembly dynamics is dominated by the motion of the disk, while $\bar{T}_k$ of order 1 indicates a blade motion dominated dynamics.

Figure 3.5 shows a plot of the natural frequencies as a function of the number of nodal diameters in the corresponding mode shape. Note the differences between Fig. 3.5 and Fig. 3.3. The curves that correspond to the first and second natural frequency at a given numer of nodal diameters *veer* away from each other at $N/8$. We observe two distinct mode groups, a group of blade modes corresponding to the two horizontal curve segments and a group of disk modes corresponding to the parabola shaped curve segments. Note that if there were no coupling between the blades and

the disk, Fig. 3.5 would show two *intersecting* curves, a parabola shaped curve similar to the one depicted in Fig. 3.3 corresponding to disk modes and a horizontal curve corresponding to a mode of a fixed blade. The fixed blade mode curve would naturally be independent of the number of nodal diameters. Since the blade and the disk *are* coupled, the curves do not intersect. Instead, the veer away from each other and the tightness of the veering is a measure of the strength of the coupling. The stronger the veering, the stronger the coupling.

In their work Cornwell and Bendiksen [34] and Bendiksen [37] took a different approach to the analysis of the same model. Using the theory of circulant matrices, they chose to eliminate the disk DOFs by applying an approximate reduction procedure, arguing that in many cases of practical interest the disk stiffness is much greater than the blade stiffness. This is equivalent to setting $m_d = 0$ and thus $\bar{m} = 0$. We have found this to be an unnecessary approximation, although the approach allows one to emulate the coupling among *all* blades (as opposed to nearest neighbor coupling) through the disk DOFs.

Three-DOF-sector model

Figure 3.6 depicts a model obtained from the one-disk-, one-blade-DOF model. The model is enhanced by adding a DOF to the attached oscillator which is now capable of capturing two mode motion in the blade.

The model presented here is not without compromises. The model of the blade could be more general — *e.g.,* by coupling the upper DOF in the blade directly to the disk DOF — but in order to limit the number of parameters in the model some flexibility was sacrificed. As we shall see in Chapter VII, this does not obviously limit the capabilities of the model. Another concession to the ease-of-use was in the form of mistuning. As in earlier models, mistuning was only considered in the blade stiffness. In the current model there are two blade stiffnesses. These could have been individually mistuned but this would have introduced considerable complications without any clear benefits.

The stiffness and mass of the additional oscillator are given as a mass ratio, μ and stiffness ratio, κ, with respect to the pre-existing oscillator.

For the analysis of forced response, damping is included in the form of structural (or hysteretic) damping for the blades (γ_b) and the disk (γ_d), and of viscous damping for the blade DOFs (c_1 and c_2). Assuming that the blade structural damping is identical for both parts of the blade, but that forcing and viscous damping of the two blade DOFs may be different, the equations of motion are

$$m_d\ddot{q}_d^i + k_b(1+j\gamma_b+\delta_i)(q_d^i - q_{b1}^i) + k_d(1+j\gamma_d)q_d^i + k_c(-q_d^{i-1} + 2q_d^i - q_d^{i-1}) = 0 \quad (3.40)$$

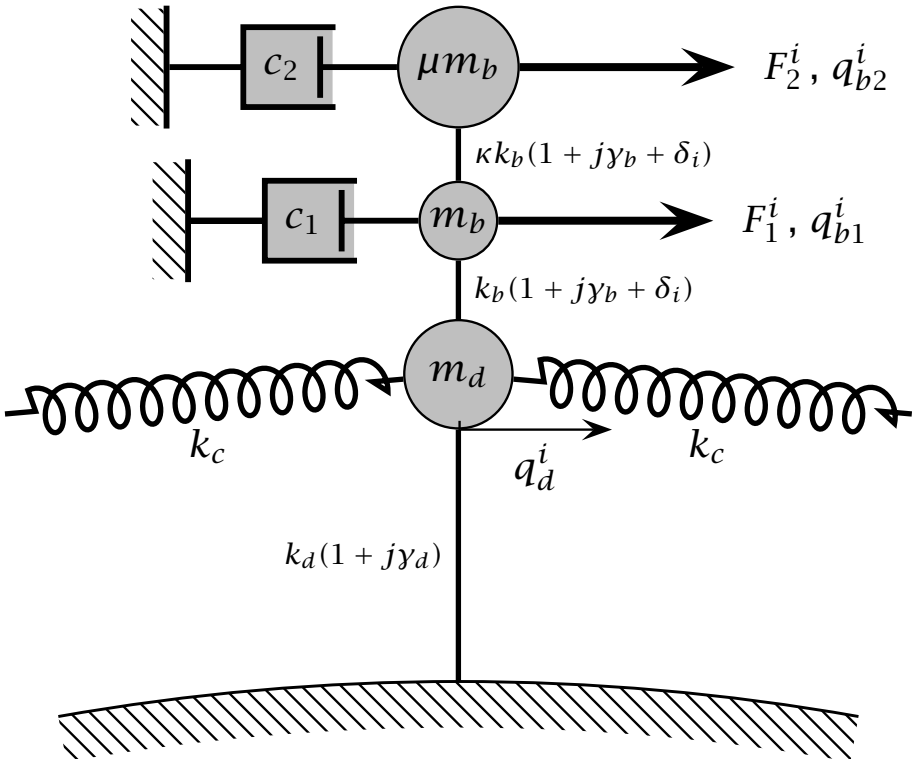

Figure 3.6 A simple model of a bladed disk featuring one disk-DOF and two blade-DOF, mono-coupled bays to model each blade/disk sector.

$$m_b\ddot{q}_{b1}^i + c_1\dot{q}_{b1} + k_b(1 + j\gamma_b + \delta_i)\left((q_{b1}^i - q_d^i) + \kappa k_b(q_{b1}^i - q_{b2}^i)\right) = F_1^i \tag{3.41}$$

$$\mu m_b\ddot{q}_{b2}^i + c_2\dot{q}_{b2}^i + \kappa k_b(1 + j\gamma_b + \delta_i)(q_{b2}^i - q_{b1}^i) = F_2^i \tag{3.42}$$

where $i = 1, \ldots, N$ with $q_{N+1} = q_1$ and $q_o = q_N$ due to cyclicity. Nondimensionalizing by scaling with the blade properties k_b and m_b and assuming harmonic motion yields

$$-\bar{\omega}^2\bar{m}q_d^i + (1 + j\gamma_b + \delta_i)(q_d^i - q_{b1}^i) + \bar{k}_d(1 + j\gamma_d)q_d^i + \bar{k}_c(-q_d^{i-1} + 2q_d^i - q_d^{i-1}) = 0 \tag{3.43}$$

$$-\bar{\omega}^2 q_{b1}^i + 2j\bar{\omega}\zeta_1 q_{b1} + (1 + j\gamma_b + \delta_i)\left((q_{b1}^i - q_d^i) + \kappa(q_{b1}^i - q_{b2}^i)\right) = \bar{F}_1^i \tag{3.44}$$

$$-\mu\bar{\omega}^2 q_{b2}^i + 2j\omega\zeta_2 q_{b2}^i + \kappa(1 + j\gamma_b + \delta_i)(q_{b2}^i - q_{b1}^i) = \bar{F}_2^i \qquad (i = 1, \ldots, N) \tag{3.45}$$

where the dimensionless parameters

$$\bar{k}_d = \frac{k_d}{k_b} \qquad \bar{k}_c = \frac{k_c}{k_b} \qquad \bar{m} = \frac{m_d}{m_b}. \tag{3.46}$$

and

$$\bar{\omega}^2 = \frac{m_b\omega^2}{k_b} \qquad \bar{F}_i = \frac{F_i}{k_b} \qquad \zeta_1 = \frac{c_1}{c_{cr}} \qquad \zeta_2 = \frac{c_2}{c_{cr}} \qquad \left(c_{cr} = 2\sqrt{k_b m_b}\right) \tag{3.47}$$

have been introduced. Equations (3.43) to (3.45) may be solved numerically for free or forced response in the mistuned case. Let us examine in more detail the free response of undamped, tuned systems that will be used in the parameter identification. We also review the condensation approach that is used for an efficient solution of the forced response of a mistuned structure.

Turning to the free response of the free undamped assembly we observe that the transformation to harmonic coordinates,

$$\mathbf{u}_k = [u_d, u_{b1}, u_{b2}]_k^T, \qquad (k = 1, \ldots, N), \tag{3.48}$$

simply requires assuming motion such that $\mathbf{q}_i = \mathbf{u}_k$. Here $\mathbf{u}_k$ is the amplitude vector of blade i as the assembly vibrates in the kth interblade phase angle mode. Then the motion of the adjacent blades is $\mathbf{q}_{i-1} = \mathbf{u}_k e^{-j\sigma_k}$ and $\mathbf{q}_{i+1} = \mathbf{u}_k e^{j\sigma_k}$, where $\sigma_k = 2\pi(k-1)/N$, and the equations of motion become

$$-\bar{\omega}^2\bar{m}u_{d,k} + u_{d,k} - u_{b1,k} + \left(\bar{k}_d + 2\bar{k}_c(1-\cos\sigma_k)\right)u_{d,k} = 0 \tag{3.49}$$

$$-\bar{\omega}^2 u_{b1,k} + u_{b1,k} - u_{d,k} + \kappa(u_{b1,k} - u_{b2,k}) = 0 \tag{3.50}$$

$$-\bar{\omega}^2\mu u_{b2,k} + \kappa(u_{b2,k} - u_{b1,k}) = 0 \tag{3.51}$$

or

$$\left(\begin{bmatrix} 1+\bar{k}_d+2\bar{k}_c(1-\cos\sigma_k) & -1 & 0 \\ -1 & 1+\kappa & -\kappa \\ 0 & -\kappa & \kappa \end{bmatrix} - \bar{\omega}_k^2 \begin{bmatrix} \bar{m} & 0 & 0 \\ 0 & 1 & 0 \\ 0 & 0 & \mu \end{bmatrix}\right)\tilde{\mathbf{u}}_k = 0 \tag{3.52}$$

Note that Eq. (3.52) corresponds to the kth block of the block-diagonalized eigenvalue problem in Eq. (2.26). The dimension of each block is equal to the number of DOFs in each sector. However, since the two blade DOFs depend only on the disk DOF, as follows

$$q_{b2}^i = q_{b1}^i \frac{\kappa}{\kappa - \mu\bar{\omega}^2} \tag{3.53}$$

$$q_{b1}^i = q_d^i \frac{(\kappa - \mu\bar{\omega}^2)}{(1+\kappa-\bar{\omega}^2)(\kappa-\mu\bar{\omega}^2) - \kappa^2} \tag{3.54}$$

the problem may be condensed down to a single dependent variable, and the block-circulant eigenvalue could be reduced to a circulant eigenvalue problem. In general, the block size in block-circulant matrix for a cyclic structure may be condensed down to the number of *coupling coordinates*.

Solving Eq. (3.52) for the natural frequencies $\bar{\omega}_k^2$ yields three solutions,

$$\begin{aligned}
\bar{\omega}_{k,1}^2 &= L_3 + L_2 - \frac{G_2}{3G_1} \\
\bar{\omega}_{k,2}^2 &= -\frac{1}{2}(L_3 + L_2) - \frac{G_2}{3G_1} + j\frac{\sqrt{3}}{2}(L_3 - L_2) \qquad k = 1, \ldots, N \\
\bar{\omega}_{k,3}^2 &= -\frac{1}{2}(L_3 + L_2) - \frac{G_2}{3G_1} - j\frac{\sqrt{3}}{2}(L_3 - L_2)
\end{aligned} \tag{3.55}$$

where

$$\begin{aligned}
L_1 &= \frac{\sqrt{3}}{G_1^2}\sqrt{4G_3^3G_1 - G_3^2G_2^2 - 18G_2G_3G_1G_4 \ + 27G_4^2G_1^2 + 4G_4G_2^3} \\
L_2 &= \left(\frac{G_2G_3}{6G_1^2} - \frac{G_4}{2G_1} - \frac{G_2^3}{27G_1^3} - \frac{L_1}{18}\right)^{\frac{1}{3}} \\
L_3 &= \left(\frac{G_2G_3}{6G_1^2} - \frac{G_4}{2G_1} - \frac{G_2^3}{27G_1^3} + \frac{L_1}{18}\right)^{\frac{1}{3}}
\end{aligned} \tag{3.56}$$

and

$$\begin{aligned}
G_1 &= -m\mu \\
G_2 &= \mu\left[k_d + 2(1 - \cos\sigma_k)k_c\right] + m\left[\kappa + \kappa\mu + \mu\right] + \mu \\
G_3 &= -\left[k_d + 2(1 - \cos\sigma_k)k_c\right]\left[\kappa + \kappa\mu + \mu\right] - \kappa(m + \mu + 1) \\
G_4 &= \kappa\left[k_d + 2(1 - \cos\sigma_k)k_c\right]
\end{aligned} \tag{3.57}$$

Figure 3.7 illustrates the natural frequencies as a function of the number of nodal diameters in an example system. The corresponding mode shapes are calculated from Eqs. (3.53) and (3.54) as

$$\tilde{\mathbf{u}}_k = \begin{bmatrix} \tilde{u}_d^{(k)} \\ \tilde{u}_{b_1}^{(k)} \\ \tilde{u}_{b_2}^{(k)} \end{bmatrix} = \begin{bmatrix} (1 + \kappa - \bar{\omega}_k^2)\left(1 - \frac{\mu}{\kappa}\bar{\omega}_k^2\right) - \kappa \\ \left(1 - \frac{\mu}{\kappa}\bar{\omega}_k^2\right) \\ 1 \end{bmatrix} = \begin{bmatrix} A_k \\ B_k \\ 1 \end{bmatrix} \qquad k = 1, \ldots, N \tag{3.58}$$

Clearly there are three such local shapes for each value of k. The free vibration modes can be classified as blade- or disk-dominated modes. Figure 3.7 depicts the natural frequencies conveniently plotted as a function of the number of nodal diameters in the corresponding mode shape. Note how the addition of a second blade DOF has introduced a second horizontal blade-mode branch that also interacts with the disk-mode branch through a veering. Classification of blade motion dominated modes and disk motion dominated modes is achieved by studying $\bar{T}_k$, the ratio of the blade kinetic energy to the total system kinetic energy in a σ_k-interblade phase angle mode:

$$\bar{T}_k = \frac{m_b\left(\dot{\tilde{u}}_{b1}^{(k)}\right)^2 + \mu m_b\left(\dot{u}_{b2}^{(k)}\right)^2}{m_d\left(\dot{u}_d^{(k)}\right)^2 + m_b\left(\dot{u}_{b1}^{(k)}\right)^2 + \mu m_b\left(\dot{u}_{b2}^{(k)}\right)^2} = \frac{B_k^2 + \mu}{\bar{m}_d A_k^2 + B_k^2 + \mu} \tag{3.59}$$

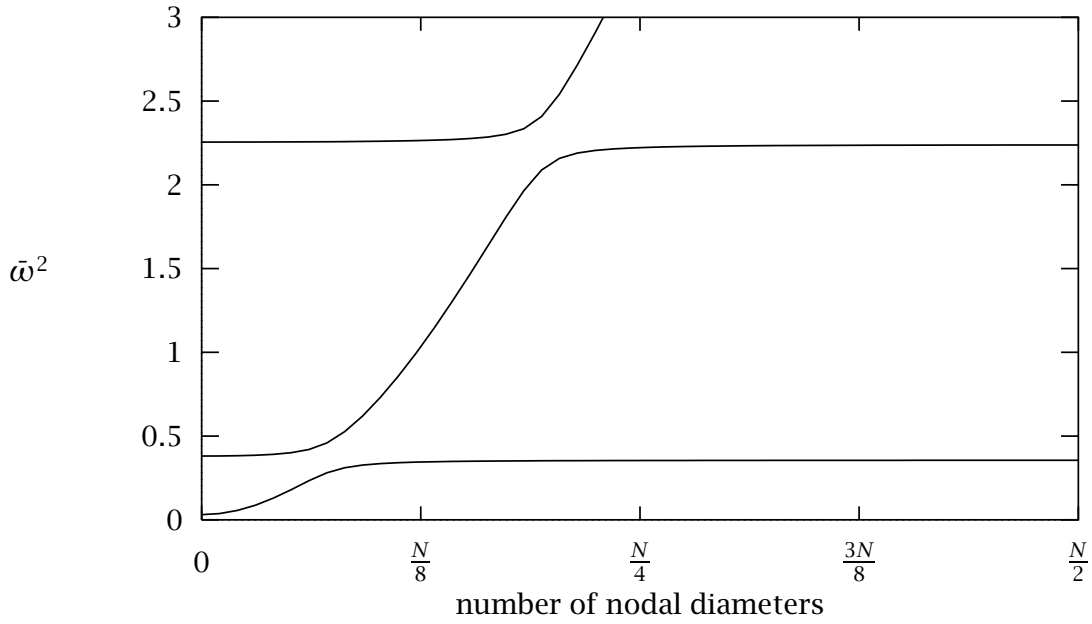

Figure 3.7 Natural frequencies as a function of the number of nodal diameters for the system: $\bar{k}_d = 1.$, $\bar{m} = 30$, $\bar{k}_c = 50$, $\kappa = .8$ and $\mu = 1$.

Modes dominated by the disk motion will be characterized by $\bar{T}_k$ close to zero, and blade-dominated modes by $\bar{T}_k$ close to unity.

Now we show how the equations of motion may be condensed in the forced response case to enhance the efficiency of the forced response solver. The condensation is based on the fact that the blade DOFs in each sector depend only on the disk-DOF of that sector. Assuming harmonic motion, we can solve Eq. (3.45) for the blade displacement q^i_{b2}

$$q^i_{b2} = \frac{\kappa(1 + j\gamma_b + \delta_i)q^i_{b1} + \bar{F}^i_2}{2j\bar{\omega}\zeta_2 - \mu\bar{\omega}^2 + \kappa(1 + j\gamma_b + \delta_i)} \tag{3.60}$$

Likewise, we have, from Eq. (3.44)

$$q^i_{b1} = \frac{\bar{F}^i_2\kappa\mathcal{K}_3(\bar{\omega}) + \bar{F}^i_1\mathcal{K}_2(\bar{\omega}) + q^i_d\mathcal{K}_3(\bar{\omega})\mathcal{K}_2(\bar{\omega})}{\mathcal{K}_1(\bar{\omega})\mathcal{K}_2(\bar{\omega}) - \kappa^2\mathcal{K}^2_3(\bar{\omega})} \tag{3.61}$$

where, for convenience, we have defined

$$\mathcal{K}_1(\bar{\omega}) = 2j\zeta_1\bar{\omega} - \bar{\omega}^2 + (1 + \kappa)(1 + j\gamma_b + \delta_i)$$

$$\mathcal{K}_2(\bar{\omega}) = 2j\zeta_2\bar{\omega} - \mu\bar{\omega}^2 + \kappa(1 + j\gamma_b + \delta_i)$$

$$\mathcal{K}_3(\bar{\omega}) = (1 + j\gamma_b + \delta_i)$$

Finally, using Eqs. (3.60) and (3.61), we can reduce Eq. (3.43) to the form

$$-q_d^{i-1} + \beta(\delta_i, \bar{\omega}) q_d^i - q_d^{i+1} = \frac{\bar{F}_2^i \kappa^2 \mathcal{K}_3^2(\bar{\omega}) + \bar{F}_1^i \kappa \mathcal{K}_3(\omega) \mathcal{K}_2(\bar{\omega})}{\bar{k}_c \left[\mathcal{K}_1(\bar{\omega}) \mathcal{K}_2(\bar{\omega}) - \kappa^2 \mathcal{K}_3^2(\bar{\omega}) \right]} \qquad (i = 1, \ldots, N) \tag{3.62}$$

where the equations of motion have been condensed down to one equation of motion in terms of the coupling coordinates, q_d^i. The dynamic properties of the system are completely captured by the β function

$$\beta(\delta_i, \bar{\omega}) = \frac{\mathcal{K}_4(\bar{\omega})}{\bar{k}_c} - \frac{\kappa \mathcal{K}_3^2(\bar{\omega}) \mathcal{K}_2(\bar{\omega})}{\bar{k}_c \left[\mathcal{K}_1(\bar{\omega}) \mathcal{K}_2(\bar{\omega}) - \kappa^2 \mathcal{K}_3^2(\bar{\omega}) \right]} \tag{3.63}$$

where

$$\mathcal{K}_4(\bar{\omega}) = -\bar{m}\bar{\omega}^2 + (1 + j\gamma_b + \delta_i) + \bar{k}_d(1 + j\gamma_d) + 2\bar{k}_c \tag{3.64}$$

Finally we point out that a transfer matrix representation of the free damped response is obtainable from (3.62) as

$$\begin{bmatrix} q_d^{i+1} \\ q_d^i \end{bmatrix} = \begin{bmatrix} \beta(\delta_i, \bar{\omega}) & -1 \\ 1 & 0 \end{bmatrix} \begin{bmatrix} q_d^i \\ q_d^{i-1} \end{bmatrix}$$

3.1.3. Bi-Coupled Models

What the models presented thus far have all had in common is a single coupling coordinate. In the following sections we shall investigate two models that have two coupling coordinates. As we will see in Chapter V the addition of a second coupling coordinate complicates the analysis of waves in the assembly because as we stated in Section 1.1.1, there are as many wave channels in a periodic structure as there are coupling coordinates.

There are two basic ways of obtaining a bi-coupled system. First, a system may consist of a chain of coupled oscillator in which only adjacent oscillators are coupled, through two coupling coordinates. Second, we may have an oscillator chain in which each oscillator communicates directly with four other oscillators, two on each side, through one coupling coordinate each. Figures 3.8 and 3.9 illustrate the two cases in a general way.

The treatment of multi-wave periodic systems usually focuses on systems where only neighboring bays are coupled through multiple coordinates, as shown in Fig. 3.8. The form required for the transfer matrix representation of the multi-coupled system depicted in Fig. 3.8 is

$$\begin{bmatrix} \mathbf{q}_{i+1} \\ \mathbf{q}_i \end{bmatrix} = \begin{bmatrix} \mathbf{B} & -\mathbf{A} \\ \mathbf{I} & \mathbf{O} \end{bmatrix} \begin{bmatrix} \mathbf{q}_i \\ \mathbf{q}_{i-1} \end{bmatrix} = \mathbf{T} \begin{bmatrix} \mathbf{q}_i \\ \mathbf{q}_{i-1} \end{bmatrix} \tag{3.65}$$

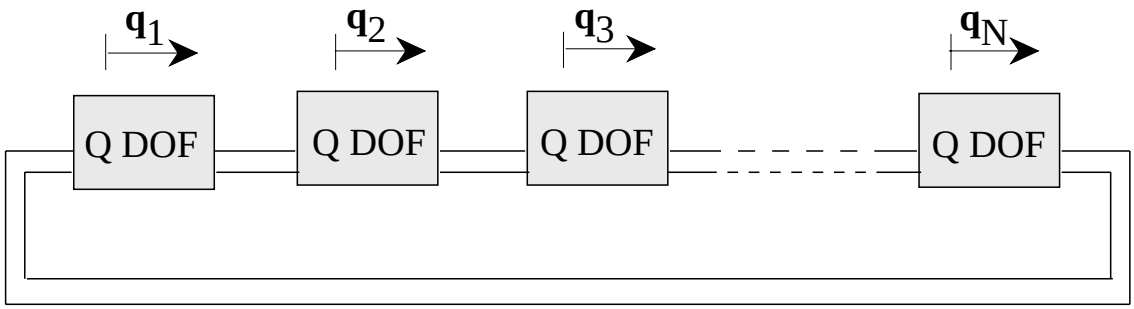

Figure 3.8 A general N-bay cyclic assembly with Q DOFs per bay, *two* of which are coupled to *one* adjacent bay *on each side*.

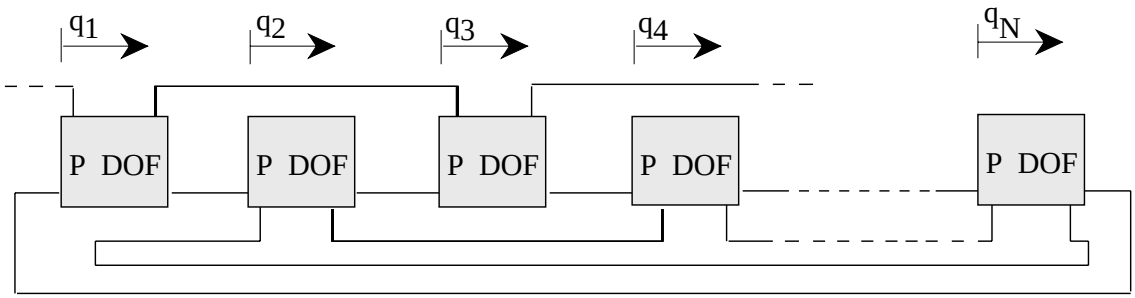

Figure 3.9 A general N site cyclic assembly with P DOFs per site, one of which is coupled to *two* adjacent sites *on each side*.

where $\mathbf{q}_i$ is the vector of coupling coordinate amplitudes at bay i. The block $\mathbf{I}$ in the matrix $\mathbf{T}$ denotes the identity matrix and $\mathbf{0}$ is a block of zeros.

The alternative method approaches bi-coupled systems ($M = 2$) through the special case of five coupled bays as depicted in Fig. 3.9. This definition of a bay does not conform to our earlier requirement that only neighboring bays be coupled. However, we will demonstrate how this case of coupled non-adjacent bays can be related to the case in which only neighboring bays are coupled. A transfer matrix representation of a system where each bay is coupled to its four nearest neighbors is

$$\begin{bmatrix} q_{i+2} \\ q_{i+1} \\ q_i \\ q_{i-1} \end{bmatrix} = \begin{bmatrix} -\alpha & \beta_i & -\alpha & -1 \\ 1 & 0 & 0 & 0 \\ 0 & 1 & 0 & 0 \\ 0 & 0 & 1 & 0 \end{bmatrix} \begin{bmatrix} q_{i+1} \\ q_i \\ q_{i-1} \\ q_{i-2} \end{bmatrix}. \tag{3.66}$$

The first row represents the equation of motion of the coupling coordinates of the ith bay and the remaining rows are trivial identities. The analysis of the additional DOFs of each bay is performed through equations of motion which are local to the bay. Were this system to be described by a circulant system matrix [51], β and $-\alpha$ would

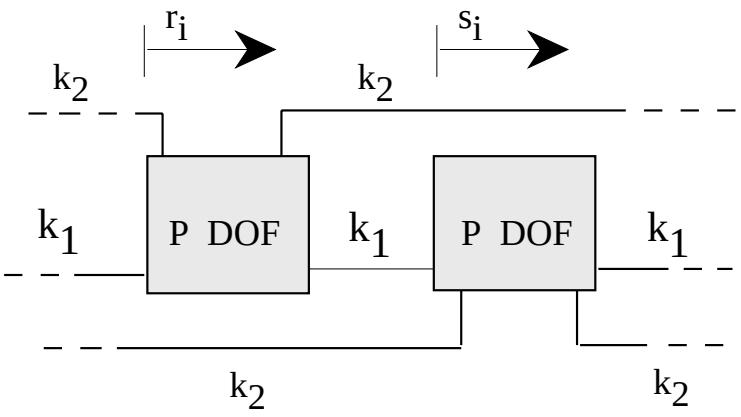

Figure 3.10 An aggregate bay of the model in Fig. 3.9, chosen so that only neighboring substructures are coupled.

be, respectively, the diagonal and the super/sub-diagonal elements of the circulant system matrix, with -1 appearing on the second off-diagonals. This would yield the system matrix $\mathbf{circ}[\beta, -\alpha, -1, 0, \ldots, 0, -1, -\alpha]$.

For those familiar with the work of Mead [21], it is interesting to study the relationship between the two approaches to bi-coupled systems, adjacent bay *vs.* nonadjacent bay coupling. Plainly, the system in the preceding section, shown in Fig. 3.9, may be modified to the form in Fig. 3.8 by regarding two adjacent bays as being one bay of the system shown in Fig. 3.8.

This aggregate bay, which possesses $Q = 2P$ DOFs, is depicted in Fig. 3.10. The corresponding form of the aggregate transfer matrix is obtained by multiplying two adjacent individual transfer matrices defined in Eq. (3.66). This yields

$$\begin{aligned}
\begin{bmatrix} \mathbf{q}_{i+1} \\ \mathbf{q}_i \end{bmatrix} &= \begin{bmatrix} -\alpha & \beta & -\alpha & -1 \\ 1 & 0 & 0 & 0 \\ 0 & 1 & 0 & 0 \\ 0 & 0 & 1 & 0 \end{bmatrix} \begin{bmatrix} -\alpha & \beta & -\alpha & -1 \\ 1 & 0 & 0 & 0 \\ 0 & 1 & 0 & 0 \\ 0 & 0 & 1 & 0 \end{bmatrix} \begin{bmatrix} \mathbf{q}_i \\ \mathbf{q}_{i-1} \end{bmatrix} \\
&= \begin{bmatrix} \alpha^2 - \beta & -\alpha\beta - \alpha & \alpha^2 - 1 & \alpha \\ -\alpha & \beta & -\alpha & -1 \\ 1 & 0 & 0 & 0 \\ 0 & 1 & 0 & 0 \end{bmatrix} \begin{bmatrix} \mathbf{q}_i \\ \mathbf{q}_{i-1} \end{bmatrix} \\
&= \begin{bmatrix} \mathbf{B} & -\mathbf{A} \\ \mathbf{I} & \mathbf{O} \end{bmatrix} \begin{bmatrix} \mathbf{q}_i \\ \mathbf{q}_{i-1} \end{bmatrix}
\end{aligned} \tag{3.67}$$

where

$$\mathbf{q}_i = \begin{bmatrix} r_i \\ s_i \end{bmatrix} \tag{3.68}$$

The more classical representation of periodic structures in terms of coupled adjacent

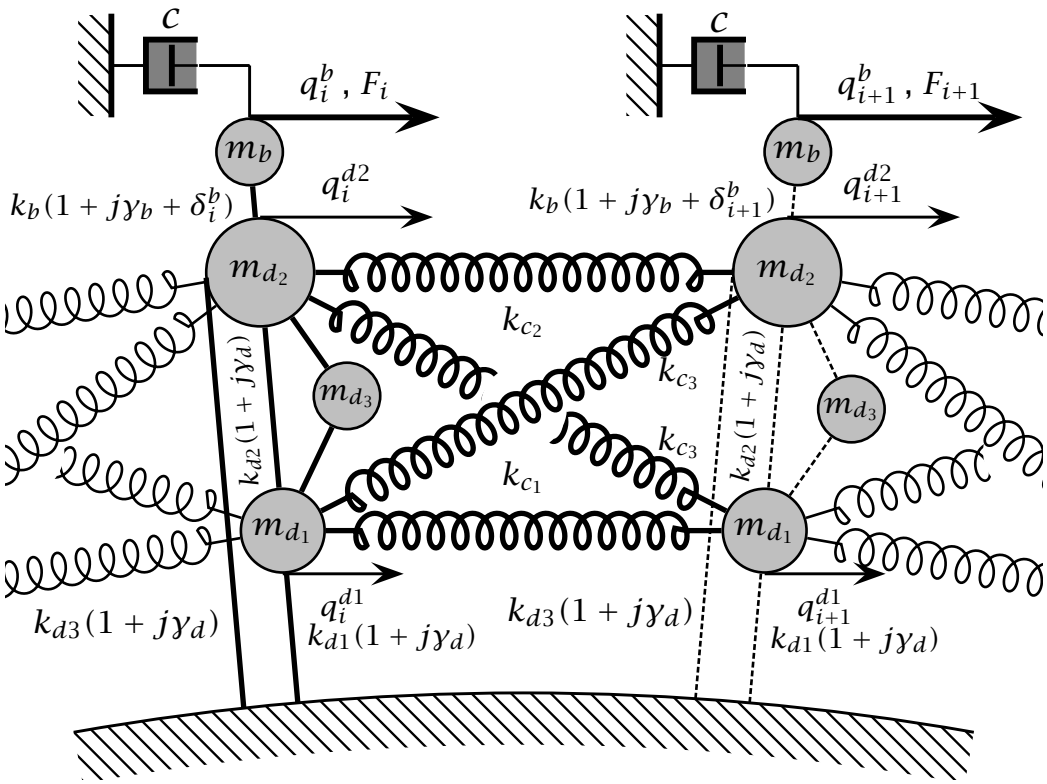

Figure 3.11 A simple model of a bladed disk featuring two disk-DOF and one blade-DOF, bi-coupled bays to model each blade-disk sector.

bays is thus easily achieved from the non-adjacent coupling formulation by a simple permutation of the state vector coordinates and the squaring of the associated transfer matrix. In the following sections we shall give examples of both types of bi-coupled systems.

Three-DOF-sector bi-coupled model

Figure 3.11 depicts an elaborate three-DOF per bay model. The modeling of the blades is identical to that for the one disk-DOF, one blade-DOF mono-coupled system. However, each disk sector is modeled as a two-DOF system, with stiffness and inertia influence coefficients which yield general (for example, non-diagonal) stiffness and mass matrices for the disk sector. Note that the "mass" m_{d_3} represents a cross-inertia. Adjacent disk sectors are also coupled in a general way, as shown in Fig. 3.11. It is noteworthy that because of the generality of the disk sector model, one can reasonably expect negative values for some of the disk parameters, particularly m_{d_3} and k_{c_3}. However there is no guarantee that any set of parameters will lead to a positive definite system. A poor choice of parameters may result in spurious, non-physical systems.

For each bay in Fig. 3.11 the three equations governing the steady-state response

to the harmonic excitation are:

$$-\bar{\omega}^2 q_b^i + (1 + j\gamma_b + \delta_i)(q_b^i - q_{d_2}^i) + 2j\zeta\bar{\omega} q_b^i = \bar{F}_i, \tag{3.69}$$

$$\begin{aligned} -\bar{\omega}^2 \left[\bar{m}_2 q_{d_2}^i + \bar{m}_3 q_{d_1}^i\right] + \bar{k}_{d_3}(1 + j\gamma_d) q_{d_2}^i + \bar{k}_{d_2}(1 + j\gamma_d)\left(q_{d_2}^i - q_{d_1}^i\right) \\ + \bar{k}_{c_2}\left(-q_{d_2}^{i-1} + 2q_{d_2}^i - q_{d_2}^{i+1}\right) + \bar{k}_{c_3}\left(-q_{d_1}^{i-1} + 2q_{d_2}^i - q_{d_1}^{i+1}\right) \\ + (1 + \delta_i + j\gamma_b)\left(q_{d_2}^i - q_b^i\right) = 0 \end{aligned} \tag{3.70}$$

$$\begin{aligned} -\bar{\omega}^2 \left[\bar{m}_1 q_{d_1}^i + \bar{m}_3 q_{d_2}^i\right] + \bar{k}_{d_1}(1 + j\gamma_d) q_{d_1}^i + \bar{k}_{d_2}(1 + j\gamma_d)\left(q_{d_1}^i - q_{d_2}^i\right) \\ + \bar{k}_{c_1}\left(-q_{d_1}^{i-1} + 2q_{d_1}^i - q_{d_1}^{i+1}\right) + \bar{k}_{c_3}\left(-q_{d_2}^{i-1} + 2q_{d_1}^i - q_{d_2}^{i+1}\right) = 0 \end{aligned} \tag{3.71}$$

where the disk parameters have been scaled by the blade parameters as follows

$$\begin{aligned} \bar{m}_1 &= \tfrac{m_{d_1}}{m_b} & \bar{k}_{c_1} &= \tfrac{k_{c_1}}{k_b} & \bar{k}_{d_1} &= \tfrac{k_{d_1}}{k_b} \\ \bar{m}_2 &= \tfrac{m_{d_2}}{m_b} & \bar{k}_{c_2} &= \tfrac{k_{c_2}}{k_b} & \bar{k}_{d_2} &= \tfrac{k_{d_2}}{k_b} \\ \bar{m}_3 &= \tfrac{m_{d_3}}{m_b} & \bar{k}_{c_3} &= \tfrac{k_{c_3}}{k_b} & \bar{k}_{d_3} &= \tfrac{k_{d_3}}{k_b} \end{aligned} \tag{3.72}$$

in addition to using the dimensionless parameters of Eq. (3.24) and the scaling the frequency of motion with the blade natural frequency, $\omega_b = k_b/m_b$.

We solve Eq. (3.69) for q_b^i, thus obtaining

$$q_b^i = \frac{(1 + \delta_i + j\gamma_b)\, q_{d_2}^i + \bar{F}_i}{(1 + \delta_i + j\gamma_b) + 2j\zeta\bar{\omega} - \bar{\omega}^2} \tag{3.73}$$

and use it to eliminate q_b^i from Eq. (3.70), which then takes the form

$$\begin{aligned} -\bar{\omega}^2 \left[\bar{m}_2 q_{d_2}^i + \bar{m}_3 q_{d_1}^i\right] + \bar{k}_{d_3}(1 + j\gamma_d) q_{d_2}^i + \bar{k}_{d_2}(1 + j\gamma_d)\left(q_{d_2}^i - q_{d_1}^i\right) \\ + \bar{k}_{c_2}\left(-q_{d_2}^{i-1} + 2q_{d_2}^i - q_{d_2}^{i+1}\right) + \bar{k}_{c_3}\left(-q_{d_1}^{i-1} + 2q_{d_2}^i - q_{d_1}^{i+1}\right) \\ + (1 + \delta_i + j\gamma_b)\left(q_{d_2}^i - \frac{(1 + \delta_i + j\gamma_b)\, q_{d_2}^i + \bar{F}_i}{(1 + \delta_i + j\gamma_b) + 2j\zeta\bar{\omega} - \bar{\omega}^2}\right) = 0 \end{aligned} \tag{3.74}$$

This leaves us with two equations, (3.71) and (3.74), and two unknowns per bay, $\mathbf{q}_d^i = [q_{d_1}^i, q_{d_2}^i]^T$. This system of equations can be written as

$$-\mathbf{A}\mathbf{q}_d^{i+1} + \mathbf{B}_i \mathbf{q}_d^i - \mathbf{A}\mathbf{q}_d^{i-1} = \bar{F}\, \mathbf{f}_i \quad i = 1, \ldots, N, \tag{3.75}$$

where

$$\mathbf{A} = \begin{bmatrix} \bar{k}_{c_1} & \bar{k}_{c_3} \\ \bar{k}_{c_3} & \bar{k}_{c_2} \end{bmatrix}, \tag{3.76}$$

$$\mathbf{B}_i = \begin{bmatrix} -\bar{\omega}^2\bar{m}_1 + 2(\bar{k}_{c_1} + \bar{k}_{c_3}) & -\bar{\omega}^2\bar{m}_3 - \bar{k}_{d_2}(1 + j\gamma_d) \\ \quad + (\bar{k}_{d_2} + \bar{k}_{d_1})(1 + j\gamma_d) & \\ & -\bar{\omega}^2\bar{m}_2 + (\bar{k}_{d_3} + \bar{k}_{d_2})(1 + j\gamma_d) + 2(\bar{k}_{c_2} + \bar{k}_{c_3}) \\ -\bar{\omega}^2\bar{m}_3 - \bar{k}_{d_2}(1 + j\gamma_d) & +(1 + \delta_i + j\gamma_b) - \dfrac{(1 + \delta_i + j\gamma_b)^2}{(1 + \delta_i + j\gamma_b) + 2j\zeta\bar{\omega} - \bar{\omega}^2} \end{bmatrix} \tag{3.77}$$

and

$$\mathbf{f}_i = \frac{1 + \delta_i + j\gamma_b}{1 + \delta_i + j\gamma_b + 2j\zeta\bar{\omega} - \bar{\omega}^2}\, \mathrm{e}^{\left[\frac{2j\pi}{N}C(i-1)\right]} \begin{bmatrix} 0 \\ 1 \end{bmatrix}. \tag{3.78}$$

The individual bay equations can be gathered in a $2N$ by $2N$ system which governs the steady-state forced response of the assembly:

$$\begin{bmatrix} \mathbf{B}_1 & -\mathbf{A} & 0 & 0 & \dots & 0 & -\mathbf{A} \\ -\mathbf{A} & \mathbf{B}_2 & -\mathbf{A} & 0 & \dots & 0 & 0 \\ 0 & -\mathbf{A} & \mathbf{B}_3 & -\mathbf{A} & \dots & 0 & 0 \\ 0 & 0 & -\mathbf{A} & \mathbf{B}_4 & \dots & 0 & 0 \\ \vdots & \vdots & \vdots & \vdots & \ddots & \vdots & \vdots \\ 0 & 0 & 0 & 0 & \dots & \mathbf{B}_{N-1} & -\mathbf{A} \\ -\mathbf{A} & 0 & 0 & 0 & \dots & -\mathbf{A} & \mathbf{B}_N \end{bmatrix} \begin{bmatrix} \mathbf{q}_d^1 \\ \mathbf{q}_d^2 \\ \mathbf{q}_d^3 \\ \mathbf{q}_d^4 \\ \vdots \\ \mathbf{q}_d^{N-1} \\ \mathbf{q}_d^N \end{bmatrix} = \bar{F} \begin{bmatrix} \mathbf{f}_1 \\ \mathbf{f}_2 \\ \mathbf{f}_3 \\ \mathbf{f}_4 \\ \vdots \\ \mathbf{f}_{N-1} \\ \mathbf{f}_N \end{bmatrix} \tag{3.79}$$

The above matrix is "block-tridiagonal circulant" (or nearly so for mistuned systems) and has a reduced dimension of $2N \times 2N$ for this $3N$-DOF assembly. The solution of the linear system, Eq. (3.79), yields the forced response amplitudes of the disk DOFs. The blade forced response amplitudes can then calculated from Eq. (3.73).

For a mistuned assembly Eq. (3.79) cannot be simplified and its solution requires the inversion of the impedance matrix. A computer program that takes into account the sparseness of the matrix and can accomplish the inversion in a very efficient manner was developed and used in this work. Hence, this $3N \times 3N$ system that under normal circumstances would require order $(3N)^2$ operations can be solved with order $2N$ operations. In the tuned assembly case a closed-form solution can be obtained, as follows.

The response of the tuned system may be easily calculated once it has been realized that an engine order C excitation only causes the $\sigma_{C+1} = 2\pi C/N$ interblade phase angle modes to respond, with all other modes remaining quiescent for all time. As we showed in Section 2.4, the forced response problem is thus reduced to

$$\left(\mathbf{B}_o - 2\cos\sigma_{C+1}\mathbf{A}\right) \begin{bmatrix} q_{d_1}^{(C)} \\ q_{d_2}^{(C)} \end{bmatrix} = \begin{bmatrix} 0 \\ \bar{F} \end{bmatrix} \frac{1 + j\gamma_b}{1 + j\gamma_b + 2j\zeta\bar{\omega} - \bar{\omega}^2} \tag{3.80}$$

with $\mathbf{A}$ and $\mathbf{B}_o$ from Eqs. (3.76) and (3.77), respectively, with $\delta_i = 0$. Equation (3.80) is readily solved for $q_{d_2}^{(C)}$. The value of $q_b^{(C)}$ is subsequently obtained via Eq. (3.73). The

final result, the magnitude of the blade response amplitude due to an engine order C excitation, $|q_b^{(C)}|$, is obtained as

$$|q_b^{(C)}| = \left| \left(\frac{f\,(1+j\gamma_b)}{\left(K_{22} - \dfrac{K_{12}^2}{K_{11}}\right)} \; + \; 1 \right) \left(1 + j\gamma_b + 2j\zeta\bar{\omega} - \bar{\omega}^2\right)^{-1} \right| \bar{F} \tag{3.81}$$

where

$$K_{12} = -\bar{\omega}^2\bar{m}_3 - \bar{k}_{d_2}(1+j\gamma_d) - 2\bar{k}_{c_3}\cos\sigma \tag{3.82}$$

$$K_{11} = -\bar{\omega}^2\bar{m}_1 + \bar{k}_{d_1}(1+j\gamma_d) + \bar{k}_{d_2}(1+j\gamma_d) + 2\bar{k}_{c_1}(1-\cos\sigma) + 2\bar{k}_{c_3} \tag{3.83}$$

$$\begin{aligned} K_{22} = &-\bar{\omega}^2\bar{m}_2 + \bar{k}_{d_3}(1+j\gamma_d) + \bar{k}_{d_2}(1+j\gamma_d) + 2\bar{k}_{c_2}(1-\cos\sigma) \\ &+ 2\bar{k}_{c_3} + 1 + j\gamma_b - \frac{(1+j\gamma_b)^2}{1+j\gamma_b - \bar{\omega}^2 + 2j\zeta\bar{\omega}} \end{aligned} \tag{3.84}$$

$$f = \frac{1+j\gamma_b}{1+j\gamma_b - \bar{\omega}^2 + 2j\zeta\bar{\omega}} \tag{3.85}$$

We are interested in the modes of the tuned system. The transformation to harmonic coordinates,

$$\mathbf{u}_k = [u_b, u_{d1}, u_{d2}]_k^T, \qquad (k = 1 \ldots N), \tag{3.86}$$

requires assuming motion such that $\mathbf{q}_i = \mathbf{u}_k$ as before. Again, $\mathbf{u}_k$ is the amplitude vector of blade bay i as the assembly vibrates in the kth interblade phase angle mode. Then the motion of the adjacent blades is $\mathbf{q}_{i-1} = \mathbf{u}_k e^{-j\sigma_k}$ and $\mathbf{q}_{i+1} = \mathbf{u}_k e^{j\sigma_k}$ where $\sigma_k = 2\pi(k-1)/N$ and the equations of motion become

$$m_b\ddot{u}_b^{(k)} + k_b(u_b^{(k)} - u_{d_2}^{(k)}) = 0 \tag{3.87}$$

$$\begin{aligned} m_{d_1}\ddot{u}_{d_1}^{(k)} + m_{d_3}\ddot{u}_{d_2}^{(k)} + k_{d_1}u_{d_1}^{(k)} + k_{d_2}(u_{d_1}^{(k)} \\ -u_{d_2}^{(k)}) + 2k_{c_1}(1-\cos\sigma_k)u_{d_1}^{(k)} + 2k_{c_3}(u_{d_1}^{(k)} - \cos\sigma_k u_{d_2}^{(k)}) = 0 \end{aligned} \tag{3.88}$$

$$\begin{aligned} m_{d_3}\ddot{u}_{d_1}^{(k)} + m_{d_2}\ddot{u}_{d_2}^{(k)} + k_{d_3}u_{d_2}^{(k)} - k_{d_2}(u_{d_1}^{(k)} - u_{d_2}^{(k)}) + 2k_{c_2}(1-\cos\sigma_k)u_{d_2}^{(k)} \\ +2k_{c_3}(u_{d_2}^{(k)} - \cos\sigma_k u_{d_1}^{(k)}) - k_b(u_b^{(k)} - u_{d_2}^{(k)}) = 0 \end{aligned} \tag{3.89}$$

Assuming harmonic motion of frequency, ω, Eqs. (3.87)–(3.89) may be written in matrix form as

$$\begin{bmatrix} 1 & 0 & -1 \\ 0 & \bar{k}_{d_1}+\bar{k}_{d_2}+2(1-\cos\sigma_k)\bar{k}_{c_1}+2\bar{k}_{c_3} & -\left(\bar{k}_{d_2}+2\bar{k}_{c_3}\cos\sigma_k\right) \\ -1 & -\left(\bar{k}_{d_2}+2\bar{k}_{c_3}\cos\sigma_k\right) & \bar{k}_{d_2}+\bar{k}_{d_3}+1+2(1-\cos\sigma_k)\bar{k}_{c_2}+2\bar{k}_{c_3} \end{bmatrix} \mathbf{u}_k$$
$$-\bar{\omega}^2 \begin{bmatrix} 1 & 0 & 0 \\ 0 & \bar{m}_1 & \bar{m}_3 \\ 0 & \bar{m}_3 & \bar{m}_2 \end{bmatrix} \mathbf{u}_k = 0 \tag{3.90}$$

Equation (3.90) leads to the characteristic frequency equation

$$\begin{aligned}
&(1-\bar{\omega}^2)\left(\bar{k}_{d_1}+\bar{k}_{d_2}+2(1-\cos\sigma_k)\bar{k}_{c_1}+2\bar{k}_{c_3}-\bar{m}_1\bar{\omega}^2\right)\\
&\qquad\left(\bar{k}_{d_2}+\bar{k}_{d_3}+1+2(1-\cos\sigma_k)\bar{k}_{c_2}+2\bar{k}_{c_3}-\bar{m}_2\bar{\omega}^2\right)\\
&-(1-\bar{\omega}^2)\left(\bar{k}_{d_2}+2\bar{k}_{c_3}\cos\sigma_k+\bar{m}_3\bar{\omega}^2\right)^2\\
&-\left(\bar{k}_{d_1}+\bar{k}_{d_2}+2(1-\cos\sigma_k)\bar{k}_{c_1}+2\bar{k}_{c_3}-\bar{m}_1\bar{\omega}^2\right)=0
\end{aligned} \tag{3.91}$$

Equation (3.91) has three frequency solutions for each admissible interblade phase angle σ_k, $k = 1,\ldots,N$ (see Eq. (2.18)). The solution in closed form is obtained by using Eq. (3.55) with

$$G_1 = \bar{m}_3^2 - \bar{m}_1\bar{m}_2$$

$$\begin{aligned}
G_2 =&\bar{m}_1\bar{k}_{d_3}+2\bar{m}_1\bar{k}_{c_2}+\bar{m}_1\bar{m}_2+\bar{m}_1+2\bar{k}_{d_2}\bar{m}_3+2\bar{m}_1\bar{k}_{c_3}-\bar{m}_3^2+\bar{m}_1\bar{k}_{d_2}+2\bar{k}_{c_1}\bar{m}_2\\
&+2\bar{k}_{c_3}\bar{m}_2+\bar{k}_{d_2}\bar{m}_2+\bar{k}_{d_1}\bar{m}_2+(4\bar{k}_{c_3}\bar{m}_3-2\bar{m}_1\bar{k}_{c_2}-2\bar{k}_{c_1}\bar{m}_2)\cos\sigma_k
\end{aligned}$$

$$\begin{aligned}
G_3 =&4[\bar{k}_{c_3}^2-\bar{k}_{c_1}\bar{k}_{c_2}]\cos^2\sigma_k+2[\bar{k}_{d_1}\bar{k}_{c_2}+\bar{k}_{d_2}\bar{k}_{c_2}+4\bar{k}_{c_1}\bar{k}_{c_2}+\bar{k}_{c_1}\bar{k}_{d_2}+\bar{k}_{c_1}\bar{k}_{d_3}\\
&+2\bar{k}_{c_1}\bar{k}_{c_3}+2\bar{k}_{c_3}\bar{k}_{c_2}+\bar{k}_{c_1}\bar{m}_2+\bar{k}_{c_1}+2\bar{k}_{d_2}\bar{k}_{c_3}+\bar{m}_1\bar{k}_{c_2}-2\bar{k}_{c_3}\bar{m}_3]\cos\sigma_k\\
&-\bar{k}_{d_1}\bar{k}_{d_2}-\bar{k}_{d_1}\bar{k}_{d_3}-2\bar{k}_{d_1}\bar{k}_{c_2}-2\bar{k}_{d_1}\bar{k}_{c_3}-\bar{k}_{d_2}\bar{k}_{d_3}-\bar{k}_{d_1}-\bar{k}_{d_2}-2\bar{k}_{c_1}-2\bar{k}_{c_3}\\
&-2\bar{k}_{d_2}\bar{k}_{c_2}-4\bar{k}_{d_2}\bar{k}_{c_3}-2\bar{k}_{c_1}\bar{k}_{d_2}-2\bar{k}_{c_1}\bar{k}_{d_3}-4\bar{k}_{c_1}\bar{k}_{c_2}-4\bar{k}_{c_3}^2-\bar{k}_{d_2}\bar{m}_2-\bar{k}_{d_1}\bar{m}_2\\
&-4\bar{k}_{c_1}\bar{k}_{c_3}-2\bar{k}_{c_3}\bar{k}_{d_3}-4\bar{k}_{c_3}\bar{k}_{c_2}-2\bar{k}_{c_1}\bar{m}_2-2\bar{k}_{c_3}\bar{m}_2-\bar{m}_1\bar{k}_{d_2}-2\bar{m}_1\bar{k}_{c_2}\\
&-2\bar{m}_1\bar{k}_{c_3}-2\bar{k}_{d_2}\bar{m}_3-\bar{m}_1\bar{k}_{d_3}
\end{aligned}$$

$$\begin{aligned}
G_4 =&-2\bar{k}_{c_1}\bar{k}_{d_2}\cos\sigma_k-2\bar{k}_{c_1}\bar{k}_{d_3}\cos\sigma_k+\bar{k}_{d_1}\bar{k}_{d_2}+\bar{k}_{d_1}\bar{k}_{d_3}+2\bar{k}_{d_1}\bar{k}_{c_2}+2\bar{k}_{d_1}\bar{k}_{c_3}\\
&+4\bar{k}_{d_2}\bar{k}_{c_3}-2\bar{k}_{d_1}\bar{k}_{c_2}\cos\sigma_k+4\bar{k}_{c_1}\bar{k}_{c_2}\cos^2\sigma_k-2\bar{k}_{d_2}\bar{k}_{c_2}\cos\sigma_k+4\bar{k}_{c_1}\bar{k}_{c_2}\\
&-8\bar{k}_{c_1}\bar{k}_{c_2}\cos\sigma_k+2\bar{k}_{c_1}\bar{k}_{d_3}+4\bar{k}_{c_3}^2-4\bar{k}_{c_3}^2\cos^2\sigma_k+\bar{k}_{d_2}\bar{k}_{d_3}-4\bar{k}_{c_3}\bar{k}_{c_2}\cos\sigma_k\\
&+2\bar{k}_{c_1}\bar{k}_{d_2}-4\bar{k}_{d_2}\bar{k}_{c_3}\cos\sigma_k+2\bar{k}_{d_2}\bar{k}_{c_2}+4\bar{k}_{c_1}\bar{k}_{c_3}+2\bar{k}_{c_3}\bar{k}_{d_3}\\
&+4\bar{k}_{c_3}\bar{k}_{c_2}-4\bar{k}_{c_1}\bar{k}_{c_3}\cos\sigma_k
\end{aligned}$$

Figure 3.12 presents a typical plot of the natural frequencies of a bi-coupled, three DOF system, plotted as a function of the number of nodal diameters in the corresponding mode shape. Note the existence of two groups of disk modes and one blade mode group.

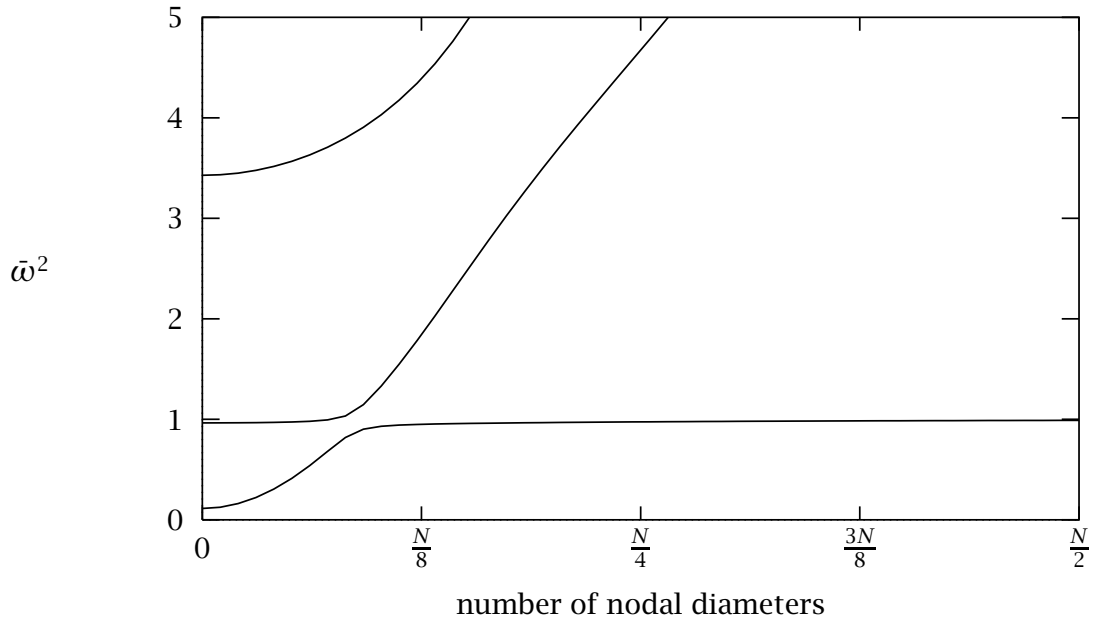

Figure 3.12 The natural frequencies of a bi-coupled, three DOF model are plotted as a function of the number of nodal diameters. Distinct blade and two mode disk type dynamics are evidenced. $\bar{m}_{d1} = 58$, $\bar{m}_{d2} = 78$, $\bar{m}_{d3} = -63$, $\bar{k}_{d1} = -18$, $\bar{k}_{d2} = 4000$, $\bar{k}_{d3} = 50$, $\bar{k}_{c1} = 1800$, $\bar{k}_{c2} = 2400$, $\bar{k}_{c3} = -2000$.

Non-adjacent neighbor coupling bi-coupled model

Dye and Henry's model of a two-DOF per site assembly presented above may be easily extended to include an extra coupling spring of stiffness k_{c2}, as illustrated in Fig. 4. The disk DOF at site i is now connected not only to sites $i-1$ and $i+1$, but to sites $i-2$ and $i+2$ as well. We distinguish between the stiffnesses of the two coupling springs k_{c1} and k_{c2}, so that a parametric study may reflect the effect this additional coupling parameter. Since the model will only be used for the investigation of free response no forcing or damping is considered.

The model is depicted in Fig. 3.13. A bay is defined as one blade-disk oscillator and the springs connecting it with the two higher numbered oscillators. In Fig. 3.13 we attempt to show the definition of a bay by drawing it with a heavier line type. The equations of motion for bay i are

$$m_b \ddot{q}_i^b + k_b^i (q_i^b - q_i^d) = 0, \tag{3.92}$$

which is identical to Eq. (3.20) for the mono-coupled two DOF system. The blade stiffness mistuning is introduced as $k_b(1+\delta_i)$. For the disk DOF, one has

$$k_{c1}(2q_i^d - q_{i-1}^d - q_{i+1}^d) + k_{c2}(2q_i^d - q_{i-2}^d - q_{i+2}^d) + k_d q_i^d + k_b^i (q_i^d - q_i^b) + m_d \ddot{q}_i^d = 0. \tag{3.93}$$

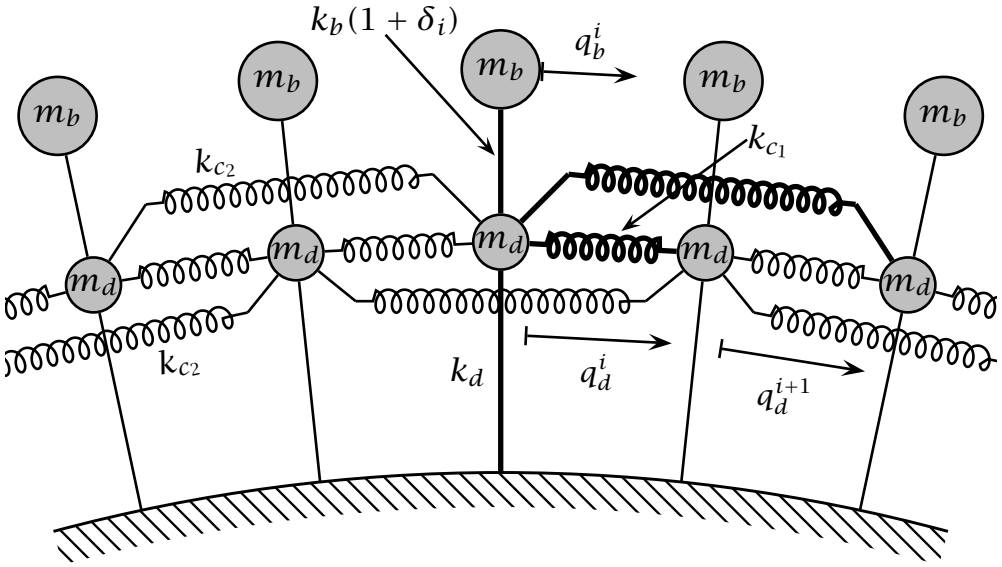

Figure 3.13 A simple model of a bladed disk featuring one disk-DOF and one blade-DOF bays coupled to four of its nearest neighbors.

In the case of harmonic motion, Eq. (3.92) may be rearranged as in Eq. (3.26). Using Eq. (3.23) to eliminate the blade coordinates from Eq. (3.93) yields

$$q_{i+2}^d = -\alpha q_{i+1}^d + \beta(\delta_i^b) q_i^d - \alpha q_{i-1}^d - q_{i-2}^d \tag{3.94}$$

corresponding to Eq. (3.66), where

$$\beta(\delta_i^b) = 2 + 2\frac{\bar{k}_{c1}}{\bar{k}_{c2}} + \frac{\bar{k}_d}{\bar{k}_{c2}} - \frac{\bar{\omega}^2(1+\delta_i^b)}{(1+\delta_i^b-\bar{\omega}^2)\bar{k}_{c2}} - \frac{\bar{m}\bar{\omega}^2}{\bar{k}_{c2}} \tag{3.95}$$

$$\alpha = \frac{\bar{k}_{c1}}{\bar{k}_{c2}} \tag{3.96}$$

and in addition to Eq. (3.22) the dimensionless parameters have been introduced:

$$\bar{k}_{c1} = \frac{k_{c1}}{k_b} \qquad \bar{k}_{c2} = \frac{k_{c2}}{k_b}$$

In the tuned case, $\delta_i^b = 0$, we have

$$\beta_o = 2 + 2\frac{\bar{k}_{c1}}{\bar{k}_{c2}} + \frac{\bar{k}_d}{\bar{k}_{c2}} - \frac{\bar{\omega}^2}{(1-\bar{\omega}^2)\bar{k}_{c2}} - \frac{\bar{m}\bar{\omega}^2}{\bar{k}_{c2}}. \tag{3.97}$$

The modes of free vibrations are obtained in much the same way as for the previous models. The problem is broken into individual spatial harmonics by a transformation to harmonic coordinates,

$$\mathbf{u}_k = [u_b, u_d]_k^T, \qquad (k = 1 \ldots N), \tag{3.98}$$

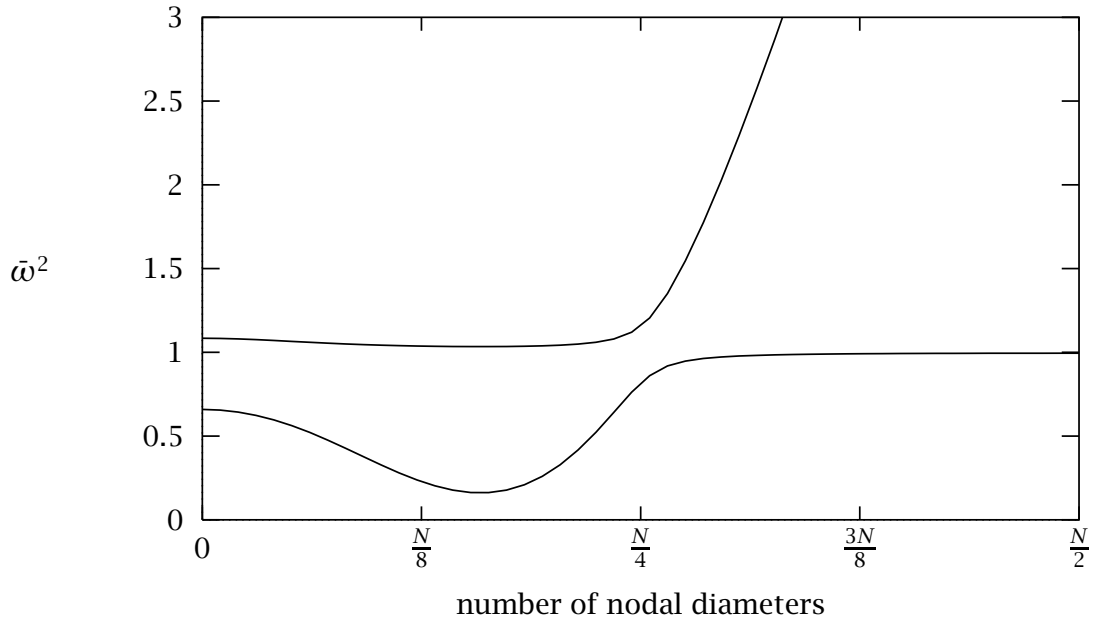

Figure 3.14 The natural frequencies of a bi-coupled, non-adjacent coupling model plotted as a function of the number of nodal diameters. Distinct blade and two mode disk type dynamics are evidenced. $\bar{k}_d = 25$, $\bar{m} = 35$, $\bar{k}_{c1} = 50$, $\bar{k}_{c2} = -23$.

such that $\mathbf{q}_i = \mathbf{u}_k$. Here, $\mathbf{u}_k$ is the amplitude vector of bay i as the assembly vibrates in the kth interblade-phase-angle mode. A slight twist arises from the fact that five adjacent bays are coupled. The motion of four adjacent blades must be considered, and is found to be $\mathbf{q}_{i-2} = \mathbf{u}_k e^{-2j\sigma_k}$, $\mathbf{q}_{i-1} = \mathbf{u}_k e^{-j\sigma_k}$, $\mathbf{q}_{i+1} = \mathbf{u}_k e^{j\sigma_k}$ and $\mathbf{q}_{i+2} = \mathbf{u}_k e^{2j\sigma_k}$ where $\sigma_k = 2\pi(k-1)/N$ after some algebra we find the natural frequencies to be

$$\bar{\omega}_n^2 = \frac{\bar{m} + K(n) + 1 \pm \sqrt{(\bar{m} + K(n) + 1)^2 - 4\bar{m}K(n)}}{2\bar{m}} \tag{3.99}$$

where

$$K(n) = \bar{k}_d + 2\bar{k}_{c1}(1 - \cos\sigma_n) + 2\bar{k}_{c2}(1 - \cos 2\sigma_n). \tag{3.100}$$

Figure 3.14 shows an example of natural frequencies of a non-adjacent coupling model plotted as a function of the number of nodal diameters. The figure highlights a special feature of this model, namely the ability to model a dip in the disk-mode curve, corresponding to initial softening of blade modes as the number of nodal diameters increases. This phenomenon is frequently observed in turbomachinery. This property of the non-adjacent coupling model will be studied in great detail in Section 5.3.1.

3.1.4. Parameter Identification

The natural frequencies of detailed finite element models of tuned bladed disks can generally be calculated at a reasonable cost through the use of cyclic symmetry, because only one blade/disk sector need to be considered. Any eigen-analysis of a mistuned system, however, would require consideration of the entire bladed-disk. Even a deterministic analysis of a single mistuned system appears to be a monumental task, and a stochastic analysis is simply impossible.

A compromise solution is to identify, for the tuned assembly, a reduced-order model which is in some sense equivalent to the detailed finite element model. This equivalence has of course to be defined. The ultimate aim of this identification would be that the reduced-order model not only captures the dynamics of the tuned assembly accurately, but also those of its mistuned counterpart, therefore rendering the prohibitive task of a systematic mistuned analysis possible because of the small number of DOF for the reduced-order model.

The analysis in the preceding sections of this chapter has yielded the natural frequencies of the several tuned two- and three-DOF per bay systems in closed form. This suggests, as a measure of equivalence between the finite element and reduced-order models, that both types of models ought to have ideally the same natural frequencies in a given frequency range. The identification problem thus consists of requiring the finite element natural frequencies to match the reduced-order model frequencies and, subsequently, of solving for the parameters of the reduced-order model from its analytical natural frequency expressions. At this point two remarks should be made. First, the natural frequency expressions are strongly nonlinear in the structural mass and stiffness parameters, leading to a difficult nonlinear inverse problem. Second, a reduced-order model typically features many more natural frequencies ($2N$ or $3N$) than there are structural parameters, and thus certain natural frequencies — only as many as there are parameters to identify — must be selected in the identification procedure. It is intuitively clear that this choice will be a decisive factor in determining the quality of the reduced-order model approximation, thereby making the entire identification procedure heuristic and thus rather delicate. One way to attempt to systematize the selection of the natural frequencies to be used in the identification is to plot the assembly natural frequencies versus the number of nodal diameters (henceforth referred to as the frequency curves), which provides a graphical description of the tuned system dynamics. From these frequency curves, the important dynamic features which ought to be captured by the reduced-order model can be identified, therefore suggesting which of the nodal diameter frequencies the system parameters ought to be extracted from. Hence the use of the frequency curves renders the identification process a bit

more systematic, although it is still largely dependent upon engineering judgment.

Besides the identification of specific bladed-disks, one of the objectives of the study was to determine which features of the frequency curves are the most important in order for the reduced-order model to reproduce properly, not only the tuned assembly dynamics, but also its sensitivity to mistuning and the effects of mistuning on free and forced response. This will be commented upon throughout the case studies presented in Chapter VII.

The parameter identification scheme can be summarized as follows. *First*, select as many finite element natural frequencies as are unknown parameters in the desired simple model. *Second*, match these frequency values with the analytical expressions of the natural frequencies of the simple model considered. *Third*, solve these nonlinear equations for the structural parameters.

The last step is carried out numerically and was observed to be a very delicate matter. In fact, in many cases it will not be possible to solve precisely for those system parameters which yield the selected finite element frequencies, and one may have to settle for reduced-order frequencies that were close, sometimes not very much so, to the selected finite element values.

3.2. Finite Element Model Order Reduction

In the previous sections we have presented several different coupled oscillator models of bladed disks. The models vary in sophistication depending on the accuracy required for sufficient modeling of sector dynamics and blade to blade interaction. It should be clear at this point that although the analysis of simple models may be a very straightforward problem, the identification of parameters in order to calibrate the model properties with the rotor under investigation may be a very cumbersome process. Even when the model parameters have been optimized, the simple model may provide a grossly inadequate model of the dynamics of the rotor.

Many will agree that only modal analysis is capable of providing satisfactory accuracy at the low orders required for Monte Carlo simulations, and given the readily available modes of free vibration of the tuned assembly a modal analysis of the mistuned problem is very tempting. However, in a direct modal analysis, all information about the blade dynamics is embedded in the modes, leaving no way of entering blade mistuning in a controlled manner. An alternative approach is that of component mode analysis in which the blades and the disk are treated as separate components. The most difficult problem in component mode analysis is the modeling of the interface between the components. This problem is effectively addressed in the several component mode techniques that have been suggested [38, 52, 53, 54, 55]. However, none of these meet the dramatic order reduction requirements outlined above. In particular, most of these techniques require an additional set of mode shapes which allow the model to span the space of possible motions of the connected structure. These additional mode shapes are typically necessitated by artificial constraints imposed at component interfaces, and are therefore often referred to as *constraint modes*. The constraint modes can lead to an unsatisfactorily large number of degrees of freedom in the reduced order model. For instance, if one were to apply the Craig-Bampton technique to a solid element FEM, there would be $3 \times N_{NI}$ constraint modes per sector, where N_{NI} is the number of finite element nodes at each disk-blade interface. This cost is unacceptable for the analysis suggested herein.

In this section, we present a reduced-order modeling technique which is tailored to representing particular mistuned bladed disk structures based on a FEM of a single disk-blade sector. We use a component-mode approach, in which the disk motion is described by finite element mode shapes of the disk, and the blade elastic motion is described by the finite element mode shapes of a blade fixed at the disk-blade interface. The motion of the blade due to the motion of the disk is described as a summation of disk mode motions at the disk-blade interface. This is in many ways similar to the method proposed by Kaza and Kielb [38] albeit much more general. By viewing blade

motion as the sum of a disk induced motion and the motion of a cantilevered blade, disk-blade attachment is achieved in a compatible way, and no constraint mode shapes are necessary. This technique:

- is systematic from the FEM of one disk-blade sector
- features the blade modal stiffnesses as explicit parameters so that the blade natural frequencies may be directly mistuned
- minimizes storage requirements
- is capable of producing models with a small number of degrees of freedom

This method places importance on the last item, and as a result it may not be as accurate as other component-mode techniques. However, with the present method, we can generate models which are of sufficiently low order as to be suitable for Monte Carlo simulations.

I would like to acknowledge the work of my co-worker Mr. Matthew Castanier who collaborated with me on the development of this technique. He is the co-author of a paper about this topic [****].

3.2.1. Nomenclature

N The number of disk-blade sectors.

P The maximum number of nodal diameters of a disk mode shape. $P = \text{int}[N/2]$.

$\widetilde{\mathbf{V}}_n$ A matrix formed with the selected n nodal diameter (n^{th} harmonic) mode shapes of the disk as its columns. The tilde signifies that each mode only contains the degrees of freedom of a single sector. When selecting modes to be considered in the analysis, both modes of a pair corresponding to a double natural frequency must be included. Note that the following analysis assumes that the vectors are normalized with respect to the mass matrix.

$\widetilde{\mathbf{U}}_n^d$ Each column of this matrix is the disk-induced motion of a single blade when the disk sector to which it is attached is vibrating in a mode shape of $\widetilde{\mathbf{V}}_n$. The ordering of these modes should correspond to $\widetilde{\mathbf{V}}_n$. The scaling of these modes follows from the normalization of the modes of $\widetilde{\mathbf{V}}_n$.

$\widetilde{\mathbf{U}}^b$ A matrix formed with the selected set of cantilevered blade mode shapes as its columns.

$\otimes$ The Kronecker product (see Appendix A).

$\mathbf{V}_n$ The n nodal diameter mode shapes of an entire disk, formed by expanding the single sector mode shapes contained in $\widetilde{\mathbf{V}}_n$, as explained in Appendix B.

$\mathbf{V}$ The matrix of all disk modes. $\mathbf{V} = [\mathbf{V}_0, \mathbf{V}_1, \ldots, \mathbf{V}_P]$

$\mathbf{U}_n^d$ Disk-induced motions of all the attached blades as the disk vibrates with the shapes in $\mathbf{V}_n$. The columns of $\mathbf{U}_n^d$ are formed like the columns of $\mathbf{V}_n$ (see Appendix B).

$\mathbf{U}^d$ The matrix of all disk-induced motions, $\mathbf{U}^d = [\mathbf{U}_0^d, \mathbf{U}_1^d, \ldots, \mathbf{U}_P^d]$

. The ordering of $\mathbf{U}^d$ corresponds to the ordering of $\mathbf{V}$.

$\mathbf{U}^b$ A block diagonal matrix, $\mathbf{U}^b = \left(\mathbf{I} \otimes \tilde{\mathbf{U}}^b\right)$, where the order of $\mathbf{I}$ is equal to N. Each block corresponds to the cantilevered mode shapes for an individual blade in the bladed disk.

$\mathbf{a}_n$ A vector of generalized coordinates corresponding to the n nodal diameter disk modes.

$\mathbf{a}$ Vector of generalized coordinates for all disk modes, $\mathbf{a} = [\mathbf{a}_0^T, \mathbf{a}_1^T, \ldots, \mathbf{a}_P^T]^T$

$\mathbf{b}_i$ A vector of generalized coordinates for blade i.

$\mathbf{b}$ The vector of generalized coordinates for all N blades. It is formed as $\mathbf{b} = \left[\mathbf{b}_1^T, \mathbf{b}_2^T, \ldots, \mathbf{b}_N^T\right]^T$.

$\mathbf{v}$ The disk deflection vector.

$$\mathbf{v} = \sum_{n=0}^{P} \mathbf{V}_n \mathbf{a}_n \tag{3.101}$$

$\mathbf{u}$ The blade deflection vector, containing the total motion of all N attached blades.

$$\mathbf{u} = \sum_{n=0}^{P} \mathbf{U}_n^d \mathbf{a}_n + \mathbf{U}^b \mathbf{b} \tag{3.102}$$

$\tilde{\mathbf{M}}_d, \tilde{\mathbf{K}}_d$ The finite element mass matrix and stiffness matrix of a disk sector.

$\mathbf{M}_d, \mathbf{K}_d$ The finite element mass matrix and stiffness matrix of the entire disk.

$\mathbf{I}, \hat{\mathbf{K}}_d$ The modal mass matrix and modal stiffness matrix of the entire disk. The modal mass matrix is the identity matrix since the modes are normalized with respect to the mass matrix.

$\tilde{\mathbf{M}}_b, \tilde{\mathbf{K}}_b$ The finite element mass matrix and stiffness matrix of a free blade.

$\mathbf{I}, \hat{\mathbf{K}}_b$ The modal mass matrix and modal stiffness matrix of a cantilevered blade with no mistuning. For simplicity, we choose the convention that blade mistuning only occurs in the blade modal stiffness matrix, and that the modal stiffness matrix of mistuned blade i is $\hat{\mathbf{K}}_b^i = (1 + \delta_i)\hat{\mathbf{K}}_b$, where δ_i is a mistuning value from a random variable.

3.2.2. Formulation

The disk motion is written in terms of modal amplitudes, $\mathbf{Va}$ (see the Nomenclature section). The motion of an individual blade then consists of two components: the motion of the blade due to the disk motion, $\mathbf{U}^d\mathbf{a}$; and an elastic blade motion written in terms of a the modes of a cantilevered blade, $\mathbf{U}^b\mathbf{b}$. Since the elastic motion of the blade is written relative to the disk-induced motion of the blade, the attachment of the blade to the disk is automatic. Note that the disk-induced motion of the blade is *not* simply a rigid body motion, since it also accounts for the deformation of the blade due to disk deformation. Later sections explain how the modes in $\mathbf{V}$, $\mathbf{U}^b$, and $\mathbf{U}^d$ may be efficiently calculated with a finite element approach.

The kinetic energy of the assembly may be written as:

$$\begin{aligned}
T =& \frac{1}{2}\dot{\mathbf{v}}^T\mathbf{M}_d\dot{\mathbf{v}} + \frac{1}{2}\dot{\mathbf{u}}^T\mathbf{M}_b\dot{\mathbf{u}} \\
=& \frac{1}{2}\sum_{n=0}^{P}\left\{\dot{\mathbf{a}}_n^T\mathbf{V}_n^T\right\}\mathbf{M}_d\sum_{m=0}^{P}\left\{\mathbf{V}_m\dot{\mathbf{a}}_m\right\} + \frac{1}{2}\left[\mathbf{U}^b\dot{\mathbf{b}} + \sum_{n=0}^{P}\mathbf{U}_n^d\dot{\mathbf{a}}_n\right]^T\mathbf{M}_b\left[\mathbf{U}^b\dot{\mathbf{b}} + \sum_{m=0}^{P}\mathbf{U}_m^d\dot{\mathbf{a}}_m\right] \\
=& \frac{1}{2}\sum_{n=0}^{P}\dot{\mathbf{a}}_n^T\dot{\mathbf{a}}_n + \frac{1}{2}\dot{\mathbf{b}}^T\dot{\mathbf{b}} + \dot{\mathbf{b}}^T\mathbf{U}^{b\,T}\mathbf{M}_b\sum_{n=0}^{P}\left\{\mathbf{U}_n^d\dot{\mathbf{a}}_n\right\} + \frac{1}{2}\sum_{n=0}^{P}\left\{\dot{\mathbf{a}}_n^T\mathbf{U}_n^{d\,T}\right\}\mathbf{M}_b\sum_{m=0}^{P}\left\{\mathbf{U}_m^d\dot{\mathbf{a}}_m\right\}
\end{aligned} \tag{3.103}$$

the first variation of which is

$$\begin{aligned}
\delta T =& \sum_{n=0}^{P}\delta\dot{\mathbf{a}}_n^T\dot{\mathbf{a}}_n + \delta\dot{\mathbf{b}}^T\dot{\mathbf{b}} + \sum_{n=0}^{P}\delta\dot{\mathbf{b}}^T\mathbf{U}^{b\,T}\mathbf{M}_b\mathbf{U}_n^d\dot{\mathbf{a}}_n \\
&+ \sum_{n=0}^{P}\delta\dot{\mathbf{a}}_n^T\mathbf{U}_n^{d\,T}\mathbf{M}_b\mathbf{U}^b\dot{\mathbf{b}} + \sum_{m=0}^{P}\sum_{n=0}^{P}\delta\dot{\mathbf{a}}_n^T\mathbf{U}_n^{d\,T}\mathbf{M}_b\mathbf{U}_m^d\dot{\mathbf{a}}_m
\end{aligned} \tag{3.104}$$

Similarly, the strain energy is

$$\begin{aligned}
U =& \frac{1}{2}\mathbf{v}^T\mathbf{K}_d\mathbf{v} + \frac{1}{2}\mathbf{u}^T\mathbf{K}_b\mathbf{u} \\
=& \frac{1}{2}\sum_{n=0}^{P}\left\{\mathbf{a}_n^T\mathbf{V}_n^T\right\}\mathbf{K}_d\sum_{m=0}^{P}\left\{\mathbf{V}_m\mathbf{a}_m\right\} + \frac{1}{2}\left[\mathbf{U}^b\mathbf{b} + \sum_{n=0}^{P}\mathbf{U}_n^d\mathbf{a}_n\right]^T\mathbf{K}_b\left[\mathbf{U}^b\mathbf{b} + \sum_{m=0}^{P}\mathbf{U}_m^d\mathbf{a}_m\right] \\
=& \frac{1}{2}\sum_{n=0}^{P}\mathbf{a}_n^T\hat{\mathbf{K}}_{d\,n}\mathbf{a}_n + \frac{1}{2}\mathbf{b}^T\mathbf{U}^{b\,T}\mathbf{K}_b\mathbf{U}^b\mathbf{b} + \mathbf{b}^T\mathbf{U}^{b\,T}\mathbf{K}_b\sum_{n=0}^{P}\left\{\mathbf{U}_n^d\mathbf{a}_n\right\} \\
&+ \frac{1}{2}\sum_{n=0}^{P}\left\{\mathbf{a}_n^T\mathbf{U}_n^{d\,T}\right\}\mathbf{K}_b\sum_{m=0}^{P}\left\{\mathbf{U}_m^d\mathbf{a}_m\right\}
\end{aligned} \tag{3.105}$$

where $\hat{\mathbf{K}}_{d\,n}$ is the block of $\mathbf{K}_d$ which contains the modal stiffnesses of the disk modes with n nodal diameters. Recall that $\mathbf{U}^d$ constitutes the blade motions due to disk motion. It is clear that in many cases, this will be almost pure rigid body motion. It is

our contention that the strain energy due to this term may often be negligible. It will, however, be included here. The first variation of the strain energy is

$$\begin{aligned}\delta U = &\sum_{n=0}^{P} \delta\mathbf{a}_n^T \hat{\mathbf{K}}_{d\,n}\mathbf{a}_n + \delta\mathbf{b}^T\mathbf{U}^{b\,T}\mathbf{K}_b\mathbf{U}^b\mathbf{b} + \sum_{n=0}^{P}\delta\mathbf{b}^T\mathbf{U}^{b\,T}\mathbf{K}_b\mathbf{U}_n^d\mathbf{a}_n \\ &+ \sum_{n=0}^{P}\delta\mathbf{a}_n^T\mathbf{U}_n^{d\,T}\mathbf{K}_b\mathbf{U}^b\mathbf{b} + \sum_{m=0}^{P}\sum_{n=0}^{P}\delta\mathbf{a}_n^T\mathbf{U}_n^{d\,T}\mathbf{K}_b\mathbf{U}_m^d\mathbf{a}_m\end{aligned} \tag{3.106}$$

We apply Hamilton's principle,

$$\int_{t_1}^{t_2}[\delta U - \delta T]\,\mathrm{d}t = 0 \tag{3.107}$$

and find

$$\begin{aligned}\delta\mathbf{a}_n: \quad &\ddot{\mathbf{a}}_n + \mathbf{U}_n^{d\,T}\mathbf{M}_b\sum_{m=0}^{P}\mathbf{U}_m^d\ddot{\mathbf{a}}_m + \mathbf{U}_n^{d\,T}\mathbf{M}_b\mathbf{U}^b\ddot{\mathbf{b}} + \hat{\mathbf{K}}_{d\,n}\mathbf{a}_n \\ &+ \mathbf{U}_n^{d\,T}\mathbf{K}_b\mathbf{U}^b\mathbf{b} + \mathbf{U}_n^{d\,T}\mathbf{K}_b\sum_{m=0}^{P}\mathbf{U}_m^d\mathbf{a}_m = 0\end{aligned} \tag{3.108}$$

$$\begin{aligned}\delta\mathbf{b}: \quad &\ddot{\mathbf{b}} + \sum_{n=0}^{P}\mathbf{U}^{b\,T}\mathbf{M}_b\mathbf{U}_n^d\ddot{\mathbf{a}}_n + \sum_{n=0}^{P}\mathbf{U}^{b\,T}\mathbf{K}_b\mathbf{U}_n^d\mathbf{a}_n \\ &+ \left(\mathbf{diag}(1+\delta_i)\otimes\hat{\mathbf{K}}_b\right)\mathbf{b} = 0\end{aligned} \tag{3.109}$$

At this point we make an important approximation. Recall that we suggested above that the strain energy due to the disk-induced motion of the blade should in many cases be a small term. Given this assumption we elect to ignore the effect of blade mistuning in this term reasoning that the effect of mistuning on this small term will be negligible. Hence, blade mistuning will only be included in the strain energy of the blades due to the deformation of blades in the cantilevered blades modes. This approximation dramatically increases the efficiency of the generation of the reduced order equations of motion of the mistuned assembly.

Using the definition of $\mathbf{a}$ and $\mathbf{U}^d$ (see Nomenclature section), we may cast our equations into the following matrix form

$$\left[\begin{array}{c|c}\mathbf{I}+\mathbf{Bdiag}\left(\tilde{\mathbf{U}}_n^{d\,T}\tilde{\mathbf{M}}_b\tilde{\mathbf{U}}_n^d\right) & \mathbf{U}^{d\,T}\mathbf{M}_b\mathbf{U}^b \\ \hline \mathbf{U}^{b\,T}\mathbf{M}_b\mathbf{U}^d & \mathbf{I}\end{array}\right]\left[\begin{array}{c}\ddot{\mathbf{a}}\\ \ddot{\mathbf{b}}\end{array}\right] + \left[\begin{array}{c|c}\hat{\mathbf{K}}_d+\mathbf{Bdiag}\left(\tilde{\mathbf{U}}_n^{d\,T}\tilde{\mathbf{K}}_b\tilde{\mathbf{U}}_n^d\right) & \mathbf{U}^{d\,T}\mathbf{K}_b\mathbf{U}^b \\ \hline \mathbf{U}^{b\,T}\mathbf{K}_b\mathbf{U}^d & \mathbf{diag}(1+\delta_i)\otimes\hat{\mathbf{K}}_b\end{array}\right]\left[\begin{array}{c}\mathbf{a}\\ \mathbf{b}\end{array}\right] = \mathbf{0} \tag{3.110}$$

where **Bdiag** denotes a block diagonal matrix, and **diag** denotes a diagonal matrix. A few comments about Eq. (3.110) are in order. First it is to be noted that no information about mode shapes in the disk is required. Only the modal stiffnesses of the disk and blade modes, the disk-induced shape functions and elastic modes in the blade, and the blade mass and stiffness matrices enter the analysis.

In the mass and stiffness matrices, the bottom right blocks are diagonal, *i.e.*, no coupling of blade modes occurs. Coupling of blade modes and disk modes appears in the top right and bottom left blocks of the mass and stiffness matrices. These blocks are in general full, hence there is full coupling of all blade and disk modes. The top left blocks feature two terms: one that corresponds to the disk alone, and a second term related to the assembly of disk and blades. Yet, we note that the top left blocks of the mass and stiffness matrices are block diagonal for the following reason: addition of blade inertia preserves the cyclicity of the assembly. Likewise, since the contribution of blade stiffness mistuning on the disk-induced strain energy in the blades was ignored, addition of blade stiffness does not alter the cyclicity of the disk. Hence there is no coupling among the different nodal diameter modes. However, the addition of the blade inertia and stiffness couples the modal circle modes that have the same number of nodal diameters.

An examination of Eq. (3.110) reveals the reason for ignoring the contribution of blade stiffness mistuning on the disk-induced strain energy. Thanks to this approximation, the mistuning random variables δ_i only appear in the bottom right hand block, which is the only block that must be generated for successive mistuning patterns. If this assumption had not been made, the entire stiffness matrix would have to be regenerated for each mistuning pattern.

As an aside, we point out the fact that individual blades are not directly coupled. Thus, the blade degrees of freedom may be written in terms of disk coordinates. This is strictly equivalent to the elimination of all degrees of freedom except the coupling coordinates that was shown to be possible in the coupled oscillator models [50]. From Eq. (3.109), assuming harmonic motion,

$$\left[\mathbf{U}^{b\,T}\mathbf{K}_b\mathbf{U}^d - \omega^2\mathbf{U}_b^T\mathbf{M}_b\mathbf{U}^d\right]\mathbf{a} + \left[\mathbf{diag}(1+\delta_i)\otimes\hat{\mathbf{K}}_b - \omega^2\mathbf{I}\right]\mathbf{b} = 0 \tag{3.111}$$

where the matrix $\left[\mathbf{diag}(1+\delta_i)\otimes\hat{\mathbf{K}}_b - \omega^2\mathbf{I}\right]$ is diagonal. For this reason, the blade degrees of freedom may be efficiently represented in terms of the disk degrees of freedom. By substituting this relationship into Eq. (3.108), thereby eliminating $\mathbf{b}$ the computational efficiency may be greatly improved. However, this elimination of blade coordinates may be of limited use in a free response analysis, because the natural frequencies become embedded in the eigenvalue problem preventing the use of canned eigenvalue solvers. The elimination of blade degrees of freedom should considered an essential part of a forced response analysis or a transfer matrix approach.

3.2.3. Pseudo-Physical Coordinate System

The coordinate system presented above features a mixture of modal amplitudes of interblade phase angle modes for the disk, and blade modal amplitudes. Hence, only the blade degrees of freedom in the reduced order model are directly associated with individual sectors. Therefore, a direct comparison with the lumped mass models hitherto utilized in the analysis of bladed disks is difficult. A coordinate transformation from the disk modal amplitude coordinates to disk sector coordinates would be useful.

Since the top left blocks of the mass and stiffness matrices are block diagonal, there exists a transformation to a block circulant form (See Eq. (2.33)). The resulting coordinate system will be referred to as *pseudo-physical* coordinates, because the transformation is to the deflections of an equivalent lumped mass model for the disk sector. The transformation does not effect the blade degrees of freedom. We define the following transformed matrices:

$$\mathbf{A} = (\mathbf{F} \otimes \mathbf{I}) \left[\mathbf{I} + \mathbf{B}\mathbf{diag} \left(\tilde{\mathbf{U}}_n^{d\,T} \tilde{\mathbf{M}}_b \tilde{\mathbf{U}}_n^d \right) \right] \left(\mathbf{F} \otimes \mathbf{I}^T \right) \tag{3.112}$$

$$\mathbf{B} = (\mathbf{F} \otimes \mathbf{I}) \left(\mathbf{U}^{d\,T} \mathbf{M}_b \mathbf{U}^b \right) \tag{3.113}$$

$$\mathbf{C} = (\mathbf{F} \otimes \mathbf{I}) \left[\mathbf{I} + \mathbf{B}\mathbf{diag} \left(\tilde{\mathbf{U}}_n^{d\,T} \tilde{\mathbf{M}}_b \tilde{\mathbf{U}}_n^d \right) \right] \left(\mathbf{F} \otimes \mathbf{I}^T \right) \tag{3.114}$$

$$\mathbf{D} = (\mathbf{F} \otimes \mathbf{I}) \left(\mathbf{U}^{d\,T} \mathbf{K}_b \mathbf{U}^b \right) \tag{3.115}$$

Eq. (3.110) may then be rewritten in the pseudo-physical coordinate basis as

$$\left[\begin{array}{c|c} \mathbf{A} & \mathbf{B} \\ \hline \mathbf{B}^T & \mathbf{I} \end{array}\right] \left[\begin{array}{c} \ddot{\mathbf{y}} \\ \ddot{\mathbf{b}} \end{array}\right] + \left[\begin{array}{c|c} \mathbf{C} & \mathbf{D} \\ \hline \mathbf{D}^T & \mathbf{diag}[\hat{\mathbf{K}}_i] \end{array}\right] \left[\begin{array}{c} \mathbf{y} \\ \mathbf{b} \end{array}\right] = \mathbf{0} \tag{3.116}$$

where $\mathbf{y}$ is the vector of disk pseudo-physical coordinates. We have introduced the notation $\mathbf{diag}[\hat{\mathbf{K}}_i]$ for the diagonal matrix of mistuned modal stiffnesses, $\mathbf{diag}(1 + \delta_i) \otimes \hat{\mathbf{K}}_b$.

Equation (3.116) still features the inertial coupling of blades that was observed in Eq. (3.110), caused by the coordinate system for the blades being relative to the disk. Yet another step is required to complete the transformation to the lumped mass models similar to the ones in the literature which usually feature absolute deflections resulting in stiffness coupling of the blades.

We define a transformation from $\mathbf{b}$, the coordinates of blade motion relative to disk motion, to $\mathbf{z}$, the coordinates of absolute blade motion.

$$\mathbf{z} = \mathbf{B}^T \mathbf{y} + \mathbf{b} \tag{3.117}$$

Applying Eq. (3.117), Eq. (3.116) becomes

$$\left[\begin{array}{c|c} \mathbf{A}-\mathbf{B}\mathbf{B}^T & \mathbf{0} \\ \hline \mathbf{0} & \mathbf{I} \end{array}\right]\left[\begin{array}{c} \ddot{\mathbf{y}} \\ \ddot{\mathbf{z}} \end{array}\right]+\left[\begin{array}{c|c} \mathbf{B}\,\mathbf{diag}[\hat{\mathbf{K}}_i]\mathbf{B}^T+\mathbf{C} & \mathbf{D}-\mathbf{B}\,\mathbf{diag}[\hat{\mathbf{K}}_i] \\ \hline \mathbf{D}^T-\mathbf{diag}[\hat{\mathbf{K}}_i]\mathbf{B}^T & \mathbf{diag}[\hat{\mathbf{K}}_i] \end{array}\right]\left[\begin{array}{c} \mathbf{y} \\ \mathbf{z} \end{array}\right]=\mathbf{0} \quad (3.118)$$

which features the more familiar stiffness coupling of individual blades through the disk. Finally, $[\mathbf{y},\mathbf{z}]^T$ may be reordered so that coordinates of each sector are grouped. The vector $\mathbf{x}^T$ is formed, where $\mathbf{x}_i$ contains both blade and disk *absolute, pseudo-physical* coordinates of sector i. In a tuned form, the equations of motion have the form presented in Eq. (2.32). In the mistuned case, the circulant form of Eq. (2.32) is destroyed giving rise to the form

$$\left(\left[\begin{array}{ccccc} \mathbf{K}_o^1 & \mathbf{K}_1^1 & \mathbf{K}_2^1 \ldots \mathbf{K}_2^1 & \mathbf{K}_1^1 \\ \mathbf{K}_1^2 & \mathbf{K}_o^2 & \mathbf{K}_1^2 \ldots \mathbf{K}_3^2 & \mathbf{K}_2^2 \\ \mathbf{K}_2^3 & \mathbf{K}_1^3 & \mathbf{K}_o^3 \ldots \mathbf{K}_4^3 & \mathbf{K}_3^3 \\ \vdots & \vdots & \vdots \ddots \vdots & \vdots \\ \mathbf{K}_2^{N-1} & \mathbf{K}_3^{N-1} & \mathbf{K}_4^{N-1} \ldots \mathbf{K}_o^{N-1} & \mathbf{K}_1^{N-1} \\ \mathbf{K}_1^N & \mathbf{K}_2^N & \mathbf{K}_3^N \ldots \mathbf{K}_1^N & \mathbf{K}_o^N \end{array}\right]-\omega^2\left[\begin{array}{ccccc} \mathbf{M}_o & \mathbf{M}_1 & \mathbf{M}_2 \ldots \mathbf{M}_2 & \mathbf{M}_1 \\ \mathbf{M}_1 & \mathbf{M}_o & \mathbf{M}_1 \ldots \mathbf{M}_3 & \mathbf{M}_2 \\ \mathbf{M}_2 & \mathbf{M}_1 & \mathbf{M}_o \ldots \mathbf{M}_4 & \mathbf{M}_3 \\ \vdots & \vdots & \vdots \ddots \vdots & \vdots \\ \mathbf{M}_2 & \mathbf{M}_3 & \mathbf{M}_4 \ldots \mathbf{M}_o & \mathbf{M}_1 \\ \mathbf{M}_1 & \mathbf{M}_2 & \mathbf{M}_3 \ldots \mathbf{M}_1 & \mathbf{M}_o \end{array}\right]\right)\left[\begin{array}{c} \mathbf{x}_1 \\ \mathbf{x}_2 \\ \mathbf{x}_3 \\ \vdots \\ \mathbf{x}_{N-1} \\ \mathbf{x}_N \end{array}\right]=\mathbf{0} \quad (3.119)$$

where the superscripts in the stiffness matrix correspond to the sector numbers.

3.2.4. Transfer Matrices

In the earlier work by the authors [56, 50], a transfer matrix approach to the analysis of bladed-disks was presented. A low number of coupling coordinates was shown the be the prerequisite to the applicability of this approach. It was hypothesized that in many cases the elements of $\mathbf{M}$ and $\mathbf{K}$ will exhibit rapid decay away from diagonal. In such cases, the dominance of the coupling between neighboring sectors may be capitalized upon by ignoring the coupling between weakly coupled sectors. Assume, for instance, that only three blocks away from the diagonal in Eq. (3.119) are deemed significant. Then the remaining blocks may be truncated and the dynamics of the system represented in a transfer matrix form

$$\begin{bmatrix} \mathbf{x}_{i+1} \\ \mathbf{x}_i \\ \mathbf{x}_{i-1} \\ \mathbf{x}_{i-2} \\ \mathbf{x}_{i-3} \\ \mathbf{x}_{i-4} \end{bmatrix} = \begin{bmatrix} -\mathbf{T}_1^i & -\mathbf{T}_2^i & -\mathbf{T}_3^i & -\mathbf{T}_2^i & -\mathbf{T}_1^i & -\mathbf{I} \\ \mathbf{I} & \mathbf{0} & \mathbf{0} & \mathbf{0} & \mathbf{0} & \mathbf{0} \\ \mathbf{0} & \mathbf{I} & \mathbf{0} & \mathbf{0} & \mathbf{0} & \mathbf{0} \\ \mathbf{0} & \mathbf{0} & \mathbf{I} & \mathbf{0} & \mathbf{0} & \mathbf{0} \\ \mathbf{0} & \mathbf{0} & \mathbf{0} & \mathbf{I} & \mathbf{0} & \mathbf{0} \\ \mathbf{0} & \mathbf{0} & \mathbf{0} & \mathbf{0} & \mathbf{I} & \mathbf{0} \end{bmatrix} \begin{bmatrix} \mathbf{x}_i \\ \mathbf{x}_{i-1} \\ \mathbf{x}_{i-2} \\ \mathbf{x}_{i-3} \\ \mathbf{x}_{i-4} \\ \mathbf{x}_{i-5} \end{bmatrix} \tag{3.120}$$

where

$$\begin{aligned} \mathbf{T}_1^i &= \left(\mathbf{K}_3^i - \omega^2 \mathbf{M}_3\right)^{-1} \left(\mathbf{K}_2^i - \omega^2 \mathbf{M}_2\right) \\ \mathbf{T}_2^i &= \left(\mathbf{K}_3^i - \omega^2 \mathbf{M}_3\right)^{-1} \left(\mathbf{K}_1^i - \omega^2 \mathbf{M}_1\right) \\ \mathbf{T}_3^i &= \left(\mathbf{K}_3^i - \omega^2 \mathbf{M}_3\right)^{-1} \left(\mathbf{K}_0^i - \omega^2 \mathbf{M}_0\right) \end{aligned}$$

Naturally, the elimination of the blade degrees of freedom as discussed above is highly advantageous since it reduces the dimension of the blocks of the transfer matrix.

3.2.5. Generating Component Modes using FEM

In this section we outline how the the finite element method may be utilized to obtain the ingredients required for the order reduction method. Two separate finite element eigenvalue analyses are required: a cyclic symmetry analysis of the disk alone, and an analysis of a fixed blade. Throughout the discussion it is assumed that eigenvectors are normalized with respect to the mass matrix. From Eq. (3.110) we make the following inventory:

- mode shapes for a fixed blade, $\widetilde{\mathbf{U}}^b$
- corresponding modal stiffnesses, $\widehat{\mathbf{K}}_b$
- the finite element mass and stiffness matrices of a free blade, $\widetilde{\mathbf{M}}_b$ and $\widetilde{\mathbf{K}}_b$
- shape functions for the attached blades that are due to nodal diameter mode shapes in the disk, $\widetilde{\mathbf{U}}^d$
- modal stiffnesses of the disk nodal diameter modes, $\widehat{\mathbf{K}}_d$

The eigenvalue analysis of a single cantilevered blade is straightforward. The blade mass and stiffness matrices may not be as easily obtained but are required for the analysis.

The method for obtaining the disk-induced shapes in the blade is less apparent. An approach fundamental to the current work is as follows. By performing the cyclic symmetry analysis of the disk component with *massless* blades attached, the required shape functions in the blade are automatically generated. This technique requires no modification to a pre-existing FEM apart from setting the blade material density to zero. Because massless blades have no inertia, they will follow the motion of the disk, and will not add spurious natural frequencies.

A serendipitous consequence of this approach is the stiffening of the disk component by the attached blades. Since this setup mimics the actual disk-blade interface, the disk mode shapes are improved. As a result modal convergence is enhanced. The analysis yields the desired number of *families* of nodal diameter modes for the disk component. A *family* refers to all nodal diameter modes of a certain type in the disk, *e.g.*, the one nodal circle out of plane bending. Only the modal stiffnesses of the modes as well as the part of the eigenvectors pertaining to the blade (the blade shape functions) are retained. The part of the eigenvectors pertaining to the disk (the disk modes) are discarded.

CHAPTER IV

CONCEPTS IN TURBOMACHINERY

A newcomer to the area of vibration analysis in turbomachinery will face some unfamiliar terminology. We have already encountered constant-interblade-phase-angle modes discussed in Section 2.5 where modes shapes corresponding to a double natural frequency are presented as a pair of counterrotating complex shapes. As discussed in Chapter II these modes are often classified by the number of nodal diameters in the mode shape, a term that those familiar with the modes of a circular plate should be comfortable with. In circular plates, modes may also be ranked by the number of nodal circles in the shape. Due to the varity of motion in the attached blades (in-plane bending, out-of-plane bending, torsion *etc.*) the nodal circle concept is not useful in turbomachinery.

In this chapter we discuss briefly two other subjects that may cause a beginner some discomfort: engine order excitation and aerodynamic coupling.

4.1. Engine Order Excitation

The primary form of excitation in the analysis of forced response in turbomachinery is that of *engine order excitation.* This forcing condition occurs due to the fact that the rotors are rotating through a steady flow that is non-uniform around the annulus [57]. The non-uniformity of the flow stems from the multiple obstructions in the flow, both up-stream and down-stream caused by stator blades and structural members through which the fluid must pass.

Each blade on the rotating assembly experiences these spatial variations in the steady flow as time-varying and therefore responds by vibrating with frequencies that are directly related to the speed of rotation. The forcing function not only has a characteristic frequency which is an integer multiple of the rotation speed but also a characteristic shape since it is applied simultaneously to all the blades around the assembly. By performing a Fourier transformation of the spatial shape of the flow field it may be broken into its spatial harmonics and, assuming linear dynamics, the response of the

assembly to each of these analyzed separately. The forcing function of a engine order C excitation of frequency ω on blade i in a blade assembly

$$F_i = f\, e^{2j\pi C(i-1)/N}\, e^{j\omega t} = f\, e^{j(2\pi C(i-1)/N+\omega t)} \tag{4.1}$$

which is a traveling wave excitation of amplitude f traveling in the positive i direction (ascending blade number) with wave speed

$$c = \frac{\omega N}{2\pi C}$$

The advantage of examining individually the spatial harmonics of the excitation is that each one harmonic excites only modes with the same number of nodal diameters as the excitation (see Section 2.4). Recall that an assembly may have several modes with a given number of nodal diameters, much like a circular plate has many modes with a different number of nodal circles for a given number of nodal diameters.

In Section 2.2.4 we discussed how a pair of mode shapes corresponding to a double eigenvalue may either be written in a real (standing wave) or a complex (traveling) form. The same is true for the engine order excitation. When the form of the excitation and the modes follows the same convention, a given engine order of the excitation will excite only one of the modes corresponding to a double natural frequency, namely the one that is parallel with. Otherwise it will excite both modes in the pair.

A convenient way to present the characteristics of forced respose due to engine order excitatione is with a Campbell or interference diagram (see Fig. 4.1). A Campbell diagram plots frequency of excitation as a function of rotational speed with an indication of the response level on a third axis. Also shown on Fig. 4.1 are horizontal lines indicationg the individual natural frequencies. These lines are plotted as horizontal signifying that they are independent of speed. This may not always be the case due to centrifucal stiffening of blade modes, flexural modes in particular. The plot also contains *order lines* indicating the frequencies of prominent excitation conditions. Where an nth order line crosses a natural frequency curve corresponding to an n nodal diameter mode a resonance condition will occur with insignificant response at other intersections.

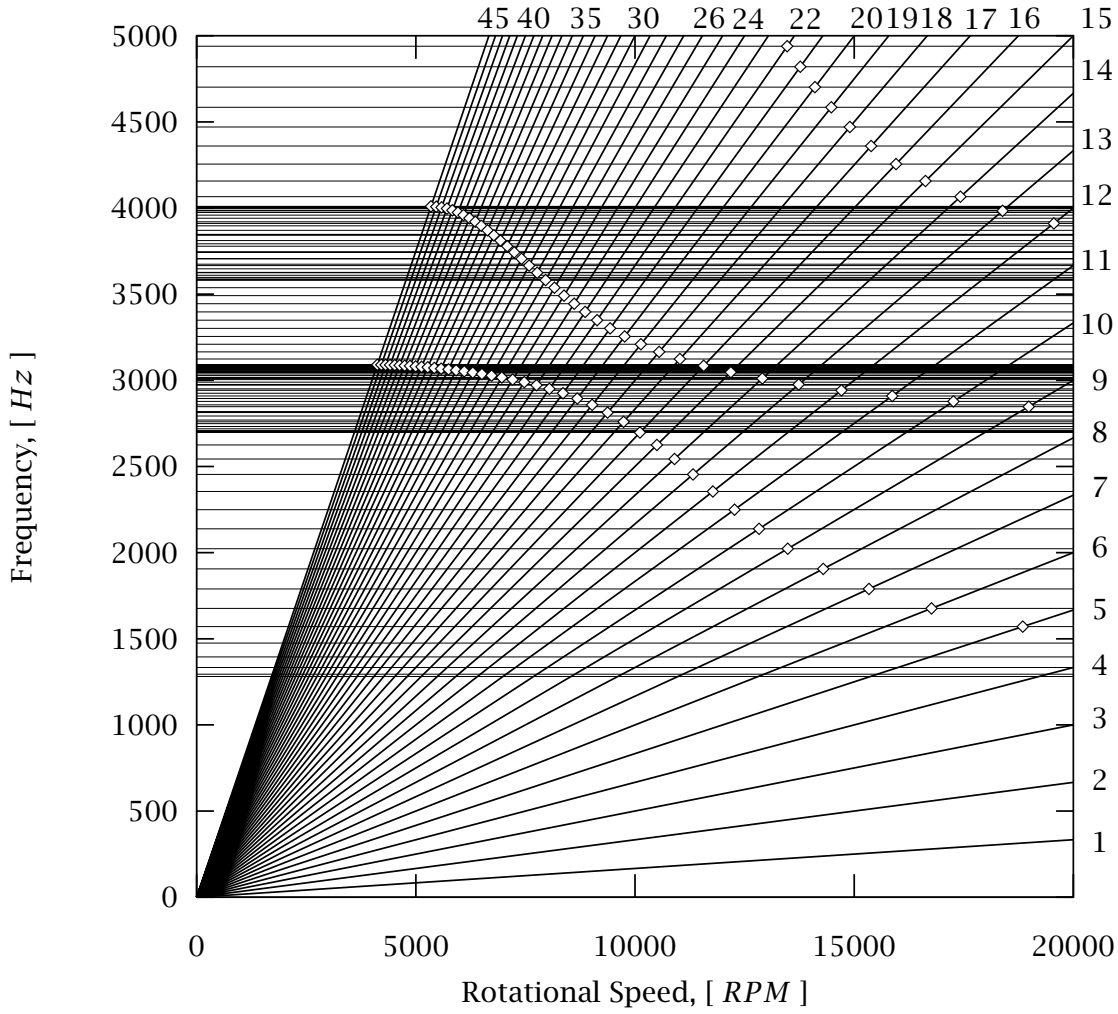

Figure 4.1 A Campbell diagram shows the relationship between frequency of excitation, the rotional speed, the engine order of the excitation (radial lines) and the natural frequencies (horizontal lines). Using the Campbell diagram resonant conditions (shown here with (◇)) may be identified at a glance.

4.2. Aerodynamic Coupling

In general, turbomachinery rotors experience interblade coupling through the gases on which the blades are acting. In the following sections we shall examine briefly how aerodynamic coupling alters the dynamics of tuned and mistuned turbomachinery rotors.

4.2.1. General Formulation for Tuned System

In a tuned system, aerodynamic coupling effects are assumed to possess the same cyclic symmetry as the rotor itself, and hence are described by circulant matrices of the same dimension as the other system matrices. The aerodynamic forces couple all the blade degrees of freedom, so the resulting aerodynamic matrix is, in general, fully populated. The aerodynamic matrix depends on an assumed frequency of blade motion, ω_a, and the flow parameters. According to unsteady aerodynamic theory, the aerodynamic forces on an airfoil are not in phase with its motion and therefore the aerodynamic matrix is complex. However, since the aerodynamic terms are assumed to be cyclic, the matrix may be block diagonalized using the Fourier matrix defined in Section 2.2. This means that aerodynamic forces do not couple modes that possess different numbers of nodal diameters. The block size in the block diagonal form of the aerodynamic matrix equals the number of degrees of freedom, P, in the model of each blade-disk sector. The aerodynamic matrix should not be assumed to be symmetric since aerodynamic forces depend on the direction of rotation. The equations of free motion of an N blade assembly with aerodynamic coupling are, in the physical coordinate system:

$$\mathbf{M}\ddot{\mathbf{q}} + \mathbf{K}\mathbf{q} + \mathbf{A}(\omega_a)\mathbf{q} = \mathbf{0} \tag{4.2}$$

where the dimension of the matrices $\mathbf{M}$, $\mathbf{K}$ and $\mathbf{A}$ is $PN \times PN$ and where ω_a is an assumed frequency at which the aerodynamic coupling terms are calculated. The dependence on ω_a will be dropped in what follows. Equation (4.2) contains no viscous damping term. This greatly simplifies the analysis and is easily justified by the fact that the viscous damping is due to the aerodynamics and is captured in the aerodynamic matrix. Structural damping is accounted for as a complex stiffness in the stiffness matrix $\mathbf{K}$.

Earlier, we examined how the study of a cyclic system may be broken into separate cases for each interblade-phase angle, σ_k, where

$$\sigma_k = \frac{2(k-1)\pi}{N} \qquad (k = 1, \ldots, N).$$

In order to achieve this we perform a transformation to *harmonic coordinates*,

$$\mathbf{u} = (\mathbf{E}^* \otimes \mathbf{I})\mathbf{q}, \tag{4.3}$$

that describe the motion of the assembly as it vibrates in each of the spatial harmonic modes. The reader is referred to a complete discussion of the various coordinate systems in Section 2.3. In the absence of aerodynamic coupling, Eq. (4.2) is transformed to harmonic coordinates, rendering the mass and stiffness matrices block diagonal,

$$\mathbf{Bdiag}\left[\widetilde{\mathbf{M}}_k\right]\ddot{\mathbf{u}} + \mathbf{Bdiag}\left[\widetilde{\mathbf{K}}_k\right]\mathbf{u} = 0 \qquad (k = 1, \ldots, N). \tag{4.4}$$

Equation (4.4) may be broken down into N smaller vector equations (each of dimension P) for the individual σ_k interblade-phase-angle modes,

$$-\omega^2\tilde{\mathbf{M}}_k\tilde{\mathbf{u}}_k + \tilde{\mathbf{K}}_k\tilde{\mathbf{u}}_k = 0 \qquad (k = 1,\ldots,N) \tag{4.5}$$

where harmonic motion has been assumed. In Eq. (4.5) $\tilde{\mathbf{M}}_k$ and $\tilde{\mathbf{K}}_k$ are the interblade-phase-angle dependent mass and stiffness matrices (Eq. (2.34)) and $\tilde{\mathbf{u}}_k$ represents the motion of a single sector when the assembly is vibrating in the σ_k interblade-phase-angle mode. Equation (4.5) may be solved to yield P natural frequencies $\omega_{k,1},\ldots,\omega_{k,P}$ with corresponding eigenvectors $\tilde{\mathbf{u}}_{k,1},\ldots,\tilde{\mathbf{u}}_{k,P}$ for the sector. Assembly eigenvectors are generated from the sector eigenvectors using the Kronecker product

$$\mathbf{u}_{k,i} = \mathbf{e}_k \otimes \tilde{\mathbf{u}}_{k,i}.$$

where $\mathbf{e}_k$ is the kth column of the Fourier matrix. The matrix of sector eigenvectors, $\tilde{\mathbf{U}}_k$, at each interblade phase angle defines the transformation to modal amplitude coordinates, $a_{k,1},\ldots,a_{k,P}$, as

$$\tilde{\mathbf{u}}_k = \tilde{\mathbf{U}}_k\mathbf{a}_k \tag{4.6}$$

The transformation in Eq. (4.6) can be applied to Eq. (4.5) resulting in the set of uncoupled equations,

$$-\omega^2\mathbf{diag}[m_{k,i}]\mathbf{a}_k + \mathbf{diag}[k_{k,i}]\mathbf{a}_k = 0 \qquad (i = 1,\ldots,P, k = 1,\ldots,N) \tag{4.7}$$

in modal amplitude coordinates, $\mathbf{a}_k$. Each equation in Eq. (4.7) has dimension P.

We now return to Eq. (4.2). Applying the transformation of Eq. (4.3) casts Eq. (4.2) into harmonic coordinates. Since the aerodynamic forces were assumed cyclic, Eq. (4.2) becomes block diagonal (see Eq. (4.4)) and may be broken down into N eigenvalue problems, each of size P.

$$\tilde{\mathbf{M}}_k\ddot{\tilde{\mathbf{u}}}_k + \tilde{\mathbf{K}}_k\tilde{\mathbf{u}}_k + \tilde{\mathbf{A}}_k\tilde{\mathbf{u}}_k = 0 \qquad (k = 1,\ldots,N) \tag{4.8}$$

The harmonic coordinate form of the aerodynamic matrix, as N $P\times P$ blocks $\tilde{\mathbf{A}}_k$, provides one compact form of representing aerodynamic coupling from which the aerodynamic matrix in physical coordinates may be reconstructed using Eq. (4.3). Normally, the aerodynamic forces on the blade coordinates will be much greater than the forces on the disk coordinates, and the elements of $\tilde{\mathbf{A}}_k$ that correspond to disk coordinates may possibly be ignored.

Equation (4.8) may be further transformed, to the $\mathbf{a}$ coordinate system of modal amplitudes of the tuned, structural-only system, using Eq. (4.6). (The transformation

directly from physical to modal amplitude coordinates is given in Eq. (2.36).) This presents aerodynamic coupling as modal influence coefficients,

$$\mathbf{diag}[m_{k,i}]\ddot{\mathbf{a}}_k + \mathbf{diag}[k_{k,i}]\mathbf{a}_k + \mathbf{L}_k\mathbf{a}_k = 0 \qquad (i = 1,\ldots,P, k = 1,\ldots,N) \tag{4.9}$$

where $\mathbf{L}_k$ is a full matrix of aerodynamic coefficients, implying a complete aerodynamic coupling of the all the σ_k interblade-phase-angle modes. The N matrices of modal influence coefficients, $\mathbf{L}_k$ provide another compact representation of the aerodynamic coupling. It is unclear which form, $\widetilde{\mathbf{A}}_k$ or $\mathbf{L}_k$, is more easily obtainable, but one form leads to another using the transformation

$$\widetilde{\mathbf{A}}_k = \mathbf{U}_k\mathbf{L}_k\mathbf{U}_k^T \tag{4.10}$$

4.2.2. Example System

Figure 4.2 presents a schematic of an assembly with two blade-degrees-of-freedom and one disk-degree-of-freedom per sector, vibrating in motions in the σ_k interblade phase angle modes. The aerodynamic effects on the disk degree-of-freedom have been ignored. The aerodynamic effects in the harmonic coordinate system are represented by interblade-phase-angle dependent springs of *complex constants* a_{11}^k,a_{21}^k,a_{12}^k,a_{22}^k.

The harmonic coordinates $\tilde{\mathbf{u}}_k = [\tilde{u}_d, \tilde{u}_{b1}, \tilde{u}_{b2}]_k^T$, describe the local shape of a bay as the assembly vibrates in the kth interblade-phase-angle mode.

The equations of motion may be found by inspection

$$m_d\ddot{\tilde{u}}_{d,k} + k_b(\tilde{u}_{d,k} - \tilde{u}_{b1,k}) + (k_d + 2k_c(1-\cos\sigma_k))\,\tilde{u}_{d,k} = 0 \tag{4.11}$$

$$\begin{aligned} &m_b\ddot{\tilde{u}}_{b1,k} + k_b(\tilde{u}_{b1,k} - \tilde{u}_{d,k}) + \kappa k_b(\tilde{u}_{b1,k} - \tilde{u}_{b2,k}) \\ &+ 2a_{11}^k\tilde{u}_{b1,k}(1-\cos\sigma_k) + 2a_{12}^k(\tilde{u}_{b1,k} - \tilde{u}_{b2,k}\cos\sigma_k) = 0 \end{aligned} \tag{4.12}$$

$$\begin{aligned} &\mu m_b\ddot{\tilde{u}}_{b2,k} + \kappa k_b(\tilde{u}_{b2,k} - \tilde{u}_{b1,k}) \\ &+ 2a_{22}^k\tilde{u}_{b2,k}(1-\cos\sigma_k) + 2a_{21}^k(\tilde{u}_{b2,k} - \tilde{u}_{b1,k}\cos\sigma_k) = 0 \end{aligned} \tag{4.13}$$

Scaling with the blade properties and assuming harmonic motion yields

$$\left(\begin{bmatrix} 1+\bar{k}_d+2\bar{k}_c(1-\cos\sigma) & -1 & 0 \\ -1 & 1+\kappa & -\kappa \\ 0 & -\kappa & \kappa \end{bmatrix} - \bar{\omega}_{k,i}^2\begin{bmatrix} \bar{m} & 0 & 0 \\ 0 & 1 & 0 \\ 0 & 0 & \mu \end{bmatrix} + 2\begin{bmatrix} 0 & 0 & 0 \\ 0 & \bar{a}_{11}^k(1-\cos\sigma_k)+\bar{a}_{12}^k & -\bar{a}_{12}^k\cos\sigma_k \\ 0 & -\bar{a}_{21}^k\cos\sigma_k & \bar{a}_{22}^k(1-\cos\sigma_k)+\bar{a}_{21}^k \end{bmatrix}\right)\tilde{\mathbf{u}}_{k,i} = 0 \tag{4.14}$$

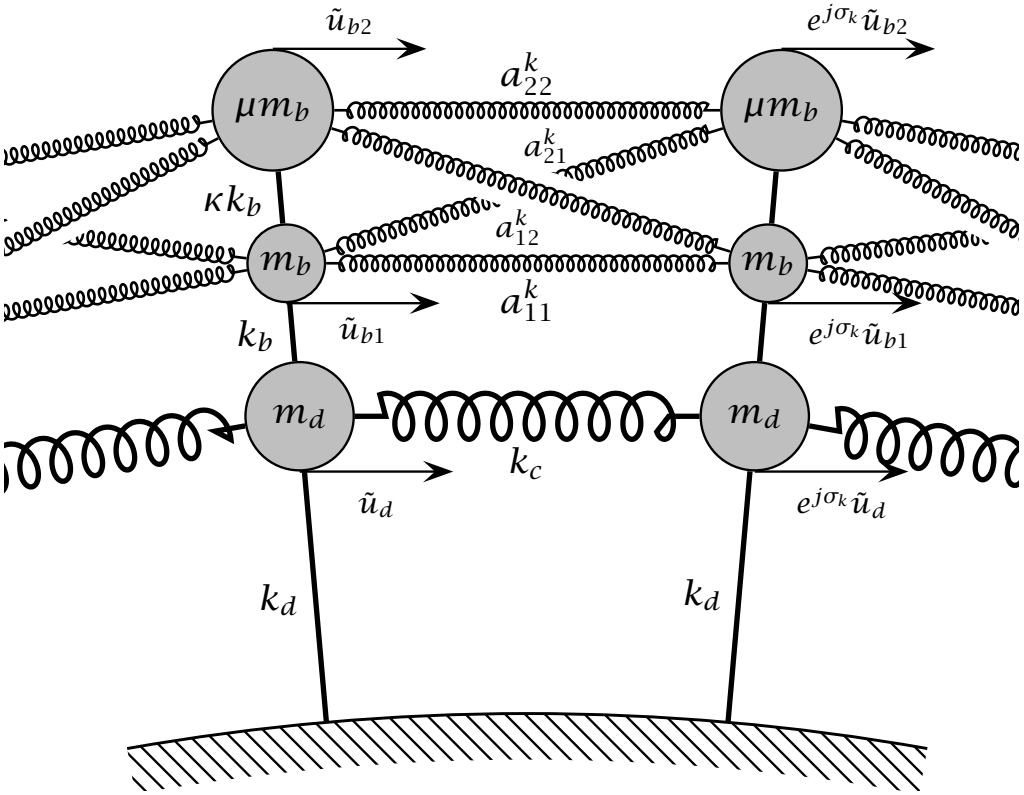

Figure 4.2 A simple model of a bladed disk featuring one coordinate *structural* coupling of bays with one disk-DOF and two blade-DOF and a simplistic model of aerodynamic blade coupling, while vibrating in a σ_k interblade-phase-angle mode.

Therefore, by comparison with Eq. (4.8),

$$\tilde{\mathbf{A}}_k = 2\begin{bmatrix} 0 & 0 & 0 \\ 0 & \bar{a}^k_{11}(1-\cos\sigma_k)+\bar{a}^k_{12} & -\bar{a}^k_{12}\cos\sigma_k \\ 0 & -\bar{a}^k_{21}\cos\sigma_k & \bar{a}^k_{22}(1-\cos\sigma_k)+\bar{a}^k_{21} \end{bmatrix}. \tag{4.15}$$

This result could have been obtained from a complete equation of motion in physical coordinates by applying Eq. (4.3).

4.2.3. Free Aeroelastic Response

The study of stability in a mistuned assembly with aerodynamic coupling and structural damping requires the solution of Eq. (4.2). If the assembly is tuned, then a transformation to either Eq. (4.8) or Eq. (4.9) provides considerable computational savings.

We assume a solution

$$q = e^{(\gamma + j\omega)t}$$

and find that

$$\left\{(\gamma + j\omega)^2\mathbf{M} + \mathbf{K} + \mathbf{A}\right\}\mathbf{q} = 0 \tag{4.16}$$

Solving for the eigenvalues of Eq. (4.16) yields values of $-\lambda = (\gamma + j\omega)^2 = [\gamma^2 - \omega^2] + 2j\gamma\omega$. Hence,

$$\omega^2 - \gamma^2 = \mathrm{Re}(\lambda)$$
$$\gamma\omega = -\frac{1}{2}\mathrm{Im}(\lambda)$$

$$\gamma = \mathrm{Re}(\sqrt{-\lambda})$$
$$\omega = \mathrm{Im}(\sqrt{-\lambda}),$$

with stable solutions for $\gamma \leq 0$ (asymptotically stable for $\gamma < 0$).

For illustrative purposes we include Fig. 4.3 that shows the eigenvalue loci for a model of a 72-blade blisk. No meaningful aerodynamic data was available and therefore the figure only shows the stabilizing effects of structural damping and mistuning. The plot also shows how the mistuning causes scattering and splitting of the (mostly) double eigenvalues of the tuned assembly.

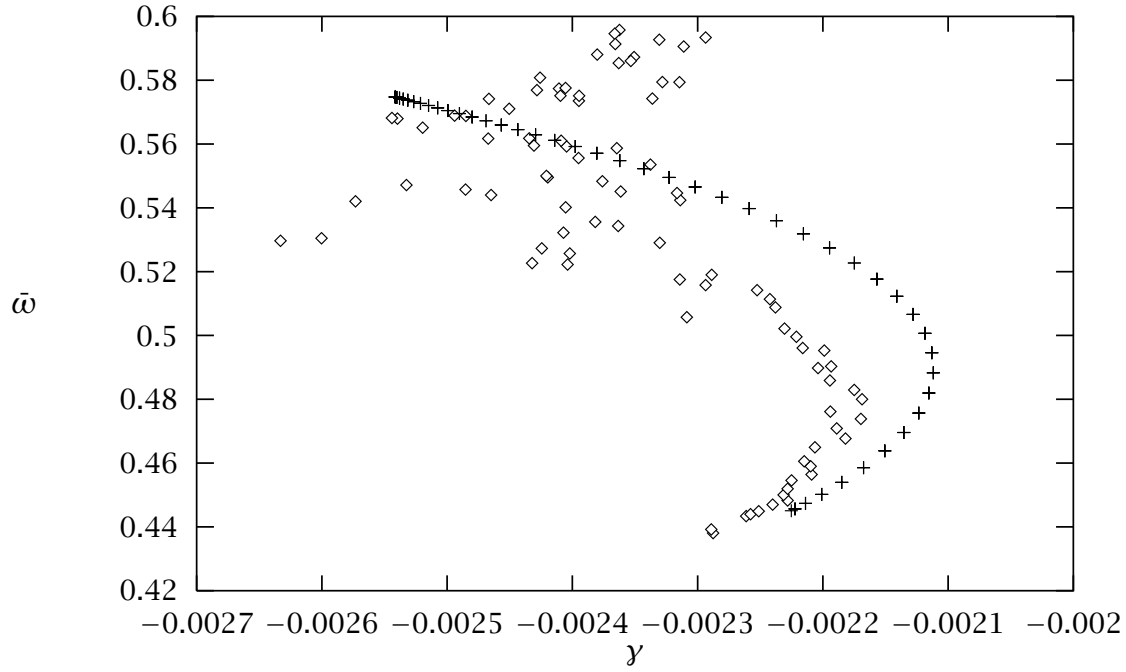

Figure 4.3 Eigenvalue loci in model **1Bg** (see Chapter '`Compressor-chapter`') of a 72-blade blisk with 7.25% blade mistuning ($\diamond$) are compared with the eigenvalue loci of a tuned assembly ($+$). The model features 0.1% structural damping but *no* aerodynamic coupling. Since $\gamma = \mathrm{Re}(\sqrt{-\lambda})$, the more negative values of γ imply greater stability. The stabilizing effect of mistuning is apparent, as is the splitting and scattering of eigenvalues due to mistuning.

CHAPTER V

WAVE PROPAGATION AND LOCALIZATION

A study of wave propagation in blade assemblies is made possible with coupled oscillator models with a low number of coupling coordinates. The analysis has little value in models obtained via order reduction of Finite Element models because of the large number of coupling coordinates.

As we shall see in this chapter, wave propagation analysis is a particularly attractive approach to a statistical study of mistuning effects on the free response in blade assemblies.

In the first part of this chapter, we review the theory of wave propagation in periodic multi-coupled structures and explain the effects of mistuning. We present a measure of mistuning effects, the *localization factor*, and derive approximate expressions for the localization factor for a general mono-coupled system with a general source of mistuning. Furthermore, we propose a measure of sensitivity to blade mistuning.

In the second part of the chapter we attempt to gain insight into localization effects in multi-coupled systems. In lieu of a rigorous mathematical analysis of localization factors in a multi-coupled assembly an attempt was made to apply some of the lessons learned from the analysis of mono-coupled systems. An examination of the modal structure of a bi-coupled model yields qualitative information about the influence of the additional coupling coordinate and when additional coupling coordinates may be ignored.

At the time of this writing, no complete method existed for quantifying localization effects in multi-coupled structures. Recent developments have brought a tool for this type of analysis in the form of Lyapunov exponents [*****].

5.1. Waves in Perfectly Periodic Structures

We examine the propagation of waves in a general infinite periodic structure whose dynamics are governed by Eq. (3.2). It has long been known that energy-carrying motions in periodic structures only occur in isolated frequency ranges known as *passbands*. Outside the passbands, only attenuated standing waves or complex waves can take place [21]. A physical understanding of these wave-propagation characteristics is achievable through the diagonalization of Eq. (3.2). This requires the solution of the eigenvalue problem:

$$\mathbf{q}_i = \mathbf{T_o}\mathbf{q}_{i-1} = \lambda\mathbf{q}_{i-1}, \tag{5.1}$$

where $\mathbf{T}_o$ is the transfer matrix of a tuned assembly. Equation (5.1) yields the eigenvalues and eigenvectors of $\mathbf{T}_o$. Its significance is as follows. The eigenvectors of $\mathbf{T}_o$ define wave-modes, or characteristic waves, which propagate along the structure in such a way that the state-vector, $\mathbf{q}_i$, is multiplied by a complex scalar, λ, as the wave passes through each bay. The independent wave-modes define the preferred means of free wave propagation along the periodic assembly — much like normal modes are the preferred form of free vibration of a structure. The normal modes form a basis for all vibration shapes in a structure. Similarly, all possible waveforms in a structure may be written as a linear combination of wave-modes.

Eigenvalues appear in reciprocal pairs, λ and λ^{-1}, that are either real or complex conjugate [21]. To each eigenvalue pair thus correspond two waves which are equivalent except for their direction of travel. The eigenvalue that has modulus greater than 1 is associated with a wave-mode traveling and/or attenuating in the direction of decreasing bay number. We shall refer to this as the left or counterclockwise direction.

Since the dimension of the transfer matrix is twice the number of coupling coordinates between bays (see Chapter III), the number of left- and right-traveling wave pairs equals the number of coupling coordinates for the assembly. A transformation between physical coordinates and wave coordinates is defined by the matrix $\mathbf{X}$ which has as its columns the eigenvectors of $\mathbf{T}_o$. The similarity transformation of $\mathbf{T}_o$ into wave coordinates thus yields a diagonal *wave transfer matrix* $\mathbf{W}_o$, as

$$\begin{bmatrix}\mathbf{L}\\ \mathbf{R}\end{bmatrix}_{i+1} = \mathbf{W_o}\begin{bmatrix}\mathbf{L}\\ \mathbf{R}\end{bmatrix}_i = \mathbf{X^{-1}T_oX}\begin{bmatrix}\mathbf{L}\\ \mathbf{R}\end{bmatrix}_i = \begin{bmatrix}\mathbf{\Lambda} & \mathbf{0}\\ \mathbf{0} & \mathbf{\Lambda}^{-1}\end{bmatrix}\begin{bmatrix}\mathbf{L}\\ \mathbf{R}\end{bmatrix}_i \tag{5.2}$$

where $\mathbf{R}$ and $\mathbf{L}$ are vectors of right- and left-traveling wave coordinate amplitudes. $\mathbf{\Lambda}$ is a diagonal matrix of eigenvalues with modulus greater than or equal to 1.

For a given eigenvalue λ_i in $\mathbf{\Lambda}$ ($i = 1, \ldots, M$), let $\lambda_i = e_i^{\mu}$ define the complex *propagation constant*, μ_i, with $\mu_i = \gamma_i + j\sigma_i$. The corresponding reciprocal eigenvalue defines the propagation constant of the right-traveling wave, $-\mu_i$. Here γ_i, the real part of the

propagation constant, is the rate of exponential attenuation of the wave amplitude L_i from one bay to the next. The imaginary part, σ_i, is the *interblade phase angle*, the difference in phase between the motion of adjacent bays. In the literature dealing with wave propagation in periodic systems [21], the interblade phase angle is usually called the *wave number*. The propagation constants contains all the information about the frequency-dependent propagation of waves through the assembly. For each eigenvalue in $\mathbf{\Lambda}$ the following cases can be distinguished depending on the frequency:

- $\lambda_i \in \mathbb{R}$: For the left-traveling wave $\gamma_i > 0$, leading to attenuation. Also, adjacent bays are vibrating either in phase or out of phase, $\sigma_i = 0$ or $\sigma_i = \pi$, which implies that these are standing waves. These frequency ranges define *stopbands*.
- $\lambda_i \in \mathbb{C},\ \lambda_i \notin \mathbb{R},\ |\lambda_i| = 1$: In this case $\gamma_i = 0$ and no attenuation occurs. These frequencies define a *passband* in which the left- and right-going waves travel without attenuation.
- $\lambda_i \in \mathbb{C},\ \lambda_i \notin \mathbb{R},\ |\lambda_i| \neq 1$: For the left-traveling wave $\mu_i = \gamma_i + j\sigma_i$ with $\gamma_i > 0$ and $\sigma_i \neq 0$ or π; hence the wave travels *with* attenuation. The corresponding reciprocal eigenvalue characterizes the right-traveling wave with propagation constant $-\mu_i$. In this case the eigenvalues λ_i and λ_i^{-1} are not complex conjugate. Therefore there must be companion pair of left- and right-traveling waves with propagation constants $\gamma_i - j\sigma_i$ and $-\gamma_i + j\sigma_i$, respectively. We refer to these waves as *complex waves* and to the associated frequency ranges as complexbands. In order for them to exist there must be at least four eigenvalues, that is, at least two coupling coordinates: hence complex waves cannot occur in a mono-coupled system. Since the two left-going (and the two right-going) waves are complex conjugates, they actually represent one wave shape. Physically, the two pairs of waves merge into one in a complexband.

5.1.1. The Mono-Coupled Assembly

For the tuned mono-coupled system described by Eq. (3.9) the eigenvalues of the two by two transfer matrix are

$$\lambda, \lambda^{-1} = \frac{\beta_o}{2} \pm \sqrt{\left(\frac{\beta_o}{2}\right)^2 - 1}, \qquad \lambda \in \mathbb{C}, \beta_o \in \mathbb{R}, \tag{5.3}$$

We choose the convention that λ has modulus greater than or equal to one. The wave-modes appear as the eigenvectors, $[1, \lambda^{-1}]^T$ and $[1, \lambda]^T$, corresponding to the eigenvalues λ and λ^{-1}, respectively. The two wave-modes could also be written as $[\lambda, 1]^T$ and $[1, \lambda]^T$, which shows that they are equivalent except for their direction of travel. This is supported by the symmetry of the problem to clockwise or counterclockwise numbering of the bays.

The eigenvectors of $\mathbf{T}_o$ are arranged as the columns of a matrix $\mathbf{X}$ which defines the transformation

$$\begin{bmatrix} q_i \\ q_{i-1} \end{bmatrix} = \mathbf{X} \begin{bmatrix} L \\ R \end{bmatrix}_i, \qquad \mathbf{X} = \begin{bmatrix} 1 & 1 \\ \lambda^{-1} & \lambda \end{bmatrix}, \tag{5.4}$$

from physical coordinates to left- and right-traveling wave coordinates at bay i, corresponding to the wave-mode basis. The displacement transfer matrix $\mathbf{T}_o$ is thus transformed into the diagonal wave transfer matrix,

$$\begin{bmatrix} L \\ R \end{bmatrix}_{i+1} = \mathbf{W_o} \begin{bmatrix} L \\ R \end{bmatrix}_i = \begin{bmatrix} \lambda & 0 \\ 0 & \lambda^{-1} \end{bmatrix} \begin{bmatrix} L \\ R \end{bmatrix}_i. \tag{5.5}$$

For this mono-coupled assembly there exists a single pair of characteristic waves. Frequency passbands and stopbands are arranged as follows:

- $|\beta_o(\omega)| < 2$: These frequencies define a *passband* in which waves travel without attenuation. From the real part of Eq. (5.3), the interblade phase angle is related to frequency by the dispersion relation:

$$2\cos\sigma = \beta_o(\bar{\omega}), \qquad 0 < \sigma < \pi. \tag{5.6}$$

  For a given value of σ, Eq. (5.6) has as many frequency solutions as there are degrees of freedom in each bay [21]. Hence, the number of passbands equals the number of degrees of freedom in each bay, P. The frequencies at which $\sigma = \pi/2$ will be referred to as *midband frequencies*. Note that the midband frequency is not necessarily located close to the mean frequency in the passband.

- $|\beta_o(\omega)| > 2$: These frequency ranges define *stopbands*.

- $|\beta_o(\omega)| = 2$: This gives $\gamma = 0$ and $\sigma = 0$ or $\sigma = \pi$, and defines the bounding frequencies or the passband/stopband edges.

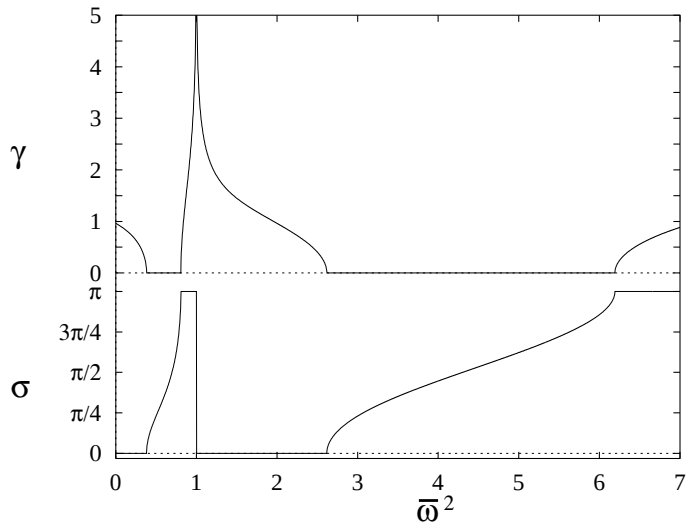

Figure 5.1 The passband/stopband structure of the assembly in Fig. 3.4, for $\bar{k}_c = \bar{k}_d = \bar{m} = 1$ (tuned case). Note the two distinct passbands, where $\gamma = 0$. Also note a singularity at $\bar{\omega} = 1$, corresponding to the natural frequency of a cantilevered blade.

Example

Figure 5.1 depicts the passband/stopband structure for the assembly in Fig. 3.4 for one set of parameter values. The rate of exponential attenuation, γ, and the interblade phase angle, σ, are displayed as a function of the dimensionless frequency. As predicted above, two frequency passbands are observed, corresponding to the two degrees of freedom per bay. In the passbands $\gamma = 0$ and unattenuated propagation of waves occurs. The wave travel is evidenced by the change of phase, $0 < \sigma < \pi$, from bay to bay. The other regions are stopbands, $\gamma \neq 0$, where standing waves decay exponentially and neighboring bays are either vibrating in phase or out of phase.

A special feature for this structure is the infinite attenuation observed at $\bar{\omega} = 1$, that is, at $\omega^2 = \frac{k_b}{m_b}$. We explain this behavior by pointing out that this is the natural frequency of a blade cantilevered at its root, hence at this frequency $q_i^d = 0$. Equation (3.23) confirms this. If the disk deflection equals zero, energy cannot be transmitted along the bays, hence the infinite attenuation of the waves.

5.1.2. The Bi-Coupled Assembly

In the tuned case the eigenvalues of the transfer matrix in Eq. (3.66) are solutions of the characteristic equation

$$\lambda^4 + \alpha\lambda^3 - \beta_o\lambda^2 + \alpha\lambda + 1 = 0 \tag{5.7}$$

where β_o is for the tuned system. Equation (5.7) simplifies to

$$\Big[\lambda^2 + \frac{1}{2}(\alpha+\kappa)\lambda + 1\Big]\Big[\lambda^2 + \frac{1}{2}(\alpha-\kappa)\lambda + 1\Big] = 0 \tag{5.8}$$

where

$$\kappa = \sqrt{4\beta_o + \alpha^2 + 8} \tag{5.9}$$

Hence the four eigenvalues of the transfer matrix are:

$$\lambda_1, \lambda_1^{-1} = -\frac{1}{4}\Big[\alpha - \kappa \pm \sqrt{(\alpha-\kappa)^2 - 16}\Big] \tag{5.10}$$

$$\lambda_2, \lambda_2^{-1} = -\frac{1}{4}\Big[\alpha + \kappa \pm \sqrt{(\alpha+\kappa)^2 - 16}\Big]. \tag{5.11}$$

To an eigenvalue λ corresponds the eigenvector $[1, \lambda^{-1}, \lambda^{-2}, \lambda^{-3}]^T$. The eigenvectors are arranged as columns of the matrix $\mathbf{X}$, yielding the transformation

$$\begin{bmatrix} q_i \\ q_{i-1} \\ q_{i-2} \\ q_{i-3} \end{bmatrix} = \begin{bmatrix} 1 & 1 & 1 & 1 \\ \lambda_1^{-1} & \lambda_2^{-1} & \lambda_1^{1} & \lambda_2^{1} \\ \lambda_1^{-2} & \lambda_2^{-2} & \lambda_1^{2} & \lambda_2^{2} \\ \lambda_1^{-3} & \lambda_2^{-3} & \lambda_1^{3} & \lambda_2^{3} \end{bmatrix} \begin{bmatrix} L_1 \\ L_2 \\ R_1 \\ R_2 \end{bmatrix}_i = \mathbf{X} \begin{bmatrix} L_1 \\ L_2 \\ R_1 \\ R_2 \end{bmatrix}_i \tag{5.12}$$

The wave transfer matrix for the system is

$$\begin{bmatrix} L_1 \\ L_2 \\ R_1 \\ R_2 \end{bmatrix}_{i+1} = \begin{bmatrix} \lambda_1 & 0 & 0 & 0 \\ 0 & \lambda_2 & 0 & 0 \\ 0 & 0 & \lambda_1^{-1} & 0 \\ 0 & 0 & 0 & \lambda_2^{-2} \end{bmatrix} \begin{bmatrix} L_1 \\ L_2 \\ R_1 \\ R_2 \end{bmatrix}_i \tag{5.13}$$

For this bi-coupled assembly there are two pairs of left- and right-traveling waves. For the study of the structure of the passbands, stopbands and complexbands of the system we note that κ is either pure imaginary or real positive. Furthermore, we assume that α is positive. If α is negative, the role of the wavetypes L_1, R_1 and L_2, R_2 is reversed.

For waves L_1,R_1,L_2 and R_2

- $4\beta_o + \alpha^2 + 8 < 0$: In this case κ is imaginary and the operand of the square root in Eqs. (5.10) and (5.11) is complex. These frequencies define a *complexband*.

For waves L_1 and R_1

- $|\alpha - \kappa| < 4$: These frequency ranges define *passbands* for waves L_1 and R_1. The dispersion relation is:
$$\cos \sigma_1 = -\frac{\alpha - \kappa}{4} \tag{5.14}$$
- $|\alpha - \kappa| > 4$: These frequency ranges define *stopbands* for waves L_1 and R_1.
- $|\alpha - \kappa| = 4$: These frequency values define *passband/stopband edges* for waves L_1 and R_1.

For waves L_2 and R_2

- $|\alpha + \kappa| < 4$: These frequency ranges define *passbands* for waves L_2 and R_2 with the dispersion relation:
$$\cos \sigma_2 = -\frac{\alpha + \kappa}{4} \tag{5.15}$$
- $|\alpha + \kappa| > 4$: These frequency ranges define *stopbands* for waves L_2 and R_2.
- $|\alpha + \kappa| = 4$: These frequency values define *passband/stopband edges* for waves L_2 and R_2.

It is noteworthy in Eq. (5.15) that since κ is positive (see Eq. (5.9)), if $\alpha > 4$ there is *no passband* for the R_2 and L_2 pair.

Example

Figures 5.2 show the interblade phase angles and rates of exponential decay for the bi-coupled system in Fig. (3.13) with $\bar{m} = 1.$, $\bar{k}_d = 1$ and $\bar{k}_{c1} = \bar{k}_{c2} = 1$. The passband, stopband and complexband structure of the assembly's two characteristic wave pairs is revealed. For this choice of parameters, each wave pair features two separate passbands ($\gamma = 0$), as expected for a two-degree of freedom per site system. Each passband for waves L_2 and R_2 is contained within the corresponding passband for waves L_1 and R_1 and the right passband edges are common to the two wave pairs.
As in the mono-coupled system we observe infinite attenuation at $\bar{\omega} = 1$, which corresponds to the natural frequency of the cantilevered blade. Also evident are two complexbands, *i.e.*, frequency ranges where there exist waves with both attenuation and phase shift. As predicted, the two pairs of waves behave as one in the complexbands.

In Fig. 5.2 the two frequencies at which the transition from passband to complexband occurs are of special importance. At complexband edges $\kappa = 0$, as it goes from pure imaginary to positive real. We noted above that in the passband for wavetype two, $|\alpha+\kappa| < 4$. Hence wavetype two has passbands if and only if $\alpha < 4$. This dramatic change as α goes through the values 4 is illustrated in Fig. 5.3.

Figure 5.3 depicts the propagation constants for the bi-coupled system with $\alpha = \bar{k}_{c1}/\bar{k}_{c2} = 5$. As predicted by Eq. (5.15), the passband for the L_2, R_2 wave pair has vanished and only stopbands and complexbands remain. The first wave pair still

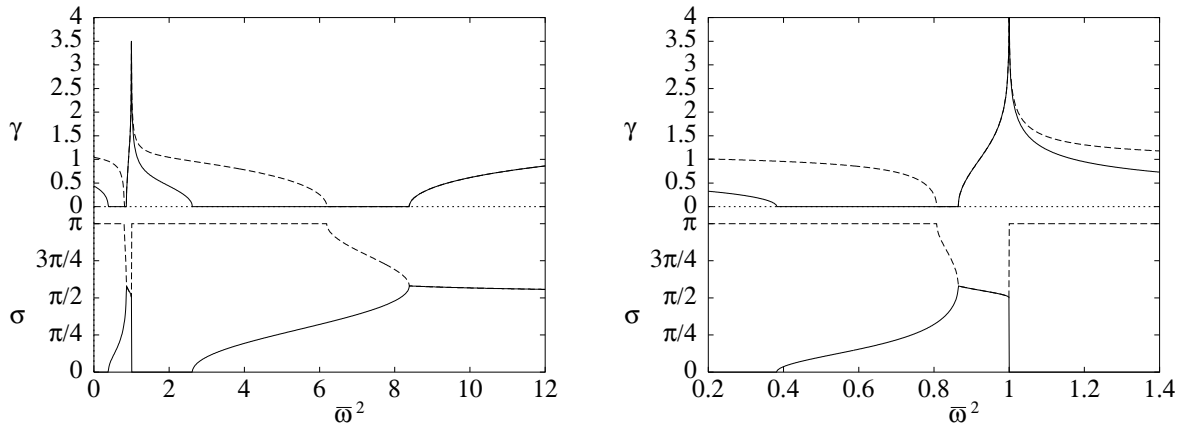

Figure 5.2 Propagation constants vs. frequency for the system in Fig. 3.13 with $\tilde{m} = 1.$, $\bar{k}_d = 1$ and $\bar{k}_{c1} = \bar{k}_{c2} = 1$. A detailed view on the right. Wave type one is (———) and type two is (– – –).

features two distinct passbands in which the interblade phase angle now changes from $\sigma = 0$ at the lower passband edge to $\sigma = \pi$ at the upper passband edge. Motions with all blades vibrating in phase ($\sigma = 0$) and alternate blades vibrating in phase ($\sigma = \pi$) do not stretch the spring k_{c2}, hence the passband edges are uneffected by k_{c2} when $\alpha > 4$.

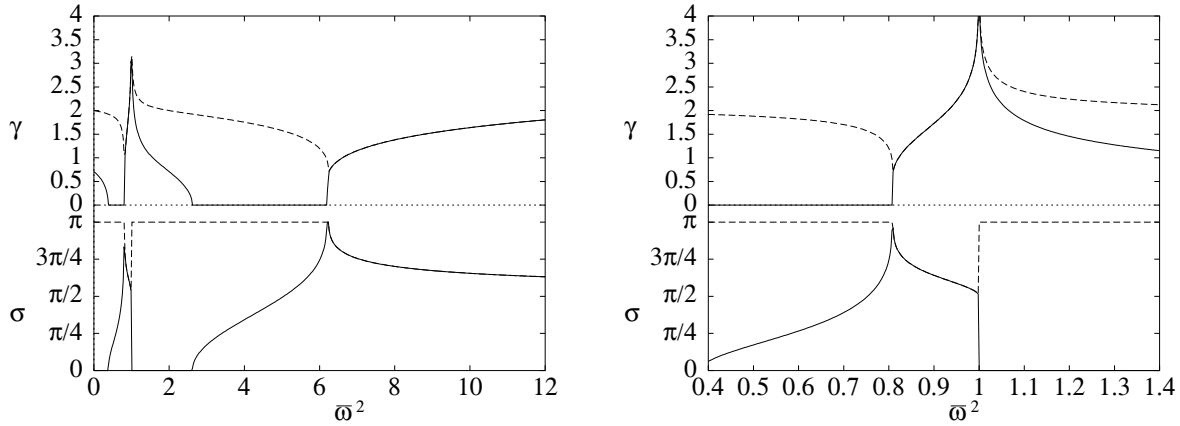

Figure 5.3 Propagation constants vs. frequency for the system in Fig. 3.13 with $\tilde{m} = 1$, $\bar{k}_d = 1$, $\bar{k}_{c1} = 1$ and $\bar{k}_{c2} = 0.2$. A detailed view on the right. Wave type one is (———) and type two is (– – –).

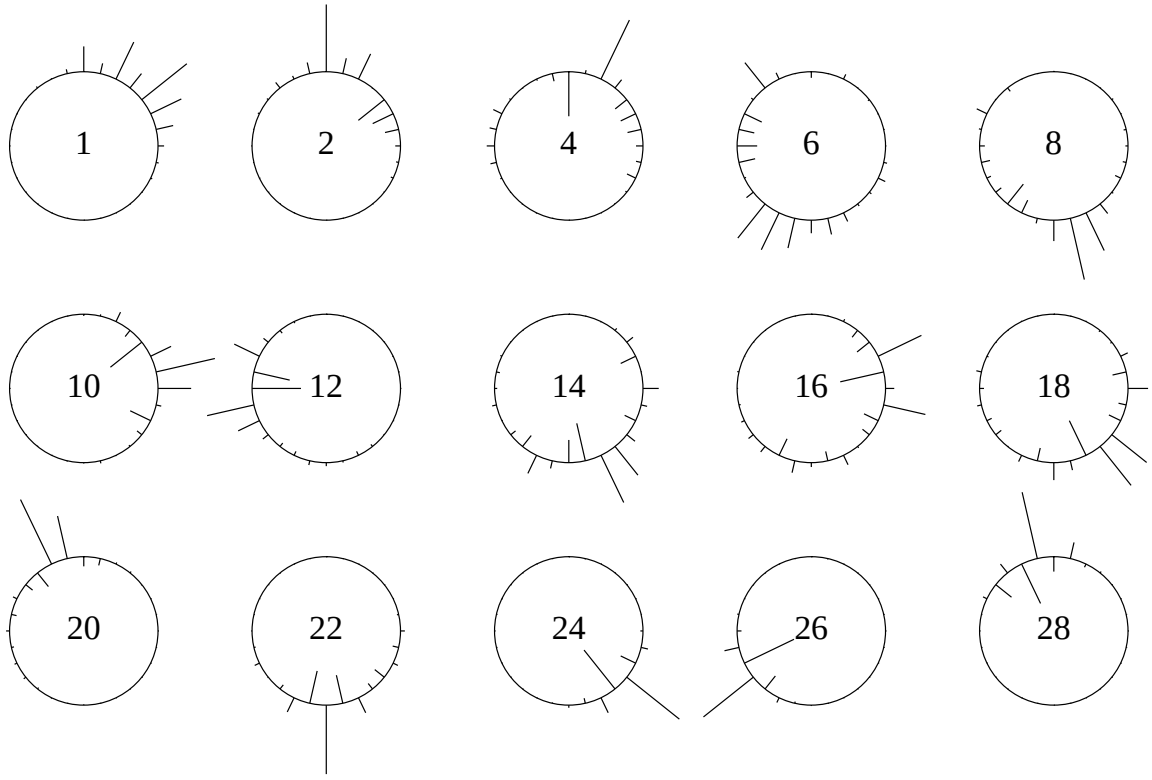

Figure 5.4 Localized modes in the second frequency cluster of a 28 blade assembly with $\bar{k}_d = \bar{m} = 1$, $\bar{k}_c = 0.1$, and uniform random mistuning in the blade stiffness with 5% standard deviation ($s_b = 0.05$). The lengths of the radial lines represent the blade displacement amplitudes. Modes are sorted by increasing natural frequency.

5.2. Localization in Mistuned Mono-Coupled Assemblies

Let us begin the analysis of mistuned systems by examining the effect mistuning has on the natural modes. When mistuning is introduced, the system is no longer symmetric with respect to the clockwise and counterclockwise directions. This loss of cyclicity results in a splitting of the double natural frequencies, such that the system has P clusters of N distinct natural frequencies, where N is the number of blades and P is the number of degrees of freedom per bay. The clusters of frequencies correspond, approximately, to the passbands of the system's tuned counterpart, although they generally are wider. The corresponding mode shapes are standing waves that no longer possess the cyclic symmetry exhibited by the tuned system, where all blades vibrate with the same amplitude. Instead, the vibration energy may be concentrated in a handful of blades that have significantly larger deflection than the majority of blades.

We refer to this phenomenon as mode localization [31].

As an example of the effect of random mistuning, we consider the mode shapes of the mistuned blade assembly model depicted in Fig. 3.4. Figure 5.4 displays some of the mode shapes in the second frequency cluster of a 28-blade assembly. The modes have changed drastically compared to the tuned modes depicted in Fig. 2.1. High levels of localization are observed, such that the vibrational energy of a localized mode shape is no longer uniformly distributed along the rotor. Such mode localization may result in a substantial increase in forced response amplitudes and in a potential decrease in fatigue life.

In order to achieve a compact characterization of localization phenomena, a stochastic approach is chosen to analyze the effects of random blade mistuning. The statistical description is not well suited to the modes of vibration because of the switching of the associated natural frequencies as the strength or the distribution of mistuning varies. We choose instead to examine the frequency-dependent propagation of incident waves in mistuned assemblies.

In order to avoid the contamination of the localization effect by the cyclicity condition, an infinite assembly is studied, which consists of a segment of N mistuned bays ($i = 1, \ldots, N$) embedded in an otherwise tuned infinite assembly. Our interest lies in the transmission of incident waves along the N-bay mistuned segment. An advantage of this setup is that a wave that exits the mistuned segment is propagated away and does not return. We then let N go to infinity in order to obtain an asymptotic characterization of wave transmission through mistuned bays.

For tuned systems, characteristic waves propagate independently of one another and, in frequency passbands, are unattenuated. Mathematically this is expressed by the fact that for a tuned bay the transformation from physical to wave coordinates renders the wave transfer matrix diagonal (see Section 3). For a mistuned bay, however, the transformation defined by $\mathbf{X}$ does not, in general, diagonalize the random bay transfer matrix, $\mathbf{T}_i$. This means that a wave incident to a mistuned segment is not fully transmitted along the segment, but rather experiences scattering at each interface between dissimilar bays, giving rise to reflected and transmitted components in all the characteristic wave types for the assembly. The effect of these multiple reflections over a number of mistuned bays is to trap the incident wave near the incidence region—this is the phenomenon referred to as *localization* [30]. Also, the conversion of the incident wave into the other wave types may cause the transmitted wave which exits the mistuned segment to be quite different, in terms of amplitude but also of wave type components, from the incident wave—a phenomenon referred to as *wave conversion* [19]. The mathematical formalism used in the study of localization and conversion

phenomena follows.

A statistical approach is chosen to examine the high sensitivity to mistuning and the occurrence of localization in randomly mistuned assemblies. A statistical description of the modes of vibration is not practical due to the switching of the associated natural frequencies as the strength or the distribution of mistuning varies. We choose instead to examine the propagation of incident waves in mistuned assemblies. This allows us to control the frequency at which we wish to examine localization. In order to avoid the contamination of the localization effect by the cyclicity condition, an infinite assembly is studied. We further assume that mistuning is restricted to a segment of N bays (numbered from $i = 1$ to $i = N$) embedded in an otherwise tuned infinite assembly. We are interested in the transmission of incident waves along the N-bay mistuned segment. An advantage of this approach is that a traveling wave that exits the mistuned segment will be propagated away and will not return. We then let N go to infinity in order to obtain an asymptotic characterization of wave transmission through mistuned bays. A full derivation of the results of this section may be found in [31].

In Section 5.1.1 we demonstrated how the transfer matrix $\mathbf{T}_o$ of a tuned bay is diagonalized by the similarity transformation defined by the matrix $\mathbf{X}$, which has as its columns the eigenvectors of $\mathbf{T}_o$. We called the diagonalized matrix a wave transfer matrix, $\mathbf{W}_o$. The transformation introduces a new set of coordinates, namely the left– and right-traveling components of a wave. The transformation defined by $\mathbf{X}$ does not, in general, diagonalize the transfer matrix of a bay belonging to the mistuned segment, $\mathbf{T}_i$ or $\mathbf{T}_{i;i-1}$ $(i = 1, \ldots, N)$, as the case may be. Instead a non-diagonal wave transfer matrix is generated. The elements of this matrix may be expressed in terms of the more familiar reflection and transmission coefficients, as follows.

At the interface between dissimilar bays, waves are split into a transmitted part and a reflected part. As illustrated in Fig. 5.5, the left traveling wave incident to bay $i-1$, L_i, is the sum of a transmitted left traveling wave, $t_i L_{i+1}$ and a reflected right traveling wave, $r_i R_i$. Likewise, the right-traveling wave incident to bay $i+1$, R_{i+1}, is comprised of a transmitted part, $\hat{t}_i R_i$, and a reflected part, $\hat{r}_i L_{i+1}$. Here t_i and $\hat{t}_i$ are transmission coefficients and r_i and $\hat{r}_i$ are reflection coefficients in the left and right directions, respectively. Transmission and reflection coefficients are the complex amplitudes of transmitted and reflected waves due to an incident wave of unit amplitude, respectively. The above defines a scattering matrix, $\mathbf{S}_i$:

$$\begin{bmatrix} L_i \\ R_{i+1} \end{bmatrix} = \mathbf{S}_i \begin{bmatrix} R_i \\ L_{i+1} \end{bmatrix} = \begin{bmatrix} r_i & t_i \\ \hat{t}_i & \hat{r}_i \end{bmatrix} \begin{bmatrix} R_i \\ L_{i+1} \end{bmatrix}, \tag{5.16}$$

where directional symmetry in the absence of aerodynamic forces dictates that $\hat{t}_i = t_i$

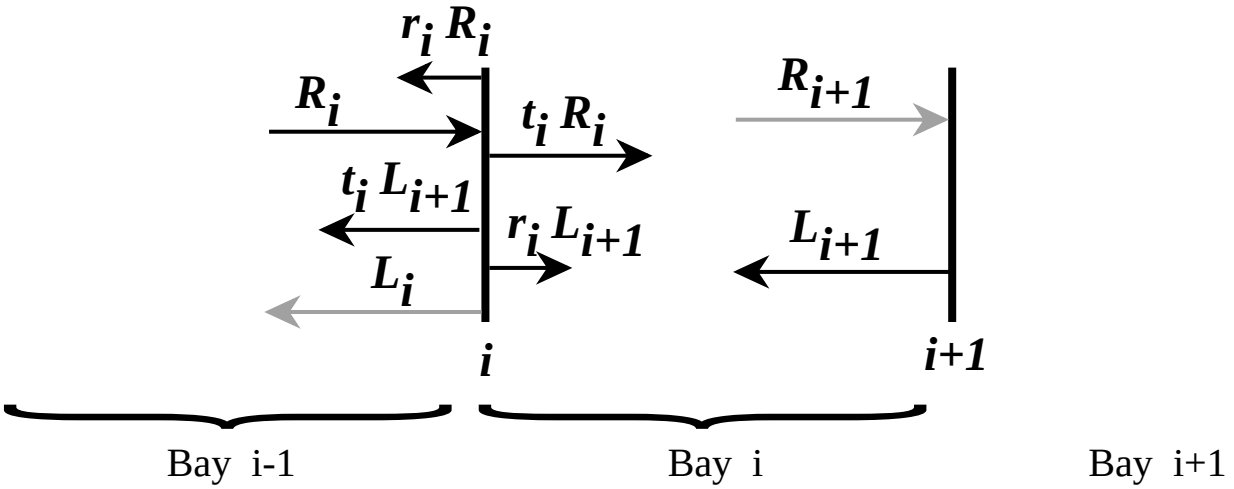

Figure 5.5 Scattering of waves at substructure interfaces in a structure with a single wave channel.

and $\hat{r}_i = r_i$. Solving Eq. (5.16) for R_{i+1} and L_{i+1} yields

$$\begin{bmatrix} L \\ R \end{bmatrix}_{i+1} = \mathbf{W}_i \begin{bmatrix} L \\ R \end{bmatrix}_i = \begin{bmatrix} \frac{1}{t_i} & \frac{-r_i}{t_i} \\ \frac{r_i}{t_i} & t_i - \frac{r_i^2}{t_i} \end{bmatrix} \begin{bmatrix} L \\ R \end{bmatrix}_i . \tag{5.17}$$

Equation (5.17) tells us that the off-diagonal elements in $\mathbf{W}_i$ govern what portion of a right or left traveling wave is reflected, thereby generating a wave in the opposite direction. The transmitted portion of the incident wave is determined from the first diagonal element in the wave transfer matrix. For a tuned bay $\mathbf{W}_i = \mathbf{W}_o$ is diagonal and there is no reflection at the interface. Hence $r_i = 0$ and the wave is fully transmitted. For a mistuned bay there is a reflection, or scattering at the interfaces between bays. A wave incident to a segment of randomly mistuned bays will experience multiple reflections whose effect may be to trap a wave near the incidence region. Only a frequency-dependent fraction of an incident wave is transmitted along to the far end of the mistuned segment. This effect is called *localization*. In a mistuned system passbands no longer exist since all waves are attenuated [31].

For a segment of N dissimilar bays the wave transfer matrix is the product of the random wave transfer matrices of the individual bays

$$\boldsymbol{\mathcal{W}}_N = \prod_{i=1}^{N} \mathbf{W}_i = \begin{bmatrix} \frac{1}{\tau_N} & \frac{-\rho_N}{\tau_N} \\ \frac{\rho_N}{\tau_N} & \tau_N - \frac{\rho_N^2}{\tau_N} \end{bmatrix} . \tag{5.18}$$

The one-one term, $1/\tau_N$, tells us which portion of an incident wave is transmitted to the far end of the mistuned segment. Obviously the behavior of the transmission coefficient for the mistuned segment, τ_N, governs the strength of the effects of mistuning and the resulting localization. We define the *localization factor* as

$$\gamma = \lim_{N\to\infty}\left[\frac{1}{N}\ln\left|\frac{1}{\tau_N}\right|\right], \tag{5.19}$$

implying that asymptotically, the ratio of emergent to incident wave decreases exponentially with an increasing number of bays, N [31]. The localization factor, γ, defines the average exponential decay rate per bay and thus is a descriptor of the strength of localization. Assuming that the random variables δ_i ($i = 1\ldots N$) from Eqs. (3.10) and (3.11) form an ergodic sequence, then the transmission coefficient, $\tau_N(\delta_1,\ldots,\delta_N)$, is also ergodic. Ergodicity implies that, with probability 1, the limit in Eq. (5.19) is equivalent to the ensemble average for a finite mistuned segment of length N:

$$\gamma = \left\langle\frac{1}{N}\ln\left|\frac{1}{\tau_N}\right|\right\rangle, \tag{5.20}$$

where $\langle\rangle$ denotes the expected value of a random variable [30].

The assumption that a cyclic structure is infinite is of course a limitation. It must be understood that this type of analysis is only applicable if the localization is strong enough that the vibration energy is confined to a sufficiently small region compared to the size of the assembly. For a nearly cyclic finite system this basically requires that the wave be adequately attenuated before reaching the incidence region again and thus interacting with other waves from the same source.

5.2.1. Sensitivity to Mistuning.

In general Eqs. (5.19) and (5.20) for the localization factor cannot be evaluated in closed form. However, analytical approximations are possible using perturbation methods, as follows.

We seek an expansion of $\frac{1}{\tau_N}$ in Eq. (5.19) in terms of the small mistuning parameter, δ_i (δ_i of order ϵ or smaller), thus treating the mistuned system as a perturbation of the tuned system. This is obtained through a Taylor expansion of the function $\beta(\delta_i)$ in Eq. (3.10):

$$\beta(\delta_i) = \beta_o + \beta'(0)\delta_i + O(\delta_i^2) \tag{5.21}$$

and subsequent expansion of τ_N and expansion and averaging of γ. The expansion in Eq. (5.21) must of course be uniform, *i.e.*, $\beta'(0)$ must be of order one (order ϵ^0) or smaller. However, if the expansion in Eq. (5.21) is nonuniform, *i.e.*, when $\beta'(0)$ is large (order ϵ^{-1} or larger) the technique breaks down. In this case the perturbation

expansion is only valid for δ_i second order (order ϵ^2) or smaller. This breakdown indicates high sensitivity to mistuning and it is when the breakdown occurs (if it occurs) that systems have been seen to enter the realm of strong localization. This suggests the use of the first-order Taylor coefficient of $\beta(\delta_i)$ as a *measure of sensitivity to mistuning*:

$$S = \beta'(0) \tag{5.22}$$

A similar scenario may take place in the Taylor expansion of the transfer matrix in Eq. (3.11), albeit with four different first-order Taylor coefficients for α and β with respect to δ_i and δ_{i-1}. We do not formally define a sensitivity measure for this case.

When the sensitivity measure, $S = \beta'(0)$, becomes large the expansion in Eq. (5.21) is nonuniform, indicating a qualitative change in the assembly's dynamics, and other avenues must be explored. Note that in the passbands of the tuned system we have $-2 \leq \beta_o \leq 2$, but when S is large, $\beta(\delta_i)$ in Eq. (5.21) has the potential to become large for first-order mistuning in that frequency range. This suggests treating the off-diagonal terms in the transfer matrix of Eq. (3.10) as small perturbations compared to the large $\beta(\delta_i)$, thus yielding an alternative expansion for the high sensitivity case.

The two techniques outlined here, for the cases of normal and high sensitivity, are detailed in the following sections.

5.2.2. Classical Perturbation Method — Normal Sensitivity.

Consider the case where the expansion (5.21) is valid for first-order mistuning (δ_i of order ϵ), *i.e.*, when $S = \beta'(0)$ is not large (S of order one or smaller). We shall refer to this case as low or normal sensitivity. The much simpler case in Eq. (3.10) is treated first to better explain the technique. In Eq. (3.10), $\beta_i = \beta(\delta_i)$ depends only on one mistuned parameter, with $\beta(0) = \beta_o$ corresponding to the tuned case. A uniform expansion of $\mathbf{T}_i$ in the small mistuning parameter δ_i yields

$$\begin{aligned}\mathbf{T_i} = \begin{bmatrix} \beta(\delta_i) & -1 \\ 1 & 0 \end{bmatrix} &= \begin{bmatrix} \beta_o & -1 \\ 1 & 0 \end{bmatrix} + \begin{bmatrix} \beta'(0) & 0 \\ 0 & 0 \end{bmatrix} \delta_i + \begin{bmatrix} \beta''(0) & 0 \\ 0 & 0 \end{bmatrix} \frac{\delta_i^2}{2} + \dots \\ &= \mathbf{T_o} + \mathbf{T}'\delta_i + \mathbf{T}''\frac{\delta_i^2}{2} + \dots \end{aligned} \tag{5.23}$$

A transformation to wave coordinates is accomplished with the matrix of eigenvectors of $\mathbf{T}_o$,

$$\mathbf{X} = \begin{bmatrix} 1 & 1 \\ e^{-j\sigma} & e^{j\sigma} \end{bmatrix}, \tag{5.24}$$

where σ is defined in Eq. (5.6). Note that the analysis is limited to the tuned system's passband, since there is already large attenuation in the stopband. The wave transfer

matrix is expanded as

$$\begin{aligned}\mathbf{W_i} = \mathbf{X^{-1}T_iX} &= \mathbf{W_o} + \mathbf{W}'\delta_i + \mathbf{W}''\frac{\delta_i^2}{2} + \dots \\ &= \begin{bmatrix} e^{j\sigma} & 0 \\ 0 & e^{-j\sigma} \end{bmatrix} + \begin{bmatrix} e^{j\sigma} & 1 \\ -1 & e^{-j\sigma} \end{bmatrix} \frac{\delta_i \beta'(0)}{2j\sin\sigma} + \begin{bmatrix} e^{j\sigma} & 1 \\ -1 & e^{-j\sigma} \end{bmatrix} \frac{\delta_i^2 \beta''(0)}{4j\sin\sigma} + \dots\end{aligned} \tag{5.25}$$

We need to evaluate the wave transfer matrix for a segment of N mistuned bays, each with its own random mistuning parameter δ_i. The random variables δ_i corresponding to each bay are considered independent and identically distributed, with zero mean and standard deviation s_δ. An assembly of N bays has the wave transfer matrix $\boldsymbol{\mathcal{W}}_N$, which, when expanded to the second order in the δ_i's, becomes

$$\begin{aligned}\boldsymbol{\mathcal{W}}_N &= \prod_{i=N}^{1} \left(\mathbf{W_o} + \delta_i \mathbf{W}' + \frac{\delta_i^2}{2}\mathbf{W}'' \right) + O(\delta_i^3) \\ &= \mathbf{W_o}^N + \sum_{i=1}^{N} \mathbf{W_o^{i-1}} \mathbf{W}' \mathbf{W_o^{N-i}} \delta_i + \sum_{i=1}^{N} \mathbf{W_o^{i-1}} \mathbf{W}'' \mathbf{W_o^{N-i}} \frac{\delta_i^2}{2} + \sum_{i=1}^{N} \sum_{\substack{j=1 \\ j\neq i}}^{N} \mathbf{R}\delta_i\delta_j + O(\delta_i^3).\end{aligned} \tag{5.26}$$

The matrix $\mathbf{R}$ in Eq. (5.26) has a highly complex form, not evaluated since that entire term will vanish in the averaging process that follows, due to independence of the random variables δ_i, $(i = 1 \dots N)$. For an approximation of the localization factor, only the first diagonal element of $\boldsymbol{\mathcal{W}}_N$, $w_{11}^N = \frac{1}{\tau_N}$, is needed. We have

$$\frac{1}{\tau_N} = e^{jN\sigma} \left[1 + \frac{\beta'(0)}{2j\sin\sigma} \sum_{i=1}^{N} \delta_i + \frac{\beta''(0)}{4j\sin\sigma} \sum_{i=1}^{N} \delta_i^2 \right] + O(\delta_i^3), \tag{5.27}$$

$$\left| \frac{1}{\tau_N} \right|^2 = \left[1 + \frac{\beta'(0)^2}{4\sin^2\sigma} \sum_{i=1}^{N} \delta_i \sum_{l=1}^{N} \delta_l \right] + O(\delta_i^3). \tag{5.28}$$

Since the δ_i's have zero mean and are independent, we have $\langle \delta_i \delta_j \rangle = 0$ for $j \neq i$ and $\langle \delta_i \delta_i \rangle = s_\delta^2$. Using the expansion $\ln(1+x) = x + O(x^2)$, we obtain the approximation of the localization factor, valid for low sensitivity,

$$\gamma = \left\langle \frac{1}{2N} \ln \left| \frac{1}{\tau_N} \right|^2 \right\rangle \simeq \frac{1}{2} \left(\frac{\beta'(0) s_\delta}{2\sin\sigma} \right)^2 = \frac{(S(\bar{\omega}))^2 s_\delta^2}{2\,(2+\beta_o(\bar{\omega}))\,(2-\beta_o(\bar{\omega}))}, \qquad O(S) \leq 1, \tag{5.29}$$

where S is the sensitivity measure defined in Eq. (5.22). Note that both S and β_o are functions of $\bar{\omega}$ and vary within the passband. The localization factor, γ, allows for localization effects to be characterized in a simple and compact way, without extensive simulations of mistuned systems. Note that Eq. (5.29) is general and applies to any mono-coupled mistuned assembly, as long as the mistuning parameter is not one that

connects two adjacent bays. It is of interest to note that the second-order Taylor coefficient, $\beta''(0)$, is cancelled from the derivation. According to Eq. (5.29), the onset of localization increases as the sensitivity measure squared. Also, to first order, the localization factor increases with the square of the mistuning standard deviation. The approximation of the localization factor becomes unbounded at frequencies which correspond to the edges of the passband of the tuned structure, $\beta_o = \pm 2$. This is reasonable, since at those frequencies the transformation matrix $\mathbf{X}$ (see Eq. (5.24)) is singular.

In order to obtain a quick estimate of the level of localization present in a system, it is advantageous to focus on the localization factor at the midband frequency. This frequency corresponds to the interblade phase angle $\sigma = \pi/2$, thus is the *median* natural frequency in the tuned system's passband. Note that $\sigma = \pi/2$ does not correspond to a natural frequency unless $N/4$ is an integer. Nonetheless, in each passband, the frequency corresponding to $\sigma = \pi/2$ (see Eq. (5.6)) will have an equal number of frequencies above and below it. Note also, that the midband frequency need not be located close to the mean frequency of the passband. One has, at midband,

$$\gamma_{mid} = \frac{S_{mid}^2 s_\delta^2}{8}. \tag{5.30}$$

which gives a good indication of the strength of localization effects in a "typical" mode of the system.

Let us now consider the case where a parameter common to two adjacent bays is disordered. In this case the transfer matrix has the general form in Eq. (3.11), where α and β are functions of two independent and identically distributed random variables, δ_i and δ_{i-1}. Assuming that β and α may be uniformly expanded in the small disorder parameters δ_i and δ_{i-1}, we find an expansion of $\mathbf{T}_{i,i-1}$:

$$\begin{aligned}
\mathbf{T_{i;i-1}} =& \begin{bmatrix} \beta(\delta_i,\delta_{i-1}) & -\alpha(\delta_i,\delta_{i-1}) \\ 1 & 0 \end{bmatrix} = \begin{bmatrix} \beta_o & -\alpha_o \\ 1 & 0 \end{bmatrix} + \begin{bmatrix} \beta_{,i-1} & -\alpha_{,i-1} \\ 0 & 0 \end{bmatrix}_{(0,0)} \delta_{i-1} \\
&+ \begin{bmatrix} \beta_{,i} & -\alpha_{,i} \\ 0 & 0 \end{bmatrix}_{(0,0)} \delta_i + \begin{bmatrix} \beta_{,(i-1)(i-1)} & -\alpha_{,(i-1)(i-1)} \\ 0 & 0 \end{bmatrix}_{(0,0)} \frac{\delta_{i-1}^2}{2} \\
&+ \begin{bmatrix} \beta_{,i(i-1)} & -\alpha_{,i(i-1)} \\ 0 & 0 \end{bmatrix}_{(0,0)} \delta_i\delta_{i-1} + \begin{bmatrix} \beta_{,ii} & -\alpha_{,ii} \\ 0 & 0 \end{bmatrix}_{(0,0)} \frac{\delta_i^2}{2} + \dots \\
=& \mathbf{T_o} + \mathbf{T_{,1}}\delta_i + \mathbf{T_{,2}}\delta_{i-1} + \mathbf{T_{,11}}\frac{\delta_i^2}{2} + \mathbf{T_{,12}}\delta_i\delta_j + \mathbf{T_{,22}}\frac{\delta_{i-1}^2}{2} + \dots,
\end{aligned} \tag{5.31}$$

where the index notation $\mathbf{T}_{,1}$ and $\mathbf{T}_{,2}$ has been adopted to denote differentiation with respect to the first variable (δ_i) and the second variable (δ_{i-1}), respectively. A transformation to wave coordinates is accomplished using the matrix $\mathbf{X}$ from Eq. (5.24). The

result is an expansion of the wave transfer matrix in the small disorder parameters δ_i and δ_{i-1}:

$$\mathbf{W_{i;i-1}} = \mathbf{W_o} + \mathbf{W}_{,1}\delta_i + \mathbf{W}_{,2}\delta_{i-1} + \mathbf{W}_{,11}\frac{\delta_i^2}{2} + \mathbf{W}_{,12}\delta_i\delta_{i-1} + \mathbf{W}_{,22}\frac{\delta_{i-1}^2}{2} + \dots \tag{5.32}$$

The wave transfer matrix of an N-bay segment is

$$\begin{aligned}\mathcal{W}_N &= \mathbf{W_{N;N-1}W_{N-1;N-2}}\dots\mathbf{W_{2;1}W_{1;0}} \\ &\simeq \prod_{i=N}^{1}\left(\mathbf{W_o} + \mathbf{W}_{,1}\delta_i + \mathbf{W}_{,2}\delta_{i-1} + \mathbf{W}_{,11}\frac{\delta_i^2}{2} + \mathbf{W}_{,12}\delta_i\delta_{i-1} + \mathbf{W}_{,22}\frac{\delta_{i-1}^2}{2}\right).\end{aligned} \tag{5.33}$$

Carrying the product out to the second order in the δ's, the one-one term is found to be, after tedious algebra,

$$\begin{aligned}\widetilde{w}_{11}^N = \frac{1}{\tau_N} \simeq e^{jN\sigma}\Bigg[1 + e^{-j\sigma}\,(\mathbf{W}_{,1} + \mathbf{W}_{,2})_{11}\sum_{i=1}^{N}\delta_i + e^{-2j\sigma}\,(\mathbf{W}_{,2}\,\mathbf{W}_{,1})_{11}\sum_{i=1}^{N}\delta_i^2 \\ + e^{-j\sigma}\,(\mathbf{W}_{,11} + \mathbf{W}_{,22})_{11}\sum_{i=1}^{N}\frac{\delta_i^2}{2}\Bigg] = e^{jN\sigma}\left[1 + C_1\sum_{i=1}^{N}\delta_i + C_2\sum_{i=1}^{N}\delta_i^2\right], \quad C_1, C_2 \in \mathbb{C}\end{aligned} \tag{5.34}$$

The tilde on $\widetilde{w}_{11}^N$ underlines the fact that a few liberties have been taken, *i.e.*, we have ignored very complicated terms that we know will vanish in the averaging process at a later stage in the derivation. The term containing $\mathbf{W}_{,2}\,\mathbf{W}_{,1}$ appears due to the occurrence of the same random variable in two adjacent matrices. Next the magnitude of $\widetilde{w}_{11}^N$ is evaluated:

$$|\widetilde{w}_{11}^N|^2 = 1 + R_1\sum_{i=1}^{N}\delta_i + R_2\sum_{i=1}^{N}\delta_i^2 + O(\delta^3), \quad R_1, R_2 \in \mathbb{R}. \tag{5.35}$$

Due to the terms linear in δ, a second-order expansion of $\ln|w_{11}^N|^2$ is required, that is, $\ln(1+x) = x - x^2/2 + O(x^3)$. Dividing by $2N$ and taking the limit as $N \to \infty$ yields the localization factor, after substantial algebra:

$$\begin{aligned}\gamma = \lim_{N\to\infty}\frac{1}{2N}\ln|w_{11}^N|^2 \simeq s_\delta^2\Bigg[\frac{\left[\beta_{,1} + \beta_{,2} - (\alpha_{,1} + \alpha_{,2})\frac{\beta_o}{2}\right]^2}{8\sin^2\sigma} - \frac{\beta_{,1}\,\beta_{,2} - \beta_o\beta_{,2}\,\alpha_{,1}}{2} \\ + \frac{\alpha_{,11} + \alpha_{,22}}{4} - \frac{(\alpha_{,1} + \alpha_{,2})^2}{8}\Bigg],\end{aligned} \tag{5.36}$$

where

$$\begin{aligned}\beta_{,1} &= \left.\frac{\partial\beta(\delta_i,\delta_{i-1})}{\partial\delta_i}\right|_{(0,0)} & \beta_{,2} &= \left.\frac{\partial\beta(\delta_i,\delta_{i-1})}{\partial\delta_{i-1}}\right|_{(0,0)} \\ \alpha_{,1} &= \left.\frac{\partial\alpha(\delta_i,\delta_{i-1})}{\partial\delta_i}\right|_{(0,0)} & \alpha_{,2} &= \left.\frac{\partial\alpha(\delta_i,\delta_{i-1})}{\partial\delta_{i-1}}\right|_{(0,0)} \\ \alpha_{,11} &= \left.\frac{\partial^2\alpha(\delta_i,\delta_{i-1})}{\partial\delta_i^2}\right|_{(0,0)} & \alpha_{,22} &= \left.\frac{\partial^2\alpha(\delta_i,\delta_{i-1})}{\partial\delta_{i-1}^2}\right|_{(0,0)},\end{aligned} \tag{5.37}$$

which reduces to the form of Eq. (5.29) for $\beta(\delta_i, \delta_{i-1}) = \beta(\delta_i)$ and $\alpha(\delta_i, \delta_{i-1}) = 1$. Finally, in the numerous cases where

$$\alpha(\delta_i, \delta_{i-1}) = \frac{f(\delta_{i-1})}{f(\delta_i)}, \tag{5.38}$$

Eq. (5.36) simplifies to

$$\gamma = s_\delta^2 \left[\frac{[\beta_{,1} + \beta_{,2}]^2}{8 \sin^2 \sigma} + \frac{\beta_{,2}}{2} \left(\beta_o \frac{f'(0)}{f(0)} - \beta_{,1} \right) + \frac{1}{2} \left(\frac{f'(0)}{f(0)} \right)^2 \right]. \tag{5.39}$$

At midband Eq. (5.39) reduces even further, to:

$$\gamma_{mid} = \frac{s_\delta^2}{8} \left([\beta_{mid,1} - \beta_{mid,2}]^2 + 4 \left[\frac{f'_{mid}(0)}{f_{mid}(0)} \right]^2 \right). \tag{5.40}$$

5.2.3. Modified Perturbation Method — High Sensitivity.

As suggested in Section 6.1 and observed in Section 6.2, the Classical Perturbation Method fails in the limit of high sensitivity , *i.e.*, when $S = \beta'(0)$ is large. Not only may this be seen by the failure of the Taylor expansion of β (Eq. (5.21)), but also by the fact that γ in Eq. (5.29) becomes large (order ϵ^{-1}) for S large, while it supposedly is a small perturbation of its zero value in the tuned system's passbands. The introduction of first-order mistuning in a system with strong sensitivity ($\beta'(0) \gg 1$) has the effect that in the passbands $\beta(\delta_i)$ becomes large (recall that in a tuned system's passband $-2 < \beta(0) < 2$). This suggests the following modified perturbation scheme, where the off-diagonal terms are regarded as the perturbation.

$$\mathbf{T_i} = \begin{bmatrix} \beta(\delta_i) & -1 \\ 1 & 0 \end{bmatrix} = \begin{bmatrix} \beta(\delta_i) & 0 \\ 0 & 0 \end{bmatrix} + \begin{bmatrix} 0 & -1 \\ 1 & 0 \end{bmatrix} = \bar{\mathbf{T}}_\mathbf{i} + \Delta\mathbf{T}. \tag{5.41}$$

A brief review of the equation of motion, Eq. (3.8), aids in a physical interpretation of the Modified Perturbation Method. The larger β becomes compared to 1, the less q_i is influenced by q_{i+1} and q_{i-1}. Consequently, in Eq. (5.41), a coupled system is treated as a perturbation of the uncoupled system. Since the modified unperturbed matrix $\bar{\mathbf{T}}_i$ is already diagonal, there is no need for a wave coordinate transformation. Hence the physical coordinates are also *"wave coordinates"* (actually, since the unperturbed structure is uncoupled it does not actually transmit waves) and $\bar{\mathbf{T}}_i$ is a wave transfer matrix for the unperturbed structure. The wave transfer matrix for the perturbed, N-bay structure is then

$$\boldsymbol{\mathcal{W}}^N = \prod_{i=N}^{1} \mathbf{T_i} \approx \prod_{i=N}^{1} \bar{\mathbf{T}}_\mathbf{i} + \sum_{l=1}^{N} \left[\prod_{i=N}^{l-1} \bar{\mathbf{T}}_\mathbf{i} \Delta\mathbf{T} \prod_{i=l-1}^{1} \bar{\mathbf{T}}_\mathbf{i} \right] = \begin{bmatrix} \prod_{i=N}^{1} \beta(\delta_i) & -\prod_{i=N}^{2} \beta(\delta_i) \\ \prod_{i=N-1}^{1} \beta(\delta_i) & 0 \end{bmatrix}, \tag{5.42}$$

where the product is expanded to the first order in the perturbation, $\mathbf{\Delta T}$. Due to the special form of $\mathbf{\Delta T}$ all terms in the sum vanish except the first one and the last one. These terms become the off-diagonal terms in the matrix product and do not affect the transmission coefficient. From Eqs. (5.42) and (5.18) we see that

$$\frac{1}{\tau_N} = \prod_{i=N}^{1} \beta(\delta_i). \tag{5.43}$$

Thus, in accordance with Eq. (5.20) the localization factor becomes

$$\gamma = \langle \ln|\beta(\delta)| \rangle = \int \ln|\beta(\delta)| \mathrm{pdf}_\delta(\delta) d\delta, \tag{5.44}$$

where $\langle\rangle$ denotes an average and $\mathrm{pdf}_\delta(\delta)$ is the probability density function of the random variable δ.

Next we attempt to express the localization factor in terms of the large sensitivity measure, $S = \beta'(0)$. Focusing on the midband frequency, where the interblade phase angle is $\sigma = \pi/2$ and $\beta(0) = 0$, the first-order approximation of β_{mid} for small δ is (assuming that the remainder of the expansion is uniform)

$$\beta_{mid}(\delta) \simeq S_{mid}\delta, \qquad O(S_{mid}) > 1. \tag{5.45}$$

Equation (5.44) may now be written as

$$\gamma_{mid} \simeq \ln|S_{mid}| + \int \ln|\delta| \mathrm{pdf}_\delta(\delta) d\delta, \tag{5.46}$$

which in the case of a uniform distribution, $\delta \in [-W, W] \equiv [-\sqrt{3}s_\delta, \sqrt{3}s_\delta]$, reduces further, to

$$\gamma_{mid} \simeq \ln|S_{mid}| + \ln(\sqrt{3}s_\delta) - 1, \qquad O(S_{mid}) > 1, \tag{5.47}$$

a remarkably simple and general characterization of localization in the high sensitivity case. Note that only the system sensitivity and the mistuning standard deviation are needed to evaluate γ. Also note that since S_{mid} is large, γ_{mid} is not first order but of order one, corresponding to a strong localization behavior. Pierre [31] examined a chain of single-degree of freedom oscillators, where $S = 1/R$, *i.e.*, the sensitivity is the inverse of the dimensionless coupling between oscillators, R. His result verifies Eq. (5.47).

In the limit of strong sensitivity, the Modified Perturbation Method treats a coupled system as a perturbation of an uncoupled, disordered system. This implies that the method is applicable only to weakly coupled assemblies and leads to an interpretation of sensitivity as an inverse of the coupling among bays. High sensitivity to mistuning has already been observed in systems with weakly coupled bays [31]. However, the

definition of coupling in complicated multi-parameter systems is not always possible, whereas the evaluation of $S = \beta'(0)$ is straightforward.

Note that the results of this section are valid only in the cases where the mistuning is not common to adjacent bays as in Eq. (3.11). Since the systems of immediate interest to us do not exhibit strong localization when common parameters are disordered, this extension is not developed here.

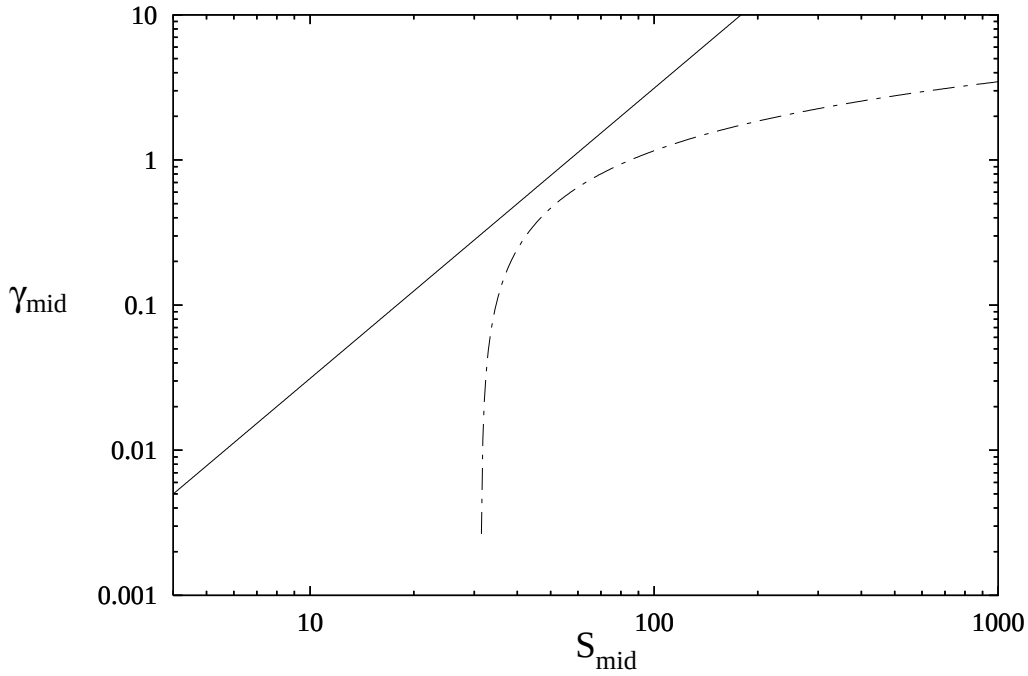

Figure 5.6 Approximation of the localization factor at the midband frequency as a function of the sensitivity measure ($S_{mid} = \beta'_{mid}(0)$). (———) corresponds to the classical perturbation result (Eq. (5.29)), valid for S_{mid} small. (— · —) corresponds to the modified approach (Eq. (5.47)), valid for S_{mid} large. The mistuning is uniform with 5% standard deviation.

Figure 5.6 illustrates the perturbation results for the mid-passband localization factor (Eqs. (5.30) and (5.47)) for a generic system described by Eq. (3.10), plotted as a function of sensitivity. The mistuning is uniform with 5% standard deviation. Equations (5.30) and (5.47) are valid in the limit of weak and strong sensitivity, respectively. Observe the rapid onset of localization, followed by a more moderate increase but large values of γ_{mid} in the limit of high sensitivity.

5.2.4. Example.

We now apply the tools developed above to the system depicted in Fig 3.4. Corresponding to the mistuned parameters k_b^i and k_d^i are measures of sensitivity to mistuning, S^{blade} and S^{disk}, according to Eq. (5.22). No such measure has been defined when the mistuned parameter is one connecting two interfaces, therefore the case where k_c is mistuned is given a different treatment. A parametric study identifies combinations of parameter values leading to high sensitivity. Analytical approximations of localization factors are obtained in the limits of weak and strong sensitivity. These approximations are verified by Monte Carlo simulations.

Measures of Sensitivity

Disk Mistuning: From the definition of β in Eq. (3.28), when $\delta_i^c = \delta_i^b = 0$, one has:

$$\beta(\delta_i^d) = 2 + \frac{\bar{k}_d}{\bar{k}_c}(1 + \delta_i^d) - \frac{\bar{\omega}^2}{\bar{k}_c(1 - \bar{\omega}^2)} - \frac{\bar{m}\bar{\omega}^2}{\bar{k}_c}. \tag{5.48}$$

Thus, from Eq. (5.22), the measure of sensitivity to disk stiffness mistuning is simply,

$$S^{disk} = \frac{k_d}{k_c} \tag{5.49}$$

Note that since $\beta(\delta_i^d)$ is linear with respect to the mistuning, its first-order Taylor expansion is exact. S^{disk} is easy to comprehend. The sensitivity increases linearly with the disk stiffness and is inversely proportional to the stiffness of the coupling spring. It is independent of the blade stiffness and the mass of the blade and the disk. The sensitivity measure is also independent of frequency and is therefore the same in both passbands. Note the obvious correlation between weak interblade coupling and high sensitivity as $k_d \to \infty$ and $k_c \to 0$. These results confirm those of Wei and Pierre [14], Pierre [31], and Cornwell and Bendiksen [34].

Blade Mistuning: For blade mistuning only, $\delta_i^d = \delta_i^c = 0$ and Eq. (3.28) simplifies to

$$\beta(\delta_i^b) = 2 + \frac{\bar{k}_d}{\bar{k}_c} - \frac{\bar{\omega}^2(1 + \delta_i^b)}{\bar{k}_c(1 + \delta_i^b - \bar{\omega}^2)} - \frac{\bar{m}\bar{\omega}^2}{\bar{k}_c} \tag{5.50}$$

Thus, from Eq. (5.22)

$$S^{blade} = \frac{\bar{\omega}^4}{(1 - \bar{\omega}^2)^2\bar{k}_c}. \tag{5.51}$$

Equation (5.51) is more complicated than it first would seem, because the location of the passbands, and hence the corresponding ranges for $\bar{\omega}$, depend on the system parameters $\bar{k}_c$, $\bar{k}_d$ and $\bar{m}$. The sensitivity is of course very different in the two passbands of the system. To give an example of how deceptive Eq. (5.51) is, one might

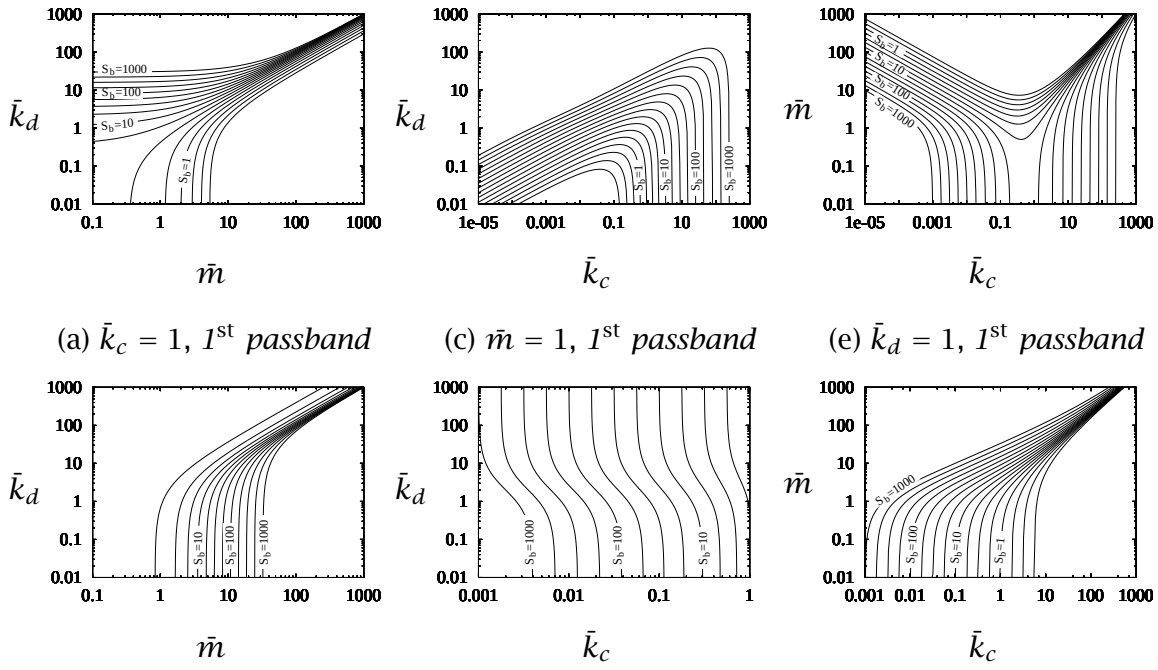

Figure 5.7 Contours of the sensitivity measure, S_{mid}^{blade}, at the two passband centers. In each plot one of the parameters $\bar{k}_c$, $\bar{k}_d$ and $\bar{m}$ is fixed while the others are varied.

wrongly assume that a large coupling spring stiffness, $\bar{k}_c$, always leads to low sensitivity. A counterexample is given below. However, small values of $\bar{k}_c$ do ensure high sensitivity, as we soon will see.

Solving Eq. (3.37) for midband frequencies ($\sigma_k = \pi/2$) and substituting the values of $\bar{\omega}_{mid}^2$ into Eq. (5.51) yields

$$S_{mid_{1,2}}^{blade} = \frac{1}{4\bar{k}_c}\left[2\bar{k}_c + \bar{k}_d - \bar{m} - 1 \mp \sqrt{\left[2\bar{k}_c + \bar{k}_d + \bar{m} + 1\right]^2 - 4\bar{m}\left[\bar{k}_d + 2\bar{k}_c\right]}\right]^2, \tag{5.52}$$

where the plus (resp., minus) sign corresponds to the first (resp., second) passband. The sensitivity to blade mistuning at midband is plotted in Fig. 5.7. The plots show contours of the surface $S_{mid}^{blade}(\bar{k}_c, \bar{k}_d, \bar{m})$ by, in turn, fixing one parameter and varying the other two. A study of the plots yields information about the combination of parameter values that lead to strong sensitivity in the two passbands.

Figures 5.7(c) and 5.7(e) tell us that strong sensitivity in the first passband may be produced by large as well as small values of $\bar{k}_c$, the coupling spring stiffness. At first it seems surprising that a large $\bar{k}_c$ leads to high sensitivity at the first midband. Validation comes in the form of a parametric study of the natural frequencies [45]

which illustrates that for large $\bar{k}_c$ all natural frequencies except the first one merge with the upper passband edge. The lower passband edge features all bays vibrating in phase, independent of the coupling spring stiffness. Hence, although the passband is large, the range of the natural frequencies becomes small, and this system has very weak coupling. A system with stiff coupling springs may be likened to a collection of blades mounted on the perimeter of a rigid ring. The blades are thus decoupled in the limit $\bar{k}_c \to \infty$, vibrating in their first mode with $q_i^d \simeq 0$. The opposite occurs in the second passband, where the bay is vibrating in its second mode that, unlike the first mode, requires a nonzero q_i^d. In this case the stiff coupling spring contributes heavily to the coupling between bays and the sensitivity decreases as $\bar{k}_c$ increases.

In addition to the above observations we note from Fig. 5.7 that if $\bar{m}$ is large enough, increasing it will cause a decrease in first passband sensitivity and an increase in second passband sensitivity. Varying $\bar{m}$ for small $\bar{m}$ has only a small effect on sensitivity, as evidenced by the lower portion of Fig. 5.7(e) and Fig. 5.7(f). Similarly we see that an increase in $\bar{k}_d$ increases first passband sensitivity except when $\bar{k}_d$ is small (Fig. 5.7(a)) or when $\bar{k}_c$ is very large (Fig. 5.7(c)). Second passband sensitivity decreases with increased $\bar{k}_d$ but only in ranges determined by $\bar{m}$ and $\bar{k}_c$. A combination of a small $\bar{k}_c$ and a large $\bar{k}_d$ leads to high sensitivity in both passbands.

Coupling Spring Mistuning: Although we have not defined a sensitivity measure for the system in Eq. (3.11), we attempt to examine its sensitivity to mistuning by considering all four possible first-order Taylor coefficients. From Eq. (3.28), with $\delta_i^d = \delta_i^b = 0$,

$$\beta(\delta_i^c, \delta_{i-1}^c) = \frac{1}{1+\delta_i^c}\left[\frac{\bar{k}_d}{\bar{k}_c} - \frac{\bar{m}\bar{\omega}^2}{\bar{k}_c} - \frac{\bar{\omega}^2}{\bar{k}_c(1-\bar{\omega}^2)} + 2 + \delta_i^c + \delta_{i-1}^c\right] = \frac{\beta_o + \delta_i^c + \delta_{i-1}^c}{1+\delta_i^c} \tag{5.53}$$

and from Eq. (3.29)

$$\alpha_{i;i-1} = \frac{1+\delta_{i-1}^c}{1+\delta_i^c} \tag{5.54}$$

from which

$$\left.\frac{\partial\beta(\delta_i^c, \delta_{i-1}^c)}{\partial\delta_i^c}\right|_{(0,0)} = 1 - \beta_o \qquad \left.\frac{\partial\beta(\delta_i^c, \delta_{i-1}^c)}{\partial\delta_{i-1}^c}\right|_{(0,0)} = 1 \tag{5.55}$$

and

$$\left.\frac{\partial\alpha(\delta_i^c, \delta_{i-1}^c)}{\partial\delta_i^c}\right|_{(0,0)} = -1 \qquad \left.\frac{\partial\alpha(\delta_i^c, \delta_{i-1}^c)}{\partial\delta_{i-1}^c}\right|_{(0,0)} = 1 \tag{5.56}$$

All four Taylor coefficients in Eqs. (5.55) and Eqs. (5.56) remain of order one or smaller for all parameter values. We conclude that in the case of coupling spring mistuning the classical perturbation is valid for all parameter values. This system is thus never

strongly sensitive to coupling spring mistuning and only weak localization may be expected to occur.

Localization Factors and Monte Carlo Simulation.

Based on the expressions for the sensitivity measure, we are now in the position to examine the localization factor due to the above three types of disorder in the limits of low and high sensitivity. Using *Monte Carlo simulations* we confirm the validity of the perturbation approximations of the localization factor and the validity of S as a measure of sensitivity.

Monte Carlo simulations were performed in the following manner. A series of random transfer matrices representing the bays of a finite, cyclic assembly were generated, based on a random sequence, δ_i, from a random number generator. We call the resulting assembly one *realization* of mistuning. The matrices were multiplied together and transformed into wave coordinates, as explained in Section 6, yielding the wave transfer matrix for the mistuned assembly (see Eq. (5.18)). The localization factor for this particular realization of an N-bay system may be calculated from,

$$\gamma_N = \frac{1}{2N} \ln \left| \frac{1}{\tau_N} \right|^2 . \tag{5.57}$$

This was repeated for a large number of realizations of the assembly and the result averaged, adding realizations until the desired accuracy had been reached. The above constitutes one Monte Carlo simulation, for a system with some set of parameters $\bar{k}_c$, $\bar{k}_d$ and $\bar{m}$ vibrating at some frequency.

One point must be made about N, the number of bays in each realization. A product of a finite number of transfer matrices does not account for the infinite number of successive reflections that occur in the bays of an infinite system. A Monte Carlo simulation based on single bay realizations, $N = 1$, would only account for direct transmission through the bay and all reflections would be truncated. A Monte Carlo simulation using two bay realizations, $N = 2$, would additionally account for the wave fractions that are reflected twice as they propagate through the assembly, but all higher order reflections would be truncated, and so on. The number of bays in each realization is especially important when localization is strong (the off diagonal terms in $\mathbf{W}_i$ are no longer very small). For the cases studied, it was found that fewer than eight bays ($N = 8$) for each realization would, for strong localization, converge to an incorrect value for the localization factor. The number of realizations required for the convergence of γ_N varied but was usually in the thousands.

Verification by Monte Carlo simulations consists of two parts. On the one hand we verify the variation of γ as a function of frequency by running a series of simulations

for a range of frequencies and plot the results along with the perturbation approximations in the passbands. The other part of the simulation process is the verification of the two perturbation solutions of γ_{mid} as a function of the sensitivity measure, S_{mid}. It is clear that both γ_{mid} and S_{mid} are functions of $\bar{k}_c$, $\bar{k}_d$ and $\bar{m}$ and may thus be parameterized with any or all of these parameters. This offers the opportunity to examine the *invariance* of the relationship between γ_{mid} and S_{mid} with respect to the system parameters, such that we would expect to obtain the same relationship no matter which of $\bar{k}_c$, $\bar{k}_d$ or $\bar{m}$ is varied. This relation should also be independent of which passband is chosen for the simulation. If this invariance is verified then the localization factor in Eqs. (5.30) and (5.47) will prove to be an extremely general tool for predicting mistuning effects when used in conjunction with the measure of sensitivity, S_{mid}.

For the Monte Carlo simulations a uniform distribution of width $2W$ was assumed for the mistuning. The standard deviation of the mistuning is $\frac{\sqrt{3}W}{3}$.

Disk Mistuning:

From the perturbation analysis, the localization factors are:

•*Weak Sensitivity*

$$\gamma_d \simeq \frac{s_d^2 k_d^2}{8k_c^2 \sin^2\sigma}, \tag{5.58}$$

$$\gamma_{d,mid} \simeq \frac{s_d^2 k_d^2}{8k_c^2}. \tag{5.59}$$

•*Strong Sensitivity*

$$\gamma_d \simeq \frac{k_c}{2\sqrt{3}s_d k_d}\left[(\beta(\sqrt{3}s_d)\ln|\beta(\sqrt{3}s_d)| - \beta(-\sqrt{3}s_d)\ln|\beta(-\sqrt{3}s_d)|\right] - 1, \tag{5.60}$$

$$\gamma_{d,mid} \simeq \ln\left|\frac{k_c}{k_d}\right| + \ln(\sqrt{3}s_d) - 1. \tag{5.61}$$

These results are plotted in Fig. 5.15 as a function of the sensitivity measure in Eq. (5.49), $S^{disk} = k_d/k_c$. Observe how the transition from the classical perturbation to the modified perturbation result, that is, from weak to strong localization, occurs at about the sensitivity value $S_{mid} \simeq 30$. Also note that the Monte Carlo results agree well with the perturbation results in the limits of strong and weak sensitivity. Figure 5.14 illustrates the validity of the perturbation approximations throughout the passbands. In Fig. 5.14(a) an excellent agreement between the simulation results and the classical perturbation solution is observed. Figure 5.14(b) demonstrates the quality of the modified perturbation solution in the passband of a very sensitive system, while the classical result grossly over-predicts the localization factor.

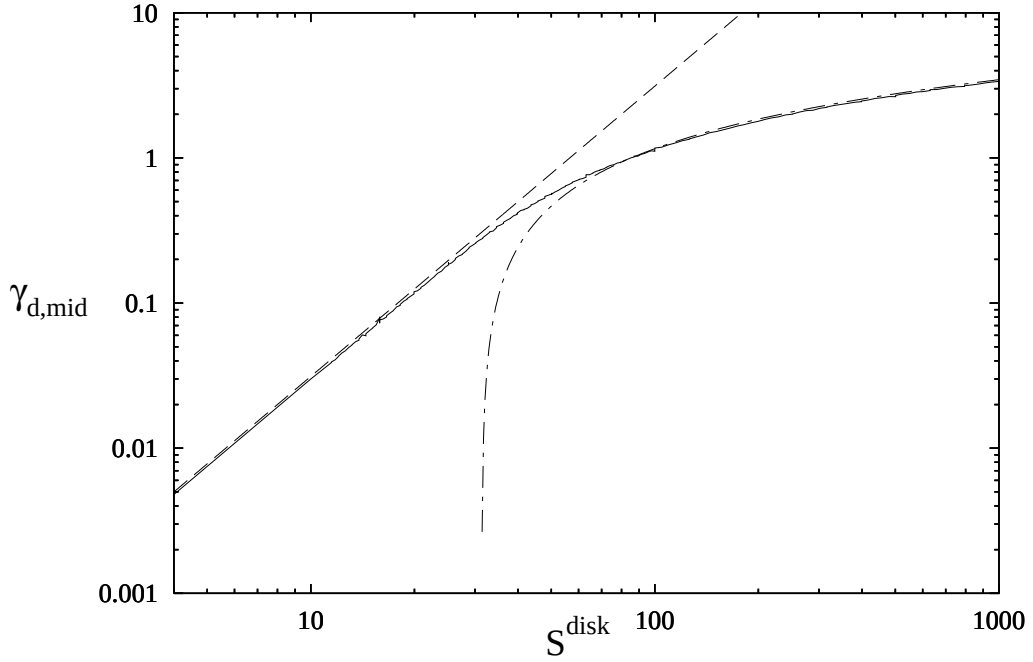

Figure 5.8 Monte Carlo simulations (———) are used to verify the invariance of Eq. (5.59) (— — –) and Eq. (5.61) (— · —) . The simulation result is a collection of data generated by varying both k_c and k_d in both passbands, with all results falling on the same curve. The standard deviation of uniform disk stiffness mistuning is 5%.

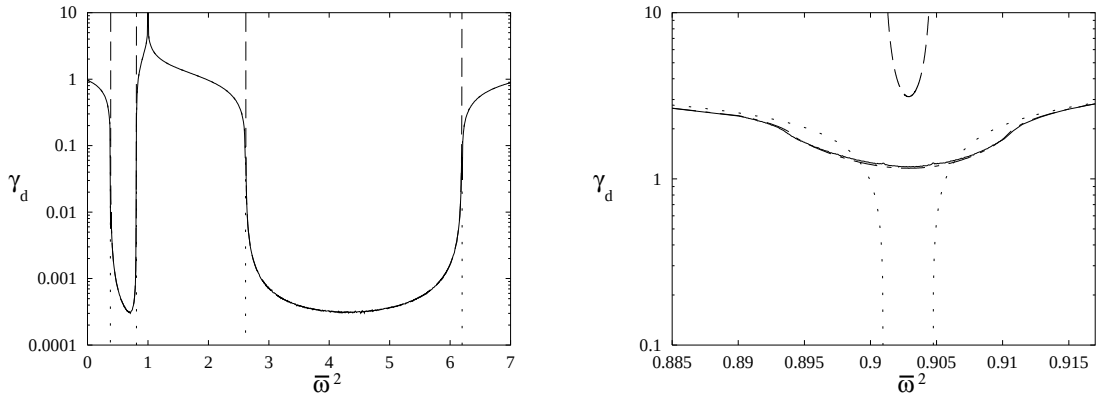

(a) $S^{disk} = 1$ (b) $S^{disk} = 100$ (1^{st} passband)

Figure 5.9 Exponential decay, γ_d, due to 5% disk stiffness mistuning *vs.* frequency. In stopbands Monte Carlo simulations (———) nearly coincide with the propagation constant for the tuned system (·····) . In (a) the simulations results overlap the classical perturbation result (— — –) , Eq. (5.58), in the passbands. In (b) the simulation agrees with the modified perturbation result (— · —) , Eq. (5.60).

Blade Mistuning:

The perturbation analyses yield the following localization factors:

•*Weak Sensitivity*

$$\gamma_b \simeq \frac{1}{\bar{k}_c^2}\left[\frac{\bar{\omega}^2}{(1-\bar{\omega}^2)}\right]^4 \frac{s_b^2}{8\sin^2\sigma} \tag{5.62}$$

$$\gamma_{b,mid} \simeq \frac{s_b^2}{128\bar{k}_c^2}\left[2\bar{k}_c+\bar{k}_d-\bar{m}-1\pm\sqrt{\left[2\bar{k}_c+\bar{k}_d+\bar{m}+1\right]^2-4\bar{m}\left[\bar{k}_d+2\bar{k}_c\right]}\right]^4 \tag{5.63}$$

where the plus and the minus signs denote the first and the second passband, respectively.

•*Strong Sensitivity*

$$\begin{aligned}\gamma_b \simeq & \frac{(1-\bar{\omega}^2)\beta_o \ln\left|\frac{\beta(\sqrt{3}s_b)}{\beta(-\sqrt{3}s_b)}\right|}{2\sqrt{3}s_b\left(\beta_o+\frac{\bar{\omega}^4}{\bar{k}_c(1-\bar{\omega}^2)}\right)}+\frac{\ln\left|\beta(\sqrt{3}s_b)\beta(-\sqrt{3}s_b)\right|}{2} \\ & -\frac{\bar{\omega}^4\ln\left|\frac{1-\bar{\omega}^2+\sqrt{3}s_b}{1-\bar{\omega}^2-\sqrt{3}s_b}\right|}{2\bar{k}_c\sqrt{3}s_b\left(\beta_o+\frac{\bar{\omega}^4}{\bar{k}_c(1-\bar{\omega}^2)}\right)}\end{aligned} \tag{5.64}$$

$$\begin{aligned}\gamma_{b,mid} \simeq & \ln\left|\frac{1}{4\bar{k}_c}\left[2\bar{k}_c+\bar{k}_d-\bar{m}-1\pm\sqrt{\left[2\bar{k}_c+\bar{k}_d+\bar{m}+1\right]^2-4\bar{m}\left[\bar{k}_d+2\bar{k}_c\right]}\right]^2\right| \\ & +\ln(\sqrt{3}s_b)-1\end{aligned} \tag{5.65}$$

with the same sign convention as above.

Figure 5.10 illustrates the transition from the classical perturbation approximation of the mid-band localization factor to that obtained by the modified perturbation approach. The sensitivity measure, S_{mid}^{blade} (Eq. (5.52)), is affected by all parameters, $\bar{m}$, $\bar{k}_c$ and $\bar{k}_d$ as well as the passband number. Figure 5.10 contains three Monte Carlo simulation curves, each obtained by varying a different system parameter. These curves overlap nearly perfectly (except for a slight discrepancy at very high sensitivity) and they also agree closely with the corresponding simulation curve in Fig. 5.15 for disk stiffness mistuning. This suggests that $S = \beta'(0)$ is indeed highly suitable as a *universal* measure of sensitivity, at least for mono-coupled systems.

Figure 5.11 shows the exponential attenuation as a function of frequency in a system that has low sensitivity in the second passband but high first passband sensitivity. In the second passband the classical perturbation solution provides an excellent prediction of weak localization. In the first passband the modified perturbation approach

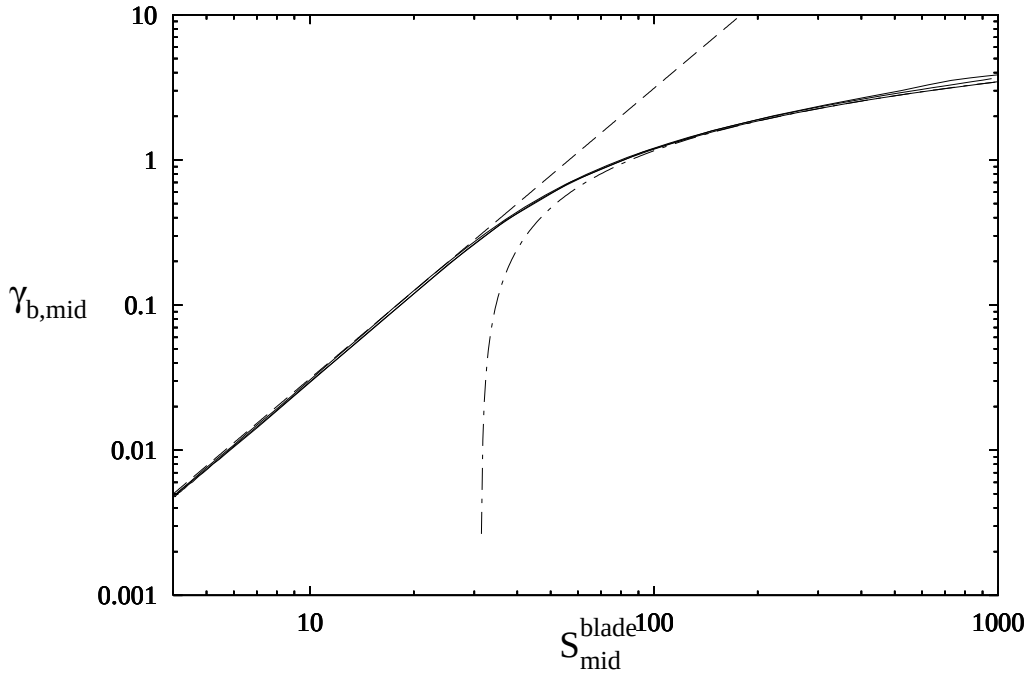

Figure 5.10 Monte Carlo simulations (———) are used to verify Eq. (5.63) (— — -) and Eq. (5.65) (— · —) . Multiple Monte Carlo simulations are obtained by varying $\bar{m}$ in 1st passband, $\bar{k}_d$ in 2nd passband and $\bar{k}_c$ in 1st passband. The standard deviation of blade stiffness mistuning is 5%. Note the near overlap of the various Monte Carlo results.

matches the simulated results, thereby confirming the strong localization approximation.

Coupling Spring Mistuning:

•*Weak Sensitivity*, from Eq. (5.39)

$$\gamma_c \simeq \frac{2-\beta_o}{2+\beta_o}\frac{s_c^2}{2} \tag{5.66}$$

$$\gamma_{c,mid} \simeq \frac{s_c^2}{2} \tag{5.67}$$

•*Strong Sensitivity* is never obtained through mistuning of $\bar{k}_c$.

In Fig. 5.12 we observe the excellent agreement between the classical perturbation result and the Monte Carlo simulations in the case of spring mistuning. This was evidenced for all other parameter values, which confirms the lack of high sensitivity to spring mistuning. It is interesting to note that the localization factor vanishes at the left passband edge. This is reasonable since at that frequency no stretching of the coupling spring occurs and mistuning of the spring stiffness is inconsequential.

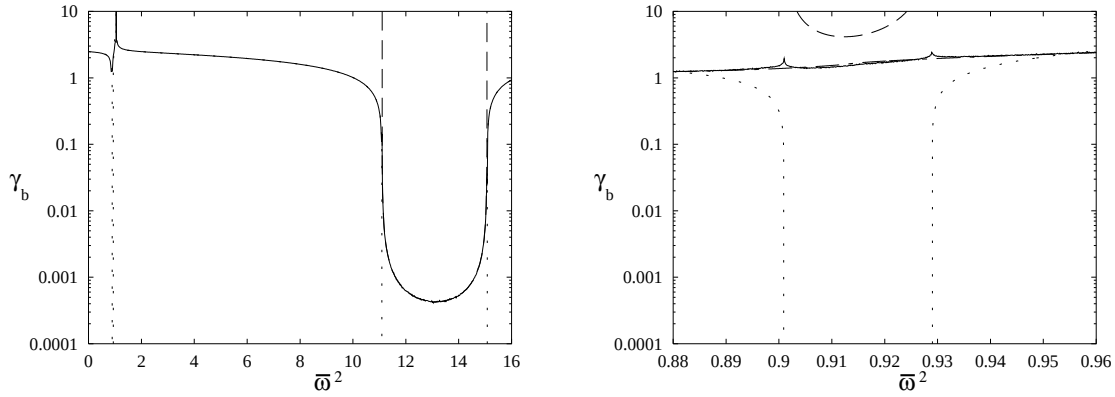

(a) $S^{blade}_{mid_2} \simeq 1.2$ (b) $S^{blade}_{mid_1} \simeq 123$ (1st passband)

Figure 5.11 Exponential decay, γ_b, due to 5% blade stiffness mistuning *vs.* frequency. In stopbands Monte Carlo simulations (———) agree with the propagation constant for the tuned system (· · · · · · ·). In (a) the simulations results overlap the classical perturbation result (— — –), Eq. (5.62), in the 2nd passband. In (b) the simulation agrees with the modified perturbation result (— · —), Eq. (5.64).

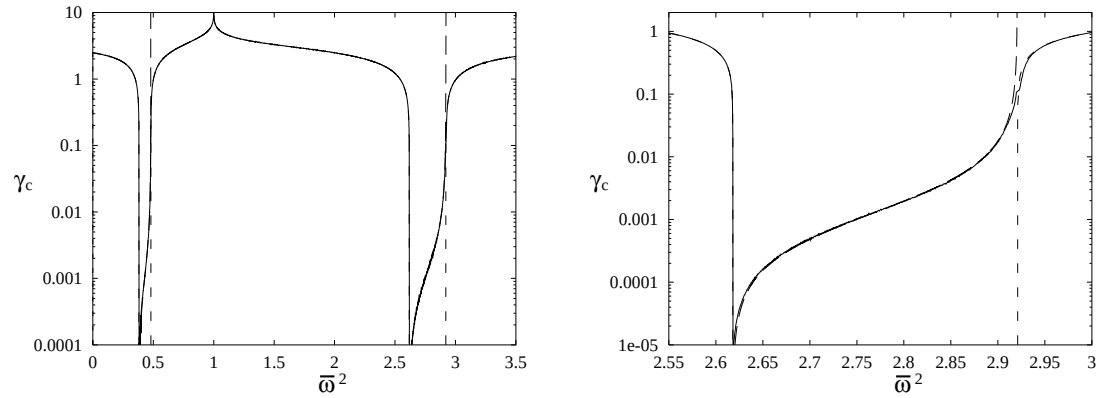

(a) $\bar{k}_d = 1.\ \bar{k}_c = 0.1\ \bar{m} = 1.$ (b) $\bar{k}_d = 1.\ \bar{k}_c = 0.1\ \bar{m} = 1.$ (detail)

Figure 5.12 Localization factor as a function of frequency in a system with coupling spring stiffness mistuning of standard deviation 5%. Results from Monte Carlo simulations (———) agree with the classical perturbation solution (— — –) in the passband and with the tuned system's propagation constant (– – –) in the stopbands. Note the lack of localization at the left passband edges and the very weak localization throughout the passbands.

5.3. Localization in Mistuned Bi-Coupled Assemblies

As stated above, localization factor approximations are not yet obtainable for assemblies with more than one coupling coordinate, hence not permitting an in-depth study of localization in the bi-coupled assembly. In Section 5.1 we have observed how the

introduction of an additional coupling coordinate introduces a second wave channel in the assembly but that it is not until the associated non-adjacent coupling stiffness is sufficiently strong ($\alpha < 4$) that the additional wave channel is capable of energy-carrying motion. This suggests that localization results obtained for mono-coupled mistuned assemblies may be applicable to bi-coupled ones as long as there are no frequency passbands associated with the additional wave type. In the following we attempt to draw qualitative conclusions about the effect of the additional coupling coordinate through the study of the example system in Fig. 3.13.

5.3.1. Effects of Bi-Coupling on Modal Structure

Explain how we will attempt to use the modal structure to get ideas about the mistuning effects.

The Mono-Coupled Assembly

From Eqs. (5.3) and (3.4), one obtains

$$\frac{\beta_o(\bar{\omega}_n^p)}{2} \pm \sqrt{\left(\frac{\beta_o(\bar{\omega}_n^p)}{2}\right)^2 - 1} = e^{j2\pi(n-1)/N} \qquad \begin{matrix} n = 1,\ldots,N \\ p = 1,\ldots,P \end{matrix}, \tag{5.68}$$

where N is the number of blades and P is the number of degrees of freedom per blade. This simplifies as

$$\beta_o(\bar{\omega}_n^p) = 2\cos\sigma_n \qquad \begin{matrix} n = 1,\ldots,N \\ p = 1,\ldots,P, \end{matrix} \tag{5.69}$$

yielding P natural frequency solutions for each value of the interblade phase angle, hence $N \times P$ natural frequencies for the assembly. From Eq. (5.69) one can easily show that all natural frequencies are double, except those corresponding to $\sigma_1 = 0$ and, if N is even, those corresponding to $\sigma_{(N+2)/2} = \pi$. Also, Eq. (5.69) indicates that $-2 \le \beta_o \le 2$, hence the natural frequencies belong to the assembly's passbands (see Eq. (5.6)), with N frequencies for each of the P passbands.

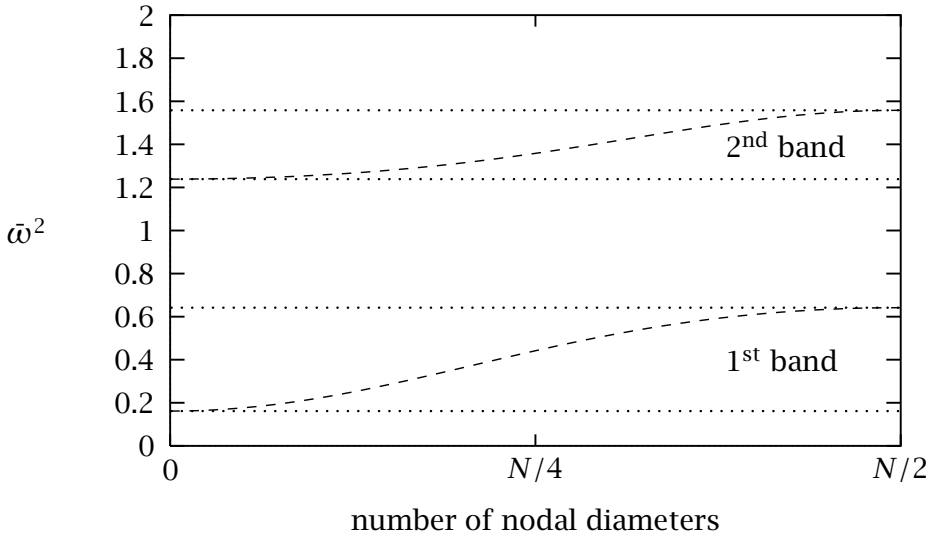

Figure 5.13 Natural frequencies as a function of the number of nodal diameters, for both passbands of the system in Fig. 3.4 with $\bar{k}_c = \bar{k}_d = 1$ and $\bar{m} = 5$.

Example

Turning our attention to the system of Fig. 3.4, we have, from Eqs. (5.69) and (3.31)

$$\beta(\bar{\omega}_n) = 2 + \frac{\bar{k}_d}{\bar{k}_c} - \frac{\bar{\omega}_n^2}{\bar{k}_c(1-\bar{\omega}_n^2)} - \frac{\bar{m}\bar{\omega}_n^2}{\bar{k}_c} = 2\cos\sigma_n, \tag{5.70}$$

which when solved for $\bar{\omega}_n^2$ yields

$$\bar{\omega}_n^2 = \frac{\bar{m} + K(n) + 1 \pm \sqrt{(\bar{m} + K(n) + 1)^2 - 4\bar{m}K(n)}}{2\bar{m}} \tag{5.71}$$

where the minus sign yields values in the first passband and the plus sign gives second passband frequencies. In Eq. (5.71), $K(n)$ denotes the associated modal stiffness of the disk

$$K(n) = \bar{k}_d + 2\bar{k}_c\,(1 - \cos\sigma_n) \tag{5.72}$$

where σ_n is the interblade phase angle of the nth mode in each of the passbands, given in Eq. (3.5). $K(n)$ increases from k_d to $k_d + 4k_c$ as the interblade phase angle varies from 0 to π.

It is customary to plot the natural frequency distribution against the number of nodal diameters. This gives an indication of the number of natural frequencies per unit frequency, *the modal density*, in a given frequency range. In Figure 5.13 this is

done for $\bar{m} = 5$, $\bar{k}_d = 1$ and $\bar{k}_c = 1$. An interesting feature, sometimes overlooked, is that the curves have local extrema at zero and $N/2$, hence the modal density is greatest at passband edges. The natural frequencies increase monotonically as the number of nodal diameters increases from 0 to $N/2$ and possess no other extrema.

It should also be noted that the natural frequency function of nodal diameters is the inverse of the interblade phase angle function of frequency illustrated in Fig. 5.1.

The Bi-Coupled Assembly

Equations (3.4), (5.10) and (5.11) yield the set of frequency equations

$$\begin{aligned} -\frac{1}{4}\Big[\alpha - \kappa \pm \sqrt{(\alpha-\kappa)^2 - 16}\Big] &= e^{j2\pi(n-1)/N} \\ -\frac{1}{4}\Big[\alpha + \kappa \pm \sqrt{(\alpha+\kappa)^2 - 16}\Big] &= e^{j2\pi(n-1)/N} \end{aligned} \qquad n = 1, \ldots, N. \tag{5.73}$$

or

$$-\frac{\alpha(\bar{\omega}) - \kappa(\bar{\omega})}{4} = \cos\sigma_n \tag{5.74}$$

$$-\frac{\alpha(\bar{\omega}) + \kappa(\bar{\omega})}{4} = \cos\sigma_n \tag{5.75}$$

with σ_n given by (3.5). Equations (5.74) and (5.75) will yield a total of $N \times P$ natural frequencies corresponding modes of type (L_1, R_1) and (L_2, R_2) respectively.

Example

Solving Eqs. (5.74) and (5.75) for the system in Fig. 3.13 yields

$$\bar{\omega}_n^2 = \frac{\bar{m} + K(n) + 1 \pm \sqrt{(\bar{m} + K(n) + 1)^2 - 4\bar{m}K(n)}}{2\bar{m}} \tag{5.76}$$

where

$$K(n) = \bar{k}_d + 2\bar{k}_{c1}(1 - \cos\sigma_n) + 2\bar{k}_{c2}(1 - \cos 2\sigma_n), \tag{5.77}$$

is the modal stiffness of the disk for the modes of interblade phase angle σ_n. Note that the expressions of the natural frequencies of the mono-coupled system, Eqs. (5.71) and (5.72), and of the bi-coupled system, Eqs. (5.76) and (5.77), are similar, except for the modal disk stiffness, $K(n)$, which is modified by the additional coupling spring. As was the case with the mono-coupled system (Eq. (5.72)), $K(n)$ has values k_d and $k_d + 4k_c$ at the interblade phase angles 0 and π, respectively. The effect of k_{c2} on $K(n)$ occurs only between $\sigma = 0$ and $\sigma = \pi$ and is largest for $\sigma = \pi/2$. The consequence is that whereas the natural frequencies of the mono-coupled system increase monotonically, we find that Eq. (5.76) may possess a maximum at an interblade phase angle given by

$$\cos\sigma = -\frac{k_{c1}}{4k_{c2}} \tag{5.78}$$

which has no solution when $\alpha = k_{c1}/k_{c2} > 4$. Recall that the frequency function in Eq. (5.76) is the inverse of the dispersion relation in the passbands plotted in Figs. 5.2 and 5.3. The maximum of Eq. (5.76) thus corresponds to the frequency of transition from passband to complexband in Figs. 5.2 and 5.3. The location of the maximum varies from $\sigma = \pi$ to $\sigma = \frac{\pi}{2}$ as $\alpha = \frac{k_{c1}}{k_{c2}}$ varies from 4 to zero. Its occurrence as α becomes smaller than 4 signifies the birth of passbands for the second wave type, as discussed in section 3.2.

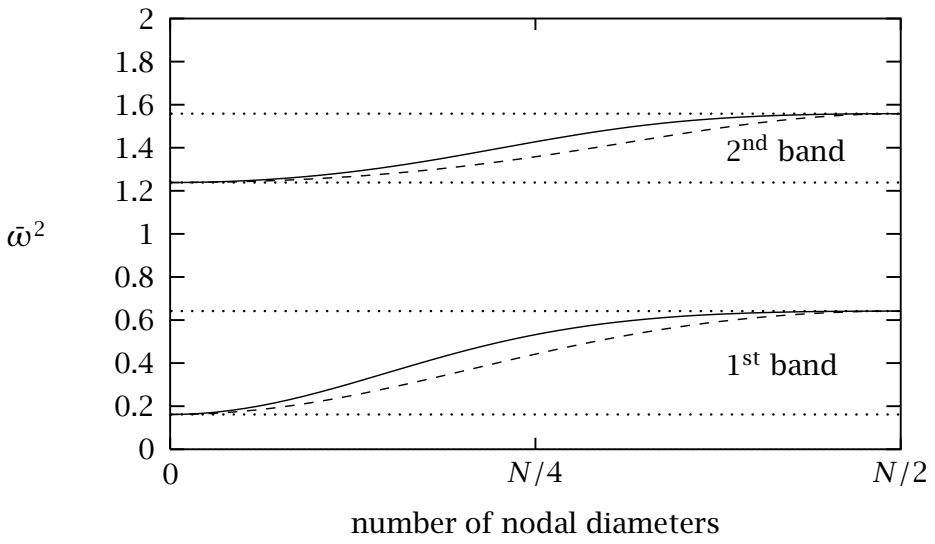

Figure 5.14 Natural frequencies as a function of the number of nodal diameters, for both passbands of the system in Fig. 3.13 with $\bar{m} = 5$, $\bar{k}_d = \bar{k}_{c1} = 1$ and $\bar{k}_{c2} = 0.2$ (———)The natural frequency curve for the mono-coupled system with $\bar{m} = 5$, $\bar{k}_d = \bar{k}_c = 1$ (– – –)is shown for comparison. Passband edges are denoted by (· · · · ·).

Figure 5.14 displays the natural frequencies in both passbands as a function of the number of nodal diameters for $\bar{k}_{c1} = 1$ and $\bar{k}_{c2} = 0.2$, *i.e.*, the coupling between nearest neighbors is five times stronger then the coupling between bays that are separated by one bay ($\alpha = 5$). In this case there are no passbands for the second wave type (see Eq. (5.15) and Fig. reffigs) and thus all normal modes are associated with the first wave type. Furthermore, since for $\alpha = 5$ the passband edges occur for $\sigma = 0$ and π (see Fig. 5.3) and since the corresponding natural frequencies are independent of the non-adjacent coupling stiffness, k_{c2} (see Eq. (5.77)), the bi-coupled system and the mono-coupled assembly feature the same frequency passbands, as depicted in Fig. 5.14. Note, however, that the variation of the natural frequencies with the interblade phase

angle, or the number of nodal diameters, is different for the mono- and bi-coupled systems, though it is monotonous in both cases. In particular, the modal density of the bi-coupled system is larger for the higher numbers of nodal diameters.

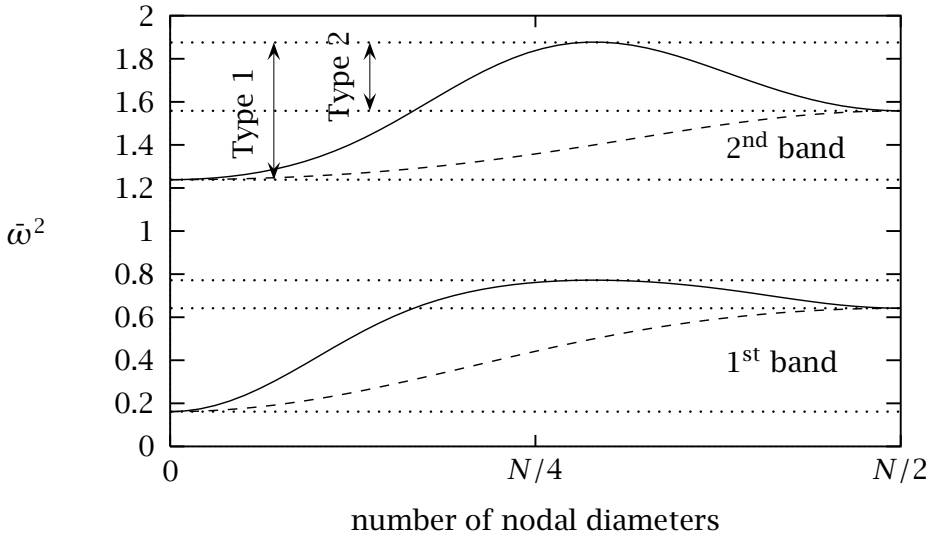

Figure 5.15 Natural frequencies as a function of the number of nodal diameters, for both passbands of the system in Fig. 3.13 with $\bar{m} = 5$ and $\bar{k}_d = \bar{k}_{c1} = \bar{k}_{c2} = 1$ (———)The natural frequency curve for the mono-coupled system with $\bar{m} = 5$, $\bar{k}_d = \bar{k}_c = 1$ (– – –)is shown for comparison. Passband edges for the two wave types are denoted by (· · · · ·).

Figure 5.15 shows the natural frequencies in both passbands as a function of the number of nodal diameters for $\bar{k}_{c1} = 1$ and $\bar{k}_{c2} = 1$, hence $\alpha = 1$. Since k_{c2} is greater than $k_{c1}/4$, Eqs. (5.14) and (5.15) indicate that passbands must exist for both wave types. Indeed, we observe in Fig. 5.15 the widening of the passbands for the type-one wave and the appearance of passbands for the second wave type (this can also be seen in Fig. 5.2). Apparent in Fig. 5.15 is the non-monotonous variation of the natural frequencies with the number of nodal diameters, as predicted by Eq. (5.78). The maxima shown in Fig. 5.15 — one for each passband — would occur for all values of $\alpha < 4$. On each frequency curve, the maximum separates the normal modes that are associated with each type of wave: the modes that feature a number of nodal diameters (or an interblade phase angle) that is smaller than that of the maximum belong to the first wave type, while those whose interblade phase angle is larger than that of the maximum are associated with the second wave type. This is also evidenced in Fig. 5.2. Clearly the number of free vibration modes associated with the second wave type increases with

the stiffness k_{c2}. From Eq. (5.78) it may be seen that as $k_{c2} \to \infty$, the location of the peak frequency goes to $\sigma = \pi/2$ ($n = N/4$), at which point the number of modes of type 1 equals (approximately) that of type 2.

It is important to note that when k_{c2} becomes greater than $k_{c1}/4$, that is, when the non-adjacent coupling spring stiffness becomes sufficiently large, the dynamic characteristics of the bi-coupled system become qualitatively different from those of the mono-coupled assembly. In these cases the adjacent coupling assumption may not be valid.

5.3.2. Mistuning Sensitivity and Modal Density

A study of the natural frequencies of the system in Fig. 3.13 demonstrated how the introduction of the non-adjacent coupling spring initially causes an increase in modal density at the upper passband edge while not affecting the passband width (see Fig. 5.14). Increasing k_{c2} (or decreasing α) beyond $k_{c1}/4$ (or below $\alpha = 4$) causes an increase in passband width and a subsequent decrease in modal density, as shown in Fig. 5.15.

Perturbation methods for the eigenvalue problems have been used previously to predict the effects of mistuning on the free dynamics of periodic structures [26, 58]. Since the second-order eigenvalue perturbations due to mistuning are inversely proportional to the distance between the tuned eigenvalues, it results that the sensitivity to mistuning, and thus localization effects, typically increase as the modal density of the tuned assembly increases. Using this result we make the following predictions about the influence of the non-adjacent coupling spring k_{c2} on the sensitivity to mistuning.

• In the range $0 < k_{c2} < k_{c1}/4$, modal density at the upper edge of the passbands (where mistuning sensitivity is the greatest) is increased compared to the mono-coupled system, causing an increase in mistuning sensitivity beyond what is predicted by the mono-coupled analysis. The modal density reaches a maximum when $k_{c1}/k_{c2} = 4$.

• For $k_{c2} > k_{c1}/4$, the modal density in the neighborhood of natural frequency of the $N/2$ interblade phase angle modes (previously the upper passband edge) decreases. Also, a widening of the passband occurs with a corresponding decrease in modal density throughout the passband, and a subsequent decrease in sensitivity to mistuning.

Localized modes provide ample evidence of this behavior. As an example, we examine the modes of vibration of a 100-blade mistuned system with $\bar{m} = 5$, $\bar{k}_d = 1$ and $\bar{k}_{c1} = 1$. For a given random mistuning pattern, we follow mode shapes occurring at $\bar{\omega}^2 \simeq 0.644$, as $\bar{k}_{c2}$ is increased from 0 to 1. This frequency is located just below the

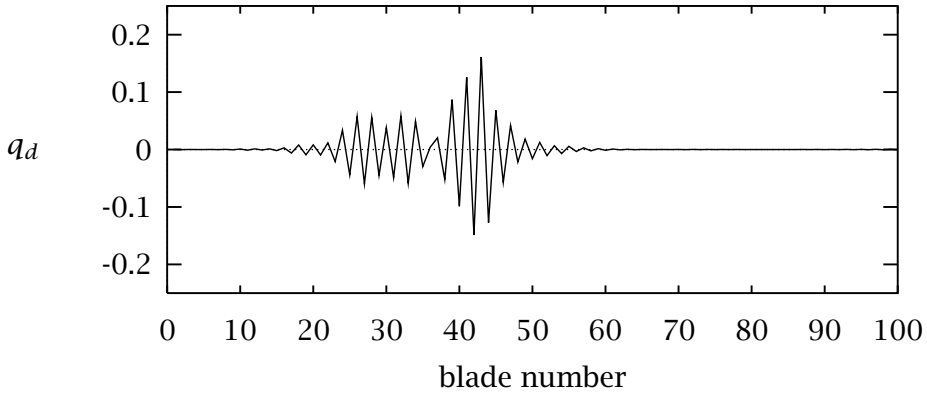

Figure 5.16 Mode 98 in a 100-blade mono-coupled assembly with natural frequency $\bar{\omega}^2 = 0.6439$. $\bar{m} = 5$, $\bar{k}_d = 1$ and $\bar{k}_c = 1$. The standard deviation of mistuning is 8%

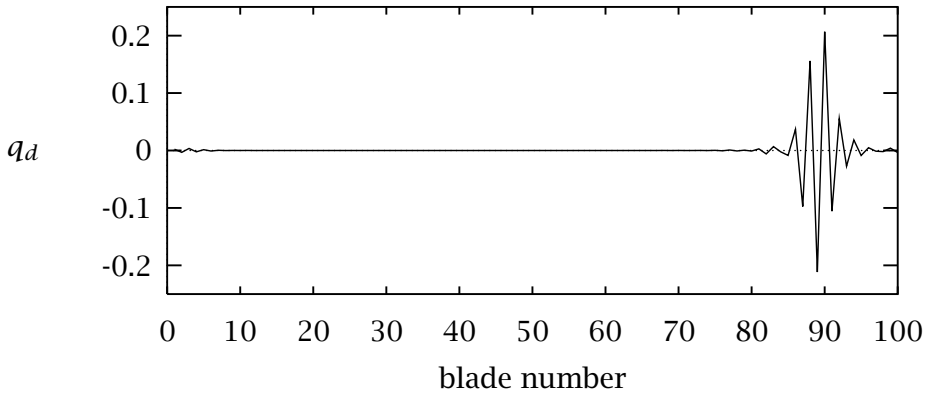

Figure 5.17 Mode 92 in a 100-blade bi-coupled assembly with natural frequency $\bar{\omega}^2 = 0.6439$. $\bar{m} = 5$, $\bar{k}_d = 1$, $k_{c1} = 1$ and $k_{c2} = 0.2$. The standard deviation of mistuning is 8%

upper edge of the first passband of the mono-coupled system and thus corresponds to the maximum localization in the mono-coupled system.

The modes studied are depicted in Figs. 5.16-5.19. The localization effect of mistuning is evident for both mono- and bi-coupled systems. Comparing Fig. 5.16 with Fig. 5.17, as $\bar{k}_c$ is increased from 0 to 0.2 the increased modal density causes increased localization. A further increase to $\bar{k}_{c2} = 0.4$ results in weaker localization, to a strength lower than that of the mono-coupled system. For $\bar{k}_{c2} = 1$, localization at $\bar{\omega}^2 \simeq 0.644$ has all but vanished. A more accurate examination of these four mode shapes is pos-

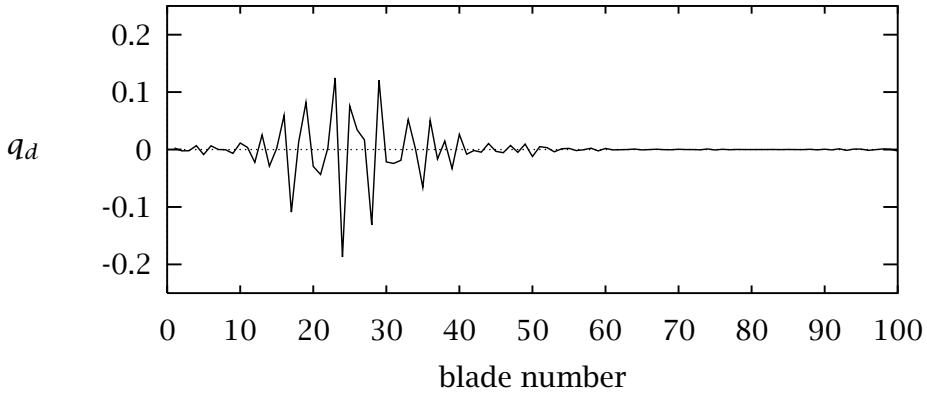

Figure 5.18 Mode 73 in a 100-blade bi-coupled assembly with natural frequency $\bar{\omega}^2 = 0.6446$. $\bar{m} = 5$, $\bar{k}_d = 1$, $k_{c1} = 1$ and $k_{c2} = 0.4$. The standard deviation of mistuning is 8%

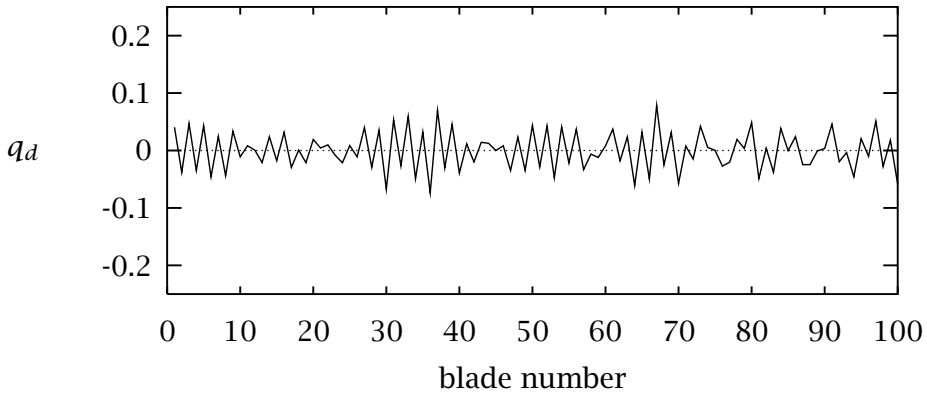

Figure 5.19 Mode 40 in a 100-blade bi-coupled assembly with natural frequency $\bar{\omega}^2 = 0.6448$. $\bar{m} = 5$, $\bar{k}_d = 1$, $k_{c1} = 1$ and $k_{c2} = 1$. The standard deviation of mistuning is 8%

sible by plotting the absolute value of the displacement of each mode on a logarithmic scale and aligning the mode peaks. Figure 5.20 demonstrates that the behavior of the rate of decay as k_{c2} increases is as outlined above.

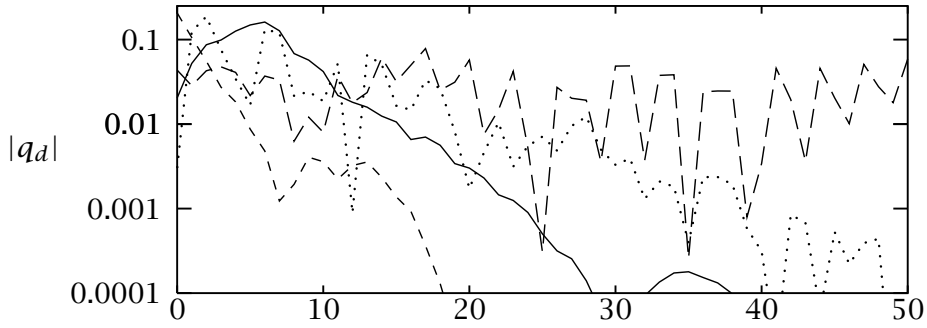

Figure 5.20 Comparison of amplitude decay for mistuned modes with natural frequency $\bar{\omega}^2 \simeq 0.644$. The absolute value of the blade displacement is plotted on a logarithmic scale with the mode peaks aligned. Mono-coupled (———), $\alpha = 5$ (− − −), $\alpha = 2.5$ (· · · · ·), $\alpha = 1$ (— —).

5.4. Conclusion

Wave propagation of mistuned mono- and bi-coupled blade assemblies were studied using a transfer matrix approach. A mono-coupled assembly may be modeled using a 2×2 transfer matrix whereas the bi-coupled system requires a 4×4 transfer matrix.

The theory of wave propagation in multi-coupled periodic structures was reviewed and detailed for the mono- and bi-coupled assemblies. The study identified that if coupling of neighboring blades is more than four times stronger than the coupling of blades separated by one blade, then the wave propagation properties of the mono- and bi-coupled assemblies are qualitatively the same.

A comprehensive methodology for quantifying localization effects in general mono-coupled systems was presented and a measure of mistuning sensitivity was presented. An investigation of an example system revealed the sensitivity measure to be a reliable universal way of quantifying mistuning sensitivity in a mono-coupled system.

A study of the natural frequency distribution of the mono- and bi-coupled assemblies revealed that mistuning sensitivity, as predicted by an analysis of a mistuned mono-coupled system, may initially increase when non-adjacent bay coupling is introduced. Sensitivity was found to reach a maximum when coupling of neighboring blades is four times as strong as the coupling of blades separated by one blade. For higher values of the non-adjacent coupling, mistuning sensitivity was decreased and localization all but vanished when the non-adjacent coupling became as strong as the adjacent coupling. These conclusions were supported by the examination of the localized modes of mistuned bi-coupled systems with various levels of interblade coupling.

CHAPTER VI

STATISTICS OF FORCED RESPONSE

In the case studies of mistuned rotors presented in Chapter VII dramatic mistuning effects were expected. All the prototype rotors that were being studied featured weak interblade coupling, a property synonymous with strong mistuning sensitivity in the free response case. Free response analysis [45] predicts that sensitivity to mistuning increases monotonically as coupling is reduced. Curiously, the mistuning effects on forced respose amplitudes were weaker than expected. Furthermore, when studying the forced response of the 36 blade compressor prototype, two different engine orders of excitation lead to stronger mistuning effects in modes with stronger interblade coupling, a trend completely opposite to the trend predicted by the free response analysis. There had been some evidence [46] that forced response of assemblies with moderately weak coupling will experience larger mistuning effects than assemblies with very weak interblade coupling, but no physical insight had been obtained. Clearly, a better understanding of the effect on forced response of the localization phenomenon was needed. This chapter focuses mainly on the effect of interblade coupling on mistuned system forced response in search of a satisfactory explanation for the mechanisms that govern this behavior.

As the work presented in Chapter VII progressed, it became increasingly clear that improved tools were required if a complete insight was to be gained into the statistics of mistuning-induced magnification of the largest blade amplitude. As a consession to computational feasibility, Monte Carlo simulations were being limited to a fixed frequency for each realization of a mistuned assembly. This led to results that left many questions unanswered, and the need for a more complete analysis — in which the peak resonance response for each realization would be calculated — became obvious. This deficiency is remidied in the current work.

The analysis contained in this chapter is purely statistical. Since analytical methods for estimating the forced response statistics are not in place, a Monte Carlo sim-

ulation approach is used. Given that many uncontrollable factors, such as in-service degradation, influence blade mistuning, the authors feel strongly that small mistuning should always be treated as a random variable and that any effort to study (and perhaps optimize) deterministic mistuning patterns is misguided.

Much of the work on the statistics of mistuned system forced response found in the literature [48, 49] is focused on the response statistics of individual blades. We believe this to be an incomplete result since it does not account for the sample size, *i.e.,* the number of blades on the disk. Response statistics of mistuned bladed disks should be presented in terms of the largest amplitude of any blade of the disk, commonly called the extreme statistics. Sinha [49] in his introduction mentions how important it is for designers to know *"the probability that the largest response amplitude on any disk* [an assembly of blades] *would exceed a critical value"*, but does not address the issue in the body of the paper. We agree with Sinha that confidence intervals for the extreme statistics would be the ideal predictive tool for designers concerned with mistuning effects. All the statistical results in this paper are in terms of the largest amplitude *magnification* (or *amplification*) occurring at any frequency in any blade of a mistuned assembly. By magnification we mean the mistuning-induced increase in amplitude relative to that predicted by the tuned analysis.

In this chapter we treat the term *coupling* rather loosely as the strength of blade to blade influence. By using the simplest model of a bladed disk imaginable (see Section 3.1.2), we have a simple, single-parameter measure of coupling. We acknowledge that in real life systems coupling may be considerably more difficult to quantify. (see discussion in Section 5.2.1). However, we believe that the mechanisms governing forced response sensitivity uncovered through the use of this model should be fully applicable to more complicated models.

6.1. Extreme Statistics and Uncoupled Oscillators

To highlight some of the concepts presented in this chapter, let us look at the response of an assembly of uncoupled oscillators. In the case of no coupling the term "assembly" is, of course, a misnomer, but it will be used to refer to the set of N oscillators. Since the goal is to study the effect of coupling, the limiting case of vanishing coupling will provide a crucial foundation. Futhermore, the assumption of zero coupling is an important simplification rendering the response of the blades statistically independent. This makes it possible to analyze the statistics in closed form.

In the absence of coupling springs, a single blade in Fig. 3.2 has the equation of forced harmonic motion

$$(1+\delta_i)q - \bar{\omega}^2 q + 2j\zeta\bar{\omega}q = \bar{F}. \tag{6.1}$$

where ζ denotes the viscous damping ratio and δ_i is a random variable representing the stiffness mistuning of the ith blade. The resonance amplitude of this single-degree-of-freedom system can be easily calculated to be

$$|q|_{max} = \frac{|F|}{2\zeta\sqrt{1+\delta_i-\zeta^2}} \tag{6.2}$$

which we scale by the resonance amplitude of the corresponding tuned system ($\delta_i = 0$) to yield

$$\mathcal{A} = \frac{\sqrt{1-\zeta^2}}{\sqrt{1+\delta_i-\zeta^2}} \tag{6.3}$$

The random variable $\mathcal{A}$ denotes the magnification of the resonance amplitude due to mistuning. It is a monotonic function for the small δ_i values that are of interest here. Given a probability density function for the mistuning random variable Δ, $f_\Delta(\delta)$, we may calculate the statistics of the magnification, $\mathcal{A}$, as:

$$f_A(\mathcal{A}) = f_\Delta(\delta)\left|\frac{d\delta}{d\mathcal{A}}\right| \tag{6.4}$$

For example, if we assume that that the mistuning is uniformly distributed with standard deviation s (see Fig. 6.1), then

$$f_\Delta(\delta) = \begin{cases} 0 & \text{if } \delta < -\sqrt{3}s \\ \frac{1}{2\sqrt{3}s} & \text{if } |\delta| \le \sqrt{3}s \\ 0 & \text{if } \delta > \sqrt{3}s \end{cases} \tag{6.5}$$

and we find

$$f_A(\mathcal{A}) = \begin{cases} 0 & \text{if } A < A_{min} \\ \dfrac{1-\zeta^2}{\sqrt{3}\,s\,A^3} & \text{if } A_{min} \le \mathcal{A} \le A_{max} \\ 0 & \text{if } \mathcal{A} > A_{max} \end{cases}$$

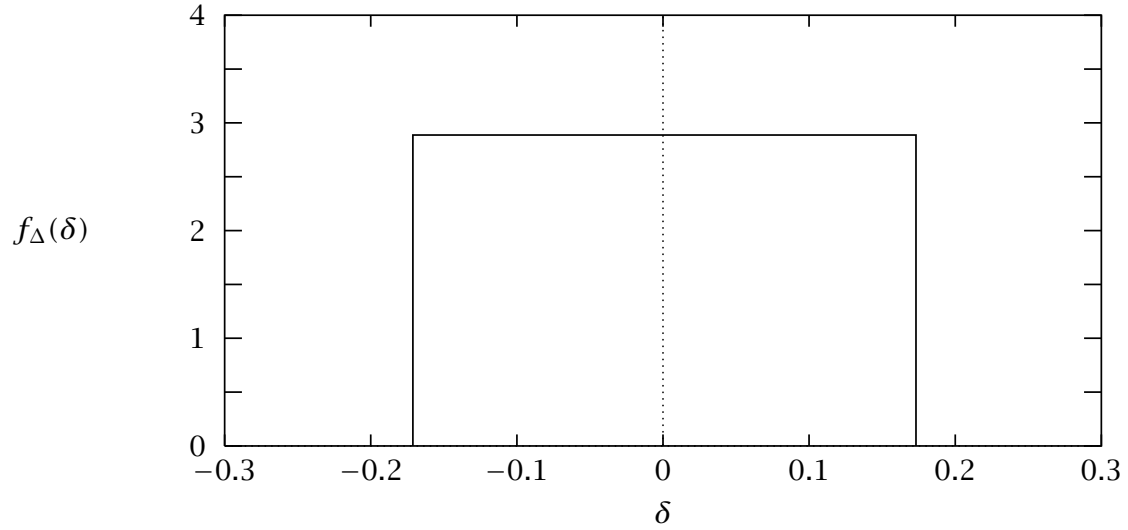

Figure 6.1 Probability density function of uniform blade mistuning with $s = 10\%$ standard deviation and zero mean.

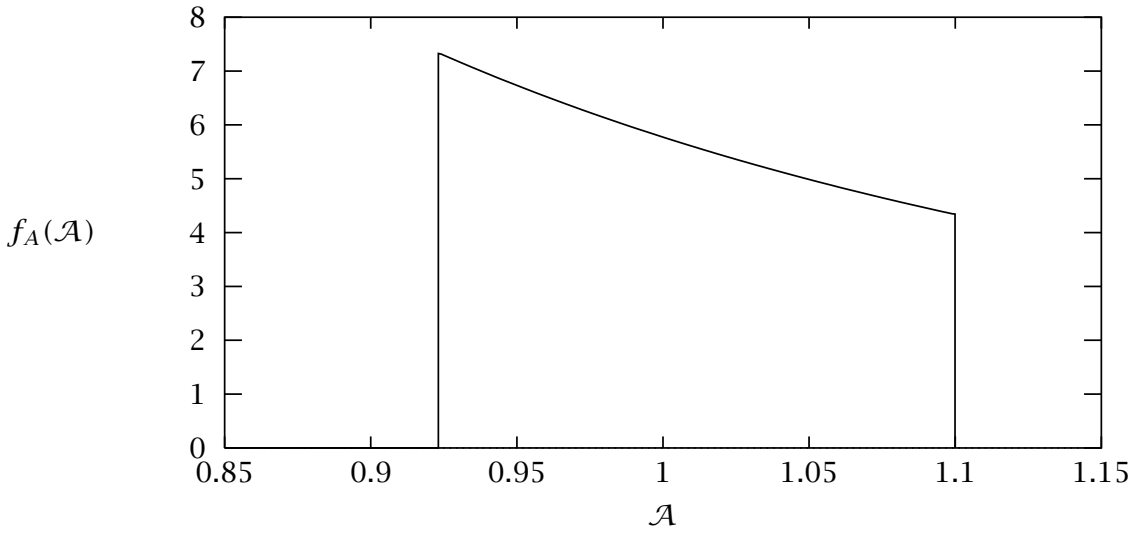

Figure 6.2 Probability density function of resonance amplitude magnification, $\mathcal{A}$, of a single oscillator that has uniform blade stiffness mistuning with 10% standard deviation.

where

$$A_{max} = \frac{\sqrt{1-\zeta^2}}{\sqrt{1-\sqrt{3}s-\zeta^2}} \qquad \text{and} \qquad A_{min} = \frac{\sqrt{1-\zeta^2}}{\sqrt{1+\sqrt{3}s-\zeta^2}}$$

The probability density function $f_A(\mathcal{A})$ is depicted in Fig. 6.2.

We are, however, much more interested in the response statistics of the one blade in an assembly of N blades that exhibits the largest resonance amplitude, at any fre-

quency. This is the subject of a field within probability theory referred to as the *"statistics of extreme values."* For a discussion of the topic the reader is referred to the classic work of Gumbel [59].

The probability distribution function of a random variable X, $F_X(x)$, corresponds to the probability that $X < x$. The probability distribution of the largest sample, X, in a set of N samples is the combined probability that $X < x$ and that all the other samples are smaller than X. Therefore, assuming that the blades are independently mistuned,

$$F_{X,N}(x) = [F_X(x)]^N \tag{6.6}$$

and the probability density function of the largest sample in a set of N samples is simply

$$f_{X,N}(x) = N\,[F_X(x)]^{N-1}\,f_X(x). \tag{6.7}$$

As an example, consider an assembly of N, uncoupled, mistuned blades like the one presented above. We find that the probability distribution function of $\mathcal{A}$ is

$$F_A(\mathcal{A}) = \frac{\zeta^2 - 1 + \mathcal{A}^2(1 + \sqrt{3}s - \zeta^2)}{2\sqrt{3}s\mathcal{A}^2} \tag{6.8}$$

and hence that the probability density function for resonance amplitude magnification in the blade with the largest amplitude is

$$f_{A,N}(\mathcal{A}) = N\left[\frac{\zeta^2 - 1 + \mathcal{A}^2(1 + \sqrt{3}s - \zeta^2)}{2\sqrt{3}s\mathcal{A}^2}\right]^{N-1}\frac{1-\zeta^2}{\sqrt{3}\,s\,\mathcal{A}^3} \tag{6.9}$$

Figure 6.3 illustrates how the number of blade, N, affects the shape of the probability density function of the extreme values. As the number of blades increases, so does the probability of a large largest amplitude. With a bigger set of samples, the chances of the set containing a large value become greater. At the same time the probability of experiencing low amplification in the blade with the largest amplitude decreases. Indeed, in a 12-blade assembly there is negligible probability that the blade with the largest amplitude has a lower amplitude than the tuned system. It is almost certain that the amplification of this blade will be between 5% and 10% greater than the tuned system.

In [45] mode localization was shown to increase monotonically with decreased interblade coupling. The extreme case of zero coupling has the individual oscillators vibrating at their natural frequencies with no participation from its uncoupled fellow blades. A mode in which only one blades vibrates would be considered fully localized. On the other hand the probability density function in Fig. 6.3 shows that for the system and mistuning type analyzed here the largest increase in peak response is only 10%.

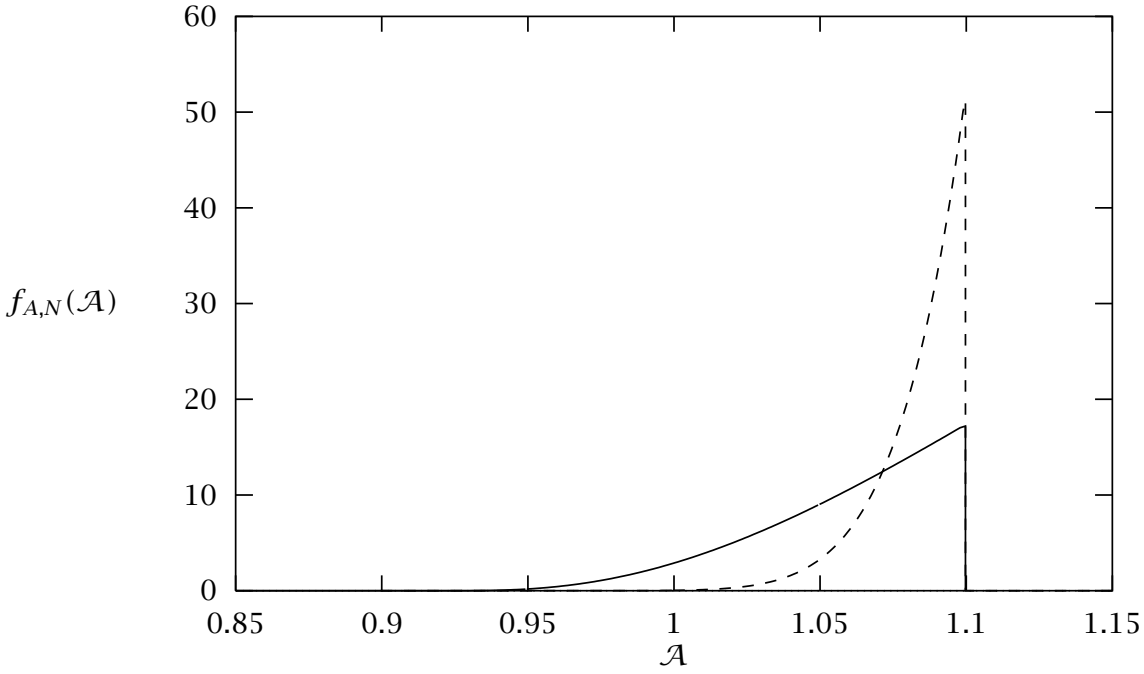

Figure 6.3 Probability density function of largest resonance amplitude magnification of an assembly of N oscillators with uniform disk stiffness mistuning with 10% standard deviation. A 4 blade assembly (———) is compared to a 12-blade assembly (− − −).

This is not a dramatic effect and is substantially lower than the 30% to 300% increases reported by various studies [24].

This surprising result raises the question as to whether mistuning effects may be contributed to by another mechanism, perhaps one that is completely different from the energy confinement mechanism that causes mode localization. We shall investigate this issue in the next section.

6.2. Coupling Effects on Forced Response Statistics

When interblade coupling is considered, analytical results for largest response statistics become tremendously difficult to obtain. Some work has been done on the response statistics of individual blades in an assembly [48, 49], but, as stated in the previous section, it is really the statistics of the blade which has the largest amplitude that are of the greatest interest. Given that information, an analyst could be provided with confidence intervals for the largest amplitude experienced by any blade in a production run of rotors. This information is not directly obtainable from the response statistics of individual blades as was done in Eqs. (6.6) and (6.7). This is because the responses of adjacent, *coupled* blades are not independent random variables and Eq. (6.6) is invalid.

However, the development of analytical methods for the extreme statistics in blade assemblies is not the goal of this work. Rather, we wish to understand the relationship between the level of interblade coupling and the statistics of largest forced response amplitudes. Therefore, for this study we will rely solely on Monte Carlo simulations.

6.2.1. Monte Carlo Simulation of Response Statistics

Monte Carlo simulations are an alternative to the analytical solution of probability density functions. An outline of Monte Carlo simulations is as follows. A mistuning pattern for one realization of a mistuned assembly is obtained using a random number generator. A frequency response analysis of this system yields the largest resonance amplitude. Note that to find this value we must sweep frequency and solve a large number of forced response problems. The largest resonance amplitude value constitutes one sample and is stored in a vector. This process is repeated until some convergence condition is met. Post-processing of the sample vector results in an approximation of the response statistics, *e.g.,* the probability density function. Clearly, this brute force method may be extremely expensive in terms of computational time. Tens of thousands of realizations may be required, each realization requiring a large number of solutions when frequency is swept to find the peak response amplitude.

In Fig. 6.4 we observe the excellent results achievable by Monte Carlo simulations if no expense is spared. The figure provides mutual verification of the analytical result in Eq. (6.9) and Monte Carlo simulation results.

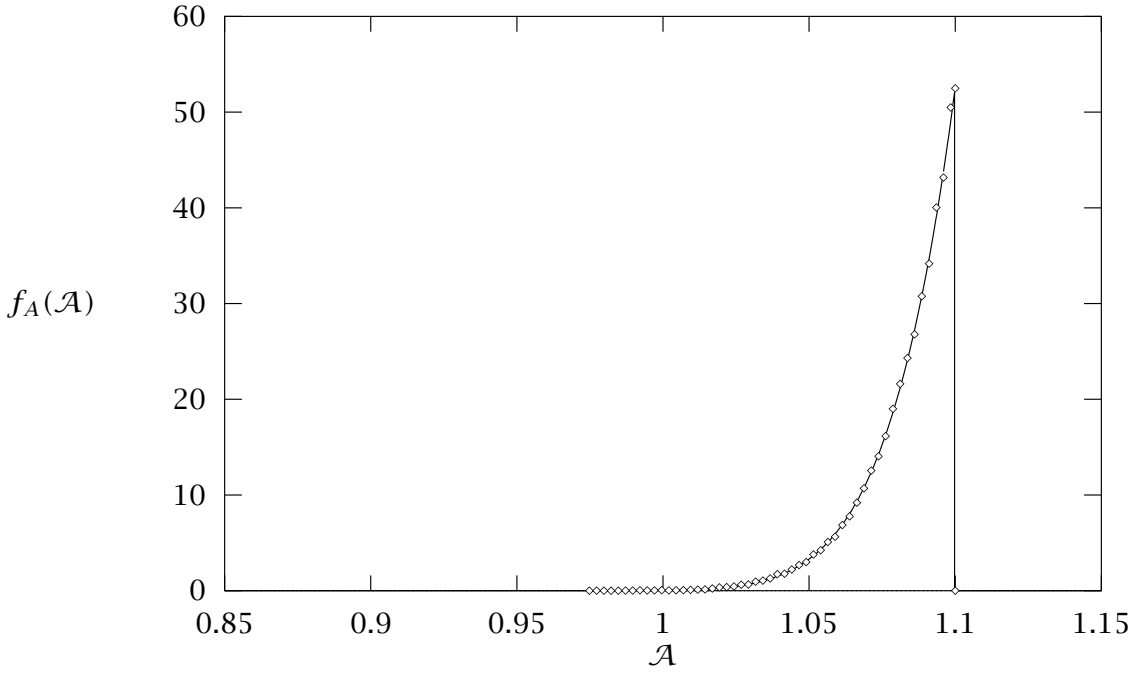

Figure 6.4 Probability density function of largest resonance amplitude magnification of an assembly of N oscillators with uniform disk stiffness mistuning with 10% standard deviation. The analytical solution for a 12-blade assembly (———) is compared to the Monte Carlo simulation of 10^5 12-blade systems ($\diamond$) .

6.2.2. Results

Figure 6.5 shows how the statistics of the largest response of the system in Fig. 3.2 evolve as the level of interblade coupling is varied. A 12-blade assembly was analyzed by Monte Carlo simulation. Of greatest importance is the curve labeled 99%. The values on this curve denote the mistuning-induced amplification of largest response that will only be surpassed by 1% of all realizations of mistuned systems. We will say that when this value deviates greatly from unity, mistuning effects are high. From the 1% curve we see that a 12-blade assembly will almost certainly experience larger amplitudes than the tuned system since the curve is above $\mathcal{A} = 1$ throughout nearly the entire range of coupling.

For high values of coupling, the effects of mistuning are weak, as predicted by the free vibration characteristics of the tuned system. When coupling is large, mistuning effects are weak and the mistuned struture possesses extended, non-localized modes [45]. This lack of sensitivity of the free response to mistuning implies small mistuning effects on the forced response. Indeed, for high coupling values the three curves

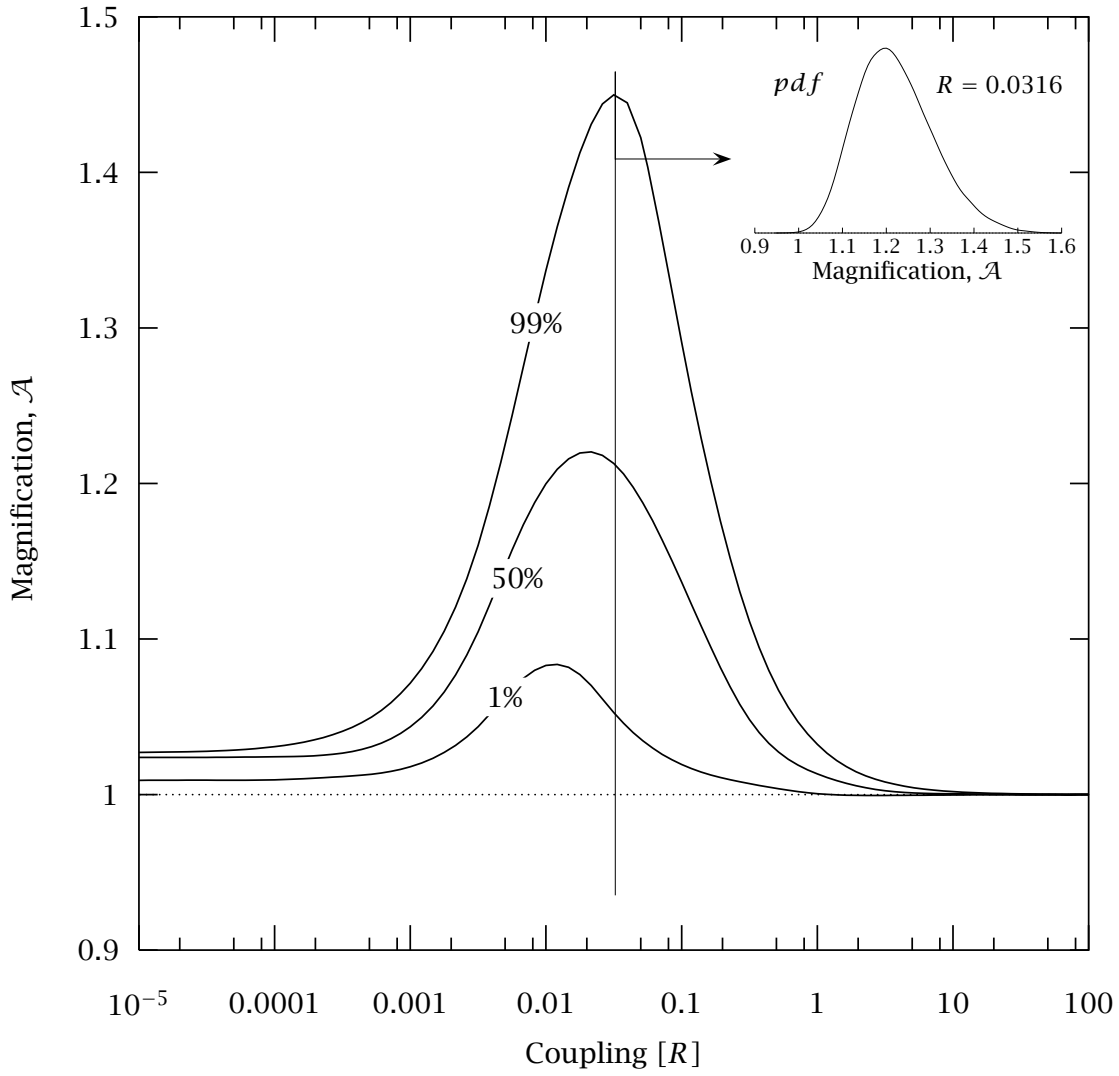

Figure 6.5 Statistics of the largest resonance amplitude magnification in a 12-blade assembly as a function of interblade coupling, R. The main plot shows the 1%, 50% and 99% percentiles of the statistics. The inserted plot shows the entire probability density function at the coupling case with the largest magnification, $R = 0.0316$. Mistuning, δ, is uniform with 3% standard deviation and excitation is engine order 3.

for the 1%, 50%, and 99% percentiles merge, signifying that the probability density function approaches a delta function, *i.e.,* the magnification, $\mathcal{A}$, approaches unity with probability one.

In the other extreme, that is, for very weak, coupling, we see the effects predicted

in Section 6.1. The probability density function for this case would be similar to the one depicted in Fig. 6.3 (except that here mistuning has 3% standard deviation instead of 10% considered earlier).

As coupling decreases from strong to weak we note a sharp increase in mistuning effects reaching a maximum for moderately weak coupling levels. For 3% mistuning the maximum occurs at $R \simeq 0.0316$, and predicts that as many as 1% of the assemblies sampled will have magnification of amplitudes in excess of 45% greater than a tuned analysis would have predicted. The inserted figure depicts the probability density function of the magnification of the largest amplitude for $R = 0.0316$. Note that it is markedly different from the one illustrated in Fig. 6.3. For instance, the probability density function now has an upper tail.

For assemblies with a different number of blades, Fig. 6.5 would change in the following way. For assemblies with fewer blades, there is an increase probability of finding assemblies with a small largest amplitude (see Fig. 6.3), and it may be likely that an assembly has a smaller largest amplitude than the tuned system's. The opposite occurs as the number of blades is increased, because with a bigger set of samples the chances of finding a large amplitude in the set becomes greater. In general, as the number of blades is increased, the 1% and 50% curves will approach the 99% curve. The 99% curve will be affected the least because the probability density beyond the 99th percentile is low and the additional samples are unlikely to fall above the 99% curve, a thereby shifting the 99th percentile.

6.2.3. Energy Flow Analysis

The behavior of mistuning effects reaching a maximum for moderate coupling has been observed before [46]. However, the mechanism at work has never been satisfactorily explained. The dynamic behavior is fully understood in the limits of strong and vanishing coupling. An assembly with strongly coupled blades features extended, unlocalized modes. Mistuning has a weak effect on the forced response of this assembly, and small mistuning-induced amplification of largest amplitude are observed. All blades vibrate with the same amplitude — vibration energy is shared equally. In Section 6.1 we observed how, in the absence of coupling the blades vibrate independently. The energy source for an isolated blade is limited to the energy contribution of the force acting on the blade. What these two cases of coupling extremes have in common is the fact that energy given to a blade through external forcing remains in that blade. Clearly, an uncoupled blade could experience greater response amplitudes if the blade could draw on the energy that is being fed to the other blades of the assembly. When interblade coupling is added to the system, this opens up a channel through

which blades can share energy. This idea prompted us to investigate the energy flow in the assembly.

For the analysis we adopt the definition of power used by Signorelli and von Flotow in [16]. The instantaneous power at a point at which a force is applied is

$$p_i(t) = \mathrm{Re}(F_i(t))\mathrm{Re}(\dot{q}_i(t))$$

where $\mathrm{Re}(F_i(t))$ is the real part of the applied force, and $\mathrm{Re}(\dot{q}_i(t))$ is the real part of the velocity of the point at which the force is applied. For harmonic motion, the *energy input* is defined as the time average of the instantaneous power over one period, $T = 2\pi/\omega$:

$$E_i = \frac{1}{T}\int_0^T p_i(t)\mathrm{d}t.$$

The energy input from the resultant force of the two springs connected to blade i is

$$\begin{aligned} E_i^s &= \frac{1}{T}\int_0^T \mathrm{Re}\left[R(q_{i+1}(t) - 2q_i(t) + q_{i-1}(t))\right]\mathrm{Re}\left[\dot{q}_i(t)\right]\mathrm{d}t \\ &= \frac{-\omega R}{T}\int_0^T \Big[(q_{i+1} - 2q_i + q_{i-1})^R \cos\omega t - (q_{i+1} - 2q_i + q_{i-1})^I \sin\omega t\Big] \\ &\qquad \Big[q_i^R \sin\omega t + q_i^I \cos\omega t\Big]\mathrm{d}t \\ &= \frac{\omega R}{2}\Big[(q_{i+1} - 2q_i + q_{i-1})^I q_i^R - (q_{i+1} - 2q_i + q_{i-1})^R q_i^I\Big] \end{aligned}$$

where the superscript s denotes that this is the energy transmitted through the *springs*.

This clearly goes to zero as the coupling R goes to zero as expected. Furthermore, as R becomes large the structure starts to behave as if it were tuned, and responds with a constant interblade-phase-angle, σ. In this case, we may write $q_i = A$, $q_{i+1} = Ae^{j\sigma}$ and $q_{i-1} = Ae^{-j\sigma}$ yielding $E_i = \frac{1}{2}\omega R(\sin(\sigma) + \sin(-\sigma)) = 0$, as expected, since the wave is perfectly transmitted through the blade.

The forcing of blade i is $\bar{f}e^{2\pi j(i-1)C/N}\, e^{j\omega t}$, where C denotes the engine order of the excitation. The energy input into the blade due to this forcing is

$$E_i^F = \frac{\omega\bar{f}}{2}\left[q_i^R \sin\frac{2\pi(i-1)C}{N} - q_i^I \cos\frac{2\pi(i-1)C}{N}\right]$$

As a measure of the contribution of the energy input into blade i through the coupling springs we define

$$\mathcal{E} = \frac{E_i^F + E_i^s}{E_i^F}.$$

Note that E is a normalized measure of energy input: the total energy given to blade i through the coupling springs and the applied external force, scaled with the energy

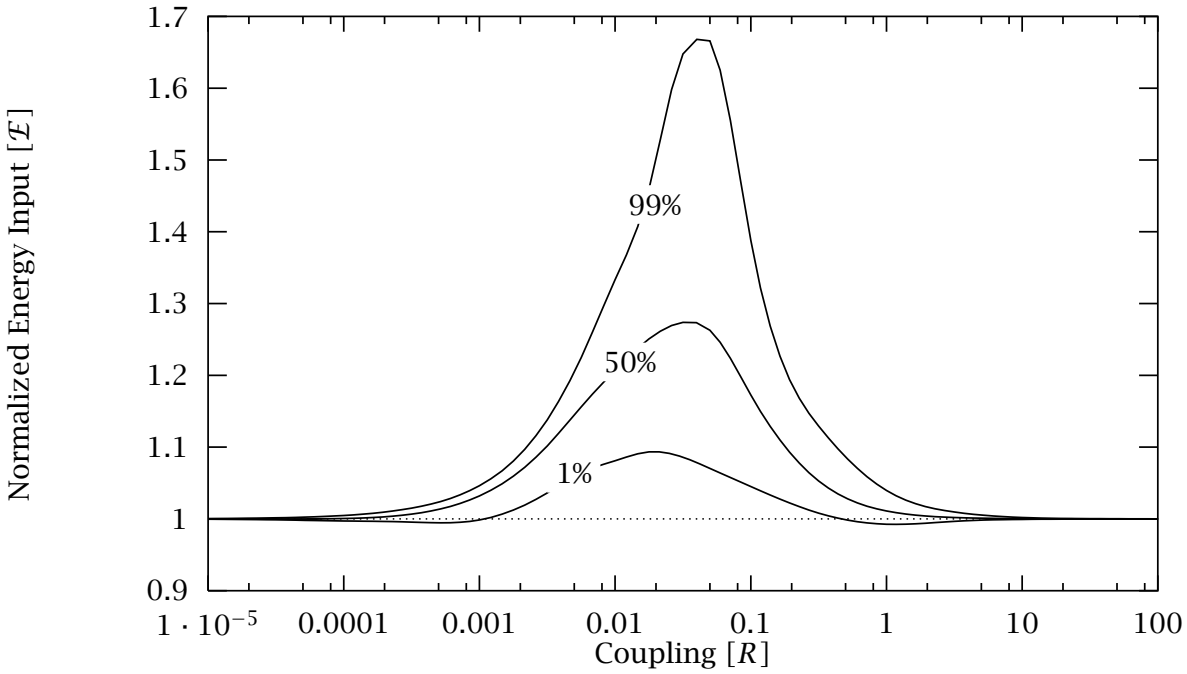

Figure 6.6 Statistics of the energy input at maximum resonance in a 12-blade assembly with 3% mistuning.

input from the blade force alone. Therefore, when there is no spring-transmitted contribution from the other blades in the system, $\mathcal{E}$ goes to unity.

Figure 6.6 depicts the statistics of $\mathcal{E}$, calculated for the blade with the largest amplitude, at resonance. The statistics were calculated by a Monte Carlo simulation, as follows. For each realization of a mistuned system the frequency was swept until the largest response of any blade at any frequency was observed. The value $\mathcal{E}$ was calculated for the largest amplitude blade at the resonance frequency. This constituted one sample from the distribution of $\mathcal{E}$. The generation of the probability density function followed the steps outlined in Section 6.2.1. The similarities of Fig. 6.6 and Fig. 6.5 are apparent. As predicted, $\mathcal{E} \to 1$ in the limits of high and low coupling. In between, we observe a sharp increase in $\mathcal{E}$ as the energy input of the force acting on the blade is augmented by as much as 70% by contributions from the other blades in the assembly. The curious occurrence of largest amplitude blades that lose energy through the springs in the neighborhood of $R = 0.001$ and $R = 1$ is most likely a numerical inaccuracy.

This proves that mistuning effects in blade assemblies undergoing engine order excitation are not governed solely by mode localization. Instead, for large mistuning

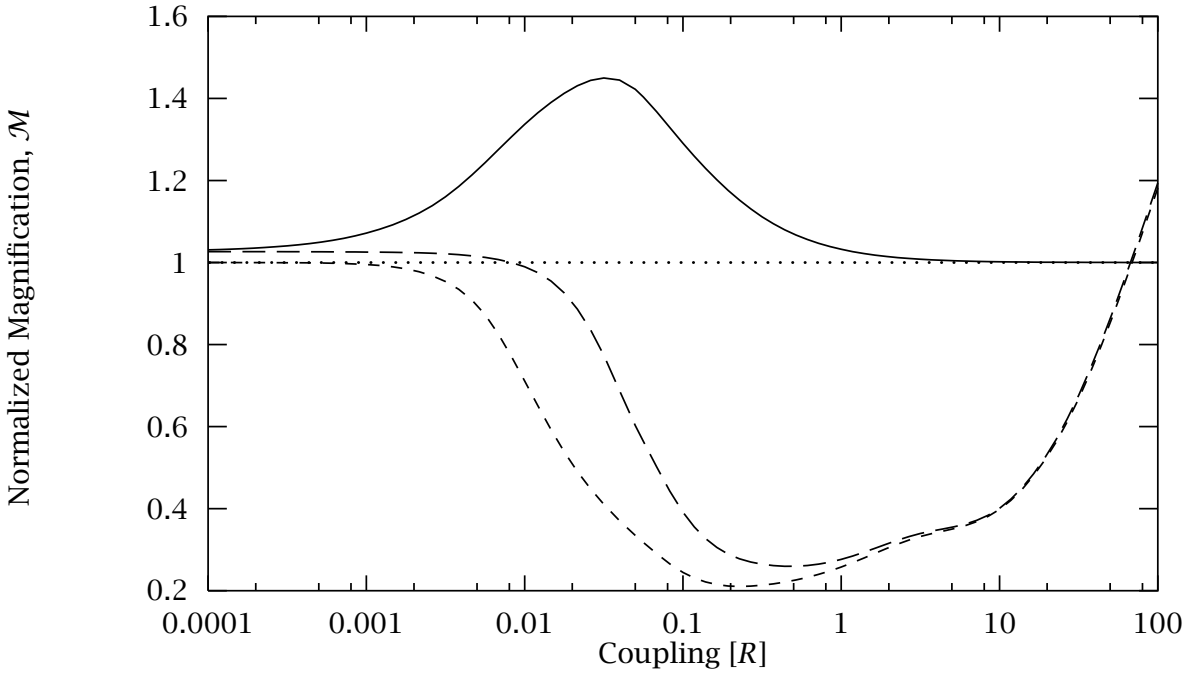

Figure 6.7 Single blade excitation *vs.* engine order three excitation illustrates the transmission of energy. All amplitudes are scaled with the tuned engine order response. Tuned, engine order excitation case features zero energy transmission making it suitable as a datum (· · · · · ·). The 99th percentile response of the engine order excitation, (———), demonstrates amplitude magnification due to energy influx. In the case of single blade excitation of a tuned system, (– – –), the largest amplitude is reduced due to energy flow to the unexcited blades. The 99th percentile response of a mistuned response, (— —), illustrates how localization prevents the flow of energy to other blades resulting in a smaller amplitude reduction.

effects to occur two conditions must be met. The mistuning to coupling ratio must be large enough that the assembly has localized modes. Additionally, coupling must be sufficiently strong that the blade around which vibrations are being localized can receive energy input from neighboring blades.

6.3. Single Blade Excitation

In order to further our understanding of the effect of energy flow through coupling, we investigate the academic problem of a blade assembly where *only one blade in the assembly is excited.* The force amplitude on that blade is the same as the force amplitude that would be applied to it in the case of engine order excitation. Above, we examined the effect of coupling on the response of tuned and mistuned systems

to engine order excitation. In this section we compare this behavior with the response of tuned and mistuned systems to single blade excitation.

In Section 6.2.3 we demonstrated how the net energy flow to a blade in a tuned assembly undergoing engine order excitation is zero. This allows us to use this case as a datum by which we scale the other cases.

Figure 6.7 depicts the increase or reduction in the largest amplitude compared with the response of the tuned, engine order excitation case. In the mistuned cases we only examine the 99th percentile values. We already explained why an increase in the largest amplitude is observed in the mistuned, engine order excitation case. The explanation of the reduction in amplitudes in the single blade excitation cases follows by much the same reasoning. Even if only one blade in the assembly is being excited, all blades partipate in the motion. Energy has leaked from the blade that is being excited to the unexcited blades. Since a mistuned system features wave localization, energy is confined to the excited blades and a smaller amount of energy leakage is observed — the energy level of the excited blade remains higher than that of the excited blade in the tuned case.

We observe the same behavior as before in the extreme coupling cases. In the limit of vanishing coupling, it becomes immaterial whether one blade or all blades are being excited. The two tuned cases merge, as do the two mistuned cases. At the opposite end of the scale, we find that mistuning effects become negligible for strong coupling. Amplitudes in the single blade excitation case become greater than in the engine order excitation case, but this is not a mistuning effect. As before, we see the coupling must be sufficiently small for great mistuning effects to take place and strong enough for energy to be able to propagate.

Note that although the single blade excitation cases show a reduction in largest amplitude compared with the engine order excitation cases, it should also be observed that mistuning effects increase the largest amplitudes in the single blade excitation case. At the coupling value $R \simeq 0.03$ the 99th percentile response is approximately twice that of the tuned system

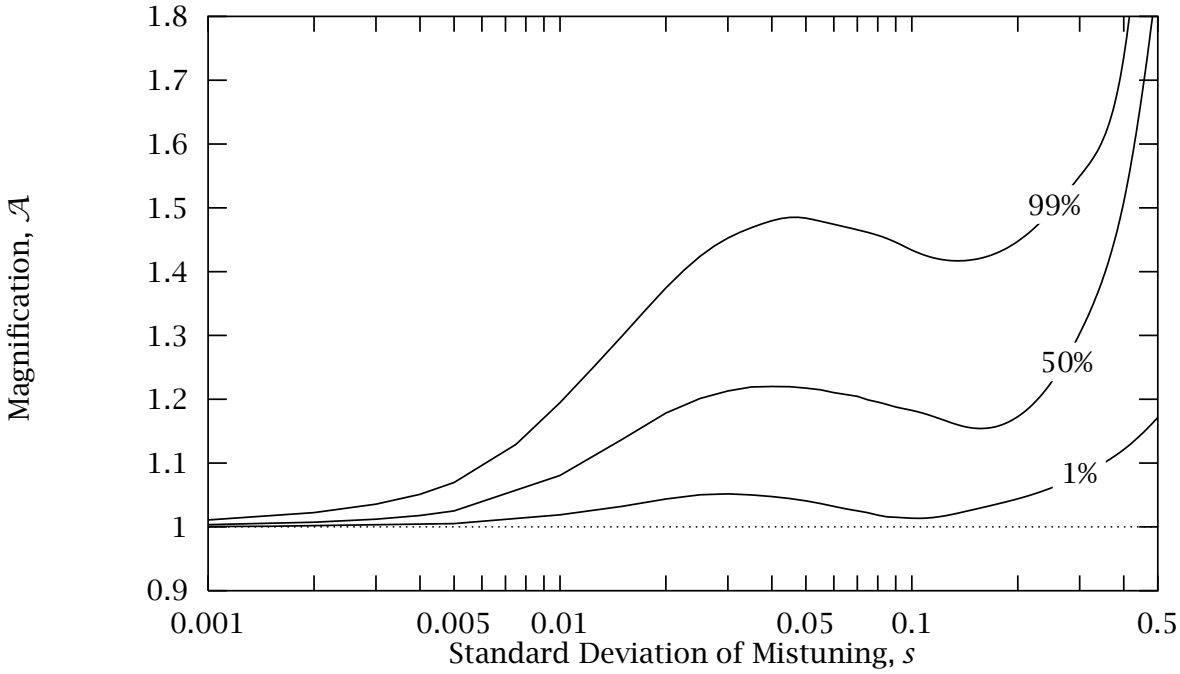

Figure 6.8 Statistics of the maximum resonance amplitude magnification in a 12-blade assembly as a function of the standard deviation of uniform blade mistuning, s. The plot shows the 1%, 50% and 99% percentiles of the statistics. Interblade coupling is $R = 0.0316$ and excitation is engine order 3.

6.4. Effects of Mistuning and Damping Strength

The observation above can be generalized somewhat to explain the effect of variations in damping and mistuning strength on the largest response amplitude. In Fig. 6.8 the magnification of maximum forced response amplitude is plotted as a function of mistuning strength. The plot is obtained at $R = 0.0316$ corresponding to the maximum amplification of largest amplitude and therefore to the most pronounced sharing of energy. For weakly mistuned systems the amplitude increase is small since the system modes are only weakly localized. As the standard deviation of mistuning is increased, the 99th percentile magnification increases up to a maximum of 50% at approximately 5% mistuning, after which it goes down, reaching a minimum at approximately 10% mistuning. The explanation is that excessive mistuning will prevent the augmentation of vibration energy in the localized blade for much the same reason that it causes localization in the first place — by preventing the propagation of energy-carrying waves to the localized blade from the other blades. This latter effect was observed in reference [46, 4] without a satisfactory explanation of the phenomenon. This interesting result

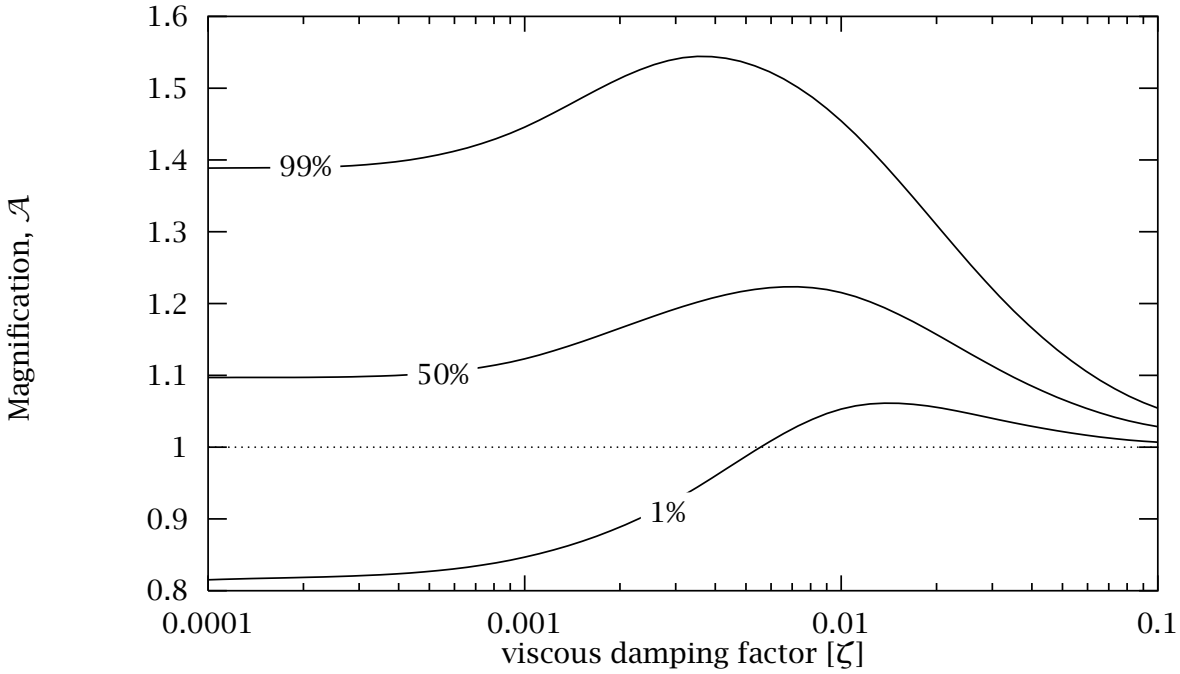

Figure 6.9 Statistics of the maximum resonance amplitude magnification in a 12-blade assembly as a function of the viscous damping factor, ζ. The plot shows the 1%, 50% and 99% percentiles of the statistics. Interblade coupling is $R = 0.0316$, mistuning has a 3% standard deviation, and excitation is engine order 3.

indicates that the best way to prevent rogue blades may be, in some cases, to increase mistuning!

As mistuning standard deviation is further increased beyond approximately 10% , the effect of mistuning starts to increase again. This should come as no surprise because of how mistuning was defined, namely as $k_b(1 + \delta_i)$. Clearly, large negative values of δ will give lead to soft blades that will dominate the motion. Indeed, a standard deviation greater than $1/\sqrt{3} \simeq 57.75\%$ will give blades with negative stiffness, which is of course unrealistic.

Damping induces spatial amplitude decay, similar to localization in its effects, but not its causes. Therefore, effects similar to those described in for the variation of mistuning might be expected. Figure 6.9 depicts the change in the statistics of largest amplitude magnification as the strength of viscous damping is varied. If damping is very strong, wave localization due to mistuning is reduced and mistuning effects are weak. As damping is reduced, localization in the normal modes is increased. At the same time the reduction in damping is enabling the propagation of energy so that

the localized blade may draw energy from the other blades in the assembly thereby increasing its own vibration energy. At $\zeta \simeq 0.5\%$, the 99th percentile of the magnification reaches a maximum, and decreases for lower values of damping. Earlier work [60] has shown that for low values of damping, localization of propagatin waves increases for a given value of coupling, thereby decreasing blade to blade interaction. It is likely that this may inhibit wave propagation in the structure, counteracting the ease of energy propagation due to low damping.

For very weak damping we observe a large dispersion in the magnification statistics. In particular, the high probability (approximately 25%) of finding mistuned assemblies with maximum amplitude smaller than the tuned assembly is puzzling. As we observed for the uncoupled assembly, this should be a rare occurrence in a 12-blade assembly. A plausable explanation is that in the low damping case, some mistuned systems may have a higher rate of energy dispersion resulting in less total vibration energy. We do not have a satisfactory explanation, but we must point out that great numerical difficulty is involved in finding the absolute peak response when damping is very low because the frequency response features well separated sharp resonance peaks. Clearly the extreme statistics of dependent random variables are a complicated affair that would necessitate further analytical development.

CHAPTER VII

CASE STUDIES IN ROTORDYNAMICS: PART 1

In this chapter we apply the first modeling approach, the coupled-oscillator models, presented in Chapter III to some example systems. The goal is to investigate how easily the methods can be implemented and to get some ideas about the quality of the results obtained using the models generated by the methods. We also hope to draw some conclusions about which factors in the dynamical behavior should be the primary focus when generating coupled-oscillator models.

We direct our attention to two compressor rotor prototypes whose computational date we were given access to. The first case, is a blisk with 72 short blades. The second case study is a that of a 36-blade compressor stage. These two prototypes will be approached by identifying parameters in simple coupled oscillator models.

7.1. Case 1: A 72-Blade Blisk — Coupled Oscillator Method

A detailed finite element analysis of the modes of free vibration of the blisk has been performed in advance, and the model identification described herein is based upon these finite element natural frequency results. The finite element data is illustrated in Fig. 7.1.

Each nodal diameter mode in Fig. 7.1, besides its interblade phase angle, is characterized by a deflection shape local to a bay, or a blade/disk sector. Depending on the relative magnitudes of the blade and disk deflection, and on the deflection shapes for the blade and the disk, modes can be classified as being blade-dominated or disk-dominated, but also in terms of the blade mode number and disk mode number which governs the deflection shape of the sector. This classification has been performed from the finite element mode-shapes, and branches of disk-dominated and blade-dominated modes are depicted in Fig. 7.1. The dynamic range considered is such that the dynamic response of the blisk takes place in the first two groups of blade modes. These two blade mode groups are characterized by two branches with horizontal asymptotes in Fig. 7.1. The lower mode group, blade bending dominated motion, will be of interest

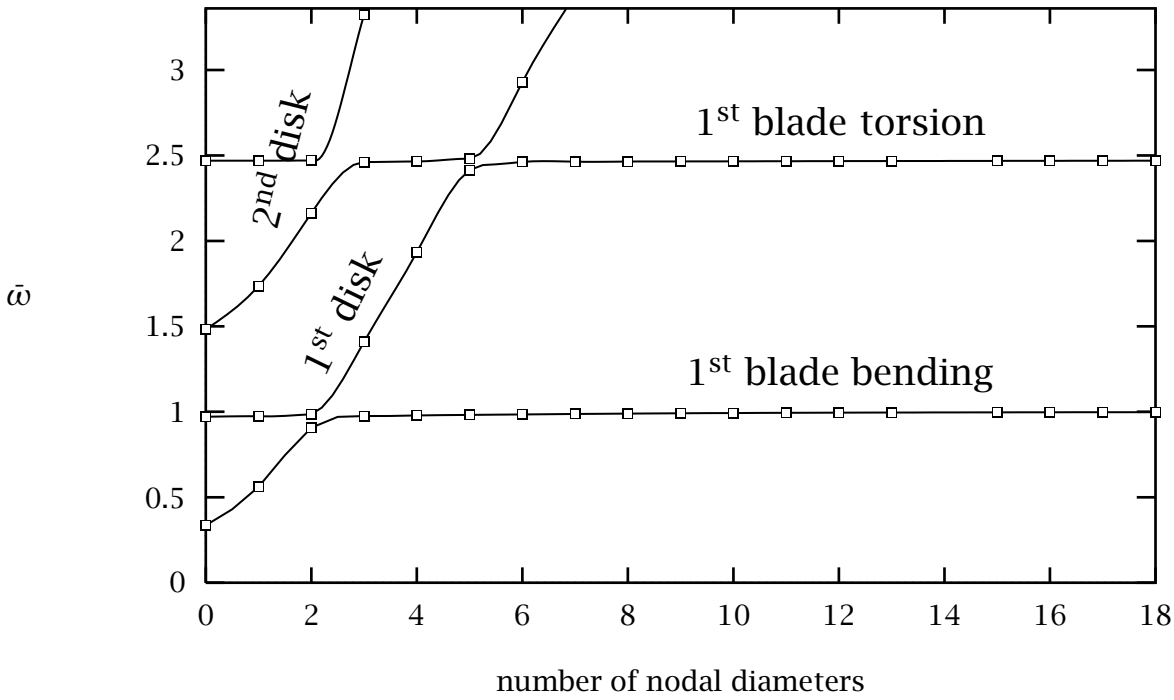

Figure 7.1 Dimensionless natural frequencies as a function of the number of nodal diameters as calculated via finite element analysis. Curve veering phenomena are evidenced. The modes for modal diameters 19-36 are not shown so as to provide more detail at the lower nodal diameters.

to us here. As may be seen by the high modal density of these modes, there is very little participation of the disk motion, except in the veering regions. We shall refer to these assembly modes as blade-bending and blade-torsion modes. Figure 7.1 also contains two families of natural frequencies that correspond to mode shapes where the disk motions dominate, with very little participation of the blade. These will be referred to as disk-modes. Note that the disk-mode frequency branches rise quite rapidly as the number of nodal diameters increases, a phenomenon due to the swift stiffening of the disk as the circumferential wave length decreases. The disk-mode frequency branches thus encounter the slowly-varying blade-mode branches, causing the occurrence of the phenomenon of curve veering and thus important disk-mode and blade-mode interactions in the veering regions.

Previous studies (Chapter V and reference [61]) have revealed that blade assemblies with weak interblade coupling are particularly susceptible to high sensitivity to mistuning. This high sensitivity may cause the localization of the mode shapes and a sharp increase in forced response amplitudes. High modal density, such as the one ev-

idenced by the families of blade bending and blade torsion modes in Fig. 7.1, is a clear indicator of weak interblade coupling. (For example, in the limit of zero interblade coupling the modal density of the tuned assembly becomes infinite.) This means that the blades of the blisk are weakly coupled in their first bending and first torsion mode motions, and thus that the compressor stage is likely to be highly sensitive to random blade mistuning. However, in Chapter VI it was evidenced that mistuning sensitivity does not increase indefinitely as coupling is decreased and that assemblies with extremely weak coupling may have reduced sensitivity to mistuning. Thus quantifying mistuning effects on the blade bending and blade torsion modes will be of special interest due to the extreme levels of modal density featured in these mode-groups for large numbers of nodal diameters.

Using three of the simple models presented in Chapter III we will be able to model two or three curves at a time using the two- and three-DOF models respectively. In two of the models the blades possess only one degree of freedom and those models only allow the study of one of the horizontal branches at a time, forcing us to treat the blade bending and blade torsion separately. The third model has two degrees of freedom in the blade allowing us to model two blade modes at once. However, whether or not the blade torsion modes are modeled, only the blade bending modes will be examined.

7.1.1. Identification of Model Parameters

In this section we consider the frequency range corresponding to the first group of blade modes. For this mode cluster each blade vibrates in its first bending mode and there is very little participation of the disk. The natural frequencies corresponding to the various nodal diameter mode shapes are spread from $\bar{\omega} \simeq 0.972$ for zero nodal diameters to $\bar{\omega} \simeq 1$ for 36 nodal diameters, with two single natural frequencies at nodal diameters 0 and 36 and double natural frequencies for all nodal diameters from 1 to 35. This narrow frequency range indicates a high modal density for the first mode group, especially for the higher nodal diameters ($N \geq 20$). This high modal density means that the blades are weakly coupled in their first bending mode motion, and thus that the compressor stage is likely to be highly sensitive to mode shape localization due to random blade mistuning.

The zero nodal circle disk-modes are born at $\bar{\omega} \simeq 0.336$ for zero nodal diameter and undergo subsequently an extremely rapid frequency increase as the number of nodal diameters increases (for $N = 9$ the frequency of the zero nodal circle disk-mode is $\bar{\omega} \simeq 4.5$). This disk-mode frequency branch therefore encounters the first bending blade-mode branch near the second nodal diameter frequency, causing the occurrence of the phenomenon of *curve veering* and thus important disk-mode and blade-mode

interactions near the veering region. In the veering region the modes of both branches feature significant contributions of the disk as well as of the blade motion.

The study of mistuning effects and localization for the blade bending modes will be carried out for four reduced-order systems, two of which are based on the two-DOF per sector mono-coupled model in Fig 3.4, one is of the three-DOF per sector mono-coupled variety depicted in Fig. 3.6 and one is a three-DOF per sector bi-coupled model as shown in Fig. 3.11. The parameter sets for each model type will be selected, through the parameter identification process outlined in Section 3.1.4, so as to capture the features of the FEM system in various ways.

Identification of Two-DOF per Bay Model Parameters

The first models identified are based on the two-DOF per sector model which is depicted schematically in Fig. 3.4. The model has three dimensionless parameters which are identified by requiring some of its natural frequencies to match the finite element frequencies. Three such constraints are needed here, and they are typically taken at low nodal diameters since the first curve approaches $\bar{\omega} = 1$ approximately, in an asymptotic manner.

Recall that one of the major limitations of the mono-coupled systems is that their frequency spectrum consists of branches, or passbands such that all frequencies in the 2^{nd} branches are higher than the highest frequency in the 1^{st} branch, the 2 branches being separated by $\bar{\omega} = 1$. It is therefore impossible to enforce the zero nodal diameter natural frequency of the second branch, $\bar{\omega} \simeq 0.971$.

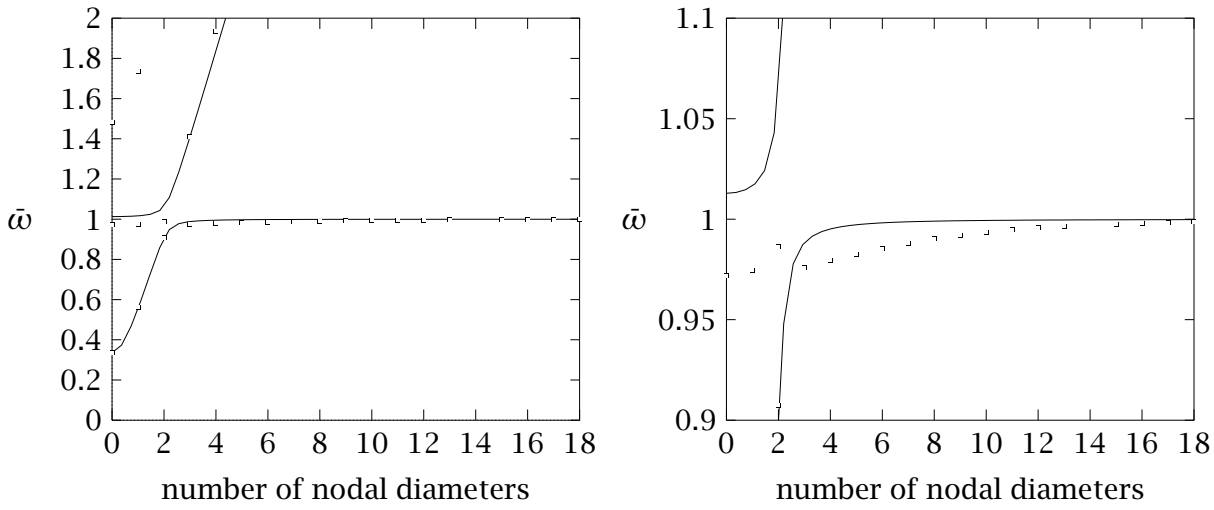

Figure 7.2 The dimensionless natural frequencies of system **1Ba** (line) globally approximate the finite element data (points)

Model 1Ba: Global Similarity

For the first identification we would like to chose points on the first and second branches such that the global shape of the branches is reproduced by the reduced-order model. Constraining the curves with the zero- and two-nodal diameter frequencies of the first curve and the three-nodal diameter frequencies of the second curve yields

$$\bar{m} = 43.3924 \qquad \bar{k}_d = 5.01330 \qquad \bar{k}_c = 1161.89 \tag{7.1}$$

The frequency curves for the reduced-order model corresponding to these parameters are depicted in Fig. 7.2. The model approximates reasonably well the tuned blisk dynamics in the first two mode groups. In particular, note that the veering away of the disk-mode and the blade-mode branches is captured by the simple model, and that the agreement is excellent for the higher nodal diameters. It is also important to note that mode shapes are exchanged through the veering region: the lower frequency branch features disk-dominated modes for $N = 0$ and 1, which become blade-dominated modes for $N \geq 3$; the converse is true for the higher frequency branch. At $N = 2$ the veering and mode switching occur, hence both system modes features important disk and blade contributions.

A detailed view of the veering region is shown in Fig. 7.2(b). In the figure we see the weaknesses of this model. First, there is considerable overshoot of the lower frequency curve at the veering, leading to a grossly exaggerated level of modal density in the simple model at nodal diameters four and higher. Second, the inability of the two-DOF per bay model to reproduce the overlapping mode groups means that the

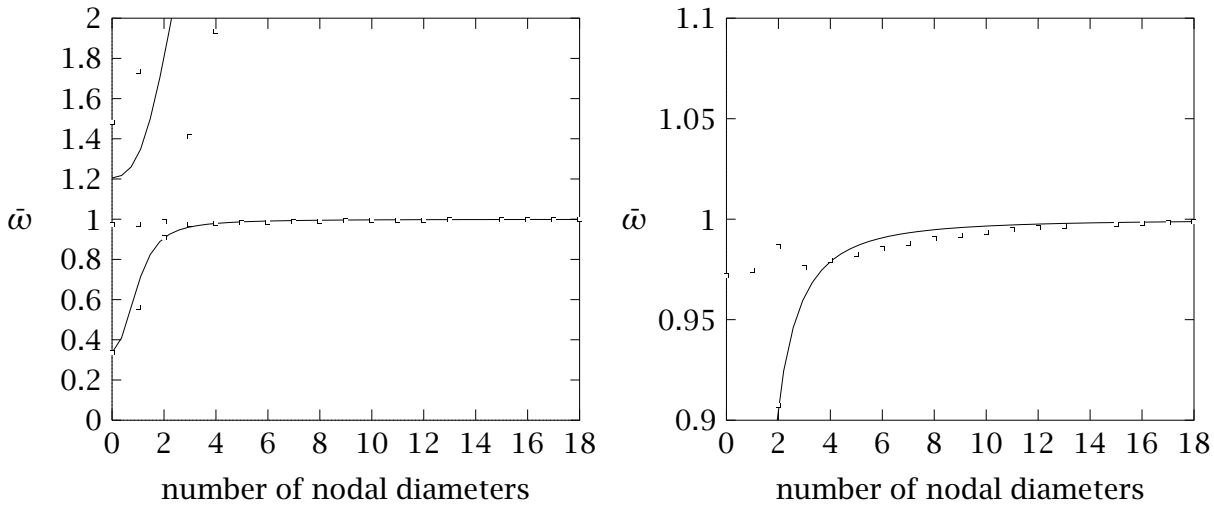

Figure 7.3 The dimensionless natural frequencies of system **1Bb** (line) approximate the flatness of the first curve of the finite element data (points)

lower three frequencies of the second branch cannot be captured accurately, because their finite elements values are smaller than the blade-alone frequency, $\bar{\omega} = 1$. This discrepancy for nodal diameters 1–3 is significant relative to the frequency spread in the blade-bending mode group.

Model 1Bb: Improved Flatness of First Branch

In this identification round we attempt to remedy the high overshot of the first frequency branch in model **1Ba**. This is accomplished by ignoring the fit of the second branch completely, placing instead full emphasis on the fit of the first frequency curve in the veering range. The result is depicted in Fig. 7.3. We chose the zero-, two- and four-nodal diameter frequencies on the first branch as the constraints and found

$$\bar{m} = 2.49369 \qquad \bar{k}_d = 0.407713 \qquad \bar{k}_c = 206.483 \tag{7.2}$$

Examining Fig. 7.3(b), we see that the fit of the first curve is greatly improved although it is not without some overshot. Placement of the zero nodal diameter frequency of the second branch suffers compared to model **1Ba**. In fact, the zero-, one-, and two-nodal diameter frequencies of the blade bending mode groups are all poorly modeled, indicating that dynamic response predicted in those modes may not be valid. Further improvement was not possible.

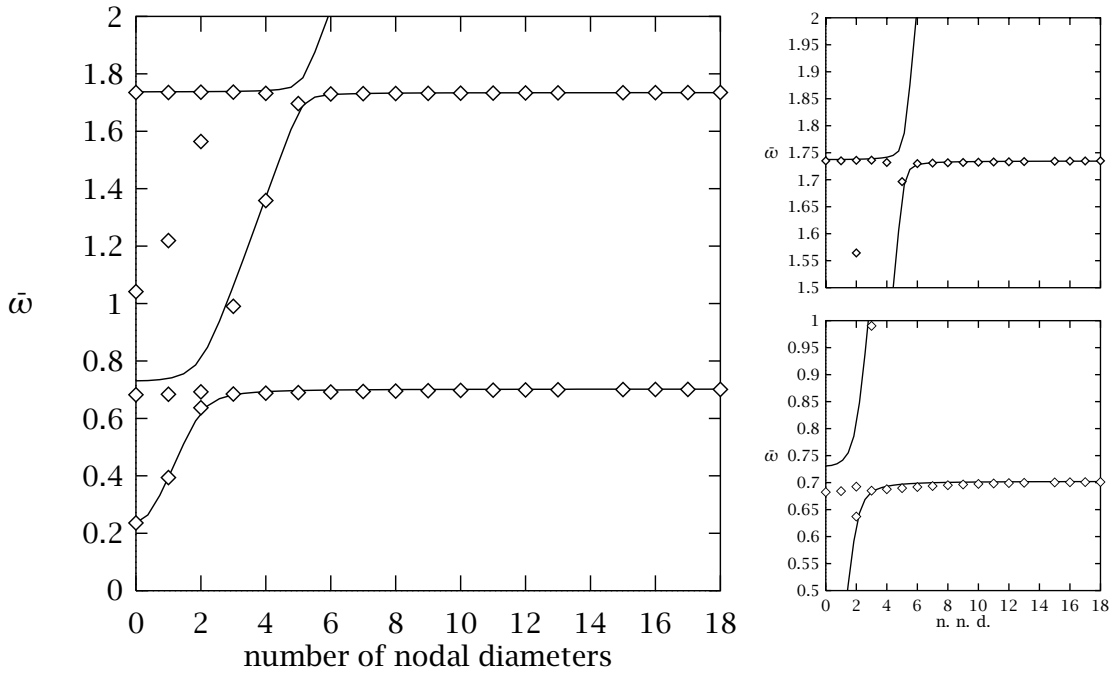

Figure 7.4 The dimensionless natural frequencies of system **1Bc**, (———), approximate globally and locally the finite element data, (◇), for the first family of disk modes and for the first *two* families of blade modes. Detailed plots of the veerings are shown on the right.

Identification of a Model with Two-DOF per Blade

One identification of the parameters for the 72-blade blisk was performed using the two-blade-DOF-per-sector model in Fig. 3.6. By selecting as constraints the 0, 4 and 18 nodal diameter modes on the first curve, the 18 nodal diameter modes on the second curve, and the 0 and 4 nodal-diameter modes on the third curve, the following parameter values were obtained:

$$\begin{aligned} \bar{k}_c &= 324.292 \qquad \bar{k}_d = 1.32788 \qquad \bar{m} = 21.9461 \\ \mu &= .685764 \qquad \kappa = 1.01804 \end{aligned} \tag{7.3}$$

The resulting fit of the natural frequencies of the rotor is illustrated in Fig. 7.4. Considering that the second curve is incapable of having a lower value than the highest value on the first curve (see the discussion in Chapter 7.1), the fit must be considered excellent both in a global and a local sense.

Note that to simplify comparison with the other models, which feature the first blade mode at $\bar{\omega} \simeq 1$, we will introduce a frequency scaling factor of 1.423.

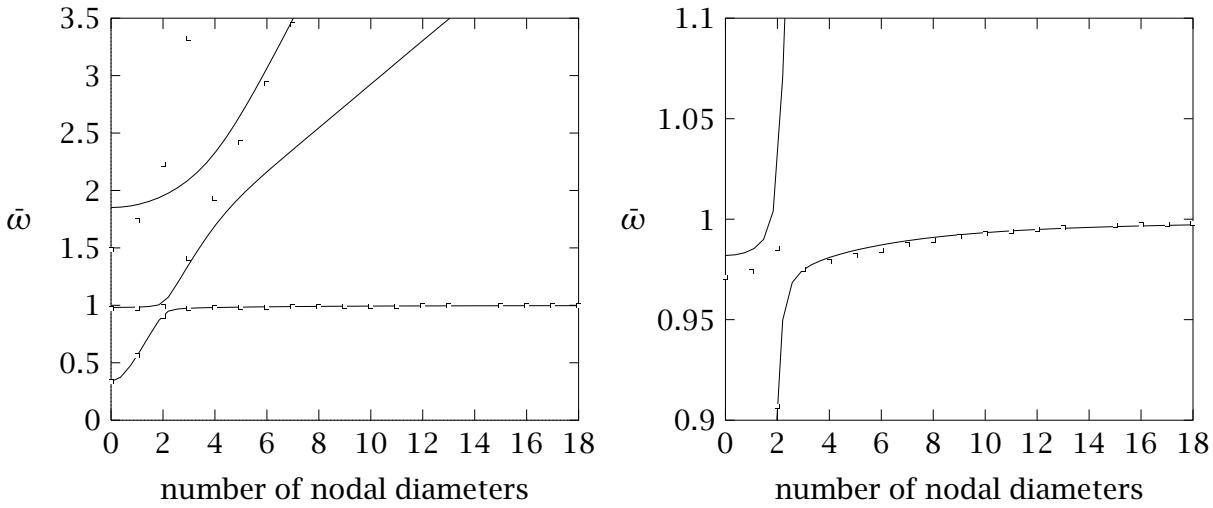

Figure 7.5 The natural frequencies of system **1Bd** (line) approximate the flatness of the first curve of the finite element data (points)

Parameter Identification for Three-DOF per Bay, Bi-Coupled Model

Now turning our attention to the more versatile three-DOF per bay system depicted in Fig. 3.11 we follow a methodology similar to the mono-coupled model identifications, albeit encountering much greater difficulty in the identification of the model parameters. Recall that the bi-coupled model features nine independent, dimensionless parameters. These are identified by requiring nine of the natural frequencies of the model to match their finite element counterparts.

In an attempt to model more closely the modal density of the first branch and thus to capture mistuning effects accurately, we relax the global constraints and perform a parameter identification based on the zero- to eight-nodal diameter modes for the first branch only, *ignoring all other branches.* This yields

$$\begin{array}{lll} \bar{m}_1 = 58.4311 & \bar{k}_{d_1} = -17.8281 & \bar{k}_{c_1} = 1760.89 \\ \bar{m}_2 = 78.2008 & \bar{k}_{d_2} = 4074.68 & \bar{k}_{c_2} = 2397.06 \\ \bar{m}_3 = -63.4161 & \bar{k}_{d_3} = 50.0048 & \bar{k}_{c_3} = -2020.31 \end{array} \tag{7.4}$$

The frequency curves of the system are depicted in Fig. 7.5. Note the much improved shape of the first frequency branch. Overshot is very moderate and modal density is accurately captured. An interesting feature is the reasonable placement of the second and third curves (especially the second curve for small numbers of nodal diameters) in the absence of any constraints.

Remarks

We have selected four simple models that we feel are representative of the blisk vibrating, near it first bending blade frequency, given different criteria and the limitations of the models used. The great difference in the various sets of parameters identified is striking, showing no clear pattern. The bi-coupled, three-DOF per bay system features negative $\bar{m}_3$ and $\bar{k}_{c3}$. Since these terms correspond to off-diagonal mass and stiffness matrix elements, this is not unexpected. The negative or negligible value of $\bar{k}_{b1}$ is more surprising, although this may be caused by the blisk's lack of a center hub.

At this point it is not clear that these quite different systems will feature dynamics that are remotely similar, even in the tuned case.

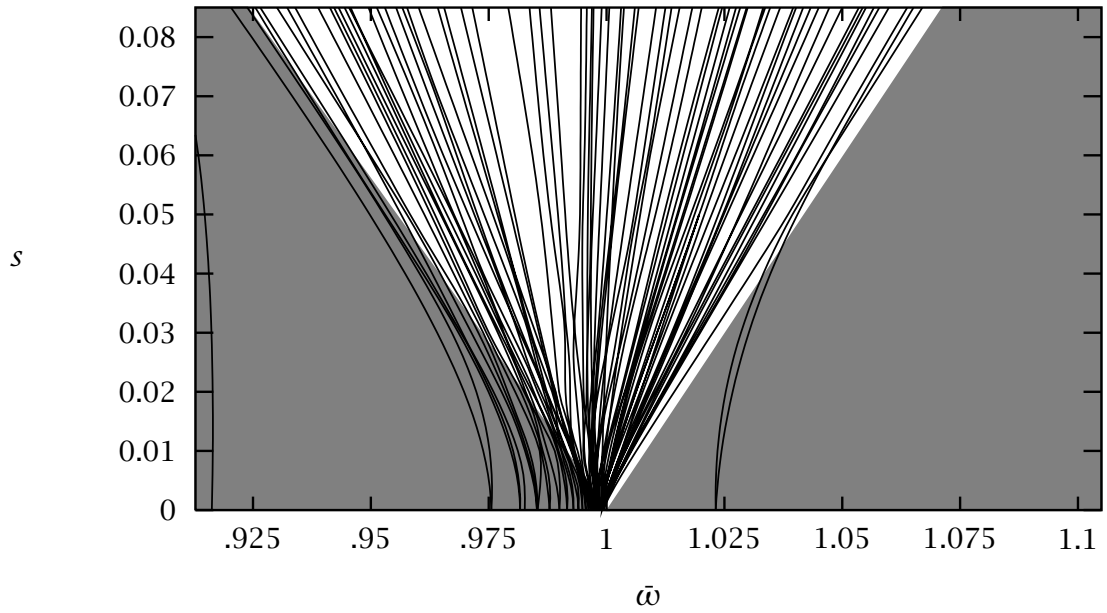

Figure 7.6 Fanning out and veering of the dimensionless natural frequencies as mistuning strength is increased. This was calculated for one realization of system **1Be** with uniform random mistuning. The white region indicates the range of the uniformly mistuned cantilevered blade natural frequencies. The quantity s denotes the standard deviations of stiffness mistuning.

7.1.2. Mistuned System Analysis

Natural frequencies of mistuned systems

We first examine the effect of mistuning on the assembly natural frequencies, as depicted in Fig. 7.6. In the tuned assembly all natural frequencies except those for $N = 0$ and $N = 36$ are double. When the blisk is mistuned, all double natural frequencies split to yield 72 single natural frequencies for each DOF in the bay. The plot was generated using the three-DOF per bay system **1Bd**, for one realization of machine-generated uniformly distributed random mistuning. A fanning out and veering away of the natural frequencies close to the blade-alone first bending frequency is observed. Also, Eq. (C.1) in Appendix C yields the spread due to mistuning of the blade-alone natural frequencies, which is illustrated as a white region in Fig. 7.6. For example, for the stiffness-mistuning standard deviation $s = 0.08$, the mistuned blade-alone frequencies, $\bar{\omega}_i^b$, belong to the interval $[\sqrt{1 - 0.08\sqrt{3}}, \sqrt{1 + 0.08\sqrt{3}}] \equiv [0.928, 1.067]$. Observe in Fig. 7.6 that the natural frequencies of the mistuned assembly, in the vicinity of the blade bending dominated modes, fall within this window of blade cantilevered frequencies, which is a clear indicator of the very weak interblade coupling. This, as much as the high modal density observed in Fig. 7.5, suggests a high sensitivity to random mistuning.

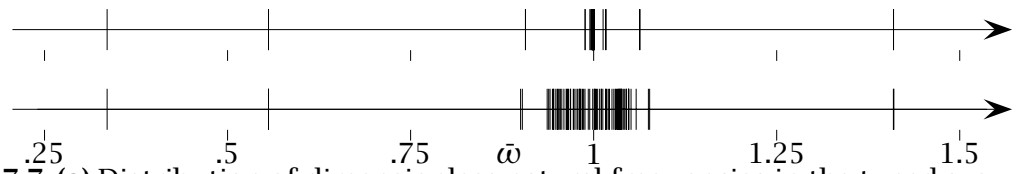

Figure 7.7 (a) Distribution of dimensionless natural frequencies in the tuned system **1Ba** (top) compared to the natural frequencies of a single mistuned system (bottom).

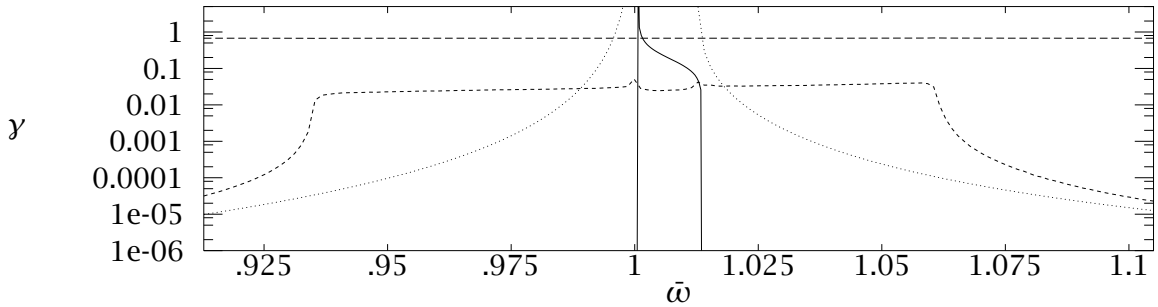

Figure 7.7 (b) Localization of waves in System **1Ba**. Shown is the exponential attenuation rate in the tuned system's stopband (———) along with Monte Carlo simulations of the localization factor (– – –) and its approximations by Classical Perturbation (· · · · ·) and Modified Perturbation (— —) ($s = 7.25\%$)

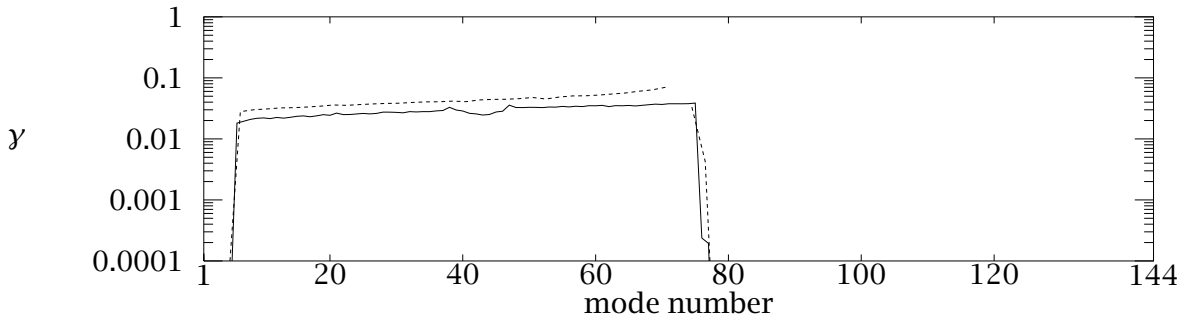

Figure 7.7 (c) Localization factor for the modes of system **1Ba**, obtained from Monte Carlo simulations using the natural frequencies of a mistuned system with a given mistuning pattern (———) and the natural frequencies of a tuned system (– – –).

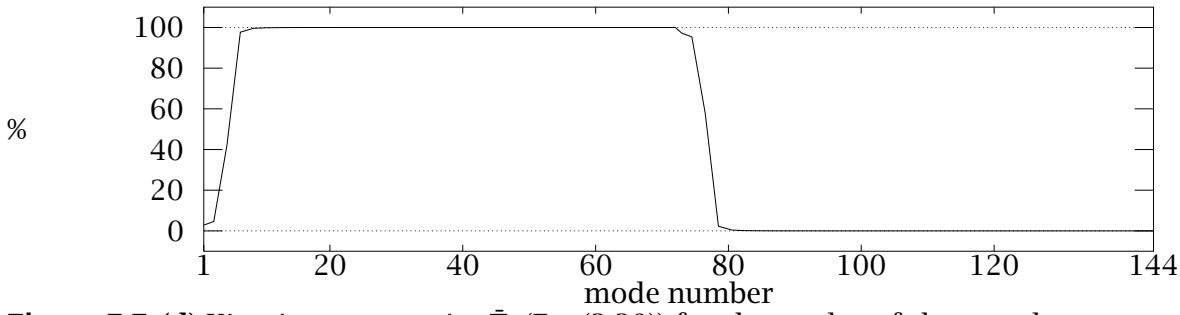

Figure 7.7 (d) Kinetic energy ratio, $\bar{T}$, (Eq. (3.39)) for the modes of the tuned system of type **1Ba**.

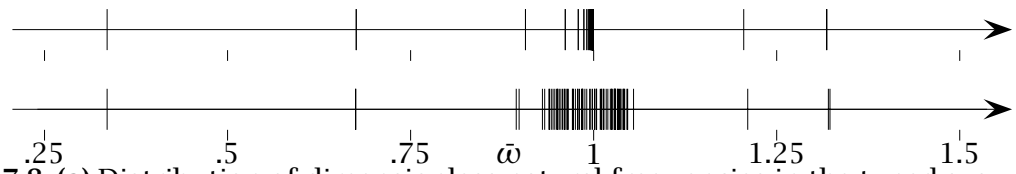

Figure 7.8 (a) Distribution of dimensionless natural frequencies in the tuned system **1Bb** (top) compared to the natural frequencies of a single mistuned system (bottom).

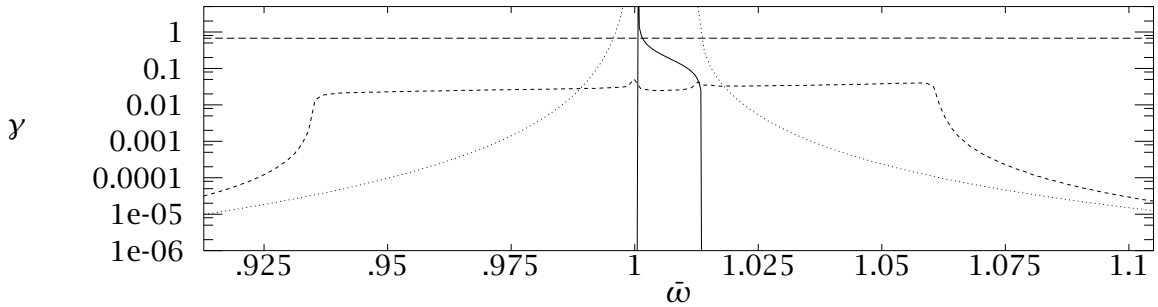

Figure 7.8 (b) Localization of waves in System **1Bb**. Shown is the exponential attenuation rate in the tuned system's stopband (———) along with Monte Carlo simulations of the localization factor (– – –) and its approximations by Classical Perturbation (· · · · ·) and Modified Perturbation (— —) ($s = 7.25\%$)

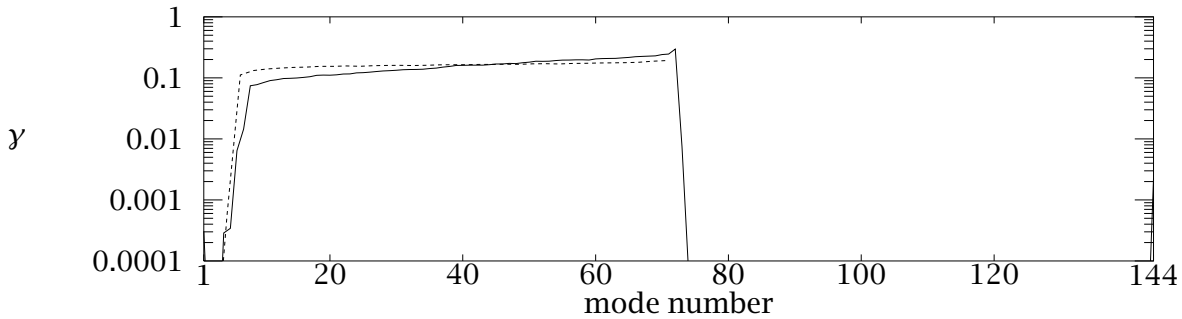

Figure 7.8 (c) Localization factor for the modes of system **1Bb**, obtained from Monte Carlo simulations using the natural frequencies of a mistuned system with a given mistuning pattern (———) and the natural frequencies of a tuned system (– – –).

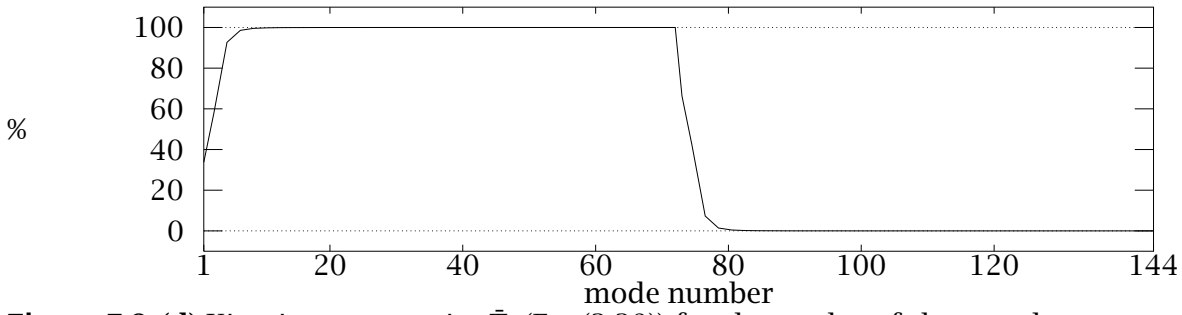

Figure 7.8 (d) Kinetic energy ratio, $\bar{T}$, (Eq. (3.39)) for the modes of the tuned system of type **1Bb**.

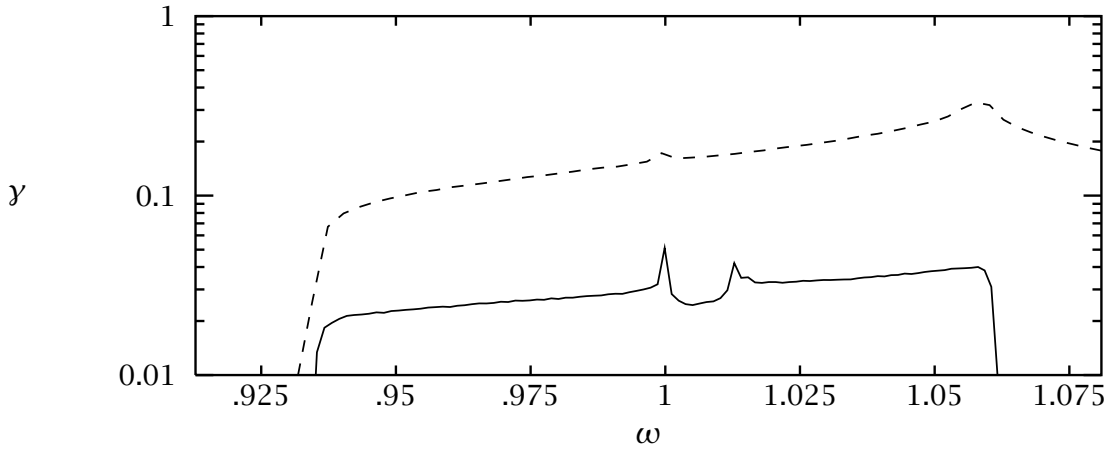

Figure 7.9 Comparison of the Monte Carlo simulations of the localization factor for the three two-DOF per bay systems **1Ba** (———) and **1Bb** (– – –), for uniform mistuning of standard deviation $s = 7.25\%$.

The illusion that the mistuned system has a larger number of modes is due to the splitting of frequencies that are double for the tuned system, as well as to the fact that the tuned system features a large number of frequencies concentrated at the right edge of the cluster. This spreading of the natural frequencies is also presented for systems **1Ba** and **1Bb** in Figs. 7.7(a) and 7.8(a), respectively.

Localization factors

Next, we examine the localization of traveling waves in the two-DOF per bay systems identified above, when uniform blade stiffness mistuning with 7.25% standard deviation is present. This type of analysis is currently not available for the three-DOF per bay systems. Localization is quantified in terms of the localization factor, γ, the rate of exponential spatial decay of waves incident to an infinite assembly. The results are depicted in Figs. 7.7(b) and 7.8(b) in terms of frequency. For clarification, each figure also shows the exponential decay rate in a tuned system (———). This brings out the passband ($\gamma = 0$) and stopband ($\gamma > 0$) structure of the tuned system. When the system is mistuned, the system passbands vanish and γ is always nonzero. Hence, waves of all frequencies are attenuated in mistuned assemblies. For each mistuned system three curves are presented: A Monte Carlo simulation of the wave propagation (– – –) is compared with perturbation results based on a Classical Perturbation approach (· · · · ·) and a Modified Perturbation approach (— —) (see 5.2).

Figures 7.7(b) and 7.8(b) show the localization factor in systems **1Ba** and **1Bb**, respectively. In Fig. 7.7(b) we see that Monte Carlo simulations predict the localization factor in **1Ba** to be largest and relatively constant in the frequency range 0.93 to 1.06.

This frequency range corresponds with the range of mistuned blade-alone frequencies at standard deviation of blade stiffness mistuning equal to $s = 7.25\%$ in Fig. 7.6. The conclusion is that localization is strongest in the blade-dominated modes and occurs in the frequency range populated by the modes of mistuned systems. This result is repeated in Fig. 7.8(b), although the effect is not as clear due to the stopbands featured by system **1Bb** in its tuned state.

A few words about the stopbands in Figs. 7.7(b) and 7.8(b) are in order. Recall that due to the mixing of the mode groups of the finite element model, there should be no stopband near the blade-alone frequency. Model **1Ba** models this most closely with only a very narrow stopband that goes undetected in the Monte Carlo simulation. Model **1Bb** has a wide stopband between approximately $\bar{\omega} = 1$ and $\bar{\omega} = 1.2$. The existence of this spurious stopband is obviously affecting the localization factor calculated for system **1Bb** above $\bar{\omega} \simeq 1.07$. Hence we feel that it is system **1Ba** which best captures the qualitative behavior of the localization factor as a function of frequency.

Figure 7.9 presents a comparison of the localization factor for the models **1Ba** and **1Bb** in the frequency range of interest. Note the high sensitivity of γ to the quality of the frequency fit achieved by the two models. In Fig. 7.9 system **1Ba** has much lower values of the localization factor than that predicted by system **1Bb**. The higher values predicted by system **1Bb** are most likely due to corruption by the proximity to the spurious passband.

Figures 7.7(b) and 7.8(b) also feature the Classical Perturbation and Modified Perturbation results. For both systems the Modified Perturbation approach provides a poor approximation of the localization factor throughout the frequency range. Since the Modified Perturbation is accurate in the limit of strong sensitivity (weak coupling), a possible conclusion is that that sensitivity is only moderate. The Classical Perturbation approach has been found to yield an accurate approximation of the localization factor in the limit of weak to moderate sensitivity. However, the Classical Perturbation method experiences numerical difficulties at frequencies corresponding to the bounding frequencies between the passbands and stopbands of the tuned system. This is clearly the case in systems **1Ba** and **1Bb**. In systems **1Ba** and **1Bb** classical approximation of the localization factor is accurate throughout the passbands. Alas, the natural frequencies are not dispersed evenly in the passband, and only a small part of the passbands is included in Figs. 7.7(b) and 7.8(b). Hence only the disk modes populating the lower regions of the passbands in systems **1Ba** and **1Bb** are approximated satisfactorily by the Classical Perturbation approach.

Figures 7.7(c) and 7.8(c), and Figs. 7.7(d) and 7.8(d), provide additional insight into the localization phenomenon in the reduced-order models. Figures (c) present the lo-

calization factor for the various system modes. This way of presenting localization factor is meaningful due to the non-uniform spacing of the natural frequencies inside the mode groups. This representation may be accomplished calculating the localization factor at the natural frequencies of either a mistuned or a tuned system. The two methods are compared in the figures. The former method, although more accurate, is somewhat more costly since the natural frequencies of a mistuned system must be calculated first, which defeats the purpose of using γ as a *predictor* of mode localization. The comparison illustrates that using the tuned mode frequencies to predict localization is a valid approximation. Figures 7.7(c) and 7.8(c) also demonstrate how the first few modes of models **1Ba** and **1Bb** are disk-modes that do not experience localization. In Figs. 7.7(d) and 7.8(d) the kinetic energy ratio of the modes of the tuned systems are studied. A comparison with Figs. 7.7(c) and 7.8(c) shows, with striking agreement, that only the blade-dominated modes (those with high kinetic energy ratio) are localized. This result is understandable. Because mistuning is only in the blades, it has a much smaller effect when the participation of the blade is small.

7.1.3. Localized modes

The analysis of localization factors is not complete without their validation by the mode shapes of mistuned systems. In this section we shall only consider the group of first bending blade modes and the neighboring disk modes.

As was shown in Chapter II, all modes of the tuned blisk are “extended” modes which feature a sinusoidal amplitude variation with the blade number and a number of nodal diameters varying from zero to 36. These modes are called extended because the entire tuned assembly participates in the motion. The two standing mode shapes associated with each double frequency can be combined to form two counter-rotating traveling waves of uniform maximum amplitudes throughout the rotor, indicating that the energy of the tuned blisk is equally shared by all blades.

When the blisk is mistuned the mode shapes may or may not experience large deviations from the nodal diameter modes of the tuned system, depending on the sensitivity to mistuning and the type of blade or disk mode considered. If large deviations occur, then the mode shapes become localized to a few of the blades, such that only these few blades experience significant amplitude motion. The spatial amplitude decay that characterizes a localized mode is, on the average or asymptotically, exponential, and the corresponding rate of decay is the localization factor, γ. This is verified below.

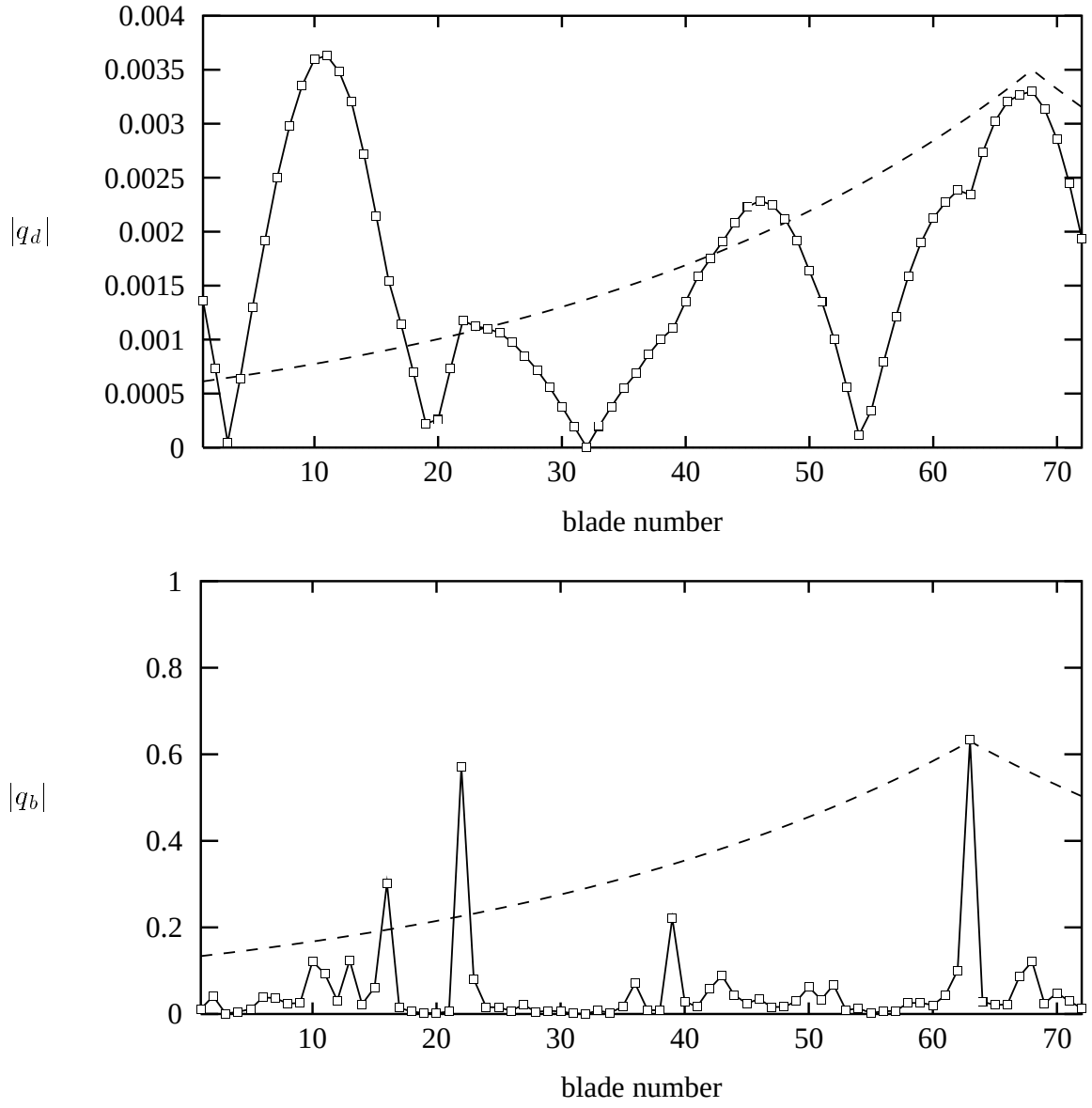

Figure 7.10 Disk deflection pattern and blade deflection pattern for mode 23 of mistuned system **1Ba**. The disorder pattern is uniformly random such that $s = 7.25\%$. The absolute value of the displacements are plotted alongside exponential functions with decay rate equal to the localization factor calculated by Monte Carlo simulation at the frequency of the mistuned mode considered, $\gamma = 0.0251$.

Localization of disk and blade amplitude patterns

In Figs. 7.10 and 7.11 we study the localization of selected mistuned modes of the mistuned systems **1Ba** and **1Bb**. Both systems feature the same pattern from a uniform random mistuning of standard deviation 7.25%. Some interesting conclusions can be

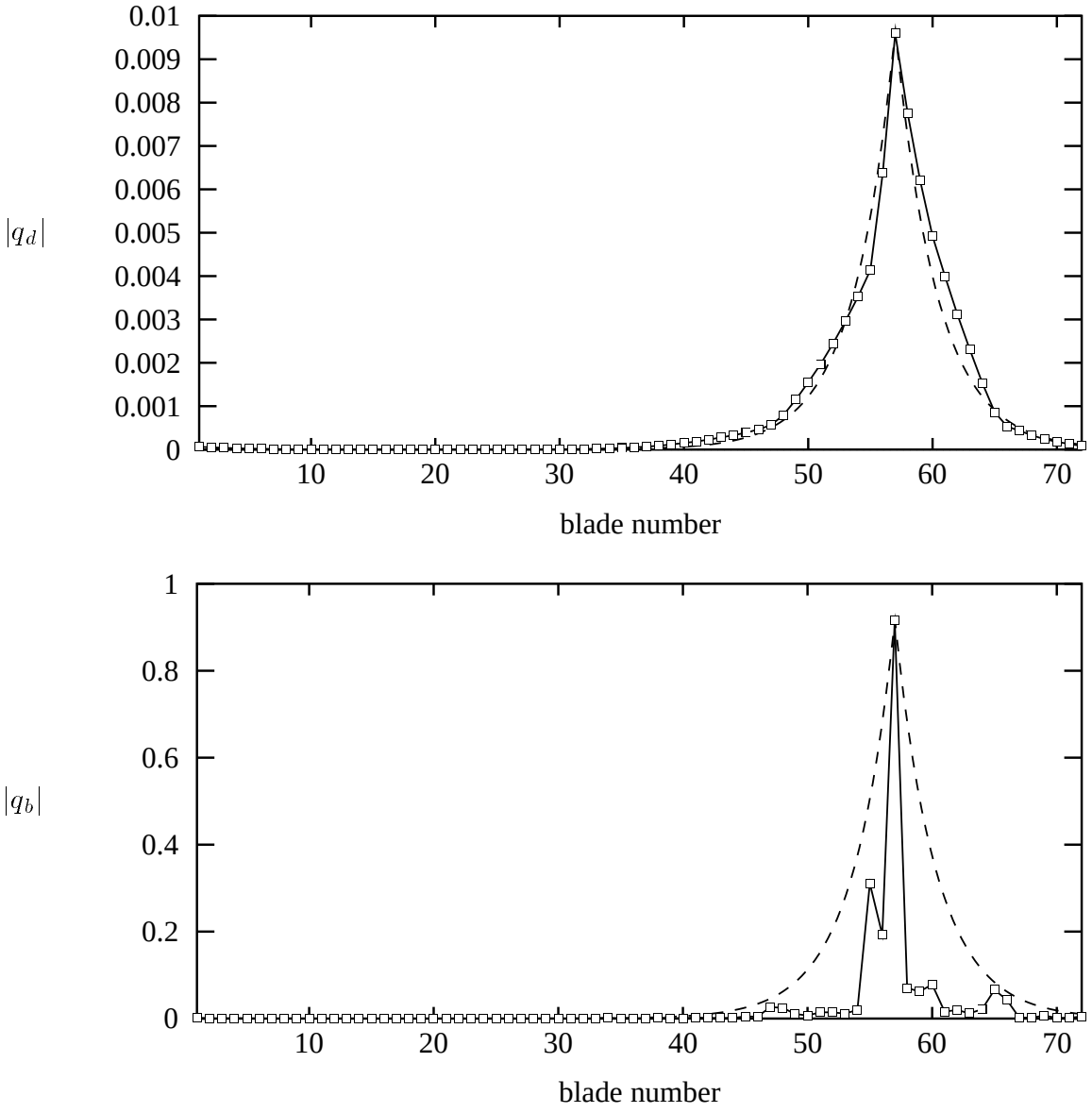

Figure 7.11 Disk deflection pattern and blade deflection pattern for mode 72 of mistuned system **1Bb**. The disorder pattern is uniformly random such that $s = 7.25\%$. The absolute value of the displacements are plotted alongside exponential functions with decay rate equal to the localization factor calculated by Monte Carlo simulation at the frequency of the mistuned mode considered, $\gamma = 0.297$.

drawn from Figs. 7.10 and 7.11. First, the high sensitivity of the mode shapes to small mistuning is observed, along with the corresponding high levels of localization. Second, the degree of localization is consistently observed to be significantly larger for the blade coordinate amplitude pattern than for the disk coordinate amplitude

pattern. Third, the values of the localization factor for the various systems appear to predict reliably the localization present in the disk coordinate patterns featured by typical modes, as demonstrated in Figs. 7.10(a) and 7.11(a). However, the decay of the blade coordinate pattern, which is of much greater practical interest to us, appears to be relatively poorly predicted by the localization factor in Figs. 7.10(b) and 7.11(b). Namely, local resonances of blades lead to spatial attenuation rates away from the maximum blade amplitude that are much higher than γ would indicate. The following reasoning justifies why this may be so.

First, it is important to recall that the localization factor characterizes the spatial amplitude decay of the physical coordinates through which energy is being transmitted along the structure, *i.e.*, the coupling coordinates. For the system in Fig. 3.4 the coupling coordinates are the disk DOF, q_d^i, thereby confirming the validity of the exponential fits to the disk DOF deflection patterns, shown in Figs. 7.10(a), and 7.11(a). Second, we explain the fact that the blade DOF's feature a different spatial decay from that of the disk DOF's. According to Eq. (3.26) the relationship between the ith disk and blade coordinates may be written as

$$q_d^i = \left(1 - \frac{\bar{\omega}^2}{1+\delta_i}\right) q_b^i, \quad i = 1, \ldots, N. \tag{7.5}$$

For the blade-dominated modes of the 72-blade blisk considered here, the assembly's natural frequencies are very close to the natural frequency of a cantilevered blade (the scaling frequency), *i.e.*,

$$\bar{\omega}^2 = 1 + \epsilon \tag{7.6}$$

where ϵ is small. An expansion of Eq. (7.5) to the first order in ϵ and δ_i yields

$$q_b^i = \frac{q_d^i}{\delta_i - \epsilon} \tag{7.7}$$

where $(\delta_i - \epsilon)$ is small, possibly approaching zero if $\delta_i \simeq \epsilon$. This tells us that the ith blade amplitude is not solely determined by the ith disk DOF amplitude, but rather by the ratio of the disk DOF amplitude to the difference between the ith blade-alone natural frequency and the natural frequency of the mistuned mode considered. Namely, if the ith blade frequency mistuning is close to ϵ, the ith blade amplitude becomes much larger than the disk amplitude, and in the limit $\delta_i \to \epsilon$, the blade amplitude becomes infinite, *i.e.*, resonance occurs. This shows that while the disk deflection spatial pattern is governed by the occurrence of mode localization, the blade amplitude pattern is determined not only by localization effects, but also by purely local resonances which occur when a blade natural frequency happens to be close to the frequency of the mistuned mode considered. Note that if the disk is stiff and interblade coupling is

weak (which is the case here) the blade-dominated mistuned modes tend to occur each at a natural frequency that nearly matches one of the mistuned blade-alone natural frequencies (this can be seen in Fig. 7.6) and each mode is localized about the blade in question.

The localized blade is then the one that undergoes a particularly significant local resonance, therefore resulting in a much larger amplitude locally and in increased "localization" for the blade amplitude patterns. The occurrence of local blade resonances superimposed to localization are clearly observed in Figs 7.10 and 7.11, by comparing the plots labeled (b) to those labeled (a). Further, note that, as surmised above, local blade resonances are only observed in the region where localization is strong (Fig. 7.11(b)) but do arise for various blades in the rotor when localization is relatively weak (Fig. 7.10(b)). The bottom line is that the "localization" for the blade DOF's is significantly greater than that for the disk DOF's and is under-predicted by the localization factor. At this point it is not clear how to characterize the spatial decay for the blade amplitudes (note that this decay is probably not even exponential). However, it is quite important to be aware of and quantify this new "super-localization" phenomenon, as it results in an actual risk for rogue blades that is much greater than would be predicted by the (disk DOF) localization factor.

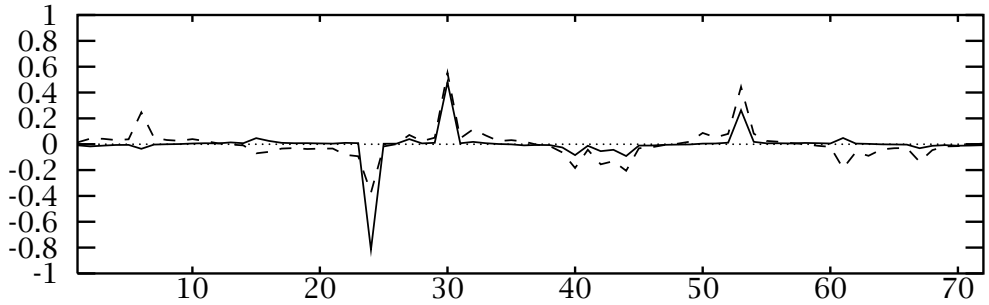

(b) Mode no. 6

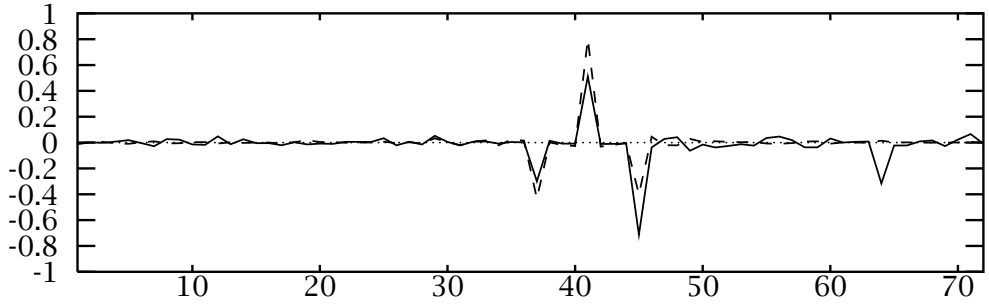

(c) Mode no. 48

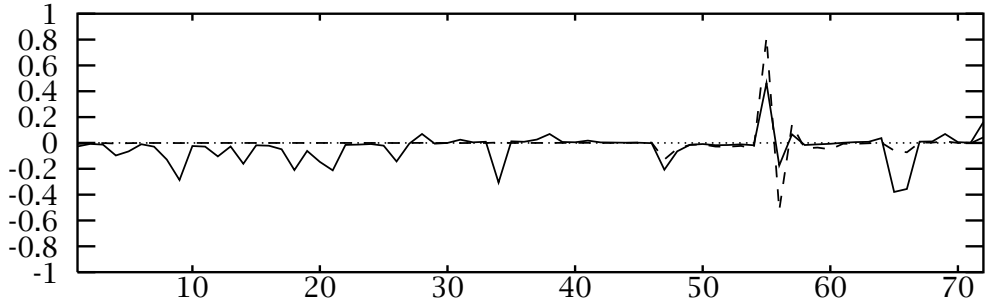

(b) Mode no. 69

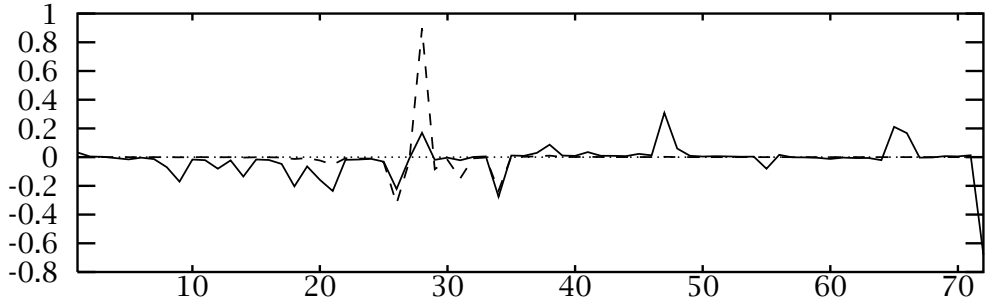

(c) Mode no. 70

Figure 7.12 Blade displacements for selected modes of mistuned systems **1Ba** (– –◇– –), **1Bb** (· · · · +· · ·) (s = 7.25%).

Localized modes of various models

Figures 7.12 compares some mistuned modes in the two two-DOF models. Agreement is generally very good, in particular the two models agree well on the location of the localization. As predicted by the localization factor, the localization in model **1Bb** is somewhat stronger than that observed in model **1Ba**.

The comparison of a mono-coupled model (**1Bb**) and a bi-coupled model (**1Bd**) is somewhat richer in flavor. Although we are unable to calculate a localization factor for the three-DOF per bay model, a comparison of the mistuned modes can yield some information about the localization effects. The comparison of the mode shapes of the two systems is depicted in Figs. 7.13 and 7.14. In all cases modes are show in terms of blade displacement. The comparison was based on selecting the modes of the two systems whose natural frequencies were closest. The mode shapes are of course eigenvectors defined up to a multiplicative constant, and hence blade deflection values can only be compared within each mode. Figure 7.13 depicts the onset of localization as the modes change from disk-motion dominated modes to blade-motion dominated modes (see Fig. 7.8(d)). Figure 7.13(a) depicts the second mode. Localization is negligible and the mode is a clean one-nodal diameter mode. Mode 6 in Fig. 7.13(b) has clearly become localized, although 6 nodes (or 3 nodal diameters) may still be identified. The results in Fig. 7.13 tell us that the disk-dominated modes, which occur before the veering of the frequency curves, are very little affected by mistuning. Note that mode 6 is more localized for the bi-coupled model. We believe this is due to the different approximations of the veering for the two models: namely, the overshot of the first frequency curve in model **1Bb** leads to an over-prediction of the modal density and a localization factor for that is too low. Figure 7.13(c) illustrates how second passband modes may exist among the first passband modes in the three-DOF model. Recall how overlapping passbands were toted as one of the desirable features of the three-DOF model. Between modes 11 and 18 of the three-DOF system we verify the existence of the first mode in the second passband. The exact number of this mode was not obtained since was sufficiently localized to be indistinguishable from the modes 12-17. This insertion of second passband modes within the first passband modes does not occur in the two-DOF model, resulting in a mismatch of the mode numbers in Fig. 7.13(c). In addition, a pair of second passband modes exists between modes 18 and 23 in the three-DOF system, hence the discrepancy of three for the mode numbers of the two systems that is held constant all the way up to the mode pairs 52 and 55 (Fig. 7.14(a)). Figures 7.14(a) and 7.14(b) show continued excellent agreement between the two models as well as high levels of localization for these blade-bending dominated modes. In Fig. 7.14(b) we observe the insertion of two more second passband modes

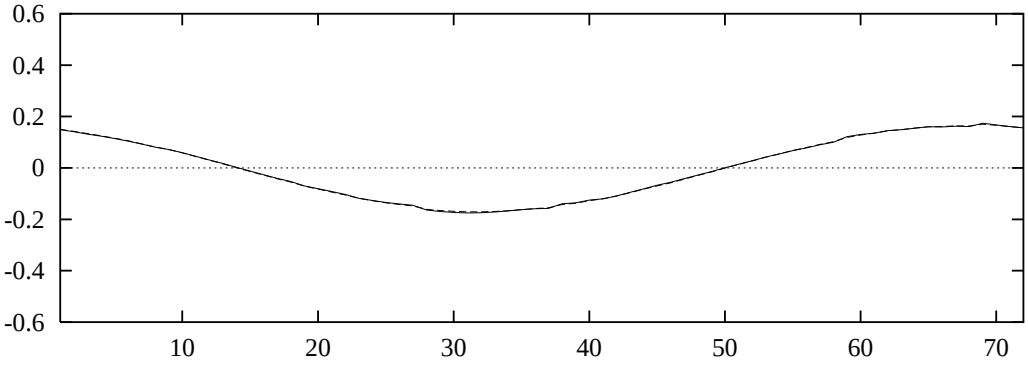

(a) Mode 2 of **1Bb** (———) *vs.* mode 2 of **1Bd** (– – –).

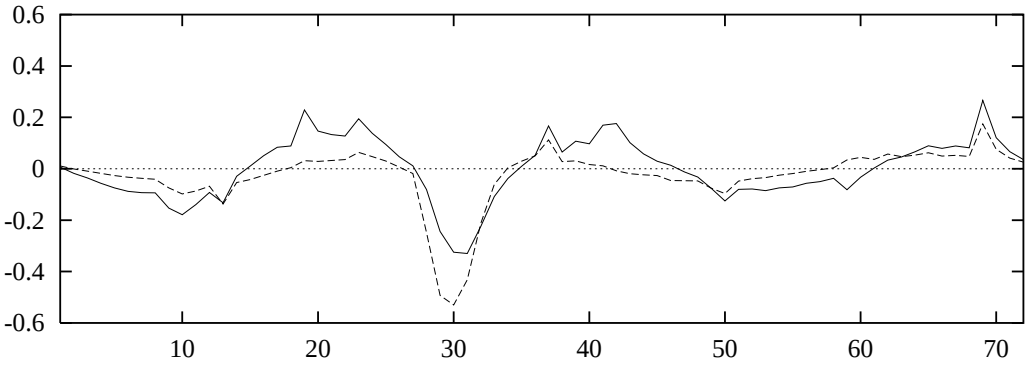

(b) Mode 6 of **1Bb** (———) *vs.* mode 6 of **1Bd** (– – –).

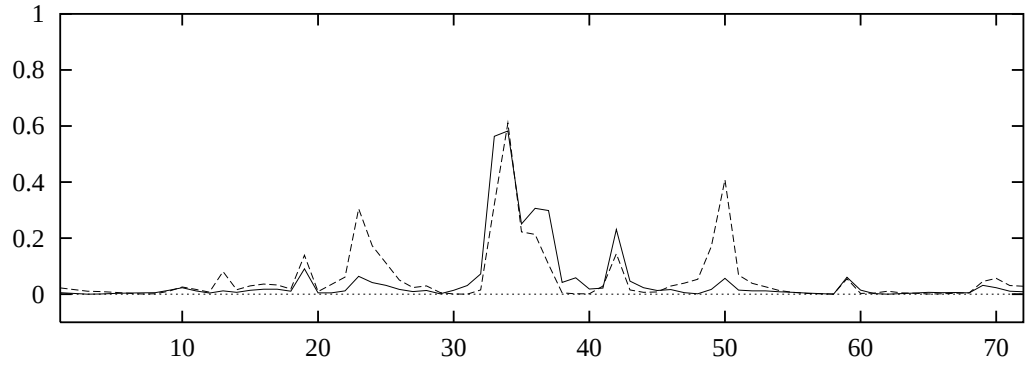

(c) Mode 17 of **1Bb** (———) *vs.* mode 18 of **1Bd** (– – –).

Figure 7.13 Modes 2 and 6 depict the onset of localization as the mode shapes are transformed from being disk-deflection dominated to blade-bending dominated. The mode pair 17-18 illustrates how a second passband mode exist amongst the first passband modes of the three-DOF system only, The plots show the blade amplitudes versus blade number.

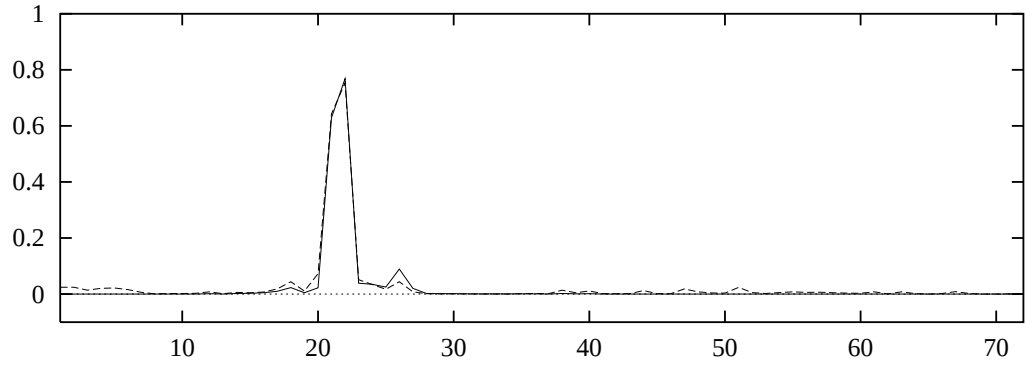

(a) Mode 52 of **1Bb** (———) *vs.* mode 55 of **1Bd** (– – –).

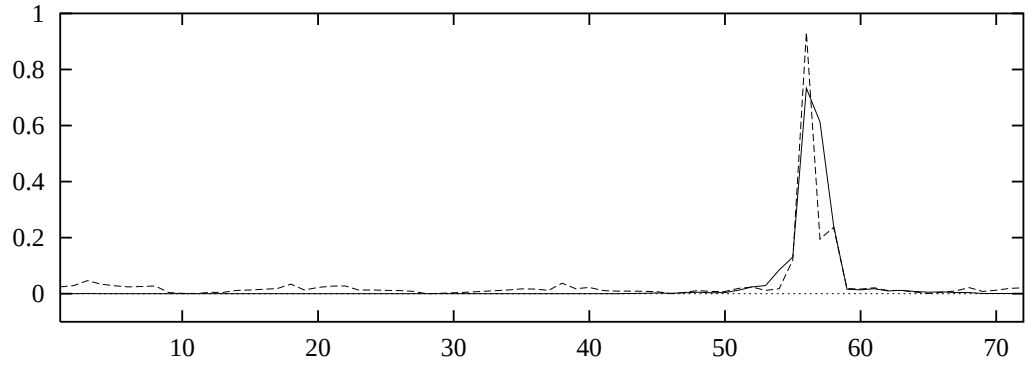

(b) Mode 71 of **1Bb** (———) *vs.* mode 76 of **1Bd** (– – –).

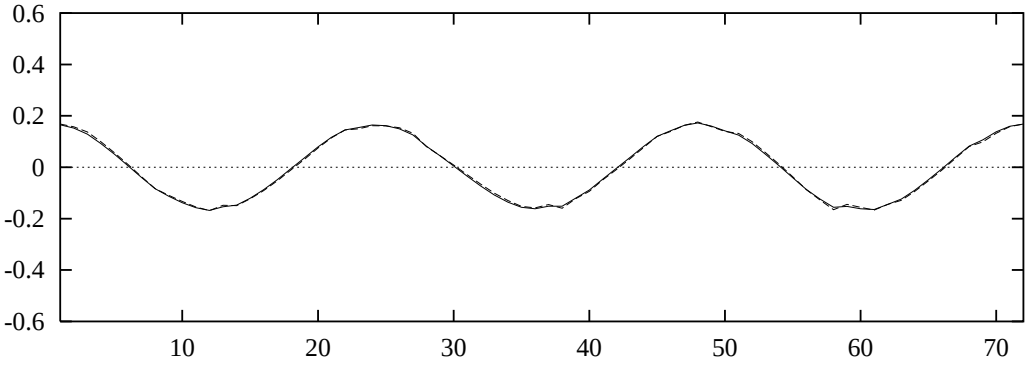

(c) Mode 78 of **1Bb** (———) *vs.* mode 78 of **1Bd** (– – –).

Figure 7.14 The mode pairs 52-55 and 71-76 illustrate how second passband modes exist amongst the first passband modes of the three-DOF system only. The exact location of these modes is difficult to obtain. Mode 78 is the first mode in **1Bd** after the blade modes. It is identical to mode 78 for **1Bb** but the corresponding natural frequencies are quite different The plots show the absolute value of the blade amplitude versus blade number.

of the three-DOF system within the first passband modes.

Figure 7.14(c) shows the sudden disappearance of localization as we move into the second passband. In the figure, we observe that mode six of the second passband (mode 78) is a disk-dominated mode. The difference in the mode numbers between the two- and three-DOF per bay systems has vanished and the two modes agree perfectly. Due to an incorrect fit at this frequency in the two models, the corresponding natural frequencies do not match well.

Comments

- Disk-dominated modes are little affected by mistuning.
- Blade-dominated modes undergo drastic changes when mistuning is introduced, to become localized to a few blades. Localization is severe for higher numbers of nodal diameters.
- The localization factor is calculated with respect to the coupling coordinates (the disk-DOF's) and does not account for local blade resonances. Therefore, the localization factor may underestimate the "super-localization" experienced by the blade displacement pattern.
- In general, there is good agreement between the modes of the three-DOF and two-DOF per sector models. The main discrepancies occur in the curve veering region and in the low-nodal diameter disk-modes. It is believed that the three-DOF per bay model provides a better approximation of the system dynamics.

7.1.4. Tuned and Mistuned Forced Responses

In the forced response case each blade DOF is excited by a harmonic force. In models with one blade-DOF, the dimensionless force amplitude, $\bar{F} = F/k_b$, is taken to be unity (this is not restrictive since the structural system is linear). This is not possible in the two-blade DOF models because the model features two blade forces. In this case we calibrate the two blade forces in such a way that the tuned forced response will agree with that of the one-blade DOF models. The excitation is of engine order 22. In addition, viscous and structural damapings are included in the model, as follows: structural, hysteretic damping of value 0.1% in the disk and blades (rendering the stiffnesses k_d, k_{d1}, k_{d2}, k_{d3}, and k_b complex), and viscous damping in the blade DOF in order to simulate aerodynamic damping. For most cases considered, and unless otherwise stated, the viscous damping value is $\zeta = 1\%$. Again, the two-DOF model features two damping values that must be calibrated to yeild results similar to that of the one-blade DOF models. All models — the two two-DOF, the one two-blade-DOF model and the bi-coupled, three-DOF per bay models — are analyzed.

In the discussion below we shall attempt to adhere to the following terminology. We will make a distinction between the terms **peak** or **resonance** amplitude on the one hand and **largest** amplitude on the other. A peak, or a resonance amplitude denotes an extreme amplitude of a blade, with respect to the excitation frequency, whereas a largest amplitude denotes, at some given excitation frequency, the largest blade amplitude throughout the rotor assembly. Futhermore, we will refer to the **maximum** amplitude which we define as the *largest peak* amplitude, namely the largest amplitude in any blade, at any frequency.

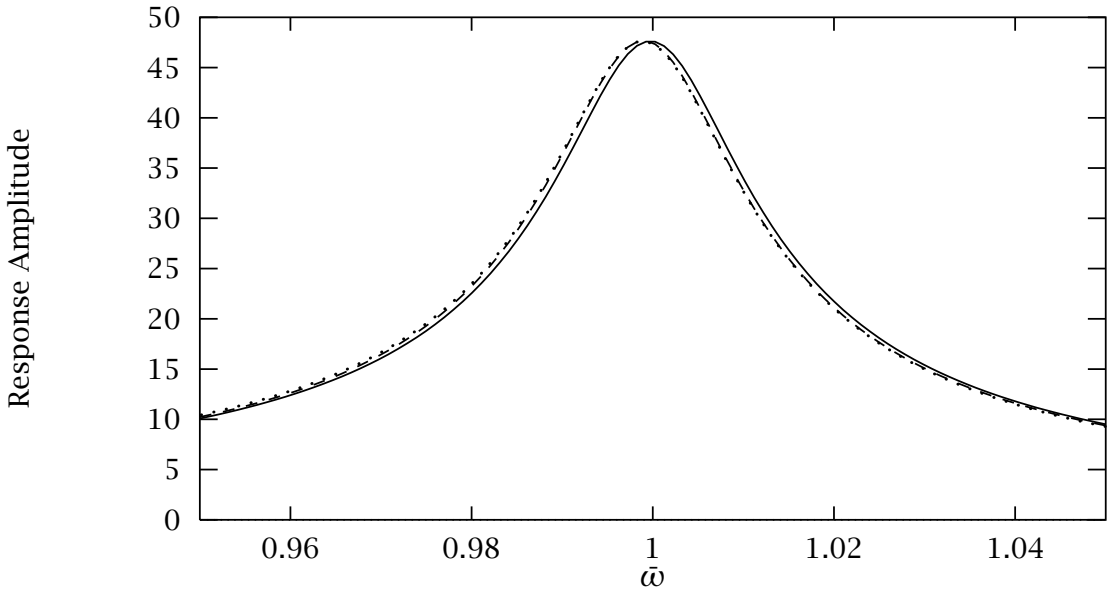

Figure 7.15 Frequency response of tuned assemblies of types **1Ba** (———), **1Bb** (– – –) and **1Bd** (· · · · ·) for engine order 22 excitation.

Tuned Assembly Response

Let us first compare the frequency response of the systems that feature one blade degree of freedom, systems **1Ba**, **1Bb** and **1Bd**, in their tuned state. We select blade viscous damping $\zeta = 1\%$ and a unit forcing of the blade degree of freedom. Figure 7.15 displays the frequency response. All blades experience the same response amplitude, which is plotted versus frequency for all the models at engine order 22 excitation. The response of a tuned assembly is characterized by a single peak, as the excitation is orthogonal to all constant interblade phase angle modes but one. Immediately obvious is the good agreement between the responses of the two two-DOF per bay systems and the bi-couped three-DOF per bay system. This is truly remarkable considering the very different structural parameter sets that characterize these systems. Note that the good agreement of the peak frequency is insignificant because the frequencies are dimensionless and may be arbitrarily scaled.

In order to make a comparison with model **1Bc** which features two degrees of freedom, a calibration of the forcing and damping is required, as well as to the previously mentioned scaling of the dimensionless frequency with the value 1.423. To study the effect of this manipulation we create forcing/damping conditions for system **1Bc** such that the peak amplitude and the width of the peak matched that of the other systems.

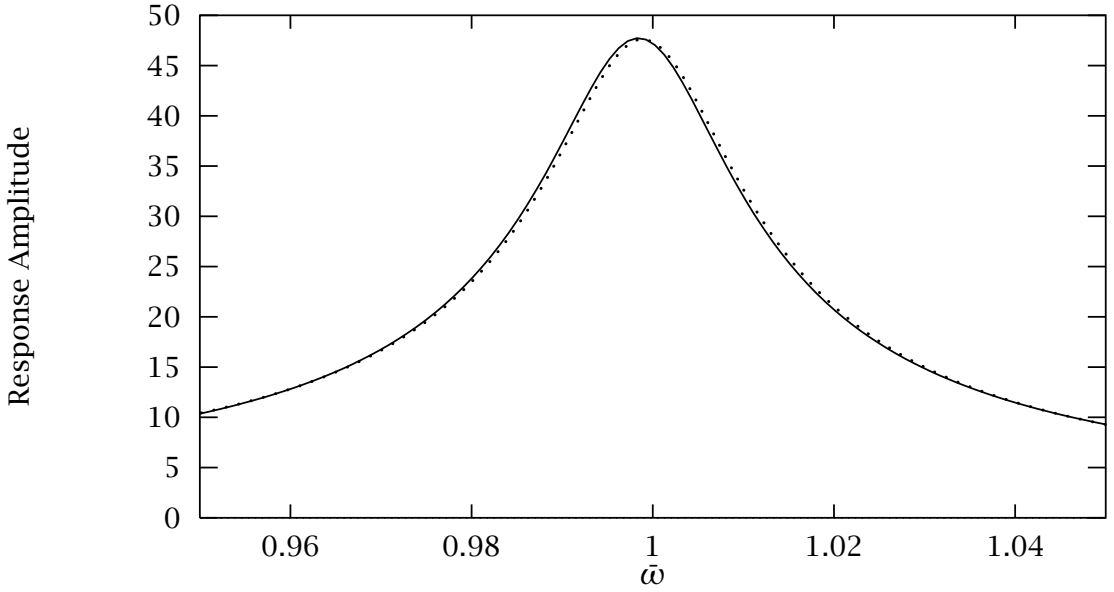

Figure 7.16 Frequency response of tuned assemblies of types **1Bc** (———) and **1Bd** (· · · · · ·) for engine order 22 excitation.

A good approximation was found for the following values.

$$\begin{aligned} F_1 &= 0. \\ F_2 &= 0.56154 \\ \zeta_1 &= 0. \\ \zeta_2 &= 0.008 \end{aligned} \tag{7.8}$$

The resulting frequency response is compared with that of system **1Bd** in Fig. 7.16.

Hence, we have access to four dramatically different systems that all exhibit identical forced response behaviour in the absence of mistuning. Next we examine the effect of mistuning.

Deterministically Mistuned System Response

One primary goal in analyzing the forced response of mistuned structures is to determine the increase in blade response amplitude compared to the response amplitude of the tuned system. For *one* mistuned assembly with some mistuning pattern, mistuning effects can be characterized by the ratio of the maximum response amplitude of the mistuned system to the amplitude of the tuned system.

Figure 7.17 displays the frequency response of blade 63 in the 72-blade blisk and provides a comparison with the maximum response amplitude of any blade throughout the rotor. Since for the mistuned system the excitation is no longer orthogonal to the mistuned mode shapes, the frequency response of any give blade ought to feature a number of resonant peaks equal to the number of blades. However, many of these peaks are small and, as shown in Fig. 7.17(a), the presence of significant damping causes the resonant peaks to decrease in height and increase in width. This results in the merging of many of the 72 resonant peaks, such that the frequency response of blade 63 features primarily one large resonant peak. It is noteworthy that the resonant amplitude of blade 63 is significantly larger than the tuned amplitude, by about 30%. Also, the primary resonant frequency for blade 63 is higher than the tuned resonant frequency, and it can be easily verified that it is nearly equal to the blade-alone frequency of the 63rd blade.

In Fig. 7.17(b), the envelope of the individual blades' frequency responses, *the largest response,* feature a large number of resonant peaks. It suggests that the various blades in the mistuned blisk reach their peak amplitude amplitude at different resonant frequencies, giving rise to a relatively broad range of resonant frequencies. These resonant frequencies correspond approximately to the blade-alone natural frequencies of the individual mistuned blades. In order to confirm this, observe how the response of the 63rd blade corresponds precisely to one of the peaks of the maximum frequency response. Similarly all peaks in Fig. 7.17(b) correspond to the resonant peak of one blade on the blisk. However, the number of resonant peaks in Fig. 7.17 is smaller than the number of blades, indicating that some blades feature a resonant amplitude that is lower than the maximum amplitude envelope, *i.e.*, the resonant peaks of some blades are overshadowed by the peaks of other blades. The above observations confirm that the blades of this weakly coupled mistuned rotor respond essentially like single-DOF oscillators, at about their blade-alone (mistuned) natural frequency. Another interpretation is that as the excitation frequency is swept, the system responds sequentially in the various localized modes in one localized mode after the other, each of which features primarily the vibration of a particular blade. It is the highest peak of the largest amplitude curve in Fig. 7.17(b) that defines the *maximum amplitude* for

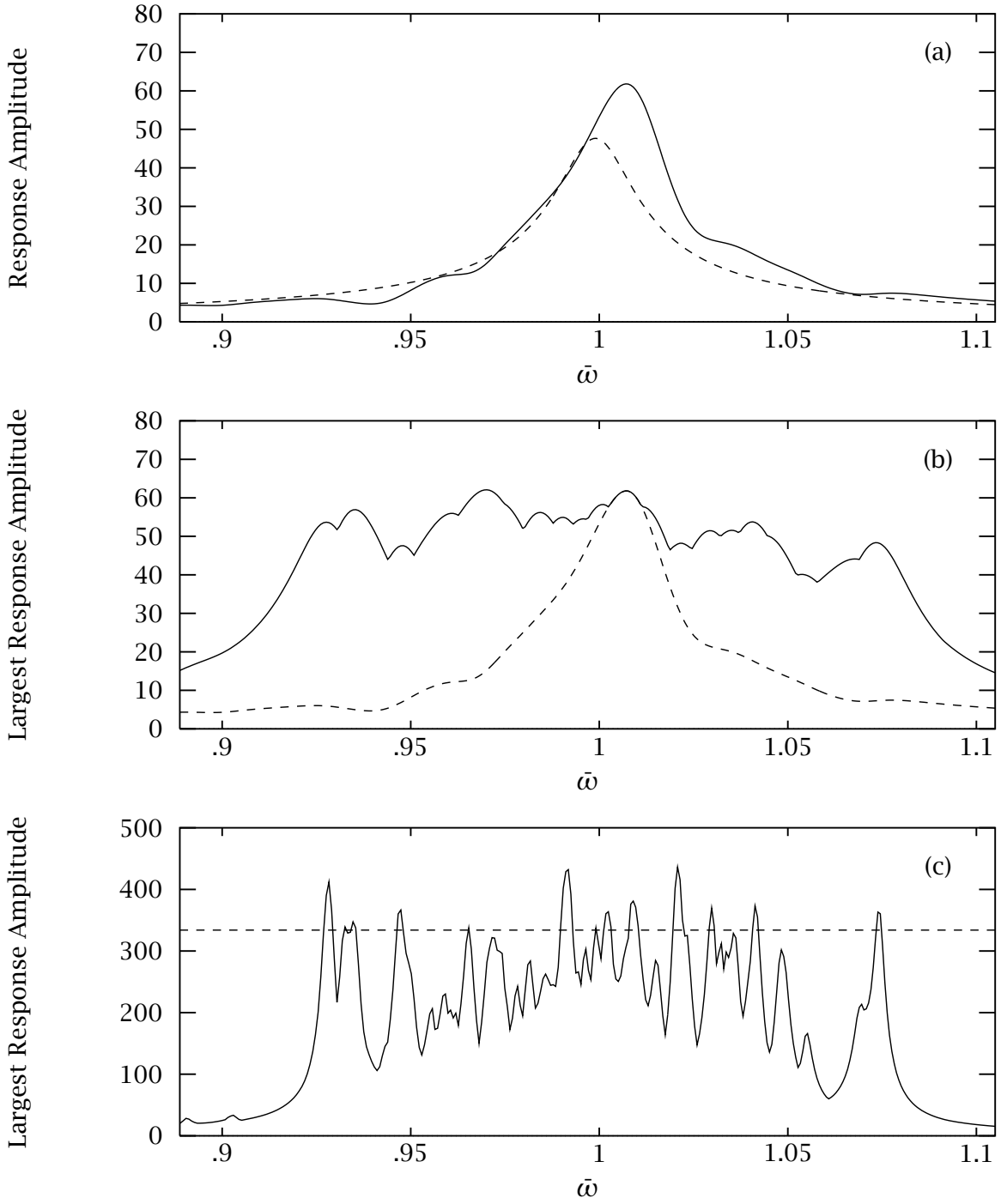

Figure 7.17 **(a)** Frequency response of the 63rd blade in a mistuned blisk (———) and of the corresponding tuned system (– – –). ζ = 1%. **(b)** Largest frequency response of any blade in the mistuned blisk (———) together with the response of the 63rd blade (– – –). ζ = 1%. **(c)** The largest frequency response in the weakly damped blisk (———) is compared with the peak response of the equivalent tuned blisk (– – –). ζ = 0.1%. All figures: Model **1Bb**, $C = 22$.

this particular mistuned rotor.

Figure 7.17(b) depicts the largest response of a relatively strongly damped rotor with a large number of blades. Since damping is strong, the individual response peaks are relatively wide, and the high number of blades ensures high density of peaks. Clearly, the largest response amplitude for a more weakly damped rotor with fewer blades would look considerably different with narrow, clearly separated peaks. Whereas the curve in Fig. 7.17(b) depicts largest response that is greater than that of the tuned system throughout the peak response range, we could easlily imagine systems of which the opposite is true. Figure 7.17(c) depicts the largest response of a 72 blade blisk (model **1Bb**) with only 0.1% viscous damping. Its largest response is predominantly lower than the peak tuned response amplitude. This will become important in the following discussion.

In summation, the most important effects of mistuning on the forced response appear to be:

- a broadening of the resonant frequency range, which corresponds to the range of the blade-alone mistuned frequencies.
- the occurrence of localized forced responses, whereby at a given frequency one or few blades of the rotor undergo vibration of significant amplitude, while the other blades remain nearly quiescent.
- an increase in largest response amplitude in — but not necessarily throughout — the resonant range. Three factors govern the dispersion of the largest response amplitudes as frequency is varied. They are:
  - The mistuning strength: the greater the mistuning, the wider the spread between the mistuned blade-alone natural frequencies and thus between the resonance frequencies.
  - The damping level: the weaker the damping, the narrower the resonant peaks and thus the greater the low-amplitude gap between them.
  - The number of blades: the larger the number of blades, the larger the number of peaks in the resonant frequency range and thus the greater the probability for a mistuned system to experience a large amplitude.

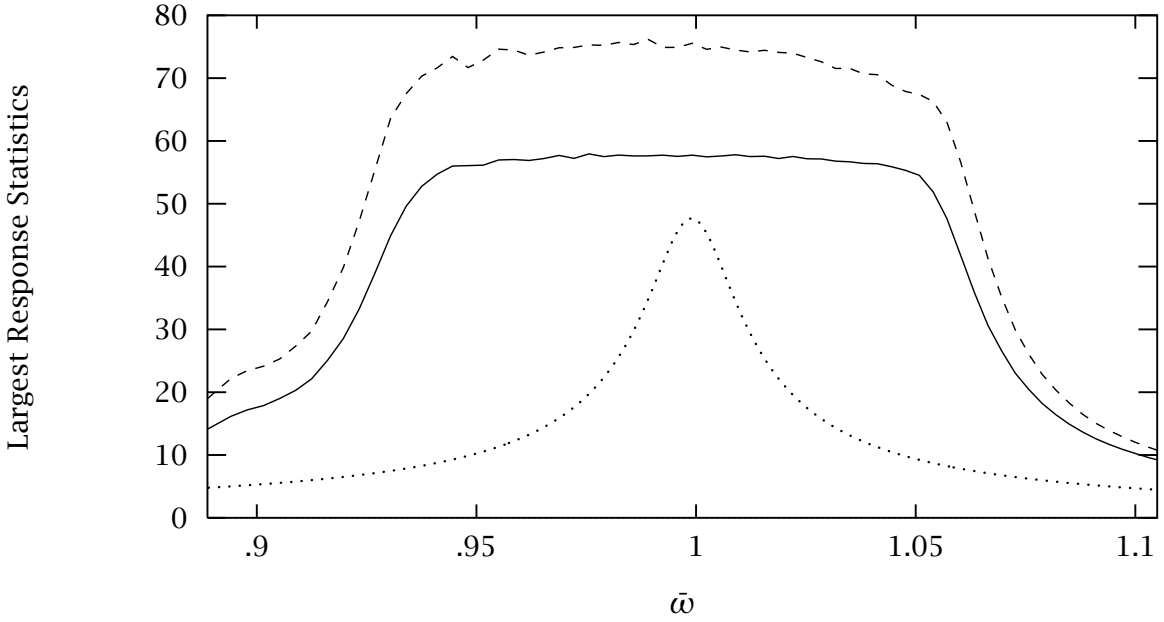

Figure 7.18 Monte Carlo simulations yield the mean largest response (———) and 2.7 σ-bound (− − −) of largest response in the blisk. The tuned system response is (· · · · ·). Model **1Bb**, $C = 22$, $\zeta = 1\%$.

Stochastically Mistuned System Response

When the mistuning pattern is not known deterministically but only in a statistical way, the characterization of mistuning effects with a single scalar is not possible any longer, and a stochastic description of the maximum amplitude is required. This is achieved here through the use of Monte Carlo simulations which, for example, yield such information as the probability density function of the ratio of the maximum response amplitude to the tuned response amplitude. This statistical description allows us to characterize the average increase in maximum response amplitude for all mistuned systems and the proportion of mistuned systems that experience a maximum response amplitude which is greater than some value.

Hence, the next level of integration comes in the form of Monte Carlo simulation of the mistuned blisk's forced response. The numerous mistuning patterns used in the simulations were obtained from a random number generator: a uniform distribution was chosen, of mean equal to the blade-alone first bending natural frequency and of standard deviation 3.6% (this translates into a $s = 7.25\%$ standard deviation of mistuned blade stiffness). This means that the blade-alone frequencies never deviate from the blade-alone mean frequency by more than $\sqrt{3} \times 3.6\%$ of its value. At each frequency of the frequency sweep a large number of mistuned assemblies is generated

and for each assembly the largest amplitude is recorded. These largest amplitudes are ensemble averaged and their standard deviation calculated for each value of frequency.

The Monte Carlo simulations thus yield approximations of the mean and standard deviation of the maximum response amplitude throughout the rotor at each frequency. We found that reasonable accuracy is achieved through the consideration of approximately 1000 realizations of mistuned systems. Figure 7.18 depicts the mean of the maximum response amplitude of any blade at a versus excitation frequency which is directly available from the Monte Carlo simulations. Also featured in Fig. 7.18 is an approximation of the 99th percentile of the maximum amplitude. At a given frequency, the 99th percentile of the maximum response amplitude is defined as the value of the maximum response amplitude such that 99% of all occurrences of mistuned systems feature maximum response amplitudes that are smaller: that is, only 1% of mistuned systems feature a maximum response amplitude that exceeds this bound at that frequency. The approximation depicted in Fig. 7.18 is based on the assumption that the 99% maximum amplitude percentile is located at approximately 2.7 standard deviations above the mean. This factor was determined empirically from subsequent observations of the probability density function of the maximum amplitude in various cases.

An interesting feature of the Monte Carlo simulation of the largest frequency response is the flatness of the mean and 99% percentile frequency response curves in the range of large amplitudes. This is due to the fanning out of natural frequencies of the mistuned assembly which is shown in Fig. 7.6. Indeed the width of this flat top corresponds to the width of the uniform distribution of the blade-alone natural frequencies used in the simulations. Besides the broadening of the resonant frequency range, mistuning causes a significant increase in the largest response amplitudes: relative to the tuned system, the increase in the mean of the maximum response is about 21% over the resonant frequency range, and that for the 99th maximum amplitude percentile is about 58%. At this point it is noteworthy to emphasize the high sensitivity of the forced response of the blisk to mistuning: a frequency mistuning of 3.6% may result in a 58% increase in the response amplitude of at least some of the blades!

We now apply a Monte Carlo simulation analysis to the mistuned forced response of all the models, **1Ba**, **1Bb**, **1Bc** and **1Bd**. Figure 7.19 depicts the result of the Monte Carlo simulations of the largest amplitude for the various systems. The frequency responses of the different systems display very similar features and are in good overall quantitative agreement. Nevertheless, the response amplitudes of the bi-coupled system, **1Bd** are a bit smaller that those of the mono-coupled systems, **1Ba**, **1Bb** and **1Bc**.

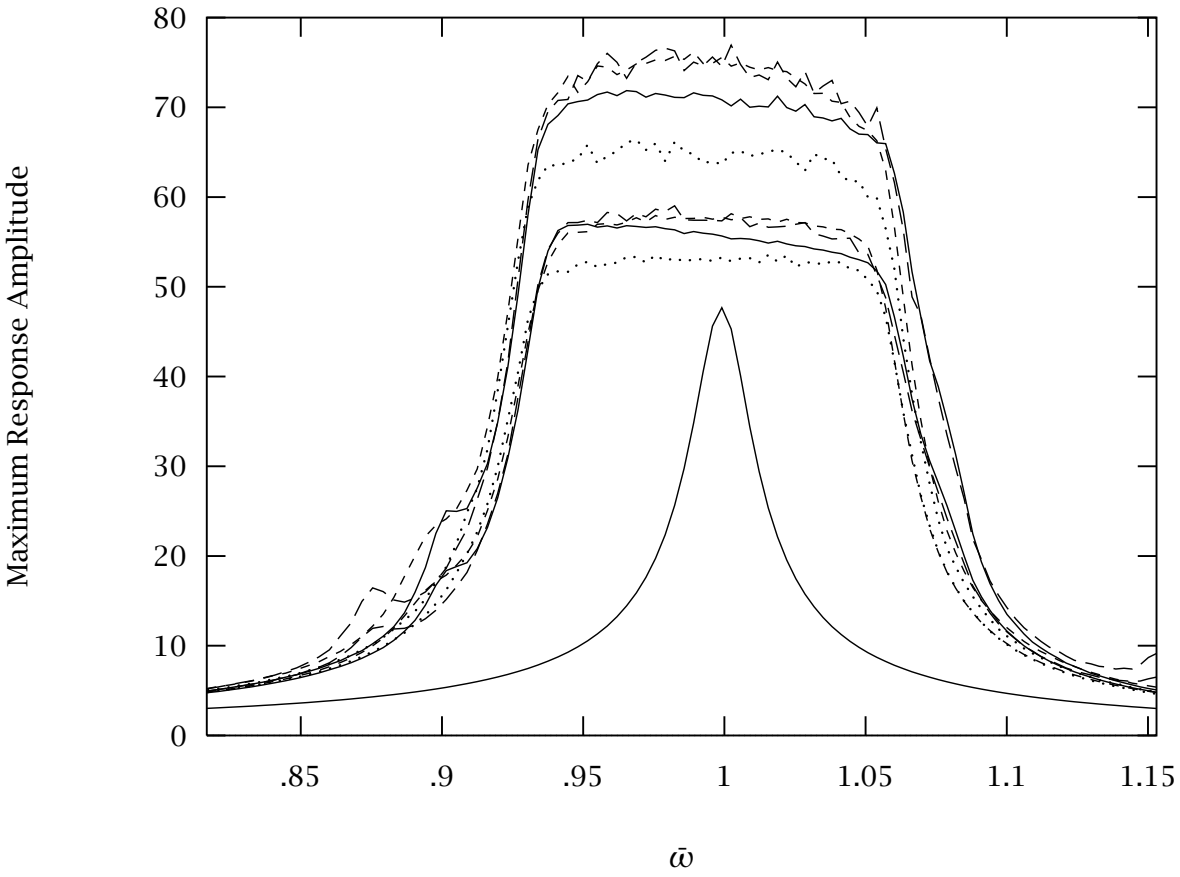

Figure 7.19 Monte Carlo simulations of the largest frequency response of various models of mistuned assemblies. The bottom curve (———) denotes the tuned system response. The mean largest amplitude forms the middle group of curves; the 2.7 σ-bound of the largest amplitude form the top group of curves. The line types are defined according to the following format. Models **1Ba** (———), **1Bb** (– – –), **1Bc** (— —) and **1Bd** (· · · · · ·). Viscous damping is $\zeta = 1\%$, $\zeta_1 = 0\%$ and $\zeta_2 = 0.8\%$ ($s = 7.25\%$). Dimensionless frequency of **1Bc** is multiplied with 1.423.

Our interpretation of these results are as follows. Systems **1Bb** and **1Bc** have a very similar frequency curve fit (see Figs. 7.3 and 7.4) which yeilds a similar approximation of the modal density and interblade coupling. This agreement translates into very good agreement on the mistuning effects. System **1Bd** features an even more accurate curve fit (see Fig. 7.5) that predicts an even lower modal density, *i.e.,* higher interblade coupling which we evidence as leading to weaker mistuning effects. System **1Ba** (Fig 7.2) blatantly overestimates the modal density (underpredicts interblade coupling) which also leads to weaker mistuning effect than those predicted by models **1Bb** and **1Bc**. For a probable explanation we refer the reader to Fig. 6.5. Model **1Ba**

has very weak interblade coupling and belongs to the left side of the hump. Model **1Bd** has considerably stronger interblade coupling placing it to the right of the hump. Models **1Bb** and **1Bc** with their intermediate levels of coupling belong on the hump. It is without question model **1Bd** with its most accurate approximation of interblade coupling that most accurately predicts mistuning effects in the blisk.

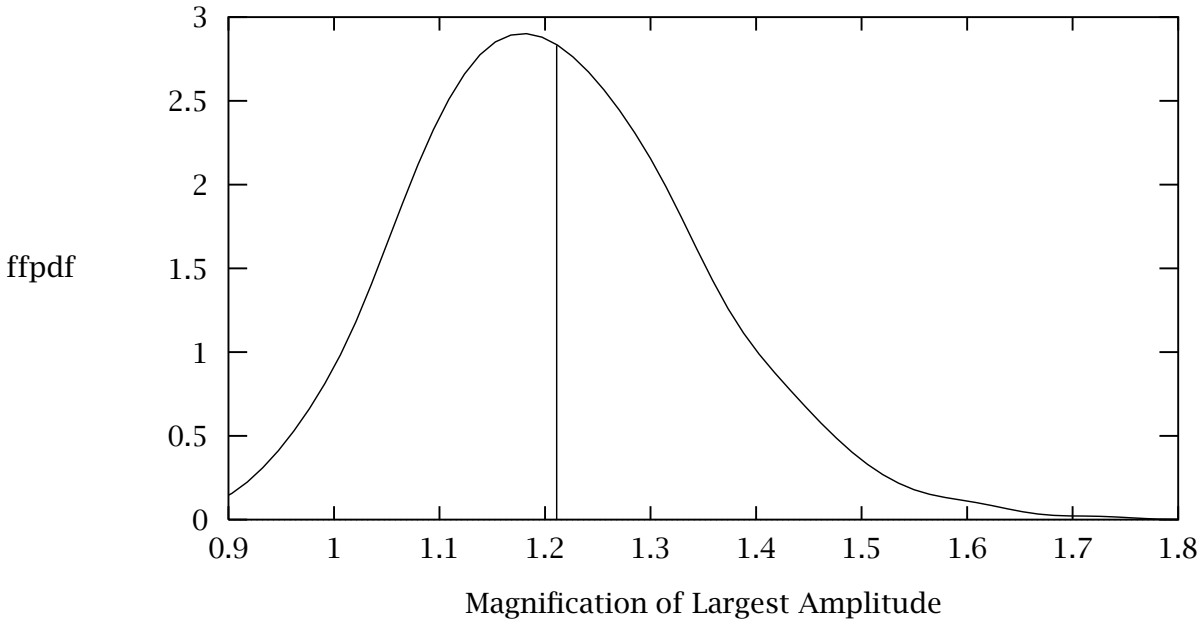

Figure 7.20 An approximation of the fixed frequency probability density function (ffpdf) is calculated at the excitation frequency which yields the largest value for the 99% percentile of the largest response amplitude. The "magnification of largest amplitude" is defined as the ratio of the largest amplitude of any blade in a mistuned rotor to the peak response amplitude of the corresponding tuned rotor. The vertical line marks the mean. Model **1Bb**, $C = 22$, $\zeta = 1\%$, $s = 7.25\%$.

Statistics of Largest Response

The largest response amplitude has an unknown statistical distribution. This distribution may vary greatly, depending for instance on the interblade coupling (see Chapter VI). Therefore, it is not sufficient to calculate the mean and standard deviation if information about confidence intervals is required. For instance, if it were known that largest response amplitude had a Gaussian distribution, the 99th percentile would be 2.33 standard deviations above the mean. However, since we do not know the distribution, the 99th percentile must be calculated explicitly from the Monte Carlo simulation output.

Therefore, the next level of sophistication for the forced response results is in the form of an approximation of the *fixed frequency probability density function* (ffpdf) for the maximum amplitude, which is calculated at the excitation frequency for which the 2.7σ-bound of the largest amplitude (or the approximation of the 99% percentile) in Fig. 7.18 is the greatest. Figure 7.20 presents the probability density function as a function of the magnification of largest amplitude due to mistuning, where the latter is the ratio of the largest amplitude of a mistuned system to the peak response amplitude of the tuned system. Observe that the ffpdf of the largest amplitude is Gaussian-like but skewed, with a long tail toward the high amplitude range, such that the magnification of the largest amplitude is larger than 58% for 1% of all possible realizations of mistuned systems, at that frequency. This statistical information leads to the prediction of confidence intervals for the maximum amplitudes, and as such the ffpdf's of the largest amplitude do provide very useful information which could be used effectively at the design stage. Obtaining the ffpdf of the largest response amplitude is a computationally intensive operation, however, even for a single excitation frequency as it is done herein. For a convergence of the 99% percentile value with 0.1% accuracy, approximately 30,000 realizations are required, yielding acceptable cost. Since the 99th percentile is likely to be the value most useful to a designer, it is a parameter z, defined as the number of standard deviations between the mean and the 99th percentile that was used as a test for convergence. Unfortunately, convergence is remarkably slow due to the low probability density in the neighborhood of the 99th percentile.

It is only through this type of analysis that the 99% percentile approximated in Fig. 7.18 by the 2.7σ-bound may be accurately determined. A counterintuitive feature of the ffpdf depicted in Fig. 7.20 is that there is a non-negligible probability (namely 0.05) that the largest response amplitude of the mistuned structure be smaller than that of the tuned assembly, *at the frequency at which the ffpdf is computed*. This feature is a direct consequence of studying the statistics at a fixed frequency. It occurs because the lower tail of the ffpdf is largely populated by assemblies that do not have

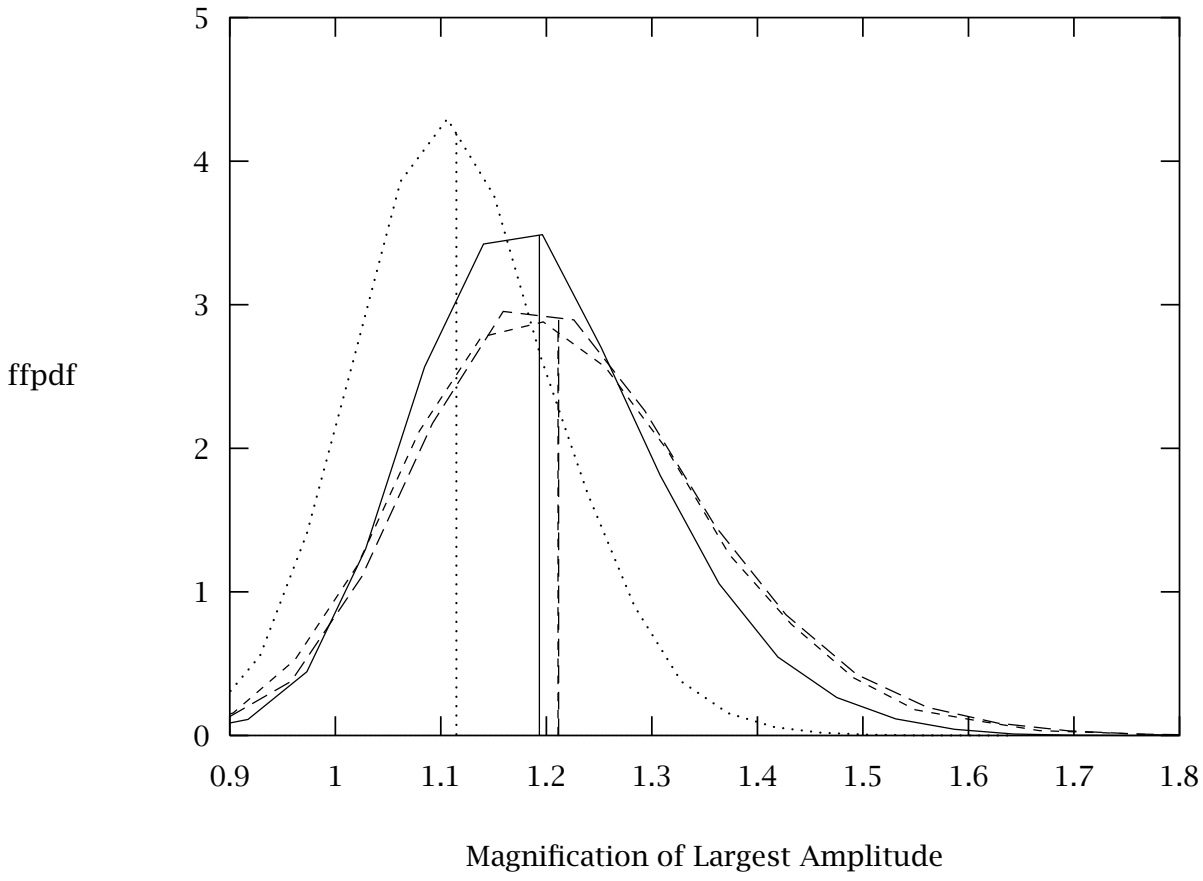

Figure 7.21 Fixed frequency probability density function of the largest response amplitude (calculated at the frequency which yields the greatest value of the 2.7σ-bound of the largest amplitude) for the various models of mistuned assemblies. Vertical bars denote the mean of the largest amplitude. The engine order if the excitation is 22. The line types are defined according to the following format. Models **1Ba** (———), **1Bb** (− − −), **1Bc** (— —) and **1Bd** (· · · · ·). Viscous damping is ζ = 1%, ζ_1 = 0% and ζ_2 = 0.8% (s = 7.25%)

a resonance at the frequency in question (see Fig. 7.17(c)).

As an example of the usage of the ffpdf, one might observe that only a very small area is contained under the curve above the amplification value 1.6, hence it is very improbable to find a system which has a largest amplitude that is 60% larger than predicted by the tuned analysis.

Figure 7.21 depicts the result of a fixed frequency analysis of the probability density function of largest amplitude. We find the continued good agreement between models **1Bb** and **1Bc**. Again, we contend that it is model **1Bd** with its fine model of the interblade coupling that best predicts the mistuning effects.

Statistics of Maximum Response

Next, we should mention the "ultimate" in statistical analysis of the forced response of bladed disks, namely the full-blown calculation of the probability density function for the *maximum* response amplitude (the largest response at any excitation frequency). This would be achieved as follows. For each of realization of mistuned systems, record the peak resonant response of the assembly, *i.e.*, the greatest value of the response amplitude at any frequency and for any blade throughout the rotor. Then calculate the statistics of this ensemble of maximum amplitudes, yielding the mean, standard deviation, and perhaps even pdf of the largest amplitude. Clearly this is a task of gargantuan proportions, requiring a full high-resolution frequency scan for each of the many thousand systems in the Monte Carlo simulation! Also note that this approach yields information in an extremely integrated form, as a *single* number—the maximum response amplitude—characterizes one realization of mistuned systems. Figure 7.22 depicts the comparison of the largest fixed frequency response probability density function and the probability density function for the maximum response. The maximum amplitude pdf does not feature a a tail reaching below the amplitude of the tuned system, since it is very unlikely that a mistuned system has its largest resonant peak be smaller than that of the tuned system.

Due to the great expense involved in the calculation of the statistics of the maximum response statistics, no comparison was performed for the various models. Only model **1Bc** was analysed in this way.

Figure 7.22 illustrates the different results obtained for the statistics of the largest blade response amplitude depending on whether frequency is swept to find the peak response of each mistuned system or if the response of the mistuned system is calculated at a predetermined frequency (chosen to be the frequency that leads to the maximum of the mean plus 2.7 times the standard deviation). As expected, the difference in the lower tails of the distributions is great. This can be explained by the fact that in the fixed frequency analysis, the chosen frequency may fall between peaks of the response for some mistuned systems. The fixed frequency probability density function could be *incorrectly* interpreted as predicting the existence of mistuned systems that possess lower largest amplitude than that of the tuned system. The truth is that the largest amplitudes of these systems occur at different frequencies. When the statistics are analyzed using a frequency sweep, thereby finding the largest resonant amplitude in each individual mistuned system, we find that it is extremely unlikely to find a mistuned system with a smaller peak response than that of the tuned system. Indeed, the probability of finding a mistuned system with *less* than a 20% increase in largest amplitude is negligible.

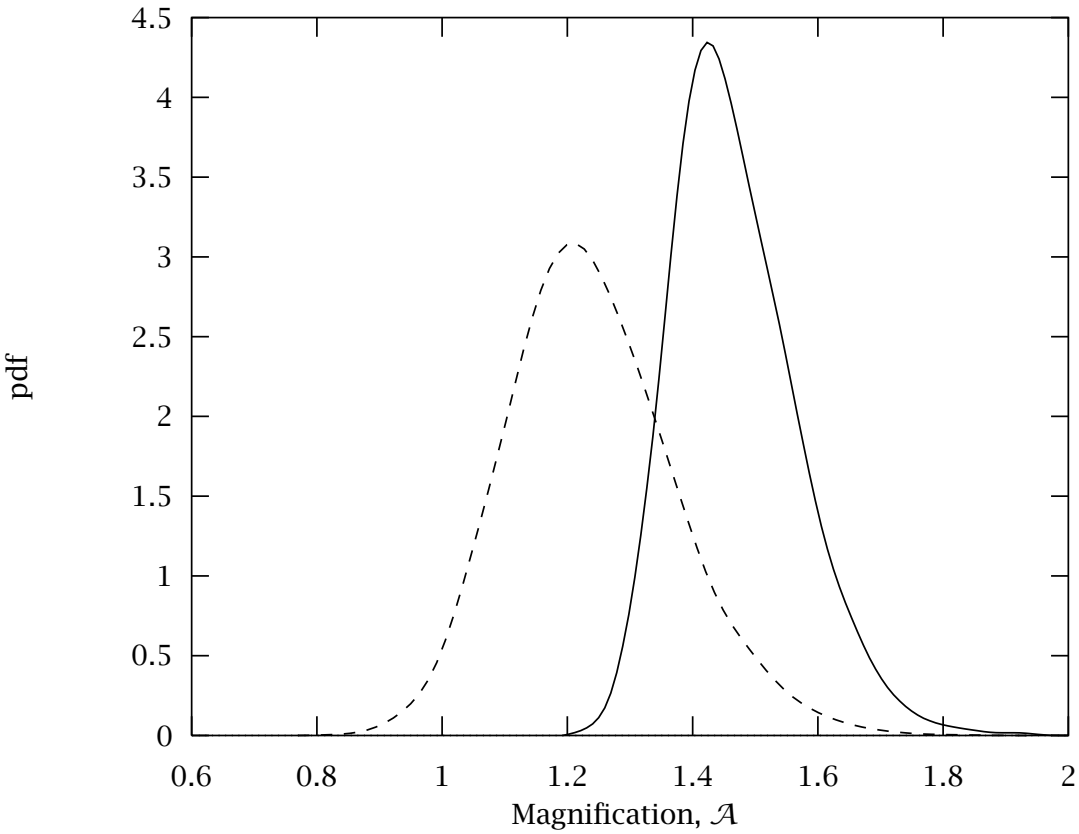

Figure 7.22 Comparison of a probability density functions of the largest response amplitudes. (———), by sweeping frequency to find the maximum resonant peak; (– – –) at a fixed frequency (the frequency leading to the greatest value of the mean plus 2.7 times the standard deviation in a frequency response analysis of a mistuned system). (**1Bc**, s = 7.25%, C = 22)

In the fixed frequency case, the 99th percentile value is approximately 1.6 times the tuned resonant amplitude. Using a frequency sweep, we find that the 99th percentile of the amplitude magnification statistics is approximately 1.75. This means that in a production run of rotors of this type, when run at a specific speed, only 1% of the rotors are expected to exceed a largest blade amplitude that is 60% greater than would have been predicted by a cyclic symmetry analysis. However, when the rotor runs through a range of rotational speeds, there is a 1% probability that it will experience an amplitude that is 75% greater than that of the tuned rotor. Thus, the fixed frequency analysis of the statistics seems to be a rather poor approximation of the actual statistics, although the fixed frequency statistics are perfectly valid in their own right.

The analysis of the actual response statistics, requires the incorporation of a full frequency sweep, and is a tremendous computational challenge. The efficient coding of the problem, in addition to having access to powerful workstations, has allowed us to tackle this type of analysis, albeit for very simple models. The problem has proven slightly less costly than initially expected since the dispersion of the values in the response statistics, when frequency is swept, is more reasonable than when frequency is fixed. This guarantees convergence for a smaller number of realizations of mistuned systems. Recall that for each realization, the peak frequency response amplitude must be calculated, a process which may require hundreds of solutions of the forced response problem at various values of the frequency.

7.1.5. Variation of Mistuning Strength

The results of Chapter VI show that — under certain circumstances — mistuning effects on forced response may not increase monotonically with increased mistuning strength (see Fig. 6.8). An examination of the statistics of the maximum response amplitudes in model **1Bc** (using a frequency sweep) reveal that this is not the case for the group of first bending modes of the 72-blade blisk. Figure 7.23 shows that in this case the mistuning effects do indeed increase monotonically with the strength of mistuning.

What remains to be explained is the absence of a local maximum, such as the one depicted in Fig. 6.8, from the curves in Fig. 7.23. It must be understood that the *humps* in the curves in Fig. 6.8 only occur when specific conditions are met, namely when localization effects are sufficiently large that the assembly features localized modes, yet the coupling is strong enough so that transmission of energy to the localized blade can occur. The value of interblade coupling used to generate Fig. 6.8 was selected such that this effect would be maximized. Generally, the non-monotonous variation of amplitude with mistuning may or may not be observed at other coupling values. For example, for zero interblade coupling, the largest blade amplitude can be easily shown to increase monotonically with mistuning strength. Accordingly, as we had observed in Section 7.1, interblade coupling in the first blade bending modes of the blisk is quite weak. It is, according to Fig. 7.23, too weak for the augmentation of localized blade energy to occur, here precluding the occurrence of the *hump.* However, non-monotonous variation might take place for other blade mode groups of the 72-blade blisk, with stronger interblade coupling.

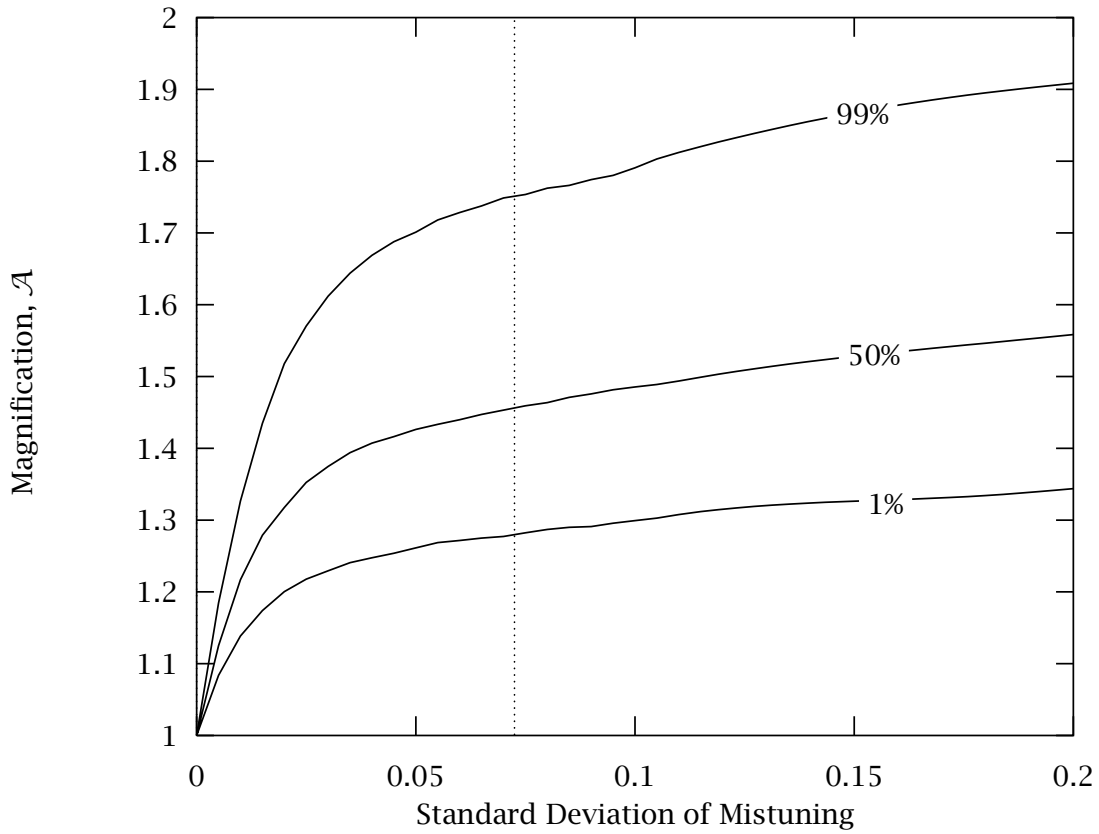

Figure 7.23 Magnification of maximum amplitude due to mistuning as a function of the standard deviation of blade stiffness mistuning, s, for model **1Bc**. The curves show the 1%, 50% and 99% percentiles of the statistics of forced response obtained by a frequency sweep. Engine order of the excitation is 9. The vertical line denotes the 7.25% mistuning strength used throughout the current work.

7.1.6. Variation of Damping Strength

As we noted in the analysis of the forced response statistics of the simple system in Chapter VI, a variation in damping may have a non-intuitive effect on mistuning sensitivity. Figure 7.24 depicts the effect of damping on the amplitude magnification for the 72-blade blisk. Damping is scaled by the a parameter, ν, *i.e.,* the viscous damping ratios are taken as $\nu\zeta_1$ and $\nu\zeta_2$ and the structural damping ratios are $\nu\gamma_1$ and $\nu\gamma_2$. Note that the figure shows the *magnification* of maximum amplitudes with respect to the similarly damped tuned system, not absolute amplitudes. Needless to say, the absolute amplitudes at $\nu = 0.1$ are two orders of magnitude greater than those at $\nu = 10$. Note the non-monotonous variation of the largest amplitude magnification

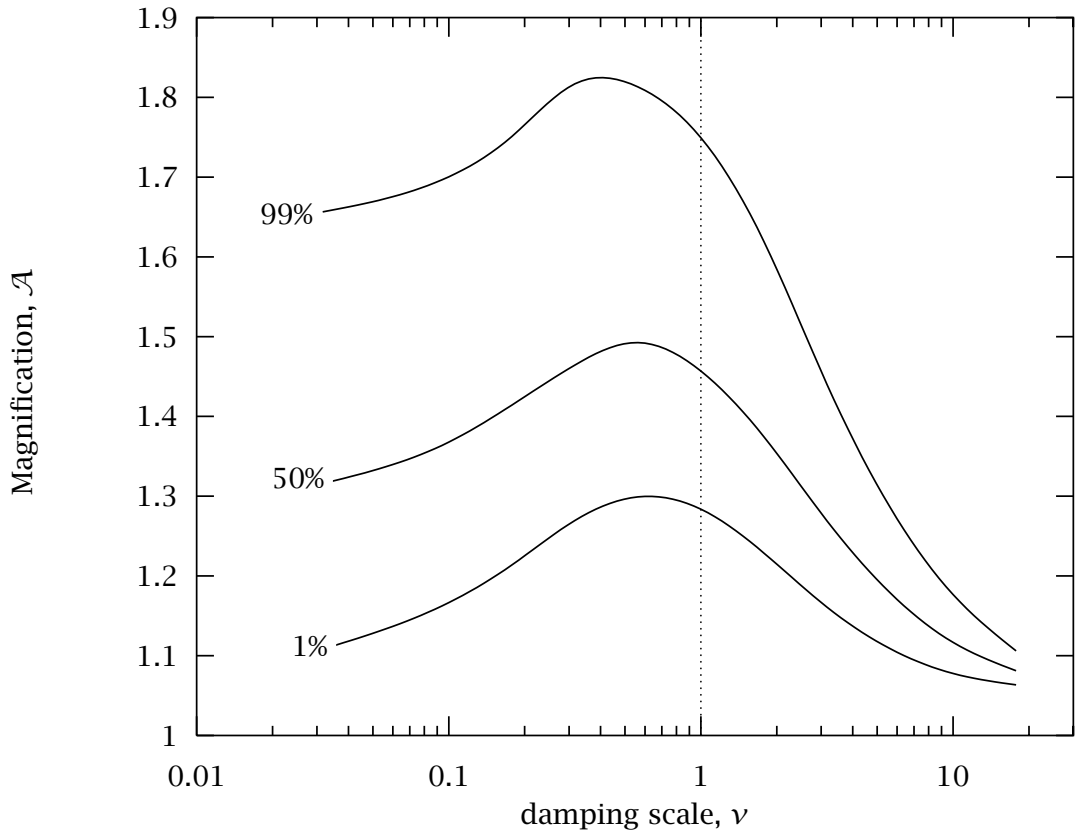

Figure 7.24 Magnification of maximum amplitude due to mistuning as a function of a damping scale, ν, for model **1Bc**. The curves show the 1%, 50% and 99% percentiles of the statistics of forced response obtained by a frequency sweep. Engine order of the excitation is 9. Viscous damping is $\nu\zeta_1$ and $\nu\zeta_2$ and the structural damping ratios are $\nu\gamma_1$ and $\nu\gamma_2$. ζ_1 and ζ_2 are given in Eq. (7.8), and $\gamma_1 = \gamma_2 = 0.1\%$. Mistuning is 7.25%. The vertical line denotes the damping value used throughout the current work.

with damping, according to the results of Chapter VI for the simple model. We find that the 72-blade blisk is operating close to the extreme case of mistuning sensitivity. At higher or lower values of damping, the response of a mistuned structure would be closer to that predicted by a tuned analysis.

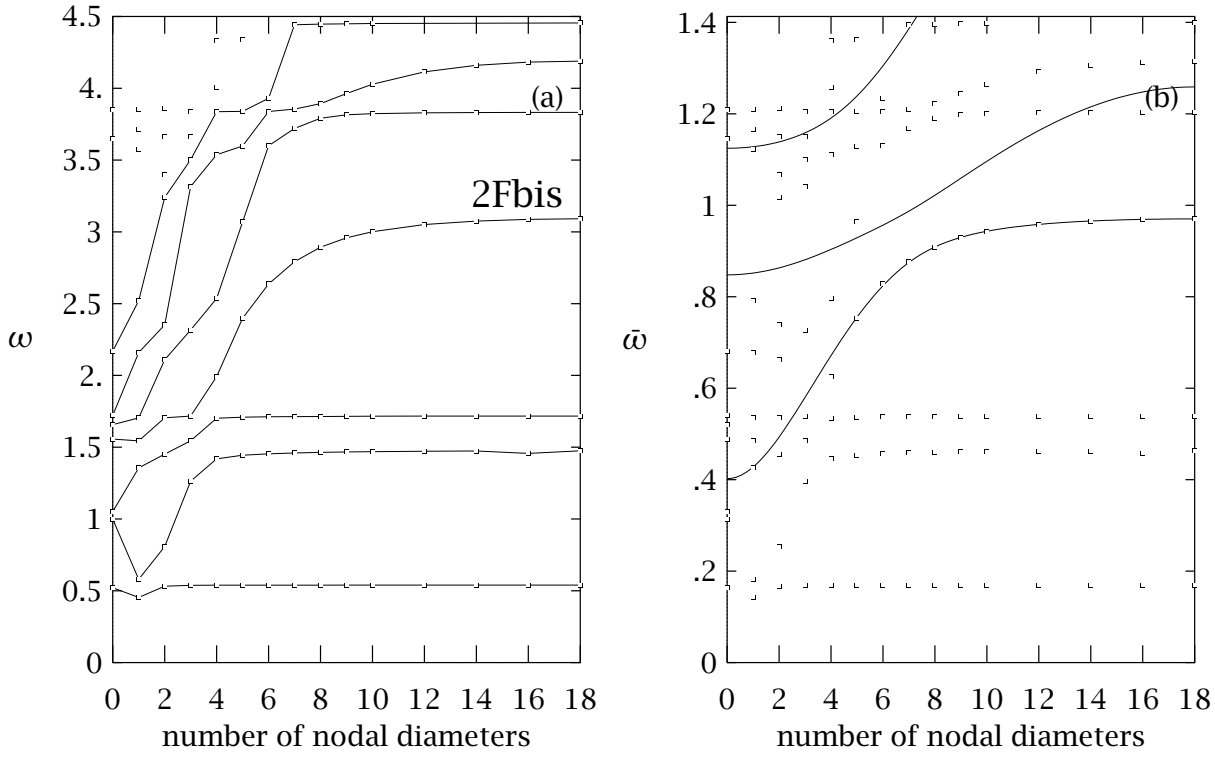

Figure 7.25 (a) The natural frequency data of the finite element model of the 36-blade compressor assembly.
(b) The natural frequencies of a three-DOF system approximate branch 2Fbis. Model **3Ba**.

7.2. Case 2: 36-Blade Compressor — Coupled Oscillators

The second coupled case study, using coupled oscillator models, is that of a 36-blade low pressure compressor stage, which consists of short blades mounted on a drum-type disk. The finite element frequency data is depicted in Figs. 7.25(a) and 7.25(b), organized with respect to the natural frequency number at each number of nodal diameters. In this frequency plot the main areas of interest are the 2Fbis blade mode family, which consists of blade-motion dominated modes in the second blade flexural mode. At this point it is important to note that the curves labeled 2Fbis feature these blade modes only for the higher numbers of nodal diameters (*i.e.*, the flat portions of the curves), but that the 2Fbis blade modes may be present in the other curves at low nodal diameters. In other words, the blade mode groups do not necessarily follow the continuous curves in Fig. 7.25(a). Strictly speaking, the coupled-oscillator models presented here are not suitable for modeling systems of this complexity. Instead, the

Finite Element order reduction technique presented in Chapter III should be used.

Only the 2Fbis group of modes will be investigated. This mode groupe features a frequency curve with a very gradual veering compared with the very sharp veering that we observed for the 72-blade blisk. We expect this study to add a new flavor to the investigation of mistuning effects. This analysis will be far less extensive than that for the blisk, mainly focusing on the differences between the two rotors.

7.2.1. Identification of Model Parameters

The frequency curve 2Fbis features seven frequency points along its very smooth veering. Due to this large amount of detail a three-DOF model was required in order to achieve a reasonable fit.

Model 3Ba: Accurate fit of the 2Fbis curve

A good fit of the first curve requires that all nine frequency constraints be placed on the first curve, and these were chosen to be at nodal diameters 1, 5, 6, 8, 9, 12, 14, 16 and 18. The result is depicted in Fig. 7.25(b). An excellent fit is achieved for nodal diameters 5 and higher. Stretching the lower tail of the 2Fbis curve to lower frequencies was impossible without seriously compromising the fit at higher nodal diameters. Hence the fit at low numbers of nodal diameters is only approximate. However, the frequency spectrum of the compressor stage at these low nodal diameters is so complex that it is not even clear what a better fit would be. Moreover, since the study calls for the analysis of the forced response at engine order 13, this choice of frequency fit was deemed appropriate. The parameters that come out of the identification process are:

$$\begin{array}{lll} \bar{m}_1 = 9972.47 & \bar{k}_{d_1} = 3138.46 & \bar{k}_{c_1} = 2282.42 \\ \bar{m}_2 = 2731.65 & \bar{k}_{d_2} = 5908.37 & \bar{k}_{c_2} = 618.552 \\ \bar{m}_3 = -5214.26 & \bar{k}_{d_3} = -1662.71 & \bar{k}_{c_3} = -1183.53 \end{array} \tag{7.9}$$

Due to the adequacy of the fit no other model was obtained. Clearly, the model proposed here fails to capture the details of the interaction with the unmodeled modes with a lower number of nodal diameters, in the frequency range of interest (see Fig 7.25(b)).

7.2.2. Tuned and Mistuned Forced Responses

For the forced response analysis it was assumed that the standard deviation of blade stiffness mistuning was 5% and that the viscous damping of the blade was 0.5%. Structural damping of blade and disk was set at 0.1%. To highlight the effect of the gradual frequency curve veering, we focus on two excitation of engine orders 7 and 13. This was so that a comparison of mistuning effects at two very different levels of modal density might be achieved (see Fig. 7.25(b)).

Deterministic Mistuned Systems

We examine first the forced response of a single mistuned system when excited by engine orders 7 and 13, respectively. Figure 7.26 illustrates the largest frequency response. In Fig. 7.26(a) we see that since model 3Ba features a low modal density in the neighborhood of the 7-nodal diameter frequency, the fanning out of the natural frequencies due to mistuning is so subtle that the response contains primarily a single resonant peak, whose frequency is close to the resonance frequency of the tuned system. Compare this to Fig. 7.26(b), where there are several distinct peaks due to the fanning out of the natural frequencies caused by the combination of mistuning and high modal density near the 13 nodal diameter frequency. Also note the much larger response due to engine order 13 excitation (for both tuned and mistuned systems). The reason is that the modes close to the 13-nodal diameter frequency are more blade-dominated than the 7-nodal diameter modes.

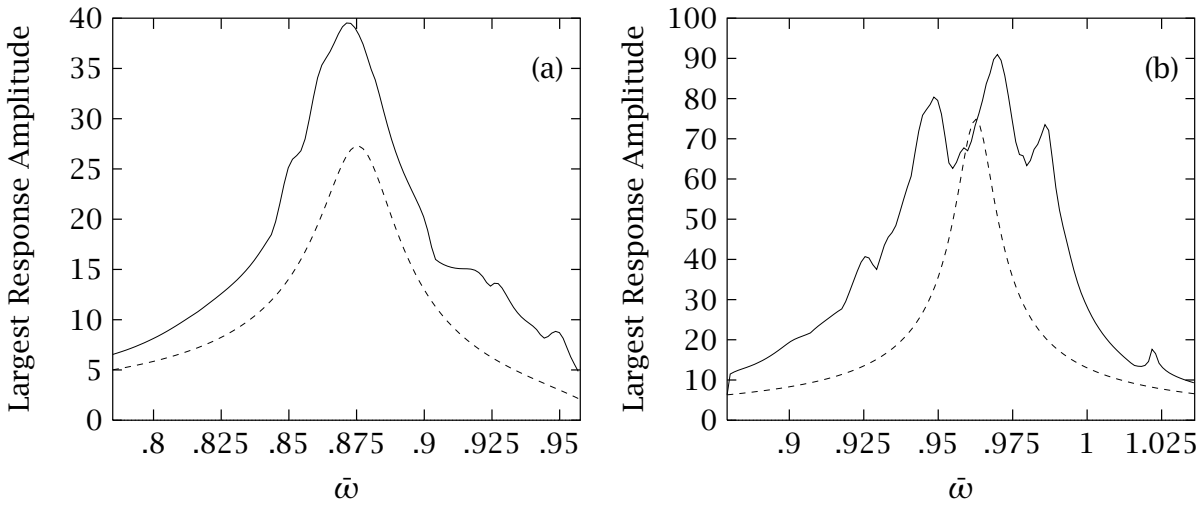

Figure 7.26 The largest frequency response of any blade throughout the assembly, for one realization of the mistuned compressor stage with random mistuning (———), is compared to the response of a tuned system (– – –). The excitation has engine order **(a)** $C = 7$ and **(b)** $C = 13$. Model **3Ba**, $\zeta = 0.5\%$, $s = 5\%$.

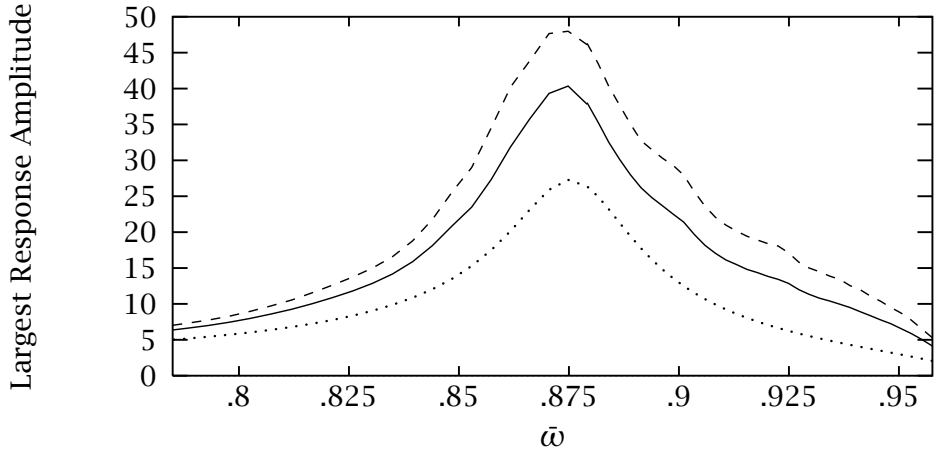

Figure 7.27 The Monte Carlo simulation of the forced response of mistuned systems yields the mean (———) and 99th precentile (– – –) of the largest response amplitude of any blade in the compressor. The tuned system response is (· · · · ·). Engine order of the forcing is $C = 7$. Model **3Ba**, $\zeta = 0.5\%$, $s = 5\%$.

Stochastic Mistuned Systems

Figures 7.27 and 7.28 depict the results of Monte Carlo simulations of the largest frequency response of the model **3Ba**, when subjected to excitation with engine order 7 and 13, respectively. Immediately obvious is the greater widening of the resonant

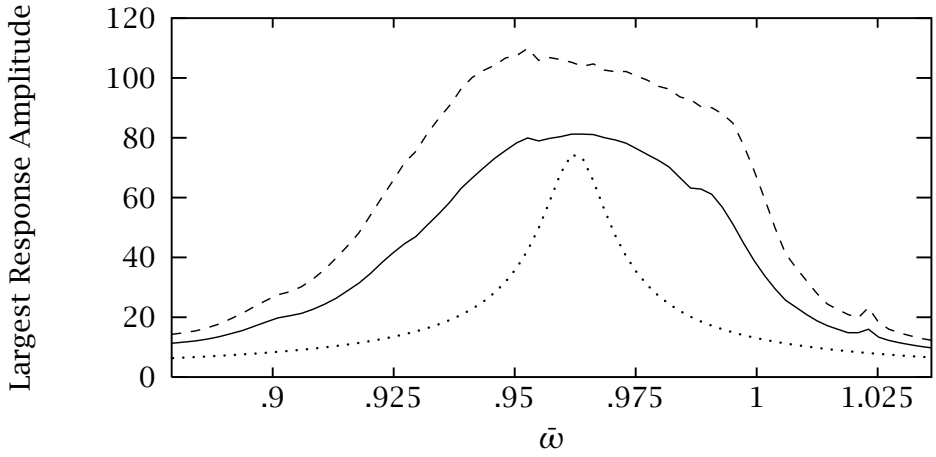

Figure 7.28 The Monte Carlo simulation of the forced response of mistuned systems yields the mean (———) and 99th percentile (– – –) of the largest response amplitude of any blade in the compressor. The tuned system response is (· · · · ·). Engine order of the forcing is $C = 13$. Model **3Ba**, $\zeta = 0.5\%$, $s = 5\%$.

frequency range due to mistuning for engine order 13 excitation compared to that for engine order 7 forcing, as predicted by Fig. 7.26.

A study of the fixed-frequency probability density functions for the largest response amplitudes to the two types of excitation reveals the familiar effect that the response to engine order 13 features a lower tail that stretches far below 1 (see Fig. 7.29). This indicates that at the frequency at which the PDF is calculated, a substantial fraction of mistuned systems have largest amplitudes smaller than the tuned system's peak amplitude. This is obviously due to the separation of the peaks depicted in Fig. 7.26(b), which results in a higher probability of finding a low largest amplitude in mistuned systems and hence in a much greater dispersion of the largest amplitudes. For the engine order 7 excitation this effect does not occur.

Figure 7.30 illustrate a comparison of the magnification statistics run at a fixed frequency *vs.* sweeping frequency. For engine order 7 we observe a fine agreement that indicates that under certaine circumstances fixed-frequency response statistics may offer an inexpensive approximation of the frequency swept analysis. The engine order 13 case, on the other hand, illustrates the circumstances where a misinterpretation of the fixed-frequency statistics could be disastrous. The figure also clearly indicates that mistuning effects are far greater for the engine order 7 than the engine order 13 excitation. The 99th percentile of the largest amplitude yields, for $C = 7$, a 74% increase in largest amplitude compared to the tuned system's peak amplitude, as opposed to only a corresponding 41% increase for $C = 13$. In Chapter VI we showed that high

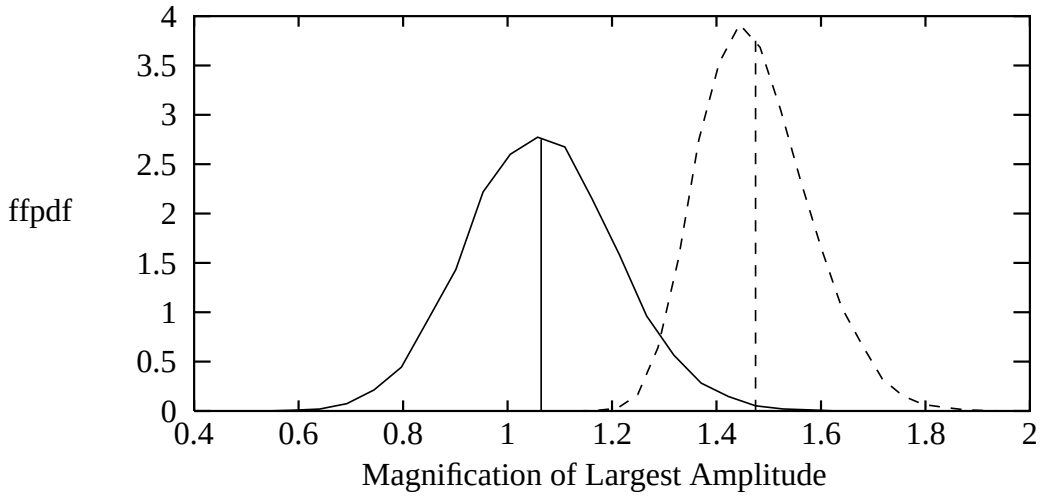

Figure 7.29 An approximation of the probability density function (PDF) is calculated at the excitation frequency which yields the largest value for the 99th percentile of the largest response amplitude. Excitation is of engine order 13 (———) and 7 (– – –). The "magnification of largest amplitude" is defined as the ratio of the largest amplitude of any blade in a mistuned rotor to the peak response amplitude of the corresponding tuned rotor. The vertical lines mark the mean values. Model **3Ba**, $\zeta = 0.5\%$, $s = 5\%$.

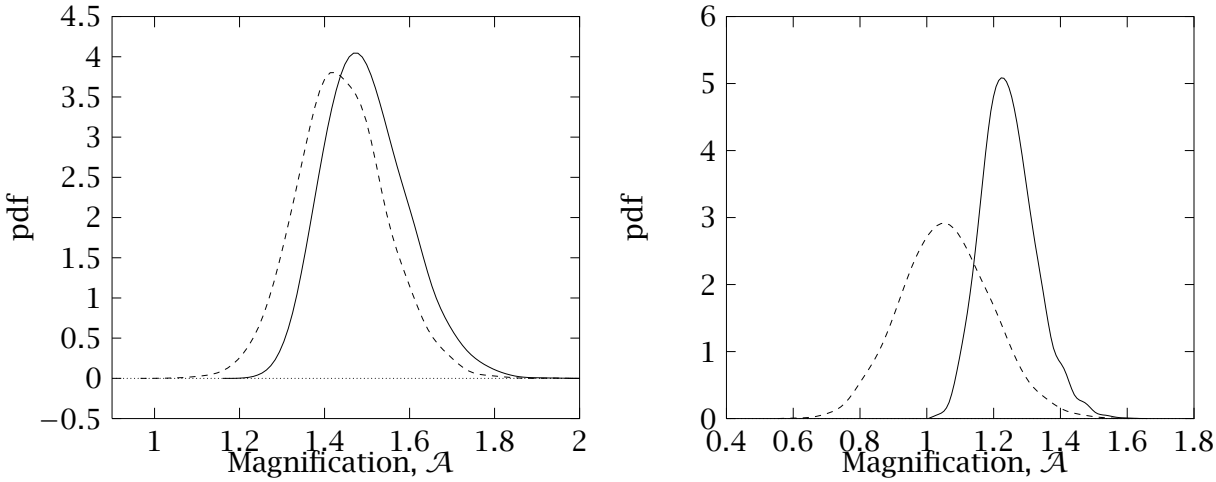

Figure 7.30 Comparison of the statistics of the magnification of largest response (– – –) and the magnification of maximum response (obtained by sweeping frequency) (———) for $C = 7$ (left) and $C = 13$ (right).

modal density (as a measure of weak coupling) normally predicts high sensitivity to

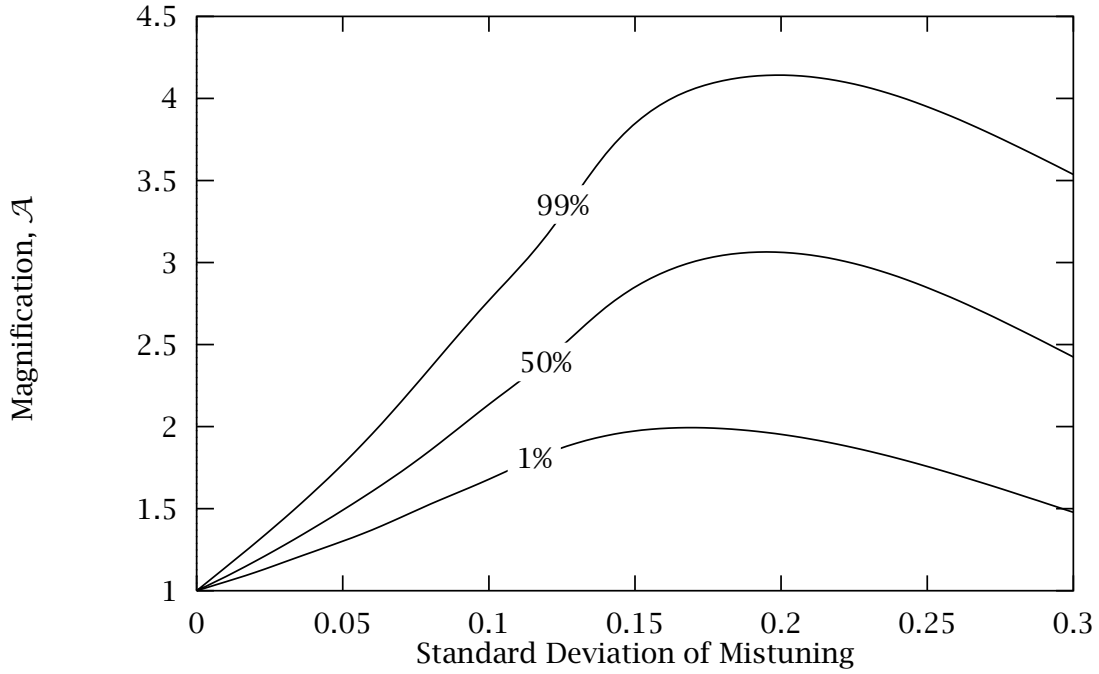

Figure 7.31 Magnification of largest amplitude due to mistuning as a function of the standard deviation of blade stiffness mistuning, s, for model **3Ba**. The curves show the 1%, 50% and 99% percentiles of the statistics of forced response obtained by a frequency sweep. Engine order of the excitation is 7.

mistuning but that very weak coupling (or very high modal density) could cause a decrease in mistuning sensitivity. The present results show this effect clearly. The modal density is far weaker at the 7-nodal diameter frequency than it is at the 13-nodal diameter frequency, yet the mistuning effects are much more pronounced for $C = 7$. This may of course only be of academic interest since, regardless of mistuning effects, the engine order 13 response is much greater than the engine order 7 response and is therefore obviously the determining factor for safe design.

7.2.3. Worst Case Mistuning Strength

The behaviour of the 36-blade rotor at the 7 nodal-diameter mode of the 2Fbis group suggests that in that region, it could feature an interblade coupling in the critical region where the interplay of localization effects and energy transmission causes strong mistuning effects. One way of examining this is by checking whether the variation of mistuning strength would lead to the *hump* featured in Fig. 6.8 but found to be absent from Fig. 7.23. Such an analysis is presented in Fig. 7.31. Non-monotonous behavior is indeed observed, leading to a 99th percentile largest amplitude that is over 4 times that predicted by the tuned analysis, albeit at unrealistically high values of mistuning.

In our opinion, the results outlined in this section offer strong validation of most of our findings for the 72-blade blisk and 36-blade compressor case, namely that for most of the first bending modes of the blisk and for most of the modes in the 2Fbis mode group of the 36-blade compressor, interblade coupling strengths are below the most critical values and consequently mistuning effects are more moderate than those observed for the engine order 7 excitation of the 36-blade compressor.

7.3. Summary

In this section we have investigated a method proposed for modeling complicated blade assemblies with simple coupled-oscillator models, based on a parameter identification technique involving finite-element natural frequency data. The simplicity of the models considered allows the modeling of an entire assembly at a reasonable cost. It is therefore possible to include mistuning caused by blade-to-blade dissimilarities in the free and forced response analyses.

From the finite element analysis the families of modes corresponding to the various frequency branches (*e.g.*, blade bending modes, disk modes, blade torsion modes, etc.) should be carefully identified. This information is essential in the identification process. In some cases, tracking the families of modes as the number of nodal diameters increases may be made easier by supplementing the natural frequency data with additional frequencies calculated for interblade phase angle boundary conditions that *do not* correspond to an integer number of nodal diameters. For instance, a complicated frequency curve veering occurring between 6- and 7-nodal diameter modes in a 50-blade assembly could be captured in greater detail by examining not only the $\sigma = 12\pi/50$ and $\sigma = 14\pi/50$ interblade phase angle mode but also the fictional $\sigma = 13\pi/50$ interblade phase angle "mode". Hence the idea is that by making the frequency curves more continuous the tracking of mode families can be done more effectively.

In the identification of the parameters of the reduced-order models a great deal of

judgment is required from the analyst. Only a small number of the natural frequencies of the finite element model can be approximated by the simple models. These frequencies must be chosen with great care if the proper features of the finite-element model are to be captured by the reduced-order model. At the beginning of the present study it was unclear which features of the finite element model were the most important ones. We can now say with some confidence that mistuning effects are most accurately modeled when the modal density of the reduced-order model closely matches that of the finite element model. Hence, during the identification process, the greatest emphasis should be placed on fitting the reduced-order model frequency curves to the finite element frequencies which are in the neighborhood of the number of nodal diameters that corresponds to the engine order of the excitation of interest.

The study of free response highlighted the effect mistuning has on natural frequencies and mode shapes. Tuned rotors with weakly coupled blades feature, in some blade mode group, natural frequencies tightly clustered near the the blade-alone natural frequency of the blade mode in question. This results in a high modal density of the assembly near the blade-alone natural frequency. When blade mistuning is introduced to this weakly coupled rotor the assembly natural frequencies fan out to become nearly the same as the blade-alone natural frequencies of the mistuned blades. Mistuned rotors with weakly coupled blades feature spatially localized modes. We introduced the *localization factor*, a measure of mode localization in mono-coupled blade-assemblies. The localization factor proved to be very sensitive to how accurately the frequency curves of the reduced-order system fit the natural frequencies of the finite element system in the frequency range of interest. Strong localization is known to occur in systems with high modal density (weak coupling). However, we found that if modal density becomes *too* high, the mistuning effects may start to decrease. From this finding we drew the conclusion that a correct representation of the modal density in the desired frequency range is the key to the accurate modeling of mistuning effects by the reduced-order system.

Localization due to blade mistuning was found to occur solely in the modes dominated by blade motion. The localization factor characterizes the spatial decay of the coupling coordinate amplitudes (*i.e.*, the disk coordinates) and it was found to agree well with the experimental decay of the localized mode shapes, when expressed in the disk coordinates. However, when the localized modes were examined in terms of blade displacements, they exhibited much more dramatic amplitude decay patterns which were not predicted by the localization factor. These effects were explained as local blade resonances, leading to a phenomenon we called “super-localization”, and were toted as a great risk factor for rogue blades. Nonetheless, the localization factor must

be heralded as a good predictor of mistuning effects, even if quantitative information should never be taken literally.

A statistical approach to the forced response analysis was presented. We introduced the concept of treating, at a given frequency, the largest response amplitude of any blade throughout a mistuned assembly as a random variable. The investigation of the statistics of the largest response amplitude was carried out by Monte Carlo simulations and major interest. First, Monte Carlo simulations of the largest frequency response were used to approximate numerically the mean and the standard deviation of the largest response amplitude of mistuned rotors for each frequency. Then, a full investigation of the statistics of the largest response amplitudes was performed by running Monte Carlo simulations at the worst-case frequency obtained from the largest frequency response simulations, yielding the probability density function of the largest response amplitude at that frequency. It was shown how these results may be of help in the design phase. We also explained how of calculating the probability density function at a fixed frequency is a compromise required by the great computational expense of a full-blown study of the frequency-independent statistics. Furthermore, we discussed how the fixed-frequency statistics depend on the damping, the interblade coupling, the mistuning strength and the number of blades in the assembly.

An interesting result of the statistical analysis of the forced response was that the two-DOF per bay models consistently demonstrated greater mistuning effects than the three-DOF per bay systems. Due to the greater precision normally associated with a larger number of degrees of freedom, as well as their more precise approximation of interblade coupling, the single most important factor influencing mistuning effects, we concluded that the results obtained with three-DOF per bay models were more accurate.

CHAPTER VIII

CASE STUDIES IN ROTORDYNAMICS: PART 2

In this chapter we apply our component-mode bases Order Reduction Method to a fictitious finite element model since no real finite element model was available. This allowed us to ensure simplicity, yet care was taken that the model was rich in challenging dynamics.

8.1. Order Reduction of a Solid Element System

As an example, we present a simple FEM of one sector of a fictitious bladed-disk structure. Top and side views of the finite element mesh are shown in Fig. 8.1. The elements are all eight-noded solid bricks. The disk sector has 15 elements, and the blade has 3 elements. In addition, there is a thin transition element that connects the blade and the disk. This element can be thought of as representing a taper. In the finite element runs, the transition element was arbitrarily considered to be part of the disk component. In general, the blade substructure may be defined as the part of the model which is to have mistuned properties.

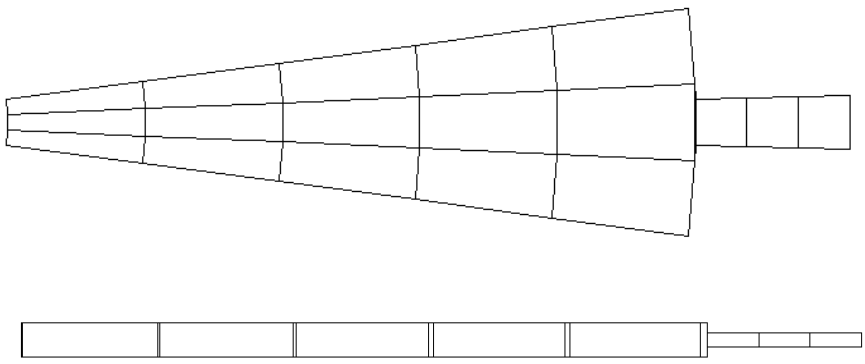

Figure 8.1 Top and side view of an example solid element finite element model.

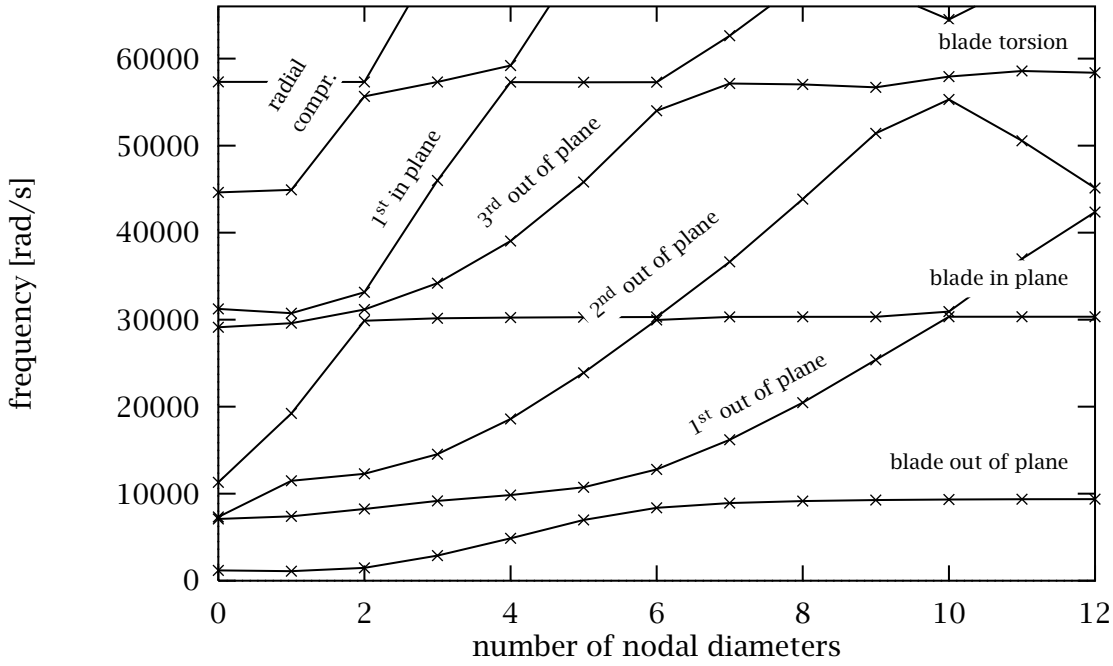

Figure 8.2 Natural frequencies of the example system shown as a function of the number of nodal diameters in the corresponding mode shape. The lines connect members of a modal families.

All nodes of the inner radius of the disk are completely constrained. Also, all elements have the same material properties. This FEM therefore represents a blisk which is clamped at the inner radius. There are 138 degrees of freedom per disk-blade sector, and a total of 24 sectors for the full blisk. All finite element work was done on NASTRAN using SOL 48 for the disk component, and SOL 103 for the cantilevered blade.

Although this model is simple, the properties and dimensions were chosen so that the dynamics would be quite challenging to reproduce with a ROM. As a benchmark , we show the natural frequencies of the FEM versus the number of nodal diameters in Fig. 8.2. Note that this plot shows several very close frequency curve veerings.

For the ROM, we take five families of disk modes, and four cantilevered elastic blade modes. Thus, there are *nine* degrees of freedom per sector for the ROM, compared to 138 degrees of freedom per sector for the FEM.

The natural frequencies found from the ROM are shown versus the finite element frequencies in Fig. 8.3. Globally, the frequency distribution is very well captured by the ROM. In particular, the disk modes are nicely approximated. The blade modes,

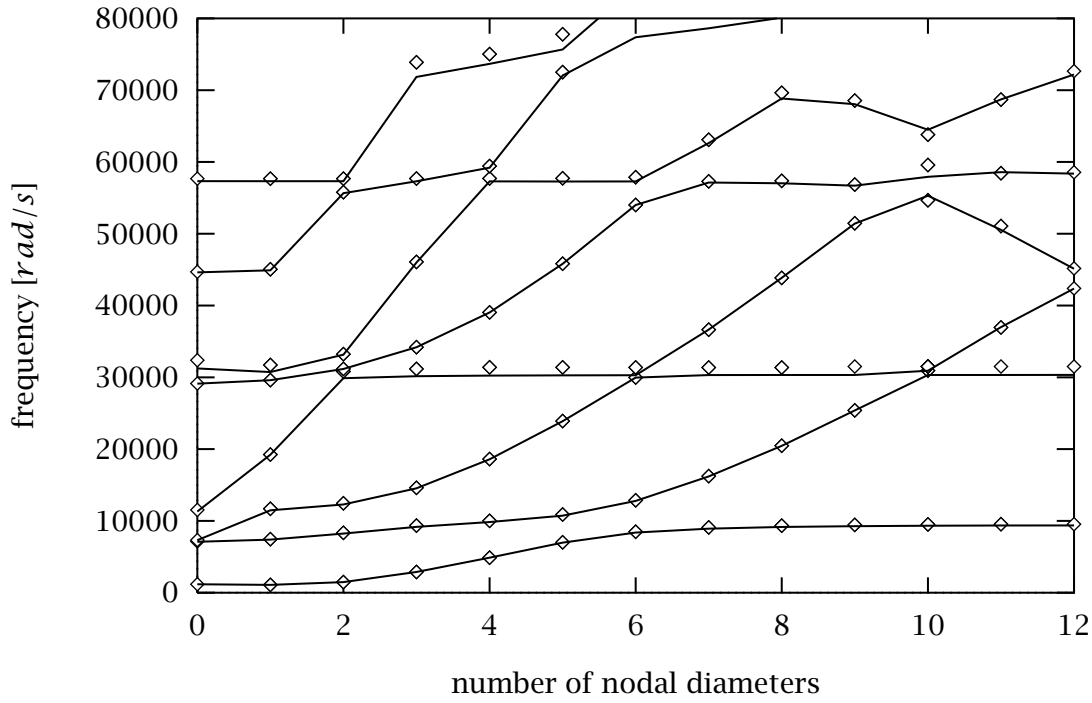

Figure 8.3 Natural frequencies of 9-degree-of-freedom ROM (◇) compare favorably with the natural frequencies of the FEM (—) when plotted as a function of the number of nodal diameters in the corresponding mode shape.

however, are not as well captured. The ROM frequencies tend to be higher than the FEM frequencies. In particular, the frequencies of the second blade mode, an in plane bending mode, are somewhat overpredicted. Note that this family of modes is almost uncoupled from the disk motion (hence the almost horizontal line). The reason that this delicate interaction between disk and blade is poorly capture is most likely due to the fact that cantilevered blade modes were used, and the fixed end boundary condition makes the blade modal stiffnesses too large. A key family of disk modes is obviously missing and these shapes may be difficult to identify and include. On the other hand, the global agreement of the two models is excellent, in particular, the the way the veerings of the multiple frequency curves is nearly impeccable?

8.1.1. Very Reduced Order System

The previous nine-degree-of-freedom model captures well the natural frequencies in a rather broad frequency range. For the purposes of mistuning analysis, however, the structural dynamicist often chooses to focus on a small frequency band which includes a set of blade modes. It is the blade modes which feature large localization, and are therefore of primary importance. We now take the first two families of FEM disk modes and the first FEM blade mode in order to create a ROM with only *three* degrees of freedom per sector.

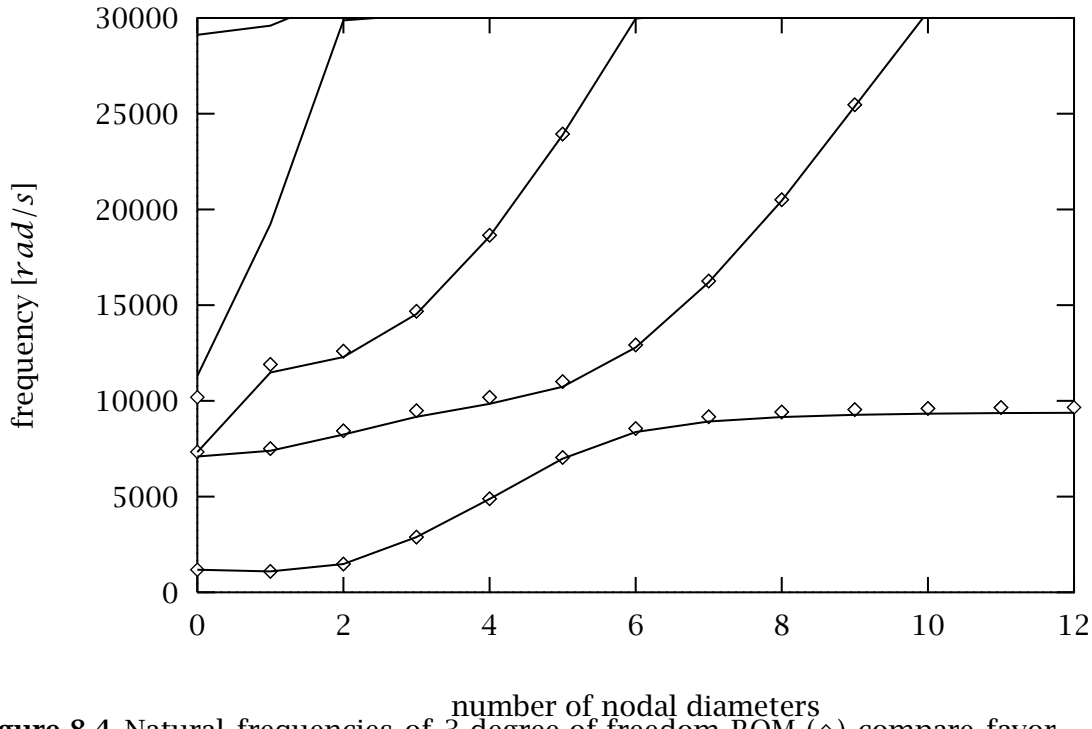

Figure 8.4 Natural frequencies of 3-degree-of-freedom ROM (◇) compare favorably with the natural frequencies of the FEM (—) in a narrow frequency band.

The natural frequencies of the three-degree-of-freedom ROM are shown in Fig. 8.4. Considering that we have approximated a 138-degree-of-freedom-per-sector model with a three-degree-of-freedom-per-sector model, the frequency fit is excellent.

8.1.2. Mistuning

In order to reproduce the dynamics of the FEM with the ROM, not only must the frequencies be well approximated, but the mode shapes must match as well. Even though the *component* mode shapes for the ROM are taken from the FEM, we are interested in comparing the mode shapes for the bladed disk assembly, which are created in the reduced-order modeling process. In addition, we need to verify that the mistuning effects are well captured by the ROM. Therefore, we proceed to validate the order reduction method by examining how well the frequencies and the localized mode shapes of the ROM compare to those of the FEM for one realization of a mistuned bladed disk.

For this validation, we constructed a FEM for the full blisk of which one sector was presented in Fig. 8.1. Mistuning was added by allowing each blade to have a different Young's modulus. The Young's modulus for each blade i, E_i, was found as:

$$E_i = E_0(1 + \delta_i) \tag{8.1}$$

where E_0 is the Young's modulus for a tuned blade, and δ_i is a sample — from a uniform distribution with standard deviation 5% — produced by a random number generator. The modal stiffnesses of the ROM were changed so that the mistuning pattern was identical to that of the FEM. Note that 5% stiffness mistuning corresponds to approximately 2.5% blade natural frequency mistuning. The FEM considered here has a total of 3312 degrees of freedom, while the ROM has only 216 degrees of freedom.

Since the mistuning destroys the cyclic symmetry of the structure, the modes will no longer be associated with a certain number of nodal diameters. We therefore plot the natural frequencies of both models versus occurrence number in Fig. 8.5. The frequencies of the two models compare very well over this frequency range.

Finally, we compare selected localized mode shapes of the FEM and ROM in Fig. 8.6. The vibration amplitude of each blade was reduced to a scalar by taking the sum of the squares of all degrees of freedom in the blade. The vector of these amplitudes was then normalized so as to have unit length.

Note that the mode shapes are very similar. Although the amplitudes at a certain blade may differ slightly, the maximum amplitudes occur at the same blade and are very close. Furthermore, the mode shapes of the FEM and ROM exhibit similar spatial amplitude decay, and we found this to be typical of the FEM and ROM modes. This is of primary importance since it demonstrates that the two models have comparable sensitivity to mistuning.

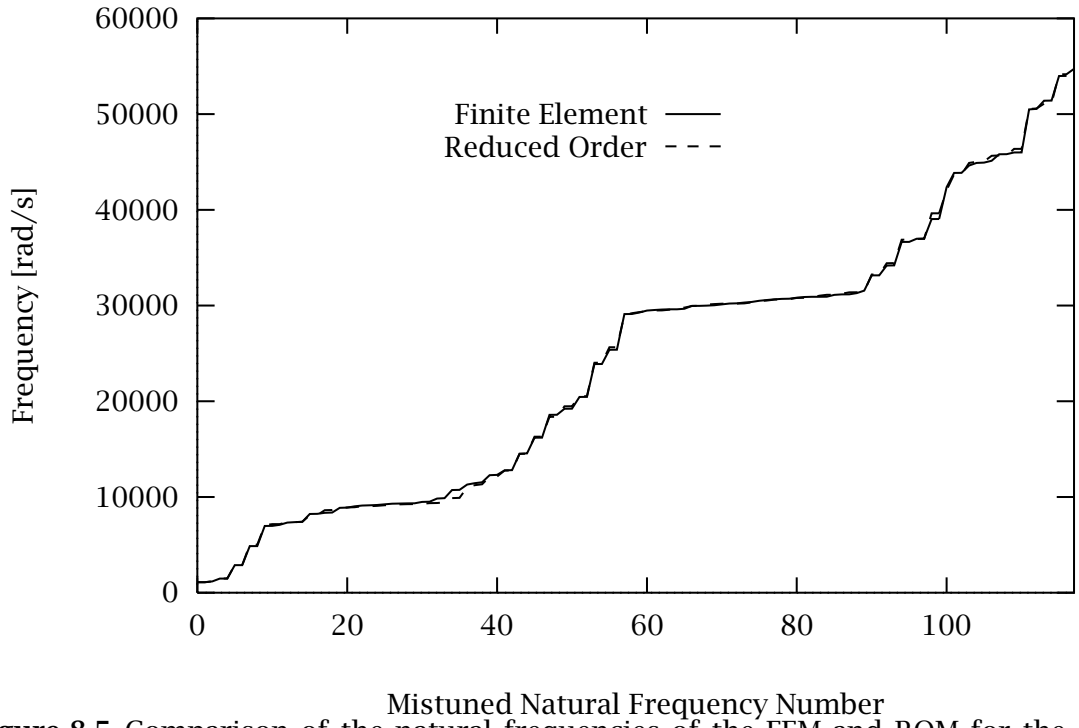

Figure 8.5 Comparison of the natural frequencies of the FEM and ROM for the mistuned case.

8.1.3. Conclusions

A reduced-order modeling technique was presented which is tailored to producing a very low-order model of an actual bladed disk structure. The method is systematic from a finite element model (FEM) of one disk-blade sector of the structure. A component mode approach is used, where the disk modal stiffnesses and the blade motion due to disk mode shapes are found from the FEM modes of the disk with *massless* blades . The blade modal stiffnesses and blade mass matrix are found from the FEM modes of the blade with all nodes at the disk-blade interface fixed. This is all the information that is needed from the FEM runs, so storage requirements are modest. Mistuning may easily be added to the reduced-order model (ROM) by slightly disordering the blade stiffness properties.

The reduced-order modeling technique performed well for the example case considered. For order reduction per sector $138 \rightarrow 9$, the system dynamics were well captured over a broad frequency range. For order reduction per sector $138 \rightarrow 3$, the system natural frequencies were approximated in the frequency band of interest. It was found that blade to disk coupling plays an important role in the dynamics of the reduced order model, and may need to be enhanced.

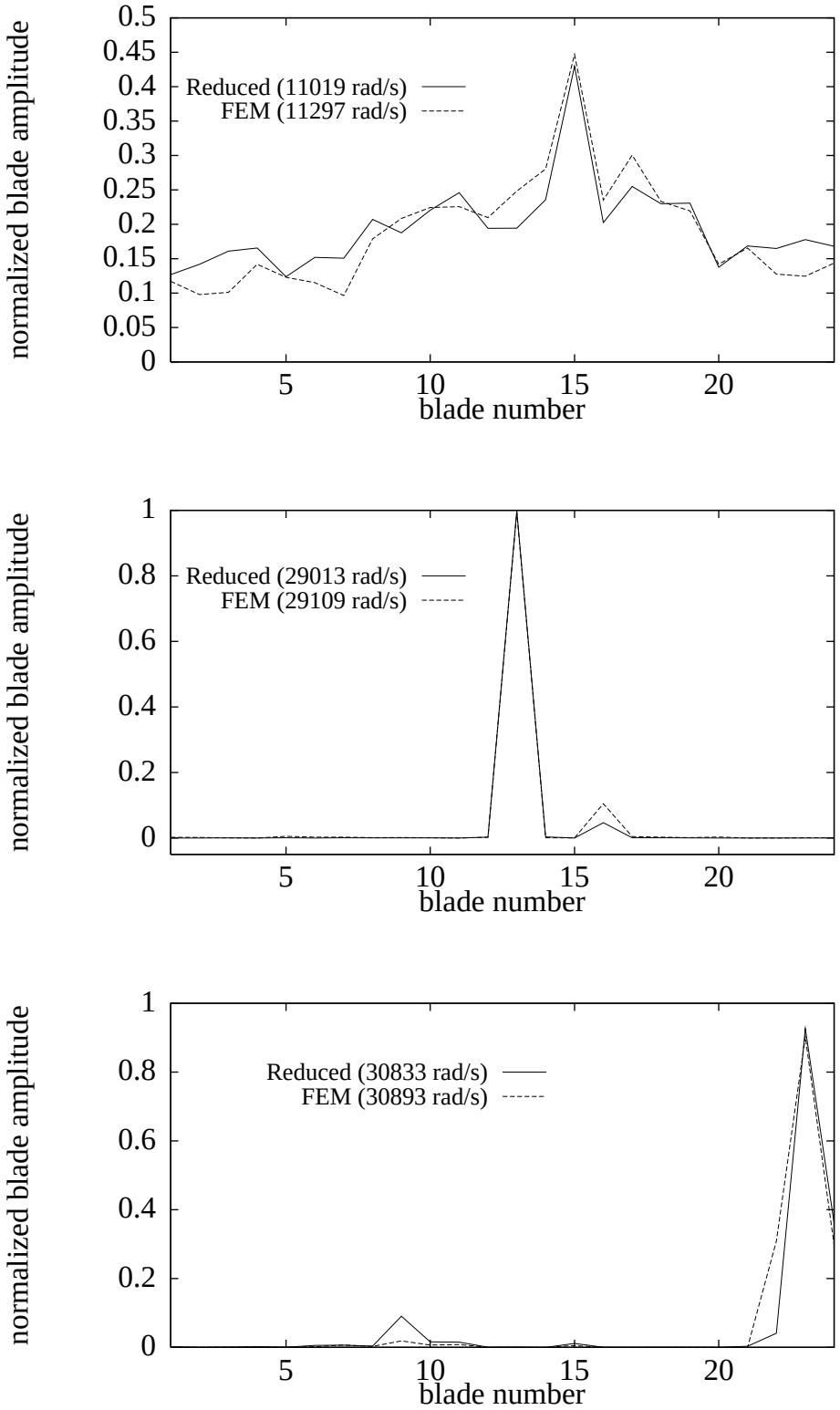

Figure 8.6 Selected localized mode shapes of a mistuned realization of the FEM compared with the ROM. Standard deviation of uniform mistuning is 5%

The frequencies and mode shapes were compared for the FEM and ROM of the example system with mistuned blade stiffnesses. The frequencies for the two models were very similar. The match between FEM and ROM mistuned mode shapes was excellent. The maximum amplitudes occurred at the same blade and were nearly equal in magnitude. Also, the spatial amplitude decay rates were similar, which means that sensitivity to mistuning is well preserved in the order reduction process.

CHAPTER IX
CONCLUSIONS

This chapter outlines the directions of the research, highlights major contributions, and summaries the main conclusion.

9.1. Research Thrusts

The research of mistuning effects on the response characteristics of mistuned bladed disks proceeded along three principal lines:

- Development of modeling techniques for mistuned bladed disks.
- Investigation of mistuning effect on free waves and free modes of vibration and the development of measures of mistuning sensitivity.
- A statistical analysis of the mistuning effects on largest response amplitudes.

9.2. Contributions

In the Chapter I we identified the areas mentioned above as being in need of development. The main contributions of the thesis have been:

- A systematic review of simple coupled-oscillator models widely used in the analysis of bladed disks, as well as the development of enhanced models with specialized properties. A technique is proposed for identifying parameters in coupled-oscillator models by correlating the natural frequencies and global mode shapes of the model with those obtained by a tuned finite element analysis of the rotor under investigation.
- A novel modeling technique based on a component mode methodology was developed. The method balances accuracy and computational efficiency, as well as making it possible to mistune individual blades in a controlled manner. This method has several advantages over simple coupled-oscillator models, namely a more complete model of interblade coupling and the ability to generate reduced order models from finite element models in an automatic manner.

- The understanding of mistuning sensitivity of free modes of vibration in mono-coupled coupled-oscillator models of bladed disks has been furthered and a reliable scalar measure of sensitivity was developed. For bi-coupled systems, parameter ranges were identified in which a mono-coupled approximation is justifiable.
- An in depth study of the statistics of largest forced response amplitudes in bladed disks has identified an energy flow mechanism that, in the case of engine order excitation, enhances the mistuning effects for sufficient levels of coupling. Hence, there exists an optimal coupling level at which the mode localization and energy augmentation phenomena collaborate.

9.3. Main Findings

- High mistuning sensitivity of modes of free vibration was shown to be synonymous with low interblade coupling.
- Correlation of simple coupled-oscillator models and real-life rotor prototypes is difficult, but if successful, may result in models that can provide useful information about mistuning effect on forced and free response. Dynamical behaviour of rotors may be too complex to be captured by the simplistic models of coupling in the coupled-oscillator models.
- The straightforward component mode modeling approach provides much more sophisticated models of blade-to-blade coupling. As interblade coupling has been shown to be the single most important factor governing mistuning sensitivity, this modeling approach holds great promise as an analysis tool.
- Contrary to the predictions of the free response, mistuning effects in forced response do not necessarily increase as interblade coupling is decreased. Instead, there may be a moderately weak level of coupling at which mistuning effects reach a maximum. Hence, sensitivity measures based on a free analysis can only be relied on to *rule out* mistuning effects. If the free analysis predicts strongly localized mode shapes, a forced response analysis must be performed.
- For certain systems, improving manufacturing tolerances in order to reduce mistuing effects may have the opposite effect since decreasing mistuning may improve energy flow into the largest amplitude blade.

APPENDIX A

THE KRONECKER PRODUCT

In the study of the block circulant matrices, that arise in the analysis of structures with cyclic symmetry, the Kronecker produce is a useful tool. A brief introduction of the product and some of its properties is in order. Many users will be be familiar with the Kronecker product of a column vector and a line vector to form a matrix

$$\mathbf{D} = \mathbf{a} \otimes \mathbf{b}^T = \begin{bmatrix} a_1 b_1 & a_1 b_2 & \dots & a_1 b_N \\ a_2 b_1 & a_2 b_2 & \dots & a_2 b_N \\ \vdots & \vdots & \ddots & \vdots \\ a_N b_1 & a_N b_2 & \dots & a_N b_N \end{bmatrix} \tag{A.1}$$

The Kronecker product of two matrices is

$$\mathbf{C} = \mathbf{A} \otimes \mathbf{B} = \begin{bmatrix} a_{11}\mathbf{B} & a_{12}\mathbf{B} & a_{13}\mathbf{B} & \dots \\ a_{21}\mathbf{B} & a_{22}\mathbf{B} & \dots & \dots \\ \vdots & \vdots & \ddots & \ddots \end{bmatrix} \tag{A.2}$$

Some of the useful properties of the Kronecker product include

$$(\mathbf{A} \otimes \mathbf{B})\,(\mathbf{C} \otimes \mathbf{D}) = (\mathbf{AC}) \otimes (\mathbf{BD}) \tag{A.3}$$

$$(\mathbf{A} \otimes \mathbf{B})^* = \mathbf{A}^* \otimes \mathbf{B}^* \tag{A.4}$$

APPENDIX B

ESTIMATION OF STANDARD DEVIATION

Say we have a set of N observations which are assumed to be independent and identically distributed random variables, $X_1, \ldots, X_N$. If we assume that they are uniformly distributed over a range of values $[a, b]$, the joint probability density function (pdf) is

$$f_{X_1 \cdots X_N}(x_1, \cdots, x_N) = \frac{1}{(b-a)^N} \qquad b > a \tag{B.1}$$

where $x_1, \cdots, x_N$ is a set of actual data points from one realization of the N observations.

If the parameters a and b are unknown, then we can use the data set to estimate these parameters. One way to do this is to use the concept of *maximum likelihood parameter estimation*. Consider an arbitrary pdf which depends on some parameter θ. The maximum likelihood estimator, $\hat{\theta}$, is the value of that parameter which is most likely to have given rise to the observed data set. Clearly, this is the value of θ which maximizes the pdf.

Thus, the maximum likelihood estimator, $\hat{a}$, of the parameter a is the value of a which maximizes the pdf of Eq. (B.1), or the value of a which is the closest possible to the value of b. However, in order for the observed data set to be possible, we have the restriction:

$$a \leq x_i \leq b \qquad i = 1, \ldots, N \tag{B.2}$$

We therefore find $\hat{a}$ to be

$$\hat{a} = \min\{x_1, \ldots, x_N\} = x_{\min} \tag{B.3}$$

Similarly, the maximum likelihood estimator for b is

$$\hat{b} = \max\{x_1, \ldots, x_N\} = x_{\max} \tag{B.4}$$

Recalling that the observations are identically distributed, the estimated pdf for a single observation is

$$f_X(x) = \frac{1}{\hat{b} - \hat{a}} = \frac{1}{x_{\max} - x_{min}} \tag{B.5}$$

In our case the N data points, $x_1, \ldots, x_N$, correspond to the N mistuned blade-alone frequencies. Equation (B.5) thus gives the pdf for the mistuned frequencies.

APPENDIX C
MEASURES OF MISTUNING

Recall that the small mistuning parameter δ is defined in terms of blade stiffness, $k_b(1+\delta_i)$, and is uniformly distributed, $\delta_i \in [-W, W] \equiv [-\sqrt{3}s, \sqrt{3}s]$, where s is the standard deviation of the mistuning. Since blade stiffness is proportional to natural frequency squared the individual blade natural frequencies are distributed in

$$\omega_i^b \in \left[\frac{k_b}{m_b}\sqrt{1-s\sqrt{3}}, \frac{k_b}{m_b}\sqrt{1+s\sqrt{3}}\right] \tag{C.1}$$

Since mistuning is considered small, s is small compared to 1 and hence the frequencies may be assumed to be approximately uniformly distributed in

$$\omega_i^b \in \left[\frac{k_b}{m_b}\left(1-s\frac{\sqrt{3}}{2}\right), \frac{k_b}{m_b}\left(1+s\frac{\sqrt{3}}{2}\right)\right] \tag{C.2}$$

So when blade stiffness mistuning is small and uniformly distributed with standard deviation s, the blade natural frequency distribution may be approximated by a uniform distribution of standard deviation $s/2$.

REFERENCES

[1] Whitehead, D. S., "Effect of Mistuning on the Vibration of Turbomachine Blades Induced by Wakes," *Journal of Mechanical Engineering Science*, vol. 8, no. 1, 1966, pp. 15–21.

[2] El-Bayoumy, L. E. and Srinivasan, A. V., "Influence of Mistuning on Rotor-Blade Vibrations," *AIAA Journal*, vol. 13, no. 4, 1975, pp. 460–464.

[3] Dye, R. C. and Henry, T. A., "Vibration Amplitudes of Compressor Blades Resulting From Scatter in Blade Natural Frequencies," *ASME Journal of Engineering for Power*, vol. 91, 1969, pp. 182–188.

[4] Ewins, D. J., "The Effect of Detuning upon the Forced Vibrations of Bladed Disks," *Journal of Sound and Vibration*, vol. 9, no. 1, 1969, pp. 65–79.

[5] Ewins, D. J., "Vibration Characteristics of Bladed Disc Assemblies," *Journal of Mechanical Engineering Science*, vol. 15, no. 3, 1973, pp. 165–186.

[6] Ewins, D. J., "Vibration Modes of Mistuned Bladed Disks," *ASME Journal of Engineering for Power*, July 1976, pp. 349–355.

[7] Srinivasan, A. V. and M., F. H., "Effect of Mistuning on Resonant Stresses of Turbine Blades," in *Structural Dynamic Aspects of Bladed Disc Assemblies, Proceedings of the ASME Winter Annual Meeting*, (New York), 1976.

[8] Fabunmi, J. A., "Forced Vibration of a Single Stage Axial Compressor Rotor," *ASME Journal of Engineering for Power*, vol. 102, no. 2, 1980, pp. 322–329.

[9] Sogliero, G. and Srinivasan, A. V., "Fatigue Life Estimates of Mistuned Blades via a Stochastic Approach," *AIAA Journal*, vol. 18, no. 1, 1980, pp. 318–323.

[10] Griffin, J. H. and Hoosac, T. M., "Model Development and Statistical Investigation of Turbine Blade Mistuning," *ASME Journal of Vibration, Acoustics, Stress and Reliability in Design*, vol. 106, 1984, pp. 204–210.

[11] Afolabi, D., "The Frequency Response of Mistuned Bladed Disk Assemblies," in *Vibrations of Blades and Bladed Disk Assemblies, Proceedings of the Tenth Biennial Conference on Mechanical Vibration and Noise*, (Cincinnati, Ohio), 1985.

[12] Basu, P. and Griffin, J., "The Effect of Limiting Aerodynamic and Structural Coupling in Models of Mistuned Bladed Disk Vibration," in *Vibrations of Blades and*

Bladed Disk Assemblies, Proceedings of the Tenth Biennial Conference on Mechanical Vibration and Noise, (Cincinnati, Ohio), 1985.

[13] Valero, N. A. and Bendiksen, O. O., "Vibration Characteristics of Mistuned Shrouded Blade Assemblies," *ASME Journal of Engineering for Gas Turbines and Power*, vol. 108, no. 2, 1986, pp. 293–299.

[14] Wei, S. T. and Pierre, C., "Localization Phenomena in Mistuned Assemblies with Cyclic Symmetry, Part I: Free Vibrations," *ASME Journal of Vibration, Acoustics, Stress and Reliability in Design*, vol. 110, no. 4, 1988, pp. 429–438.

[15] Lin, Y. K. and McDaniel, T. J., "Dynamics of Beam-Type Periodic Structures," *ASME Journal of Engineering for Industry*, vol. 91, no. 4, 1969, pp. 1133–1141.

[16] Signorelli, J. and von Flotow, A. H., "Wave Propagation, Power Flow, and Resonance in a Truss Beam," *Journal of Sound and Vibration*, vol. 126, 1988, pp. 127–144.

[17] Mead, D. J., "Free Wave Propagation in Periodically Supported, Infinite Beams," *Journal of Sound and Vibration*, vol. 11, 1970, pp. 181–197.

[18] Brillouin, L., *Wave Propagation in Periodic Structures*. New York: Dover, 1953.

[19] Chen, W. J. and Pierre, C., "Vibration Localization and Wave Conversion Phenomenon in a Multi-Coupled, Nearly Periodic Disordered Truss Beam," in *Proceedings of the AIAA Dynamics Specialists Conference (AIAA Paper 92-1115)*, (Dallas, Texas), 1992.

[20] Mead, D. J., "Wave propagation and natural modes in periodic systems, I: mono-coupled systems," *Journal of Sound and Vibration*, vol. 40, no. 1, 1975, pp. 1–18.

[21] Mead, D. J., "Wave propagation and natural modes in periodic systems, II: multi-coupled systems, with and without damping," *Journal of Sound and Vibration*, vol. 40, no. 1, 1975, pp. 19–39.

[22] Anderson, P. W., "Absence of Diffusion in Certain Random Lattices," *Physical Review*, vol. 109, no. 5, 1958, pp. 1492–1505.

[23] Hodges, C. H., "Confinement of Vibration by Structural Irregularity," *Journal of Sound and Vibration*, vol. 82, 1982, pp. 411–424.

[24] Ewins, D. J. and Han, Z. S., "Resonant Vibration Levels of a Mistuned Bladed Disk," *ASME Journal of Vibration, Acoustics, Stress and Reliability in Design*, vol. 106, April 1984, pp. 211–217.

[25] Friedmann, P. P., Lust, S. D., and Bendiksen, O. O., "Free and Forced Fesponse of Nearly Periodic Multi-Span Beams and Multi-Bay Trusses," in *Proceedings of the 32nd AIAA/ASME/ASCE/AHS/ASC Structures, Structural Dynamics and Materials Conference (AIAA Paper, 91-0999)*, (Baltimore, Maryland), April 1991.

[26] Pierre, C. and Cha, P. D., "Strong mode localization in nearly periodic disordered structures," *AIAA Journal*, vol. 27, no. 2, 1989, pp. 227–241.

[27] Pierre, C. and Dowell, E. H., "Localization of vibrations by structural irregularity," *Journal of Sound and Vibration*, vol. 114, 1987, pp. 529–564.

[28] Lust, S. D., Friedmann, P. P., and Bendiksen, O. O., "Mode Localization in Multi-Span Beams," in *Proceedings of the 31st AIAA Dynamics Conference*, (Long Beach, California), 1990.

[29] Bouzit, D. and Pierre, C., "Vibration Confinement Phenomena in Disordered, Mono-coupled, Multi-span Beams," *ASME Journal of Vibration and Acoustics*, vol. 114, no. 4, 1992, pp. 521–530.

[30] Kissel, G. J., *Localization in Disordered Periodic Structures*. PhD thesis, Massachusetts Institute of Technology, 1988.

[31] Pierre, C., "Weak and strong vibration localization in disordered structures: a statistical investigation," *Journal of Sound and Vibration*, vol. 139, 1990, pp. 111–132.

[32] Ottarsson, G. S. and Pierre, C., "Vibration and Wave Localization in a Nearly Periodic Beaded String," in *Presentation of Invited Paper at the ASME 13th Biennial Conference on Mechanical Vibration and Noise*, (Miami, Florida), September 1991.

[33] Hodges, C. H. and Woodhouse, J., "Vibration isolation from irregularity in a nearly periodic structure: theory and measurements," *Journal of Acoustical Society of America*, vol. 74, no. 3, 1983, pp. 894–905.

[34] Cornwell, P. J. and Bendiksen, O. O., "Localization of vibrations in large space reflectors," *AIAA Journal*, vol. 27, no. 2, 1987, pp. 219–226.

[35] Levine-West, M. B. and Salama, M. A., "Mode Localization Experiments on a Ribbed Antenna," in *The Proceedings of the 33rd AIAA/ASME/ASCE/AHS/ASC Structures, Structural Dynamics and Materials Conference*, (Dallas, Texas), April 1992.

[36] Ibrahim, R. A., "Structural Dynamics With Parameter Uncertainties," *Applied Mechanics Reviews*, vol. 40, no. 3, 1987, pp. 309–328.

[37] Bendiksen, O. O., "Flutter of Mistuned Turbomachinery Rotors," *ASME Journal of Engineering for Gas Turbines and Power*, vol. 106, no. 1, 1984, pp. 25–33.

[38] Kaza, K. R. V. and Kielb, R. E., "Effects of Structural Coupling on Mistuned Cascade Flutter and Response," *ASME Journal of Engineering for Gas Turbines and Power*, vol. 106, no. 1, 1984, pp. 17–24.

[39] Whitehead, D. S., "Torsional Flutter of Unstalled Cascade Blades at Zero Deflection," Aeronautical Research Council, R & M, no. 3429, 1964.

[40] Srinivasan, A. V., ed., *Structural Dynamics Aspects of Bladed Disc Assemblies, Proceedings of the ASME Winter Meeting*, (New York), 1976.

[41] Ewins, D. J. and Srinivasan, A. V., eds., *Vibrations of Bladed Disk Assemblies, Proceedings of the Ninth Biennial Conference on Mechanical Vibration and Noise*, (Dearborn, Michigan), 1983.

[42] Kielb, R. E. and Rieger, N. F., eds., *Vibrations of Blades and Bladed Disk Assemblies, Proceedings of the Tenth Biennial Conference on Mechanical Vibration and Noise*, (Cincinnati, Ohio), 1985.

[43] Kielb, R. E. and Crawley, E., eds., *Bladed Disk Assemblies, Proceedings of the 11th Biennial Conference on Mechanical Vibration and Noise*, (Boston, Massachusetts), 1987.

[44] Srinivasan, A. V., "Vibrations of Bladed-Disk Assemblies — A Selected Survey," *ASME Journal of Vibration, Acoustics, Stress and Reliability in Design*, vol. 106, no. 2, 1984, pp. 165–168.

[45] Ottarsson, G. S. and Pierre, C., "A Transfer Matrix Approach to Vibration Localization in Mistuned Blade Assemblies," *NASA Technical Memorandum 106112, ICOMP-93-10 and ASME paper 93-GT-115*, 1993.

[46] Wei, S. T. and Pierre, C., "Statistical Analysis of the Forced Response of Mistuned Cyclic Assemblies," *ASME Journal*, vol. 28, no. 5, 1990, pp. 861–868.

[47] Wei, S. T. and Pierre, C., "Localization Phenomena in Mistuned Assemblies with Cyclic Symmetry, Part II: Forced Vibrations," *ASME Journal of Vibration, Acoustics, Stress and Reliability in Design*, vol. 110, no. 4, 1988, pp. 439–449.

[48] Mignolet, M. P. and Christensen, K. R., "Probabilistic Analysis of Mistuned Bladed Disks: A Combined Closed Form-Perturbation Approach," in *The Proceedings of the 35th International Gas Turbine and Aeroengine Congress (ASME paper 90-GT-191)*, (Brussels, Belgium), June 1990.

[49] Sinha, A., "Calculating the Statistics of Forced Response of a Mistuned Bladed Disk Assembly," *AIAA Journal*, vol. 24, November 1986, pp. 1797–1801.

[50] Ottarsson, G. S. and Pierre, C., "A Transfer Matrix Approach to Vibration Localization in Mistuned Blade Assemblies," in *The Proceedings of the International Gas Turbine and Aeroengine Congress*, no. 93-GT-115, (Cincinnati, Ohio), May 1993.

[51] Davis, P. J., *Circulant Matrices*. New York: Wiley-Interscience, 1979.

[52] Hurty, W. C., "Dynamic Analysis of Structural Systems Using Component Modes," *AIAA Journal*, vol. 3, no. 4, 1965, pp. 678–685.

[53] Craig, R. R. and Bampton, M. C. C., "Coupling of Substructures for Dynamics Analyses," *AIAA Journal*, vol. 6, no. 7, 1968, pp. 1313–1319.

[54] Benfield, W. A. and Hruda, R. F., "Vibration Analysis of Structures by Component Mode Substitution," *AIAA Journal*, vol. 9, no. 7, 1971, pp. 1255–1261.

[55] Dowell, E. H., "Free vibrations of an arbitrary structure in terms of component modes," *ASME Journal of Applied Physics*, vol. 4, 1972, pp. 1145–1161.

[56] Ottarsson, G. S. and Pierre, C., "Vibration Localization in Mono- and Bi-Coupled Bladed Disks — A Transfer Matrix Approach," in *The Proceedings of the 34th*

AIAA/ASME/ASCE/AHS/ASC Structures, Structural Dynamics and Materials Conference, vol. 6, (La Jolla, California), pp. 3683–3697, April 1993.

[57] Ewins, D. J., "Structural Dynamic Characteristics of Bladed Assemblies," in *AGARD Manual on Aeroelasticity in Axial-Flow Turbomachines* (Platzer, M. F. and O'Carta, F., eds.), vol. 2, ch. 15, North Atlantic Treaty Organization (NATO), 1988.

[58] Murthy, D. V. and Pierre, C., "Stochastic Sensitivity Measure for Mistuned High-Performance Turbines," *NASA Technical Memorandum 105821*, 1992.

[59] Gumbel, E. J., *Statistics of Extremes*. New York: Columbia University Press, 1958.

[60] Castanier, M. P. and Pierre, C., "Individual and Interactive Mechanisms for Localization and Dissipation in a Mono-Coupled Nearly-Periodic Structure," *Journal of Sound and Vibration*, vol. 168, no. 3, 1993, pp. 479–505.

[61] Pierre, C., "Mode Localization and Eigenvalue Loci Veering Phenomena in Disordered Structures," *Journal of Sound and Vibration*, vol. 126, no. 3, 1988, pp. 485–502.

SUBJECT INDEX